COMSAT
Technical Review

Volume 14 Number 1, Spring 1984

COMSAT TECHNICAL REVIEW is published twice a year by Communications Satellite Corporation (COMSAT). Subscriptions, which include the two issues published within a calendar year, are: one year, $10 U.S.; two years, $15; three years, $20; single copies, $7; article reprints, $1.50. Air mail delivery is available at an additional cost of $10 per year. Make checks payable to COMSAT and address to Treasurer's Office, Communications Satellite Corporation, 950 L'Enfant Plaza, S.W., Washington, D.C. 20024, U.S.A.

COMSAT TECHNICAL REVIEW
Volume 14 Number 1, Spring 1984

Foreword

Dr. Pier L. Bargellini retired from COMSAT on January 1st of this year, just before celebrating his 70th birthday. Among his accomplishments during 15 years at COMSAT Laboratories was his founding of *COMSAT Technical Review* in 1971. Over the past 13 years, as Chairman of the *COMSAT Technical Review* Editorial Board, Dr. Bargellini established the *COMSAT Technical Review* as a significant technical journal by maintaining standards of quality at the highest levels. To found any new enterprise is a challenging task. To found and edit a magazine in other than one's first language is a true accomplishment and a tribute to the world view he brought from his Florentine background.

As Chairman of the *COMSAT Technical Review* Editorial Board, Dr. Bargellini is succeeded by Dr. Geoffrey Hyde, a student of his when both were at the University of Pennsylvania.

Joseph V. Charyk
Chairman of the Board and
Chief Executive Officer
Communications Satellite Corporation

Index: computer communications, error control, networks, small terminals

An international high-speed packet-switching experiment*

J. S. McCoskey, W. Redman, W. Morgart, B. Hung, and A. Agarwal

(Manuscript received June 14, 1983)

Abstract

An experimental high-speed data communications link between Clarksburg, Maryland, and Oberpfaffenhofen, Federal Republic of Germany, was established to field test and examine the performance of a communications processor in high-speed digital satellite circuits, and to demonstrate possible communications services. Two communications processors were connected via 1.544-Mbit/s links provided by rooftop earth terminals and 14/11-GHz spot beam transponders in an Atlantic Ocean region INTELSAT V satellite.

Experimental results showed that integrated services such as simultaneous freeze-frame teleconferencing, high-speed host file transfers, facsimile, and low-speed asynchronous terminal and host communications are possible. The effect of data communications protocols on throughput efficiency and overall network performance was investigated. A hybrid multiplexing scheme was implemented that allowed both stream and packet traffic to share a common channel.

*This paper is based on work performed at COMSAT and DFVLR under the sponsorship of the Communications Satellite Corporation and the German Aerospace Research Establishment. Parts of this paper were presented at the Sixth International Conference on Digital Satellite Communications, Phoenix, Arizona, September 1983, [1].

Introduction

In the past, COMSAT Laboratories and the German Aerospace Research Establishment (DFVLR) have jointly conducted experiments involving high-speed packet transmission via satellite. These early experiments verified the feasibility of connecting geographically distributed computers via high-speed satellite circuits; however, they also showed that substantial mainframe computing power was required to control and manage satellite networking functions [2]. Also, the necessary communications hardware and software for network interfaces had to be custom designed. These special requirements led to the development of a programmable interface processor (PIP), which controls all functions of the satellite network and provides network services such as virtual circuit establishment and control, transparent protocol conversion, and a network monitoring and control facility. Such a processor moves the task of network processing away from the host computers, freeing them for applications tasks. Interfaces to the PIP include well-defined and frequently implemented standard interfaces; however, the PIP can be programmed to match the interface characteristics of nonstandard devices.

This paper presents the results of recent experiments jointly conducted by COMSAT and DFVLR that involve high-speed international packet switching (HIPS), which demonstrated new techniques and technology, including a field test of the PIP developed by COMSAT Laboratories [3].

System Description

Figure 1 represents the system configuration of the HIPS experiment. Communication between the two processors was based on a full-duplex 1.544-Mbit/s satellite link established between rooftop earth stations located at COMSAT Laboratories and DFVLR headquarters. The space segment was provided by INTELSAT, using two 14/11-GHz spot beam transponders in an Atlantic Ocean Region INTELSAT V satellite (one transponder each for the west-east and east-west links). Four-phase phase-shift-keying (PSK) modems with rate 3/4 forward-error-correction (FEC) coding were used.

At each site, a PIP connected various data terminal equipment to the single high-speed channel interface of the modem/FEC hardware. In addition to the link control, switching, and multiplexing functions of the network, the PIP served as an intelligent interface between the data, voice, and video terminal equipment and the transmission subsystem. The PIP provided virtual circuit network interconnections for data terminal equipment by using protocols selected to perform well with a satellite transmission medium. Using the PIP hybrid multiplexer module (HMUX), statistically multiplexed virtual circuit

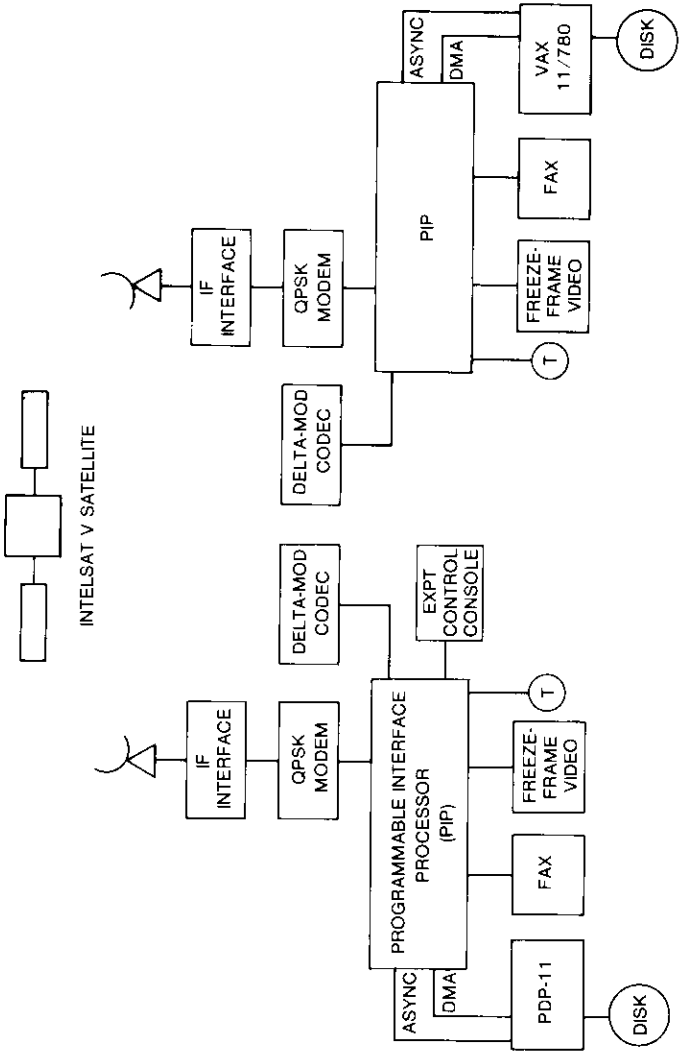

Figure 1. *System Configuration of HIPS*

(*i.e.*, packet) data are further multiplexed with synchronous end-to-end circuits. Data devices may connect to the PIP through either the packet interfaces or direct synchronous circuit interfaces. Data devices accessing the network with packet interfaces benefit from the high-integrity data transfer, increased utilization, and transparent compensation of satellite delay, which yield low delay and high-throughput data communications services.

The PIP implementation is based on a tightly coupled multiprocessor configuration (*i.e.*, multiple microprocessors closely interconnected through a high-speed parallel bus) and an optimized operating system that together provide the substantial computing power required for packet processing and interface functions at 1.544 Mbit/s.

The PIP HMUX module was programmed to interface with the packet statistical multiplexer, a 32-kbit/s delta-modulated speech codec, and with freeze-frame video codecs. Data from these sources were multiplexed into the 1.544-Mbit/s transmission channel by using the frame format and bandwidth allocation shown in Figure 2. Voice and packet input interfaces to the HMUX contain a "bandwidth-required" line activated by the source to capture its allocated share of the hybrid frame. The HMUX is programmed to allocate to video any idle bandwidth not required for voice or packets, on a frame-by-frame (2-ms) basis.

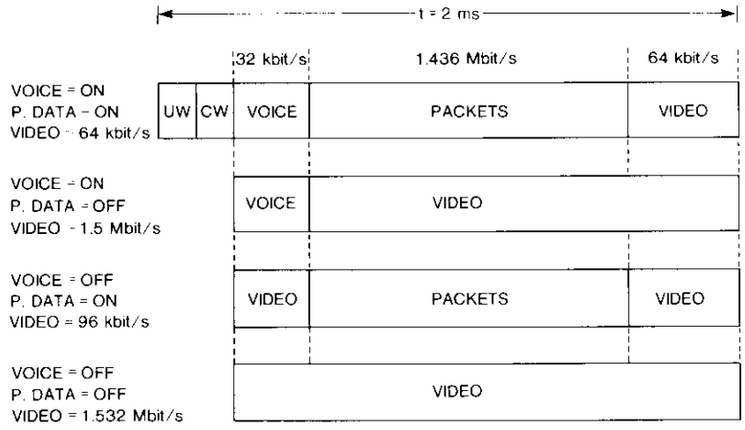

Figure 2. *Hybrid Multiplexer Frame Formats*

In addition to the interfacing and packet processing functions, the PIP contains an executive function that monitors and controls tasks such as accumulation of traffic statistics, network status, and error logging. Other features include remote control and a debugging capability, permitting an operator to exercise any module on the network as though it were a local module with a direct connection.

Experimental program

Objectives

Specific objectives of the HIPS experiment were as follows [3]:

a. to field test the PIP developed by COMSAT Laboratories and configured as a high-speed packet-switching network node;

b. to verify the performance of protocols for use with high-speed packet-switching services via satellite;

c. to demonstrate the support of integrated services and evaluate techniques used to support multiple service requirements through a single network; and

d. to verify and demonstrate an adaptive hybrid multiplexing scheme that provides both circuit and packet functions on a common channel.

The experimental program was conducted in three distinct phases:

a. transmission system performance verification and evaluation,
b. network protocol evaluation, and
c. applications evaluation.

Two kinds of transmission system performance experiments were used to examine the hardware elements of the network: modem and earth terminal testing and PIP hardware testing. The network protocol experiments examined the effect of various protocol parameters, traffic loads, and configurations on network performance. The applications experiments demonstrated and evaluated capabilities that could be provided by a high-speed satellite communications network.

Transmission system performance

The purpose of these experiments was to study the relationship between various transmission subsystem parameters and their effect on network performance. Error rates, propagation delay, and high-level data link control (HDLC) frame size all affected the overall network performance. These parameters were varied in this phase of the experimental program to observe the effects on transmission characteristics. Two categories of transmission system tests were conducted: first, the modem, FEC, and earth terminal equipment; then the PIP hardware.

TRANSMISSION CHANNEL CHARACTERIZATION

Before point-to-point satellite communications links were established, a series of tests was performed to examine the back-to-back bit-error-rate (BER) performance of each satellite modem, followed by loopback testing through the INTELSAT V satellite.

After the first sequence of modem/FEC tests, the communications system was configured with two point-to-point satellite links, allowing measurements of modem performance for each link. Test results in the form of C/N_o and BER measurements were gathered daily at the beginning of each test period. A representative portion of these results is shown in Figure 3, as measured at the Clarksburg site. The shaded portion of the figure corresponds to BER values that exceed 10^{-8}. The results show a considerable variation in the measured value of C/N_o. Several factors are likely to contribute to this variation, including differences in transmitted power levels, antenna pointing, satellite positioning, and atmospheric conditions.

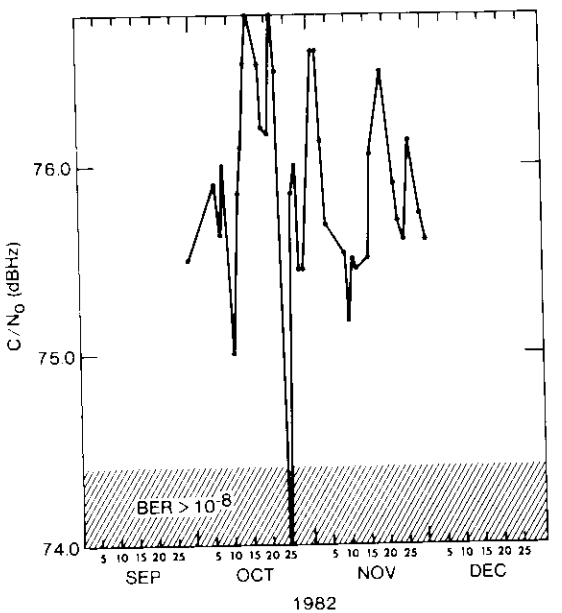

Figure 3. *Received Signal Levels at Clarksburg, October-November 1982*

PIP HARDWARE TESTING

A portion of the transmission system performance testing period was used to verify the correct operation of the satellite communications interface

module (SCIM) hardware of the PIP. This hardware, which controls all HDLC framing functions [including bit stuffing and frame check sequence (FCS) generation and checking] and transfers data frames to and from each PIP mass memory, is controlled by a single processor in each PIP.

The test configuration at each site consisted of a PIP with SCIM controlled by test software. Each SCIM was connected to a satellite modem, creating a bidirectional link between the two PIPs. This testing configuration did not include the adaptive HMUX between the SCIM and the satellite modem; hence, individual SCIMs were provided with the full 1.544-Mbit/s bandwidth for each link.

PIP HARDWARE THROUGHPUT TESTING

These tests consist of hardware PIP-to-PIP throughput measurements, which indicate the efficiency of the PIP hardware, without communications protocols, in using the satellite channel capacity to transfer blocks of data. The PIP SCIM hardware was designed to transfer data between the shared mass memory and the satellite channel with virtually no interframe idle periods (*i.e.*, HDLC flag sequences), which is the dominant hardware throughput factor in such a transfer. Other hardware throughput degradations are related to HDLC framing and consist of opening/closing flags, FCS character insertion, bit stuffing (for transparency), and frames with errors detected by FCS at the receiving SCIM.

Frame sizes and data patterns were varied for these tests, and the results are presented in Figure 4. Patterns provided two extremes of bit stuffing overhead. In the first test, an alternating one/zero pattern was used, which required no bit stuffing for data transparency within the HDLC frame. In the second set of tests, an all-ones pattern was used, with a zero insertion after each five data bits (hence, a 17-percent overhead addition because of bit

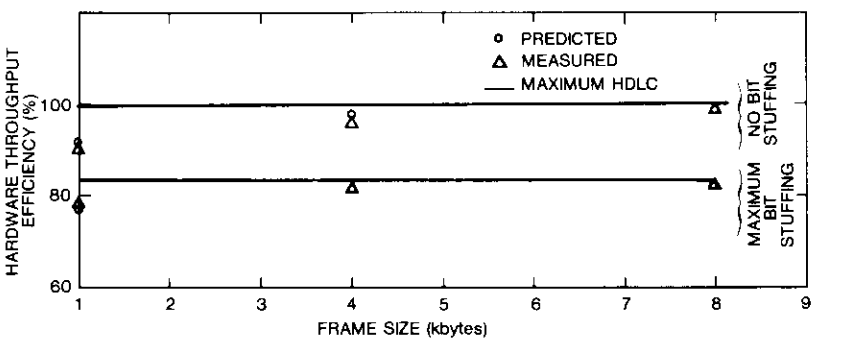

Figure 4. *PIP Hardware Throughput Results*

stuffing). Predicted points were based on measured interframe idle periods, and maximum HDLC values assumed a single flag between HDLC data frames (*i.e.*, no interframe idle periods).

Some deviation exists between the measured results and the theoretical HDLC maximum throughput for smaller frame sizes. Although the hardware transfers data with no periods of interframe idle, the software supporting this test caused approximately 270-μs delays in setting up the hardware, thus introducing a 270-μs interframe idle period between HDLC data frames. These delays resulted in channel utilization inefficiencies (thus reducing throughput), which increased as the HDLC frame size decreased.

PIP DATA ACCURACY TESTING

A series of tests was performed to verify the data accuracy of transfers between the two PIPs via the satellite communications links. A known data pattern was used as a transmitted frame, and those frames received without FCS-detected errors were compared to the known data pattern. These tests were performed in both directions and with various frame lengths and data patterns to ensure that no element of either PIP was injecting undetected errors into the data streams.

Network protocol evaluation

The objective of the protocol evaluation experiments was to examine the use of a specialized communications processor in high-speed satellite communications, as well as the throughput performance of such a system, by using a modified asynchronous balanced mode (ABM) HDLC protocol with a reject error recovery scheme [4]. Modifications included extensions of header fields and the addition of some fields. The format of each transmitted frame is shown in Figure 5.

Throughput performance was evaluated in a unidirectional mode with various transmitted data frame sizes and various HDLC maximum outstanding frame (MAXOUT) values.

Each PIP was configured with SCIM control software, a single traffic generator/sink pair, and HDLC software. The physical interconnection of the SCIM modules was via the HMUX connection; thus, the maximum data rate provided for packet traffic was 1.436 Mbit/s (see Figure 2). Only non-bit-stuffing patterns were used for this series of experiments, and the BER performance of each satellite link was less than 10^{-8}, simulating normal link conditions. Control parameters of frame size and HDLC MAXOUT were varied from 1 to 4 kbytes and from 1 to 255, respectively.

Results of throughput efficiency experiments are shown in Figures 6 through 9 for MAXOUT values of 1, 7, 127, and 255, respectively. Analytical

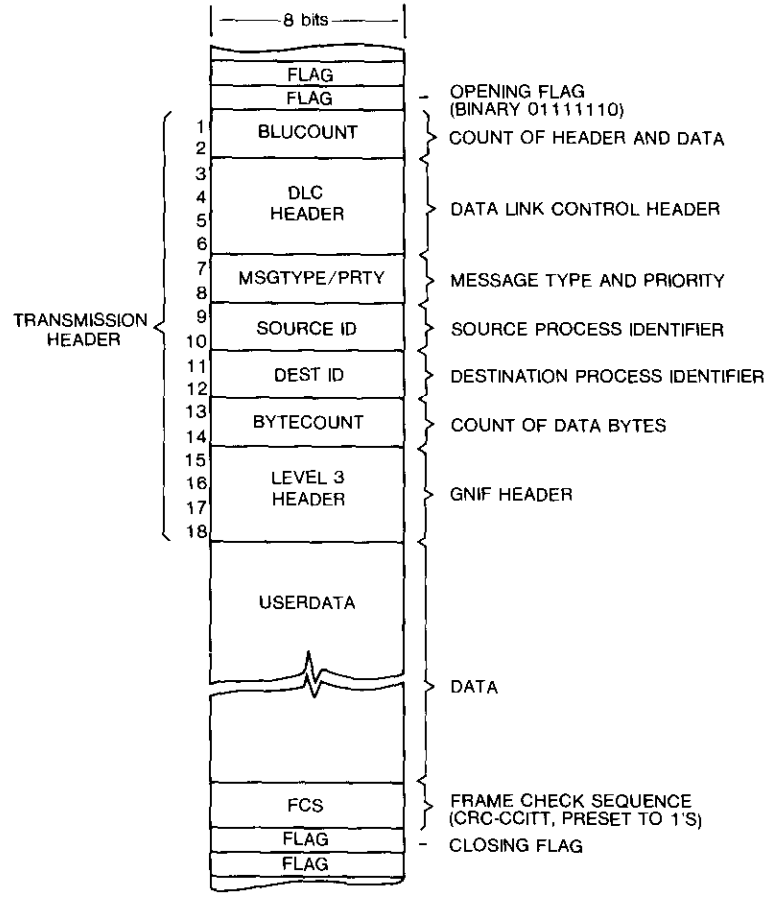

Figure 5. *Transmitted Frame Format*

results for both maximum theoretical HDLC performance and predicted network performance were based on a predictive model developed by Kaul [5]. The net throughput, η, for a full-duplex ARM HDLC link is

$$\eta = \frac{S(b-A)(1-S^N)}{b\{S(1-S^N)+(1-S)[2+d-(N+1)S^N]\}}; \qquad N < 1+d$$

$$\eta = \frac{S(b-A)}{b[1+(1+D)(1-S)]}; \qquad N \geq 1+d$$

where

N = MAXOUT parameter (or required buffer size in frames)
b = frame length in bits, including overhead
C = link capacity in bits per second
T_R = round-trip delay in seconds
$d = CT_R/b$ = round-trip delay in frames
$D = [d]^*$
S = probability of successful frame transmission (no errors or losses)
A = overhead bits per frame.

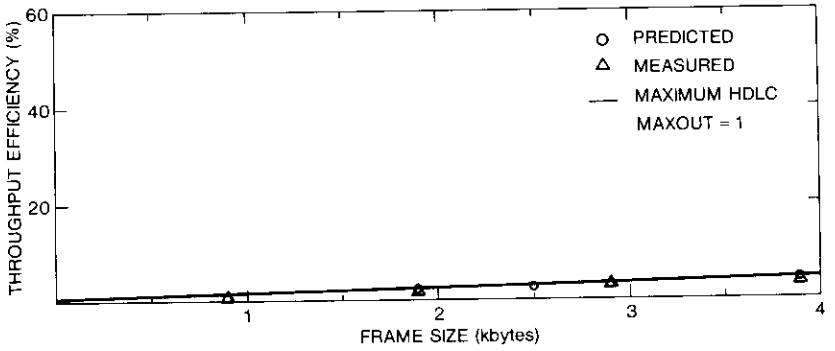

Figure 6. *Throughput Efficiency* vs *Frame Size, MAXOUT = 1*

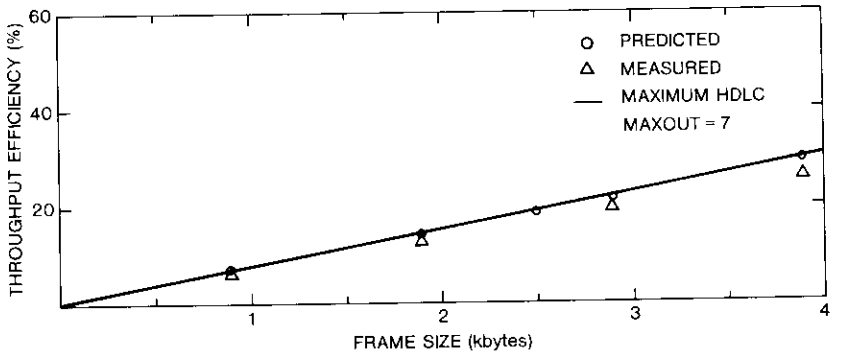

Figure 7. *Throughput Efficiency* vs *Frame Size, MAXOUT = 7*

* $\lfloor x \rfloor = x$ for integer x or the next highest integer value of x for noninteger x.

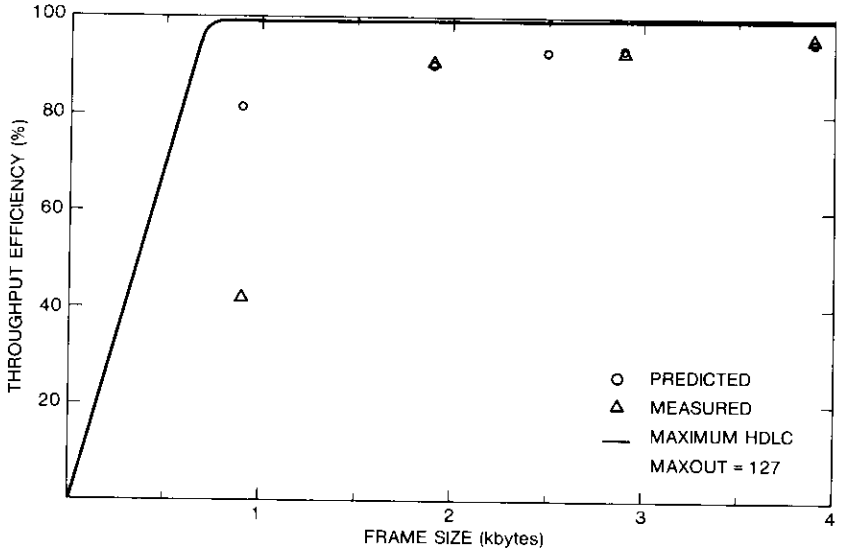

Figure 8. *Throughput Efficiency* vs *Frame Size, MAXOUT = 127*

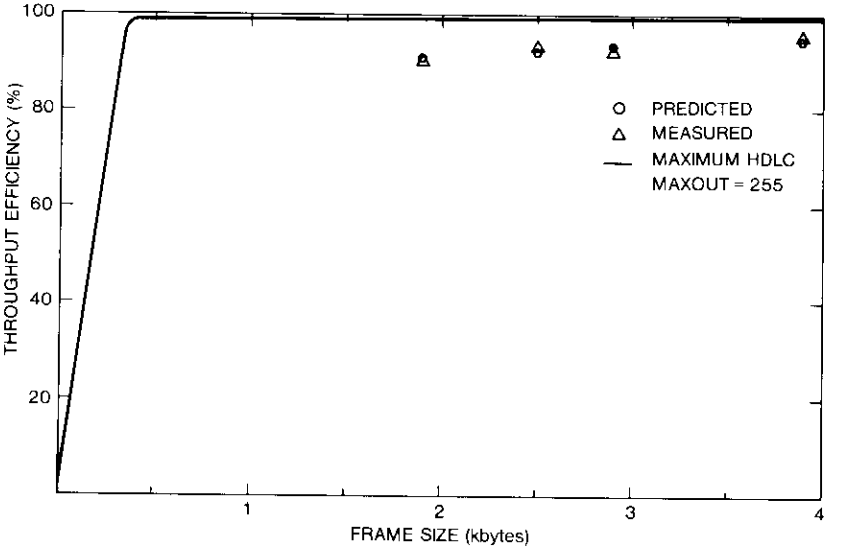

Figure 9. *Throughput Efficiency* vs *Frame Size, MAXOUT = 255*

The points for maximum HDLC performance on each of these figures were based on the following assumptions:

a. no bit errors on the link,
b. packet overhead consisting only of flag and FCS fields, and
c. no interframe idle periods (single flag between successive frames).

Predicted performance points were based on measured performance parameters. The BER was assumed to equal 1×10^{-9}; the interframe idle period (caused by software) was measured at 1 ms; and a round-trip propagation delay of 540 ms was used in the predictive model.

Deviation of the maximum HDLC case from the predicted network performance was caused primarily by the 1-ms interframe idle period required between frames for delays in software setup. For smaller frame sizes, this idle time occupied a larger portion of the available bandwidth, resulting in greater deviation. Also, the introduction of bit errors and the addition of overhead bits in each packet (18 bytes per packet) contributed slightly to the decrease in throughput efficiency. With a BER value of 1×10^{-9}, used for predicting results, and with frame sizes no larger than 4 kbytes, the effect of errors was negligible.

Comparison of predicted and measured results shows a close correlation between frame sizes of approximately 2 kbytes and larger. Variations in these larger frame sizes may be attributed to time measurement accuracy and to a slight variation in actual interframe idle periods. With frame sizes smaller than 2 kbytes, measured performance closely matches predicted performance, except with MAXOUT = 127.

The MAXOUT value used is a dominant factor in the throughput efficiency of high-rate satellite communications protocols. Figure 10 shows the relative performance of the network for various MAXOUT values associated with typical protocols. Thus, the figure also shows the expected performance for BISYNC (MAXOUT = 1), SDLC (MAXOUT = 7), and X.25 modulo 8 (MAXOUT = 7) protocols over the 1.544-Mbit/s satellite channel.

Link BER values were lower than 10^{-8} during most of the experimental period.

Applications

The objective of the applications experiment was to demonstrate the capability of a PIP-based network to provide integrated services (*e.g.*, multiple-media teleconferencing and host-to-host, terminal-to-host, and terminal-to-terminal communications) through a single, full-duplex satellite channel. Powerful network monitoring and control techniques were also evaluated and tested.

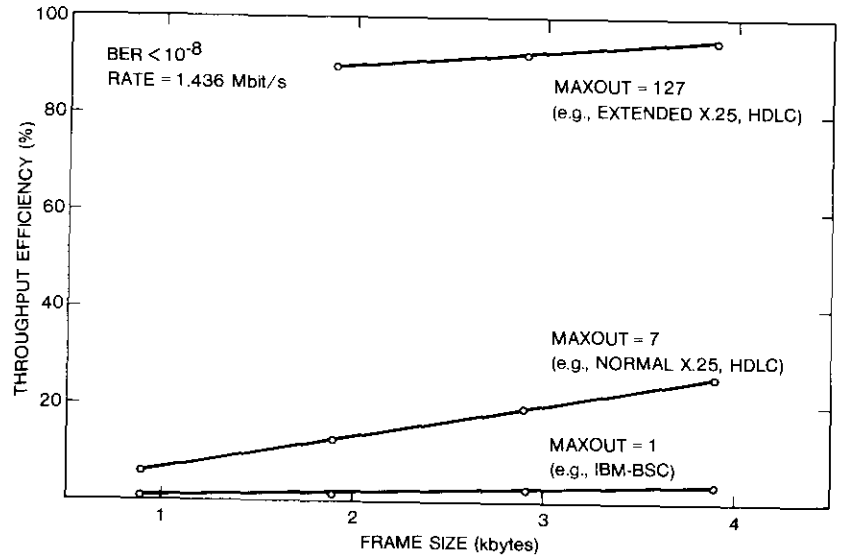

Figure 10. *Relative Throughput Efficiencies*

FREEZE-FRAME TELECONFERENCING

The freeze-frame teleconference capability of the network was subjectively evaluated during testing and via several conferences between COMSAT and DFVLR personnel. Voice communication was provided by the delta-modulation speech codec.

The evaluations showed that freeze-frame video at transmission rates of approximately 1.5 Mbit/s is quite acceptable for business conference use. The frame refresh rate of about three frames per second provided for effective face-to-face conferencing, after participants became accustomed to the jerkiness of movements and the lack of synchronization between audio and video. Close-up shots of participants exaggerated these weaknesses of freeze-frame conferencing; however, longer range shots of participants were generally acceptable, perhaps because lip movements cannot be distinguished (hence, the lack of audio synchronization is less evident), and also because the viewer has a larger viewing field composed of more static elements.

The effect of satellite delay was not significant, since audio and freeze-frame relationships were identical from room to room or over the satellite link conferences. The effects of transmission errors, however, were often noticeable as streaks or color changes on the received frozen images, which, in the case of a poor link (*i.e.*, a high error rate), were quite distracting. For use in such an environment, the video could be routed via a protocol protected

packet path rather than through the circuit path used for this experiment. This high-speed packet video service was being developed at the time of the HIPS experiment, but was not completed before the final experimental period. Since that time, the interface has been completed and provides error-free freeze-frame video service.

At rates of 96 and 64 kbit/s, the freeze-frame video was not effective for facial contact because of a frame update time of several seconds. At these rates, however, the video is still quite effective for slide or blackboard presentations.

The teleconference facility demonstrated in this experiment was based on small room setups and relatively low-cost equipment, not on the "million-dollar-room" philosophy. This low-cost approach makes it convenient to bring the facility to the users rather than requiring users to come to an expensive centralized facility. A diagram of one of the conference rooms used during the HIPS experiment is presented in Figure 11. With the high-resolution facsimile machine and terminals, the network supported a true multimedia conference facility.

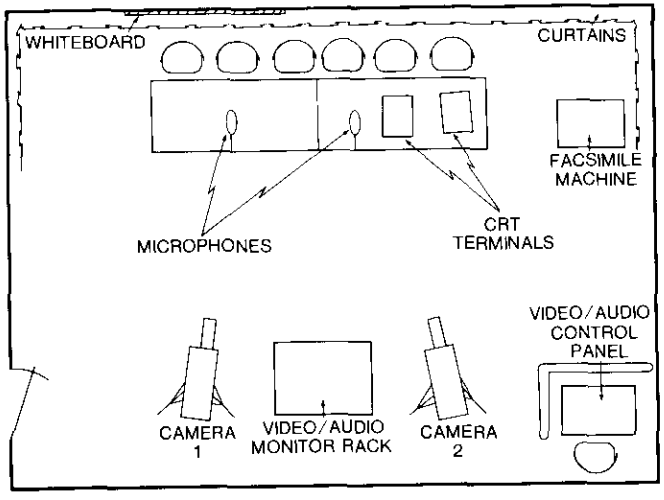

Figure 11. *Low-Cost Teleconference Room Layout*

Another capability tested during the teleconference applications experiment was a video control module that allowed a single operator to enter simple keyboard commands to control both freeze-frame video codecs from a single control terminal attached to the network.

Control functions included full or partial (upper only or lower only) screen transfer, continuous *vs* single frame transfer, camera selection, pause, reset, and monitor connection to either the input source or the received frozen picture. Each controllable feature had a corresponding status indicator, and the operator's console display was updated if a status changed. In this way, a teleconference operator could control the video parameters of the entire network through a single command terminal.

FILE TRANSFER EXPERIMENTS

The file transfer protocol (FTP) experiments verified the file-handling capabilities of the PIP-based network. A secondary benefit of the file transfer capability was the ability to down-line load software between the PIPs and to quickly transfer or store software or data.

The important performance parameter for file transfers is throughput, the effective, error-free transfer rate between the source and destination of a transfer. Figure 12 shows the throughput results obtained during the file transfer experiments, which provide a representative selection of possible sources, destinations, and file sizes (as shown in the legend to Figure 12). File transfer throughput was determined by dividing the file size by the time required to complete the transfer, which yielded the effective transfer rate. For example, in the case of the 4-hop handshake and file size 1 in Figure 12, the effective transfer rate was between 200 and 250 kbit/s. These throughput results are affected by the following major factors:

a. satellite hop delays during initial handshaking (*i.e.*, opening files for transfer),
b. limited buffer allocation, and
c. host computer disk access throughput.

Satellite propagation delays associated with the FTP process add overhead whenever a transfer occurs between the two remote PIPs. Depending on the mode of transfer, either two or four hops are required for this initial handshake exchange between the PIPs. This causes a delay of approximately 1 or 2 *s*, depending on the number of hops. For PIP transfers, which are accomplished within seconds, this factor has a significant effect on the measured throughput. Obviously, the shorter the file, the greater the effect will be on total throughput degradation.

Limited buffer allocation also causes degradation in the overall throughput of FTP transfers. The total number of buffers allocated to the FTP is essentially

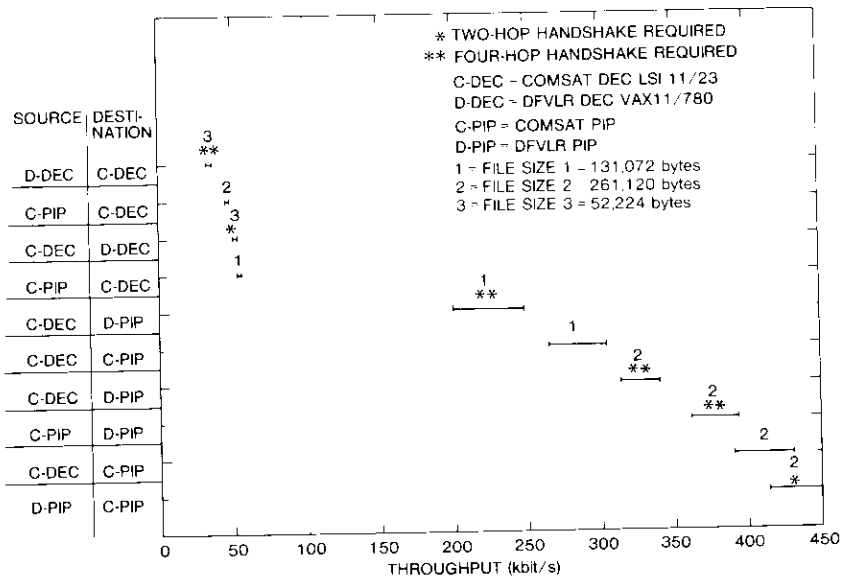

Figure 12. *File Transfer Results*

a flow control for the transfers, because idle periods occur when the sending process is waiting for buffers to be returned. In the present configuration, with 24 buffers of 1.5 kbytes each, the maximum effective throughput is approximately 500 kbit/s.

The final major factor that affects FTP throughput is the throughput of the DEC disk access mechanisms, since the speed of these access mechanisms is governed by software on the DEC computers and by the disk hardware itself. This overhead is especially noticeable with disk writing on the COMSAT LSI-11/23 computer. Since the LSI-11/23 is not an especially powerful computer and the disk writing process implemented uses a sector-by-sector linked list, the resulting throughput is low. Measurements have shown that if disk accesses are removed from transfers to the LSI-11 computer, throughput values above 300 kbit/s are obtained between the associated PIP memory and the computer memory. Measurements of throughput on file reads from either the LSI-11/23 disk or memory show that degradation caused by disk read accesses is indistinguishable from that of direct memory reads.

One additional effect on the file transfer throughput results was caused by inaccuracies in measuring the time required for each transfer. An inaccuracy of ± 0.25 *s* was assumed. This effect is reflected in Figure 12 as a throughput range for each test (*e.g.*, the range of 200 to 250 kbit/s for the example discussed above).

Improvements in FTP performance may be achieved by using contiguous files on disks rather than linked lists, which require increased processing. Also, more powerful computers can increase disk throughput. If faster file transfers are required between two PIP systems, the buffer allocation to the FTP processes must be increased within each PIP. With these improvements, the throughput of the PIP system should be maximized.

ASYNCHRONOUS TERMINAL/HOST APPLICATIONS

The asynchronous terminal interface modules in each PIP allowed the connection of terminal-to-terminal, terminal-to-host, and asynchronous host-to-host ports between either colocated or remote devices. Experiments with these connections helped in evaluating various transfer techniques such as line-level and transparent transfer schemes. In the line-level transfer scheme, characters were buffered until a forwarding character (carriage return) was received, at which time the string of buffered characters entered the network as a packet. In this mode, local echoing of characters is provided for cathode-ray tube (CRT) terminals, along with some editing functions (*e.g.*, backspace, line delete). In the transparent transfer mode, characters are buffered and the contents of the buffer are delivered to the network periodically (in milliseconds) without the need for a forwarding character. Character echo was optionally configurable as local or remote, to evaluate the effect of satellite delay on the echo path. With the local echo options, satellite delay was indistinguishable from host delays and command response times.

Any terminal could connect to any other asynchronous port simply by entering a 4-digit code corresponding to the associated port. This code could be extended if additional port numbers were to be supported. Once established, the connection could then be disconnected or reset at any time by either of the connected ports. The key to this adaptable system is its ability to support direct terminal-to-terminal communications without a host computer. Such a capability is necessary in providing effective advanced network services to users.

FACSIMILE

The facsimile applications experiment consisted of testing facsimile transfers by using the various page sizes and resolution modes available on the facsimile equipment. Because of the nature of the machines used, facsimile transfers were available only in a half-duplex mode. Each side could, however, initiate a facsimile transfer as long as a transfer was not already in progress. As expected, the received facsimile copies showed no traces of error streaks [since there was automatic repeat request (ARQ) protection of data], although the quality was sometimes poor because of incorrectly adjusted elements in the machines themselves (*e.g.*, toner flow).

Although only two facsimile machines were used for this experiment, the network provides for switched fax-to-fax connections. The facsimile services were a powerful addition to the teleconferencing facilities, as described below in the section on Integrated Services.

NETWORK MONITORING AND CONTROL

Facilities within each PIP performed executive functions that centralized the control and monitoring of the entire network. The following capabilities of the executive facilities were evaluated:

a. HDLC link monitoring and control,
b. remote control of the system executive module in the remote node,
c. exercising of local executive functions in various modules,
d. control of the traffic emulation software,
e. auto-polling of system status changes,
f. control of all video codecs, and
g. control of the file transfer facility.

The HDLC link monitoring and control functions allowed an operator at the executive console to examine the status indicators from the HDLC control software in each PIP. Also, the HDLC modules could be set to a tracing mode, which displayed on the console all transmissions, receptions, and retransmissions. The message type was identified, and associated header fields were displayed on the console, as shown in Figure 13.

The remaining HDLC controls could change various protocol parameters (*e.g.*, MAXOUT), initialize or reset the link between HDLC modules, and drop specified fractions of received packets to simulate transmission errors.

Each PIP provided executive monitoring and control facilities for devices connected to itself, and a remote control capability allowed an executive in one PIP to control the executive in the other. In this way, a single module could initiate all executive functions at both the local and remote PIP, thus forming an executive for the entire network. This capability allowed experimenters at Clarksburg to configure and monitor the equipment at Oberpfaffenhofen. An additional benefit of the remote-control capability was a text message path between the system executive consoles of the two PIPs. This message path allowed 'silent' communication (useful for teleconference operator applications) and also a teletypewriter-like record of messages if a hardcopy console was used.

Local executive functions such as module memory read/write were used primarily for debugging and not during the actual experimental period. These functions allowed an operator to examine and modify software and data fields


```
NSS  NSR  NSA  MAXOUT
0005 000B 0005 0100

                                    TX          RX
                                  ---------   ---------
Valid Data Frames ..... 0000 0005   0000 000B
Command Frames ........ 0000 000B   0000 0005
Data Frames Rtx/dropped ... 0000 0000   0000 0000
RR ..................... 0000 000B   0000 0005
RNR .................... 0000 0000   0000 0000
REJECTS ................ 0000 0000   0000 0000
Time-outs/Bad Recvd Pkts .. 0000 0000   0000 0000
```

```
     TYPE          CMDPS PFPR DMMB SADR DADR USD1 USD2
Command out :  0006 0100 000F FE1A 0115 0215 0000 0000
Input Frame :  0000 020F 500F FFCB 020D 010D 011E 0000
Input Frame :  0000 0210 530F FF8B 020D 010D 0003 0009
Command out :  0006 0100 0010 FE1A 0115 0215 0000 0000
Command out :  0006 0100 1011 FE1B 0115 0215 0000 0000
```

Figure 13. *HDLC Trace Mode and Status Examples*

within a module without using a console connected directly to that module.

From the executive console, an operator could invoke any of the possible traffic emulation facilities. These emulators were used to measure the performance of various communications paths in the network. As with other network executive controls, these traffic emulators can also be controlled from a console connected directly to the traffic emulation module. In fact, since the network executive is connected in parallel with the direct console, use of the executive does not preclude or affect the direct connection.

A useful executive facility, referred to as the "auto-poiler," provided an operator with the status of the various modules in each PIP. The operator entered a list of modules to be polled, and the polling function scanned the list sequentially, soliciting responses from the addressed modules. If a module failed to respond, it was flagged as "down." Messages were sent to the executive console only if a change in status occurred. The current status of all modules on the poll list could be questioned at any time, and individual modules could be added or deleted from the list.

With the executive remote control facility, a single console could be used for all operational and experimental functions of the network. This does not preclude the use of individual consoles for controlling modules; rather, a parallel path can be provided for these controls. Extension of the facility to

a multiple-node network is valid because the powerful monitoring and control capabilities from a single point within such a network would be a useful, valuable asset.

INTEGRATED SERVICES

The final phase of the HIPS experiment was the evaluation and demonstration of integrated services support by the experimental network. In this phase, various interfaces were implemented simultaneously. The resulting configuration was then evaluated with actual teleconference applications. Specifically, simultaneous communications were established by using the following:

a. freeze-frame video,
b. terminal-to-terminal and terminal-to-host communications,
c. high-resolution facsimile,
d. file transfers between minicomputers, and
e. various monitoring and control capabilities (including control of the video codecs).

Operators of the freeze-frame video equipment quickly learned to avoid close-in shots of participants' faces to avoid the lack of audio/video synchronization inherent in freeze-frame systems; wide-angle views of participants, figures, or blackboards were used. In fact, the color transmission of both figures and blackboards (a "whiteboard" with felt-tip markers worked best) was extremely effective with the freeze-frame video.

One major area of interest was the effect of sharing a common channel between the freeze-frame video and other preemptive data sources, such as delta-mod speech, facsimile, file-transfer, and terminal data sources. Because of the bursty nature (high peak-to-average ratio) of the packet data sources, their effects on the freeze-frame video were limited.

It should be noted that these packets of data are transmitted at 1.436 Mbit/s; however, because of the short time required to send them at such high rates, the video codec is also perceived to perform at a continuous 1.5-Mbit/s transmission rate (see Figure 2). In fact, for terminal-to-terminal, terminal-to-host, facsimile, and monitoring and control paths, the slowing down of video frames could not be visually observed. When using the file transfer facility for large files, the slowing down was seen as a very short freeze in the frame update, but only in the wipe mode of display. In the flip-flop mode, even this was not perceptible. This effect of both video and data appearing to be transferred at about 1.5 Mbit/s through a single 1.5-Mbit/s channel was observed as long as the data were bursty, as is usually the case. The effects of the 32-kbit/s speech channel were also imperceptible, even while the speech data were being switched in and out of the shared channel.

Satellite delay effects were noticed in two cases: audio echo and remote host character echo for terminal connections. Audio echo is to be expected with any satellite teleconference configuration, and echo cancellation equipment should be used to eliminate this problem. For the HIPS experiment, an echo canceller developed by COMSAT Laboratories was used. As mentioned above, it is desirable to use a local echo of characters to a terminal rather than a remote echo, which is delayed by both satellite propagation and host processing.

Conclusions

Efficient use of high-speed satellite circuits may be achieved by employing a specialized communications processor. With transparent protocol conversion and device control, a network can be optimally designed to take advantage of high-speed satellite circuit characteristics while interfacing with a number of different devices. Without such an optimized system, many existing user protocols result in performance degradation caused by satellite propagation delay. An important aspect of this technology, as applied to host-to-host computer communications, is the removal of the communications processing load from host computers. With a hybrid multiplexing technique, the programmable interface processor makes efficient use of satellite resources by combining packet and circuit traffic on a common channel in a demand-assigned manner. This ability to support both packet and circuit channels results in an extremely flexible interfacing capability that can support many different devices. The easily reconfigurable and upgradable multiprocessor-based node is a powerful tool for research and development activities aimed at the implementation of protocols specifically designed for high-speed satellite communications.

The network described in this study can perform an acceptable teleconferencing function and simultaneously support other data traffic, such as terminal, host, and facsimile transfers. It was also demonstrated that a low-cost room can be used to implement a powerful teleconferencing facility on a user's premises.

Extensions of the experimental work presented here will include networks with multiple nodes and multiple satellites. Integrating newer generations of processors into the modular communications processor will allow greater processing power and increased flexibility. Also, recent advances in video processing technology should substantially improve teleconferencing with full-motion video at reduced data rates.

Acknowledgments

The authors thank everyone involved with the planning, implementation, and execution of this packet-switching experiment. Special thanks to A. Kaul and W. Cook at COMSAT Laboratories, and to H. Dodel and H. Lang at DFVLR, without whom this experiment could not have taken place.

References

[1] A. K. Kaul et al., "An Experiment in International High-Speed Packet Switching via Satellite," Sixth International Conference on Digital Satellite Communications, Phoenix, Arizona, September 19–23, 1983, *Proceedings*, pp. II.34–II.43.

[2] W. Cook et al., "An International Experiment in High-Speed Computer Networking via Satellite," *COMSAT Technical Review*, Vol. 10, No. 1, Spring 1980, pp. 27–89.

[3] A. K. Kaul et al., "An Experiment in High-Speed International Packet Switching," AIAA 9th Communications Satellite Systems Conference, San Diego, California, *Proc.*, 1982, pp. 130–134.

[4] International Standards Organization, Documents ISO 4335-1979 (E); ISO 4335-1979/Add. 1-1979 (E); ISO 4335-1979 (E)/Add. 2-1982 (E); and ISO 6256-1981 (E), American National Standards Institute, New York.

[5] A. K. Kaul, "Performance of High-Level Data Link Control in Satellite Communications," *COMSAT Technical Review*, Vol. 8, No. 1, Spring 1978, pp. 41–87.

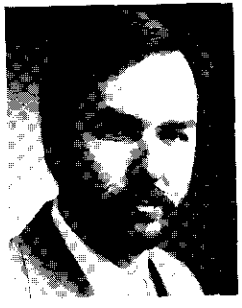

John S. McCoskey received a B.S.E.E. degree in 1979 from Bucknell University and an M.S. degree in computer science from The Johns Hopkins University in 1984. He joined COMSAT Laboratories in 1979 and is currently a Member of the Technical Staff in the Network Analysis Department of the Network Technology Division. Since joining COMSAT, he has been involved in the design of advanced computer architectures and networks. His current responsibilities include research activities directed toward the analysis of data communications networks and architectures for use with data communications, teleconferencing, and business satellite networks.

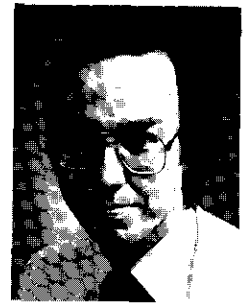

Wayne A. Redman received a B.S.E.E. degree from McGill University in 1975 and an M.S.E.E. degree from Carleton University, Ottawa, Canada, in 1977. Before joining COMSAT Laboratories, Mr. Redman worked at Carleton University as a systems programmer in the specification, design, and implementation of communications software in a multi-microprocessor-based node operating in a packet communications network. Mr. Redman joined COMSAT in 1977 as a Member of the Technical Staff. Since that time, he has acted as Project Manager for development of the programmable interface processor (PIP) and was responsible for the development of several hardware and software modules within the PIP. Currently, Mr. Redman is Manager of the Network Processing Department, where he continues his work in the design and development of multiprocessor-based communications systems that act as nodes in various network topologies.

William S. Morgart received a B.S.E.E. degree from Carnegie-Mellon University in 1979. Since joining COMSAT Laboratories in 1979, Mr. Morgart has been a Member of the Technical Staff in the Network Processing Department. He is responsible for the design of the programmable interface processor (PIP) operating system, programmable interface processor multiprocess operating system (PIPMOS), as well as several of the device interfaces used in the high-speed international packet-switching (HIPS) experiment.

Brian T. Hung received a Bachelor of Engineering (Electrical) degree from the University of Canterbury, New Zealand, and an M.S.E.E. degree from the University of South Carolina. He joined COMSAT Laboratories in 1979, and is a Member of the Technical Staff in the Network Processing Department. His work at COMSAT has included development of the programmable interface processor (PIP) bus controller, the PIP/host computer interface, and the X.25 level 3 interface. Mr. Hung is a member of IEEE, Tau Beta Pi, and Eta Kappa Nu.

Anil K. Agarwal received a B. Tech in electrical engineering from the Indian Institute of Technology, Bombay, India in 1979, and an M.S. degree in computer science from the University of Maryland in 1981. He joined COMSAT Laboratories in 1981, where he is Assistant Manager of the Network Processing Department. He has been involved in various projects in the development of computer networks, advanced computer architectures, operating systems design, and facsimile and multimedia message systems. He is member of the IEEE.

Index: interference, modulation, demodulation, modems, synchronization

Carrier synchronizer for overlapped raised cosine pulse amplitude modulation

W. C. HAGMANN

(Manuscript received November 11, 1983)

Abstract

It is well known that high bandwidth efficiency can be achieved by the use of a signaling scheme with overlapping signal pulses. Such schemes can result in appreciable intersymbol interference (ISI), which deteriorates the detection and synchronizer performance. This paper describes the ISI effects on an 8-phase PSK carrier synchronizer and illustrates the necessary analysis procedure for this special case. The computations are based on a raised cosine pulse shape with 50-percent overlap to each side. The demonstrated methods are equally applicable to any other pulse shape.

The effects of ISI on carrier synchronization can easily be reduced by a simple transverse equalizer in conjunction with the synchronizer. Equations are derived for the tracking variance resulting from both additive white Gaussian noise (AWGN) and the self-noise associated with ISI. Computer simulation results for carrier synchronizer performance, with and without ISI equalization, are in close agreement with theoretical predictions from derived equations.

Introduction

On many of today's communications links, high bandwidth efficiency (the number of transmitted bits per second per Hertz of bandwidth) and rapid spectral fall-off must be achieved to conserve the available spectrum. Spectral efficiency can be achieved by either increasing the number of signals in the

signal space (increasing the number of bits per symbol) or by introducing intentional correlation between the channel symbols. Either approach can yield a significant decrease in the channel bandwidth requirements and hence increase the spectral efficiency. The introduction of intentional correlation between the channel symbols provides the additional benefit of fast spectral roll-off. Naturally there is a penalty associated with achieving higher spectral efficiency, since nature is not normally so generous as to enable improvements without any side effects. One penalty is a more difficult carrier synchronization recovery.

Both methods used to obtain spectral efficiency are closely related, because the introduction of correlation between the channel symbols in essence results in an increase of the number of signals in the signal space and a reduced distance between them, as is demonstrated in this paper.

Either method affects the recovery of a coherent carrier in two ways. First, the reduced distances between the signals in the signal space require a more accurate carrier reference to maintain detection performance at an acceptable level. Second, in a more complicated signal space, the loss associated with modulation removal is generally greater. (This loss is sometimes termed "squaring loss" for cases in which squaring or frequency doubling are used to remove modulation.)

Earlier studies, such as References 1 and 2, have dealt with combined adaptive equalizers and synchronizers. Equalizers are most frequently applied over channels with a time-varying amount of ISI caused by channel filtering and line switching, as in telephone channels. In such applications, it is necessary to employ adaptive equalization to obtain the best possible system performance.

The case discussed in this paper assumes a quasi-linear AWGN channel with a constant channel characteristic that causes ISI by intentional pulse overlapping. Such a technique might be employed in satellite communications with single-channel-per-carrier (SCPC) communications to increase the number of channels per satellite transponder. In such cases, even very simple transversal equalizer structures result in large performance improvements. Furthermore, with an AWGN channel, it is possible to evaluate the effect of self-noise on synchronizer performance.

The tracking performance of a carrier synchronizer is influenced by the additive white Gaussian channel noise and by self-noise, which is caused by pulse shaping or correlation between adjacent symbols. Self-noise is normally neglected in the performance analysis of carrier synchronizers. This is justified in cases where no intentional correlation is introduced between adjacent symbols as, for example, in quadrature phase-shift keying (QPSK) and minimum-shift keying (MSK) systems. A mathematical justification for

neglecting the self-noise can be given by observing that its power spectral density has a zero at the nominal carrier frequency [3].

For intentional symbol correlation, neglect of the self-noise may no longer be justified. However, the effects of the ISI on synchronizer performance can be reduced by either narrowing the synchronizer bandwidth or canceling most of the ISI effects with an equalizer. ISI equalizers are often used to improve detection performance. For the present application, ISI equalization is also used to improve synchronization performance. This paper shows the basic methods which can be used to evaluate synchronizer performance, taking into account the self-noise for a special class of sampled carrier synchronizers that employ decision-directed feedback. Carrier synchronizer performance is evaluated with and without the equalizer to demonstrate the performance gain attributable to ISI equalization. Most of the derivations are given for the special example of an overlapped raised cosine pulse shape applied to 8-phase PSK modulation. The results are applicable to any other quadrature amplitude modulation (QAM) scheme with an arbitrary pulse shape.

The sections that follow evaluate the ISI that is generated by pulse overlapping and describe the effect of ISI on signal space. It is shown that the ISI effects can be reduced drastically by processing the received signal with a simple fixed ISI equalizer. A statistical model of the ISI phase process is developed and used to evaluate synchronizer performance. Lastly, the effects of decision feedback errors on synchronizer performance are discussed and the results are summarized.

ISI for overlapped raised cosine pulses

The transmitted signal is assumed to be of the form

$$s(t) = Re\{[x(t) + jy(t)]e^{j(\omega t+\theta)}\} \tag{1}$$

where $x(t)$ and $y(t)$ are the in-phase and quadrature baseband modulation signals given by

$$x(t) = \sum_{k=-\infty}^{+\infty} a_k g(t - kT) \tag{2a}$$

$$y(t) = \sum_{k=-r}^{+\infty} b_k g\left(t - kT - \ell\frac{T}{2}\right) \quad . \tag{2b}$$

The pair (a_k, b_k) represents the coordinates of the k-th symbol in the symbol space, $\ell = 0$ for unstaggered timing alignments of a_k and b_k, and $\ell = 1$ for

staggered signaling. It is assumed here that $\ell = 0$ (the staggered case will be explained later) and that the pulse, $g(t)$, is of the form

$$g(t) = \begin{cases} \frac{1}{2}\left[1 - \cos\left(\frac{2\pi t}{\tau}\right)\right] & 0 \le t \le \tau \\ 0 & \text{otherwise} \end{cases} \quad (3)$$

where τ is the pulse time duration. Austin and Chang have shown that this pulse shape results in a transmitted signal spectrum with a narrow main lobe and fast roll-off [4].

If the detection is based on a matched filter receiver matched to the τ-second-long pulse, $g(t)$, as in Figure 1, then the output of the matched filter in either the in-phase or quadrature channel resulting from a pulse i symbols removed from the desired one is

$$\begin{aligned} X_i(t;\tau) &= \frac{1}{4}\int_{iT}^{\tau}\left[1 - \cos\left(\frac{2\pi t}{\tau}\right)\right]\left[1 - \cos\frac{2\pi(t - iT)}{\tau}\right]dt \\ &= \frac{1}{4}\left[(\tau - Ti) + \frac{3\tau}{4\pi}\sin\left(\frac{2\pi Ti}{\tau}\right)\right. \\ &\quad \left. + \frac{(\tau - Ti)}{2}\cos\left(\frac{2\pi Ti}{\tau}\right)\right] \end{aligned} \quad (4)$$

where τ is the pulse duration and T is the pulse spacing; that is, T^{-1} is the symbol rate and $iT < \tau$. The maximum occurs for

$$X_0(T;\tau) = \frac{3\tau}{8} \quad ; \quad (5)$$

therefore, the normalized matched filter output can be defined as

$$\begin{aligned} h_i(T;\tau) \triangleq \frac{X_i(T;\tau)}{X_0(T;\tau)} &= \frac{2}{3}\left[1 - \frac{iT}{\tau} + \frac{3}{4\pi}\sin\left(2\pi\frac{iT}{\tau}\right)\right. \\ &\quad \left. + \frac{1}{2}\left(1 - \frac{iT}{\tau}\right)\cos\left(2\pi\frac{iT}{\tau}\right)\right] \end{aligned} \quad . \quad (6)$$

Table 1 shows some values of the relative ISI attributable to the nearest neighbors at the sampling instant as a function of T/τ.

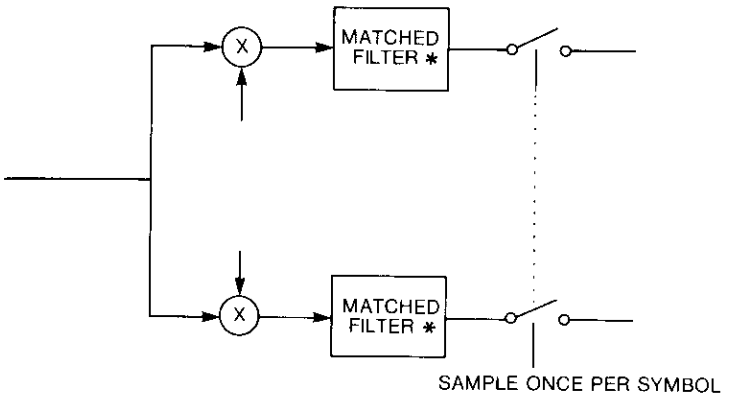

* MATCHED TO τ-SECOND-LONG PULSE

Figure 1. *I-Q Receiver Structure*

TABLE 1. NORMALIZED ISI DUE TO NEAREST NEIGHBOR

T/τ	$h_i(T;\tau)$
1.0	0
0.5	1/6
0.33	0.47
0.25	0.66
0	1

The numerical examples given in this paper treat only the special case where the pulse duration is equal to two symbol durations, $\tau = 2T$. In this case, the magnitude of ISI from an adjacent pulse is one-sixth of the magnitude of the detected value resulting from the desired symbol.

Effect of ISI on signal space

Once the values $h_i(T;\tau)$ are known, the in-phase and quadrature values at the detection sampling points U_i and V_i can be computed as

$$U_i = \sum_{k=-K_-}^{K_+} a_{i+k}\, h_k(T;\tau) \quad (7a)$$

$$V_i = \sum_{k=-K_-}^{K_+} b_{i+k}\, h_k(T;\tau) \quad (7b)$$

where the pair (a_i, b_i) is the set of coordinates of the i-th signal, and K_- and K_+ are the number of symbols preceding and following symbol i, respectively, that influence the value of the i-th detection sample.

For the special case of 2-symbol raised cosine pulses, the general formulas reduce to

$$U_i = \frac{a_{i-1}}{6} + a_i + \frac{a_{i+1}}{6} \tag{8a}$$

$$V_i = \frac{b_{i-1}}{6} + b_i + \frac{b_{i+1}}{6} \quad . \tag{8b}$$

In the present case, (a_i, b_i) is one of the possible 8-phase signal points, as shown in Figure 2.

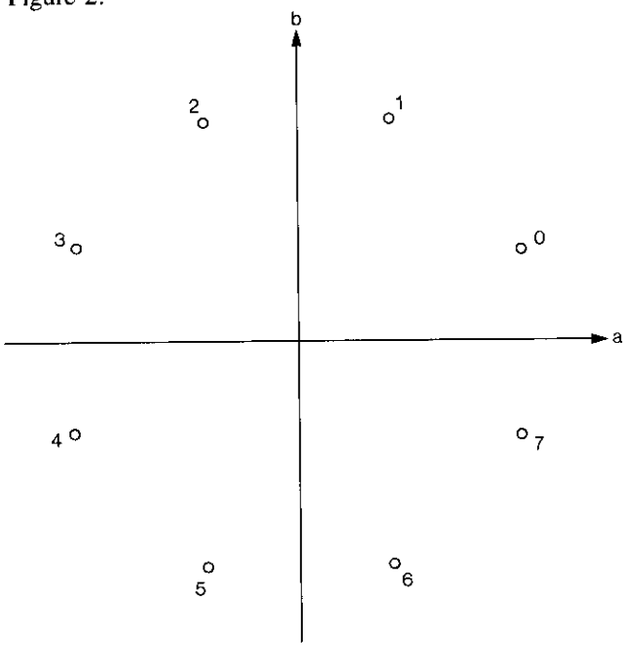

Figure 2. *8-Phase Signal Set*

To demonstrate the signal space expansion, the i-th signal can be fixed at, say, octal symbol 0 (see Figure 2). In this case, $a_i = 0.924$ and $b_i = 0.383$. The expansion of the signal space is then attributable to the effects of the two adjacent symbols (a_{i-1}, b_{i-1}) and (a_{i+1}, b_{i+1}). The resulting signal points at the sampling instant (U_i, V_i) are illustrated in Figure 3. It can be seen

from these evaluations that the ISI results in a large spread in the signal space. With regard to detection, either an extended-state Viterbi decoder [5] or a simple transversal equalizer can be employed to counteract ISI effects. Without some form of ISI reduction, the synchronizer cannot perform well on the expanded signal set, since self-noise would result in a greatly increased phase error variance. The situation for the synchronizer can be improved in two ways: by decreasing the synchronizer bandwidth and/or reducing ISI by equalization.

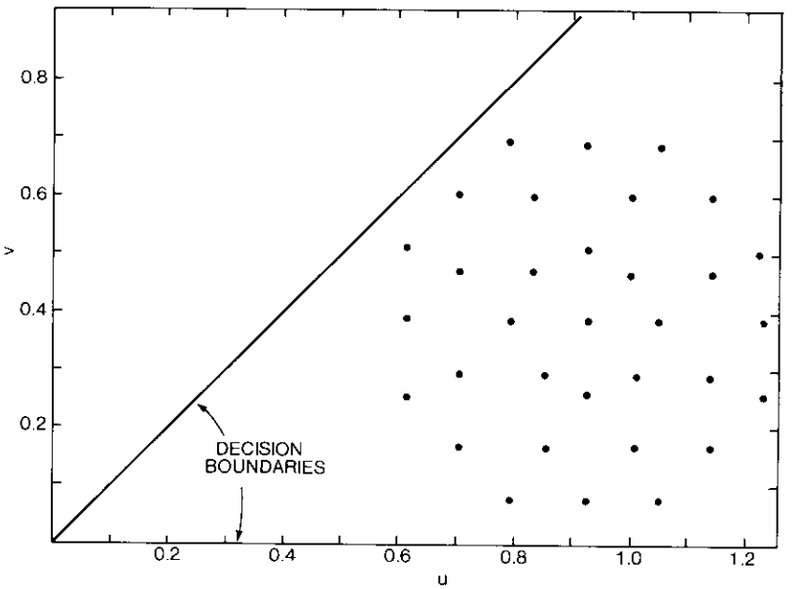

Figure 3. *Signal Spread for Signal 0 Without Equalization*

Decreasing the synchronizer bandwidth can help to reduce the pattern-induced phase error in uncoded systems because decision errors are rare. The only penalty resulting from the narrower synchronizer bandwidth is an increased acquisition time. In coded systems, however, ISI equalization may be necessary to achieve a symbol error probability sufficiently small so that errors in the decision feedback produce only a small performance loss. A more detailed discussion of this effect follows in a later section.

Reducing ISI effect on synchronizer by equalization

For a linear channel, the ISI effect can be predicted from the results given above. Instead of making symbol decisions and phase error measurements

for the synchronizer on the basis of the samples (U_i, V_i) given by equation (7), the synchronizer can be based on the pair (X_i, Y_i) given by

$$X_i = \sum_{\ell=-K_-}^{K_+} g_\ell U_{i+\ell} \tag{9a}$$

$$Y_i = \sum_{\ell=-K}^{K_+} g_\ell V_{i+\ell} \quad . \tag{9b}$$

The values $\{g_\ell\}$ correspond to the tap gains of a transversal equalizer. Appendix A shows how these gains can be computed to satisfy a minimum mean-squared-error criterion. For the special case of interest here, the following assignment results in a drastic reduction of the ISI. Let

$$X_i = -U_{i-1} + 6U_i - U_{i+1} = -\frac{a_{i-2}}{6} + \frac{17}{3}a_i - \frac{a_{i+2}}{6} \tag{10a}$$

$$Y_i = -V_{i-1} + 6V_i - V_{i+1} = -\frac{b_{i-2}}{6} + \frac{17}{3}b_i - \frac{b_{i+2}}{6} \tag{10b}$$

where the two expressions on the right were obtained by using equation (7). Normalizing (X_i, Y_i) by 3/17 yields

$$X_i^n = \frac{3}{17}(-U_{i-1} + 6u_i - U_{i+1}) = -\frac{a_{i+2}}{34} + a_i - \frac{a_{i+2}}{34} \tag{11a}$$

$$Y_i^n = \frac{3}{17}(-V_{i-1} + 6V_i - V_{i+1}) = -\frac{b_{i-2}}{34} + b_i - \frac{b_{i+2}}{34} \quad . \tag{11b}$$

Appendix A shows that the above weight assignment, derived intuitively, is close to optimum (up to two significant digits). It can be seen that the pair (X_i, Y_i) shows no ISI effect from the two symbols directly adjacent to symbol i; however, there is now some ISI resulting from symbols at two symbol intervals to the right and left, but with greatly reduced magnitude. The spread of (X_i, Y_i) in the signal space, assuming that the i-th signal was octal symbol 0, is shown in Figure 4. The signal spread is greatly reduced, as compared to the unequalized case illustrated in Figure 3. Thus, it is now possible to implement a decision-directed carrier synchronizer that operates on the sample pairs (X_i, Y_i) instead of the pairs (U_i, V_i). Figure 5 is a block diagram of the synchronizer.

For staggered signaling, the same synchronizer structure can be employed; however, the sampling instants for the in-phase and quadrature channels are

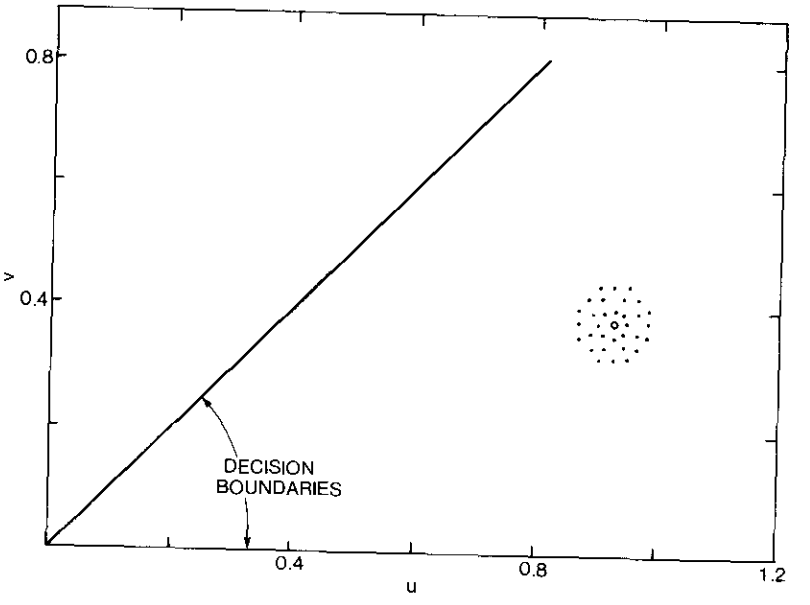

Figure 4. *Signal Spread for Signal 0 With Equalization*

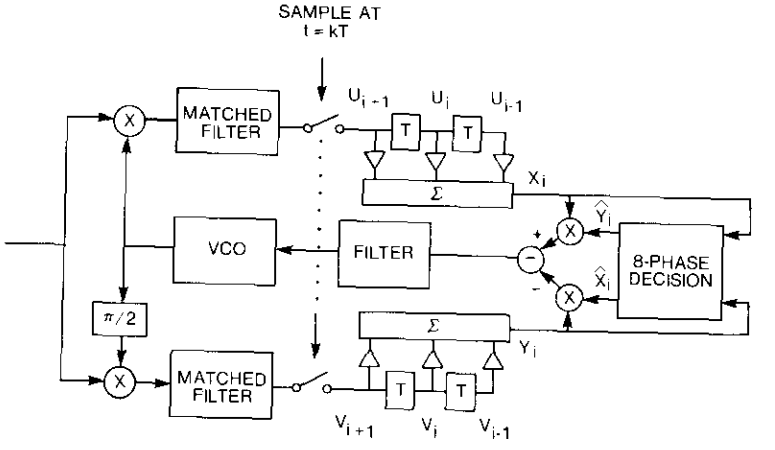

Figure 5. *Carrier Synchronizer Implementation With Equalizer for Unstaggered Signaling*

staggered or offset by $T/2$. This means that U_i and V_i have been obtained at two points in time separated by $T/2$ seconds (where T is a symbol duration).

However, the properties of the pairs (U_i, V_i) and (X_i, Y_i) are still as described above. Figure 6 depicts the synchronizer implementation with the necessary delays.

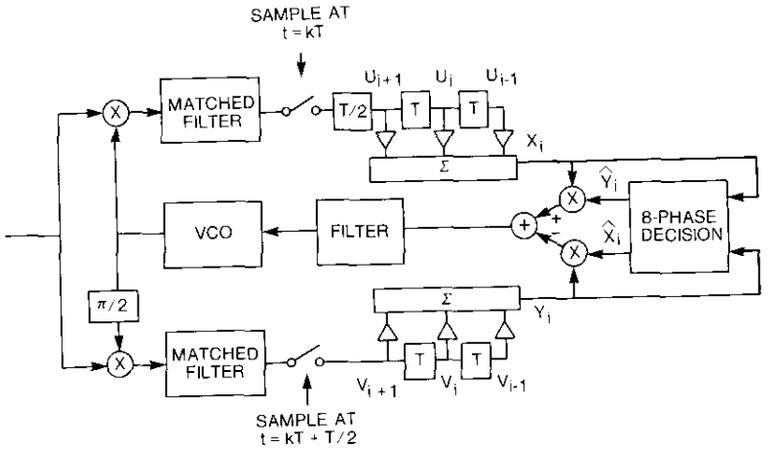

Figure 6. *Carrier Synchronizer With Equalizer for Staggered Signaling*

Statistical modeling of ISI phase process

The ISI phase process must be modeled statistically to evaluate the carrier synchronizer performance. Let the sequence of ISI-induced phase errors be $\{\phi(i)\}$. In the unequalized synchronizer, $\phi(i)$ is computed as

$$\phi(i) = Im[(U_i + jV_i)(\hat{X}_i - j\hat{Y}_i)] = \hat{X}_i V_i - \hat{Y}_i U_i \tag{12}$$

where $(\hat{X}_i, \hat{Y}_i)$ is the output of the 8-phase decision block during the i-th symbol interval (see Figure 6). Assuming perfect signal estimation, *i.e.*,

$$\hat{X}_i = a_i; \qquad \hat{Y}_i = b_i \tag{13}$$

and using equation (12) results in

$$\phi(i) = \frac{1}{6}[a_i(b_{i-1} + b_{i+1}) - b_i(a_{i-1} + a_{i+1})] \tag{14}$$

Assuming that the individual 8-phase PSK symbols (a_i, b_i) in the data stream $\{(a_i, b_i)\}$ are independent and equally probable, it can be shown (see Appendix B) that

$$E[\phi(i)\,\phi(i+k)] = \begin{cases} \dfrac{1}{36}\text{ rad}^2 & \text{for } k = 0 \\ \dfrac{-1}{72}\text{ rad}^2 & \text{for } k = \pm 1 \\ 0 & \text{otherwise} \end{cases} . \tag{15}$$

The z-transform of the phase ISI covariance function is therefore

$$\Phi_\phi(z) = \frac{1}{72}(-z + 2 - z^{-1}) \quad . \tag{16}$$

The power density spectrum $P_\phi(\omega)$ of the phase ISI is

$$P_\phi(\omega) \triangleq \Phi_\phi(e^{j\omega}) = \frac{1 - \cos\omega}{36} \quad . \tag{17}$$

Of interest is the null of the spectrum at $\omega = 0$. Because the power density spectrum of the ISI phase process is not flat, it follows that the ISI effect on the synchronizer is not proportional to the first power of the synchronizer bandwidth, as is the case for AWGN.

In the presence of the equalizer, the phase ISI statistics are computed as follows. The phase ISI is given by

$$\phi(i) = Im[(X_i + jY_i)(\hat{X}_i - j\hat{Y}_i)] = Y_i\hat{X}_i - \hat{Y}_i X_i \tag{18}$$

where (X_i, Y_i) is the output of the equalizer, given by equation (10). Again, assuming perfect feedback decisions

$$\hat{X}_i = a_i; \qquad \hat{Y}_i = b_i \tag{19}$$

yields

$$\phi(i) = \frac{1}{34}[b_i(a_{i-2} + a_{i+2}) - a_i(b_{i-2} + b_{i+2})] \tag{20}$$

which is similar to the form obtained for the unequalized case of equation (14).

The correlation function can be computed as outlined in Appendix B for the unequalized case. The result is

$$E[\phi(i)\,\phi(i+k)] = \begin{cases} \dfrac{1}{(34)^2} & \text{for } k = 0 \\ \dfrac{-1}{2(34)^2} & \text{for } k = \pm 2 \\ 0 & \text{otherwise} \end{cases} . \tag{21}$$

The z-transform of the equalized phase ISI covariance function is, therefore,

$$\tilde{\Phi}_\phi(z) = \frac{-z^2 + 2 - z^{-2}}{2(34)^2} . \tag{22}$$

Measurements through computer simulation of the variance of the phase ISI process were in close agreement with the theoretically predicted values, as shown in Table 2.

TABLE 2. COMPARISON OF PREDICTED AND MEASURED PHASE ISI VARIANCE

	$\phi_{(i)}^2$ (rad^2)	
CASE	THEORY	MEASUREMENT
Unequalized	2.77×10^{-2}	2.83×10^{-2}
Equalized	8.65×10^{-4}	8.65×10^{-4}

Performance of sampled carrier synchronizer

The tracking performance of the sampled carrier synchronizer shown in Figure 5 (with or without equalization) can be obtained with sufficient accuracy by a linear system analysis. The z-transform methods are used because discrete processing is employed.

The tracking performance of the synchronizer is affected by the AWGN channel and the ISI-induced phase error process. For most practical purposes, these sources of tracking jitter can each be modeled as an independent random process. They are both characterized by their covariance functions, $\Phi_n(kT)$ and $\Phi_\phi(kT)$.

The covariance function of the phase error process, $\phi(kT)$, can best be obtained in the z-domain by [3]

$$\tilde{\Phi}_\phi(z) = H(z) \cdot H(z^{-1})[\tilde{\Phi}_n(z) + \tilde{\Phi}_\phi(z)] \tag{23}$$

where $\tilde{\Phi}(z) = Z[\Phi(kt)]$ is the z-transform of the sequence $\{\Phi(kt)\}$, and $H(z)$ is the linearized loop transfer function. The function $H(z)$ is described in Appendix C for a first-order loop without equalization.

Performance of unequalized synchronizer

Using the results from Appendices B through D in equation (23) yields

$$\tilde{\Phi}_\phi(z) = \left[\frac{4B_LT}{z - (1 - 4B_LT)}\right] \cdot \left[\frac{4B_LT}{z^{-1} - (1 - 4B_LT)}\right] \cdot \left[\frac{(-z + 2 - z^{-1})}{72} + \sigma^2\right] \tag{24}$$

where B_L is the one-sided synchronizer noise bandwidth in Hertz, and σ^2 is the noise variance of the noise component entering the equivalent phase-locked loop, as given in equation (D-9) of Appendix D.

After some tedious but straightforward manipulations, equation (24) results in

$$\tilde{\Phi}_\phi(z) = \frac{(4B_LT)^2}{72}\left\{\frac{1}{a} - \left[\frac{(1-a)^2}{1-a^2} \cdot \sum_{i=1}^{\infty} a^{i-1}/z^i\right] - \left[\frac{(1-a)^2}{a(1-a^2)} \sum_{i=0}^{\infty} (az)^i\right]\right\} + \frac{(4B_LT)^2\sigma^2}{1-a^2}\left\{az^{-1}\sum_{i=0}^{\infty}(az^{-1})^i + \sum_{i=0}^{\infty}(az)^i\right\} \tag{25}$$

where $a = 1 - 4B_LT$.

The phase error tracking variance σ_ϕ^2 can be obtained as the coefficient of z^0, as

$$\sigma_\phi^2 = \frac{(4B_LT)^2}{36} \cdot \frac{1}{2 - (4B_LT)} + \frac{4B_LT\sigma^2}{2 - 4B_LT} = \frac{2(B_LT)^2/9 + (B_LT)N_o/E_s}{1 - 2B_LT} \tag{26}$$

where $\sigma^2 = N_o/2E_s$ was substituted from equation (D-9), and E_s is the average channel symbol energy of the modulated data stream, as defined in equation (D-3).

Computer simulations with no AWGN were performed to check the validity of equation (26) for jitter from self noise only. Table 3 shows the theoretical and simulated results. Good agreement exists for sufficiently small B_LT values. The theory is applicable only when the phase errors are small, and is therefore not valid for high B_LT values since phase slips occur under such circumstances even in the noise-free case. The results clearly show the nonlinear dependence of the ISI-induced phase error variance on the synchronizer bandwidth. A practical carrier synchronizer usually has an effective averaging time of many symbol intervals to produce only small tracking errors from additive noise. Thus, $B_LT << 1$ is normally required. For small B_LT values, the ISI-induced phase error variance is proportional to the square of the synchronizer bandwidth.

TABLE 3. COMPARISON OF THEORY AND COMPUTER SIMULATION RESULTS FOR NOISELESS UNEQUALIZED CARRIER SYNCHRONIZER

	σ_ϕ^2	
$(B_LT)^{-1}$	THEORY	MEASUREMENT
8	4.63×10^{-3}	*
16	9.92×10^{-4}	1.01×10^{-3}
32	2.31×10^{-4}	2.36×10^{-4}
64	5.6×10^{-5}	5.72×10^{-5}
96	2.4×10^{-5}	2.51×10^{-5}

* Cycle slips occurred.

Figure 7 shows the phase error tracking variance as a function of E_s/N_o, with B_LT as a parameter. It is obvious that the ISI-induced phase error is small for most practical purposes. However, the previous analysis neglected the influence of decision errors on the performance. This is justified in uncoded communications systems where a reasonably low symbol error probability can be expected. In coded systems, however, the raw symbol error probability is high and symbol errors in the decision feedback cannot be ignored. A more detailed discussion of the loss associated with detection errors is given in a later section.

Performance of equalized synchronizer

To avoid tedious mathematics, the performance of the equalized synchronizer is computed approximately. In a real system, the equalizer is part of the synchronizer loop, which results in a complicated loop transfer function. For small B_LT values, *i.e.*, with the loop bandwidth much smaller than the symbol rate, a system that has the equalizer in front of the synchronizer can

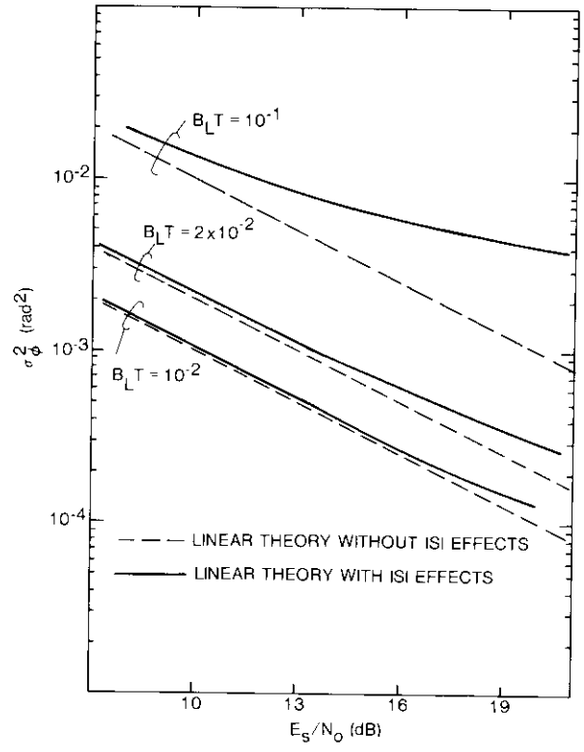

Figure 7. *Effect of ISI on Tracking Variance Without Equalizer*

be expected to show approximately the same results as the actual case in which the equalizer is located within the feedback loop. Figure 8 is a block diagram of the real system and the approximation.

It has been shown that the z-transform of the auto covariance function of the phase ISI process in the equalized case is

$$\tilde{\Phi}_\phi(z) = \frac{-z^{-2} + 2 - z^2}{2(34)^2} \quad . \tag{27}$$

The noise variance is increased by a factor 18/17 in the presence of the equalizer, and the autocovariance function of the phase error process is again given by [6]

$$\Phi_\phi(z) = H(z) \cdot H(z^{-1}) \left[\frac{-z^{-2} + 2 - z^2}{2(34)^2} + \frac{18}{17}\sigma^2 \right] \tag{28}$$

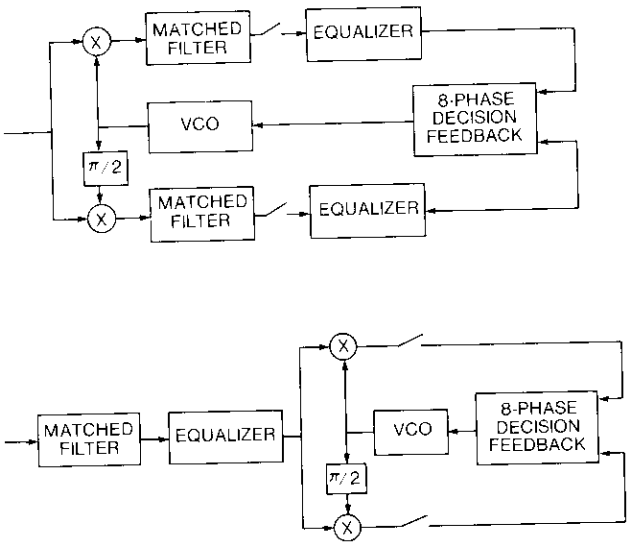

Figure 8. *Real System and Approximation*

where $H(z)$ is given by equation (C-5) of Appendix C and σ^2 is given by equation (D-9). Some lengthy but straightforward calculations yield

$$\Phi_\phi(z) = \frac{(4B_LT)^2}{2(34)^2}\left\{\frac{z}{a} + \frac{1+a^2}{a^2} + \frac{z^{-1}}{a} - \frac{1-a^2}{az}\sum_{i=0}^{\infty}(az^{-1})^i - \frac{1-a^2}{a^2}\sum_{i=0}^{\infty}(az)^2\right\} + \frac{(4B_LT)^2}{1-a^2}\frac{18}{17}\sigma^2 \cdot \left\{az^{-1}\sum_{i=0}^{\infty}(az^{-1})^i + \sum_{i=0}^{\infty}(az)^i\right\} \quad (29)$$

where $a = 1 - 4B_LT$.

The phase error tracking variance becomes, in the equalized case (coefficient of z^0),

$$\sigma_\phi^2 = \frac{(4B_LT)^2}{(34)^2} + \frac{4B_LT \cdot 18\sigma^2/17}{2 - 4B_LT} = \frac{4(B_LT)^2}{(17)^2} + \frac{18}{17}\frac{(B_LT)N_o/E_s}{(1 - 2B_LT)} \quad (30)$$

A computer simulation without AWGN was conducted to check the theoretical results for the self-noise effects. The outcome, given in Table 4, shows good agreement between theory and measurements. In contrast to the unequalized

TABLE 4. COMPARISON OF THEORY AND SIMULATION FOR EQUALIZED CARRIER SYNCHRONIZER

$(B_LT)^{-1}$	σ_ϕ^2	
	THEORY	SIMULATION
8	2.16×10^{-4}	3.74×10^{-4}
16	5.4×10^{-5}	5.99×10^{-5}
32	1.35×10^{-5}	1.27×10^{-5}
64	3.38×10^{-6}	2.93×10^{-6}

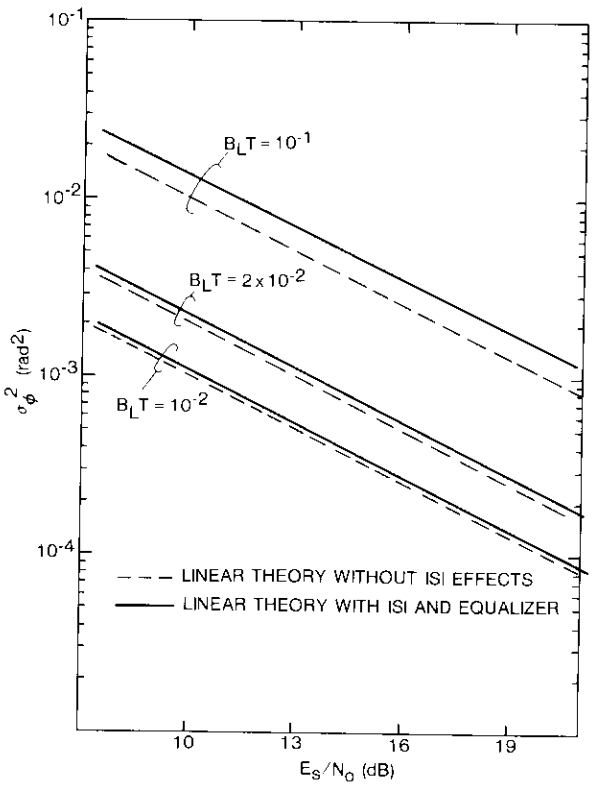

Figure 9. *Effect of ISI on Tracking Variance With Equalizer*

case, no cycle slips occurred for the higher B_LT value of 1/8 because of the reduction of pattern jitter by the ISI equalizer. Figure 9 shows the behavior of the phase error tracking variance of the equalized synchronizer as a function of E_s/N_o with B_LT as a parameter. It can be seen that the performance deterioration caused by ISI is small for practical systems with small B_LT values.

Effect of decision errors

So far, the analysis has not taken into account the effect of decision errors on tracking performance. Decision errors inject large noise spikes into the synchronizer feedback loop. These spikes have little effect as long as they occur infrequently and the synchronizer time constant is significantly larger than the mean time between errors. These conditions are certainly satisfied in a practical uncoded communications system. Coded communications systems, however, operate at high symbol error probabilities and can therefore experience considerable losses.

The error signal in a decision-directed PSK synchronizer is proportional to [7]

$$\cos(\theta - \hat{\theta}) \sin\phi + \sin(\theta - \hat{\theta}) \cos\phi \tag{31}$$

where ϕ is the carrier phase error and $(\theta - \hat{\theta})$ is the phase error between the actual symbol and its estimate. Decision feedback has two deleterious effects on tracking performance. The first is a reduction of the average loop gain, $E[\cos(\theta - \hat{\theta})]$. If

$$P_i = Pr\left\{\theta - \hat{\theta} = \frac{2\pi}{8} i\right\}$$

$$P_c = 1 - P_F = Pr\{\text{correct symbol decision}\} = P_0 \quad . \tag{32}$$

then

$$E[\cos(\theta - \hat{\theta})] = P_0 + \frac{1}{\sqrt{2}}(P_1 + P_{-1}) + 0 \cdot (P_2 + P_{-2}) - \frac{1}{\sqrt{2}}(P_3 + P_{-3}) - P_4$$

$$\simeq P_0 + \frac{2}{\sqrt{2}} P_1 \simeq 1 - P_F \frac{\sqrt{2} - 1}{\sqrt{2}} \simeq 1 - 0.3P_F \tag{33}$$

where, for 8-phase PSK, $P_F \simeq 2P_1$ and $P_{-i} = P_i$. The loop gain can be restored to its original value by use of a gain multiplication factor $(1 - 0.3P_F)^{-1}$. This gain compensation increases the equivalent noise in the loop by a factor of $(1 - 0.3P_F)^{-2}$.

The second effect of decision feedback is the injection of noise caused by decision errors. Assuming that the synchronizer is locked, $\phi \simeq 0$ results in an error signal of $\sin(\theta - \hat{\theta})$. Because the nearest neighbor errors are the most likely to occur, the variance, σ_j^2, of the error signal injected into the loop becomes approximately

$$\sigma_j^2 \simeq \sin^2(45°) \cdot P_F = \frac{P_F}{2} \quad . \tag{34}$$

This term combines with the additive noise term, σ_N^2, in the detector output over one symbol period, namely

$$\sigma_N^2 = \frac{1}{2E_s/N_o} \quad . \tag{35}$$

The total noise power, σ_T^2, at the equivalent phase detector is therefore

$$\sigma_T^2 = \sigma_N^2 + \sigma_j^2 = \frac{1}{2E_s/N_o} + \frac{P_F}{2} = \frac{1}{2E_s/N_o} \cdot \frac{1}{\lambda} \tag{36}$$

where

$$\lambda = \frac{1}{1 + P_F E_s/N_o} \quad .$$

The total loss in loop carrier-to-noise ratio, CNR_L, is then

$$\Gamma = \frac{(1 - 0.3P_F)^2}{1 + P_F E_s/N_o} \quad . \tag{37}$$

Table 5 shows the resulting loss in decibels for a few cases of interest.

TABLE 5. LOSS IN LOOP CARRIER-TO-NOISE RATIO FOR EQUALIZED AND UNEQUALIZED SYNCHRONIZERS

E_s/N_o (dB)	Γ (dB)	
	UNEQUALIZED	EQUALIZED
8	4.5	3.6
10	4.76	3.0
12	4.94	1.9
14	5.0	0.77

The relation between P_F and E_s/N_o is taken from Figure 10, which depicts equalized and unequalized 8-phase PSK performance.

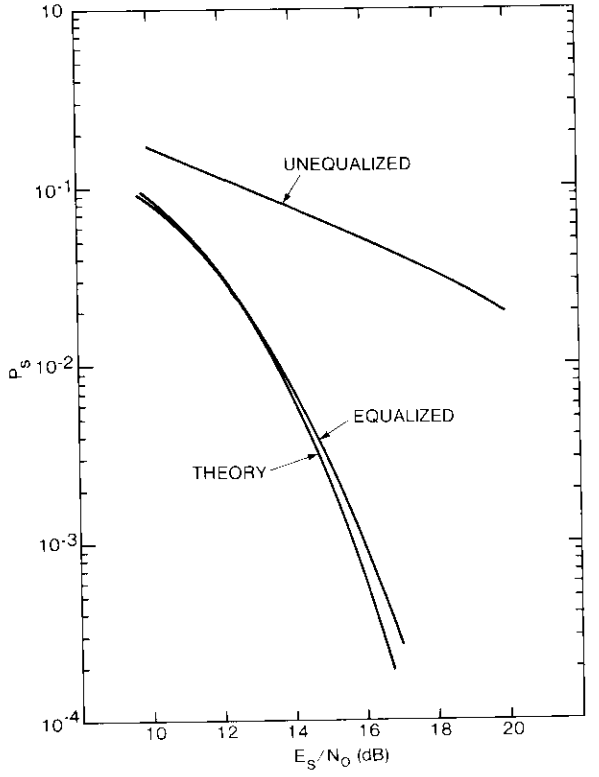

Figure 10. *Uncoded 8-Phase PSK Performance*

Conclusions

Investigation of a practical example (overlapped raised cosine) has revealed that ISI can introduce large amounts of pattern jitter into the carrier synchronizer. However, the effects of ISI can be reduced drastically by augmenting the synchronizer with an equalizer. The same approach can be taken for arbitrary pulse shapes, as long as the channel is quasi-linear.

References

[1] D. D. Falconer, "Jointly Adaptive Equalization and Carrier Recovery in Two Dimensional Communications Systems," *Bell System Technical Journal*, Vol. 55, May 1976, pp. 317–334.

[2] R. W. Chang and R. Srinivasagopalan, "Carrier Recovery for Data Communications Systems With Adaptive Equalization," *IEEE Transactions on Communications*, COM-28, No. 8, August 1980, pp. 1142–1153.

[3] R. M. Gardner, "Self-Noise in Synchronizers," *IEEE Transactions on Communications*, COM-28, No. 8, August 1980, pp. 1159–1163.

[4] M. Austin and M. Chang, "Quadrature Overlapped Raised Cosine Modulation," *IEEE Transactions on Communications*, COM-29, No. 3, March 1981, pp. 237–249.

[5] J. Hui, Private Communication.

[6] Openheim and Schafer, *Digital Signal Processing*, Englewood Cliffs, New Jersey: Prentice Hall, 1975.

[7] W. C. Lindsey and M. K. Simon, *Telecommunication Systems Engineering*, Englewood Cliffs, New Jersey: Prentice Hall, 1973.

Appendix A. Derivation of optimum equalizer tap gains

This derivation is performed for ISI that extends over $\pm k$ adjacent symbols or $2k + 1$ successive sample values. Then, the in-phase or the quadrature matched filter output can be expressed as

$$U \triangleq \begin{bmatrix} U_{i\ k} \\ \cdot \\ \cdot \\ \cdot \\ U_i \\ \cdot \\ \cdot \\ \cdot \\ U_{i-k} \end{bmatrix} = \begin{bmatrix} h_{\ k} & \cdots & h_0 & \cdots & h_k, 0, \ldots 0 \\ 0, h_{\ k} & \cdots & & h_0, . & h_k, 0, . 0 \\ & & \cdot & & \\ & & \cdot & & \\ & & \cdot & & \\ 0, \ldots\ldots, 0, & h_{-k} & \cdots & h_0, & \ldots h_k \end{bmatrix} \cdot \begin{bmatrix} a_{i-2k} \\ \cdot \\ \cdot \\ \cdot \\ a_i \\ \cdot \\ \cdot \\ \cdot \\ a_{i+2k} \end{bmatrix} \triangleq H \cdot \underline{A} \qquad \text{(A-1)}$$

The above relationship follows easily from equation (7a), in which the short notation h_ℓ was used for $h_\ell(T;\tau)$. The equalizer output, $\hat{a}_i$, is an estimate of a_i based on U; that is

$$\hat{a}_i = \underline{G}^T \cdot \underline{U} \tag{A-2}$$

where $\underline{G}$ is a vector of equalizer tap gains

$$\underline{G}^T = [g_{-k}, \ldots, g_0, \ldots, g_k] \quad . \tag{A-3}$$

In this application, $\underline{G}$ is chosen to minimize the mean-squared error. The mean-squared error, σ_e^2, is given by

$$\sigma_e^2 = E\{(a_i - a_i)^2\} = E\{a_i^2\} - 2E\{\underline{G}^T \cdot H \cdot \underline{A} \cdot a\}_i + E\{\underline{G}^T H \underline{A}\underline{A}^T H^T \underline{G}\} \tag{A-4}$$

where the expectation is performed over the data. The minimum value is influenced only by the last two terms because only these terms depend on the equalizer tap weights $\underline{G}$. Assuming that the data symbols satisfy

$$E\{a_i a_k\} = \begin{cases} \sigma_i^2 & k = i \\ 0 & k \neq i \end{cases} \tag{A-5}$$

then

$$E\,\underline{A}\underline{A}^T = \sigma_i^2 \cdot I_{4k+1}$$

$$E\,\underline{A}a_i = [\underbrace{0, \ldots, 0}_{2k}, \sigma_i^2, \underbrace{0, \ldots, 0}_{2k}] = \sigma_i^2 \cdot \underline{1}_i \quad .$$

where I_n is an n × n identity matrix. The following function of $\underline{G}$ must be minimized:

$$f(\underline{G}) = \underline{G}^T H H^T \underline{G} - 2\underline{G}^T H \cdot \underline{1}_i \quad . \tag{A-6}$$

The minimum can be found by taking the derivative with respect to the vector $\underline{G}$ and equating the result to zero, as

$$\frac{dF(\underline{G})}{d\underline{G}} = 2HH^T\underline{G} - 2H\underline{1}_i = 0 \quad . \tag{A-7}$$

Equation (A-7) can easily be solved for the equalizer tap weights which minimize the error variance as

$$\underline{G}(\text{opt}) = (H \cdot H^T)^{-1} \cdot H\underline{1}_i \quad . \tag{A-8}$$

This expression cannot be simplified any further in the general case because H is generally not a square matrix. For example, for the raised cosine pulse with 50-percent overlap to each side, the resulting H matrix is

$$H = \begin{bmatrix} \frac{1}{6} & 1 & \frac{1}{6} & 0 & 0 \\ 0 & \frac{1}{6} & 1 & \frac{1}{6} & 0 \\ 0 & 0 & \frac{1}{6} & 1 & \frac{1}{6} \end{bmatrix}$$

and

$$H \cdot H^T = \frac{1}{36}\begin{bmatrix} 38 & 12 & 1 \\ 12 & 38 & 12 \\ 1 & 12 & 38 \end{bmatrix}$$

$$H \cdot 1_i = \begin{bmatrix} \frac{1}{6} \\ 1 \\ \frac{1}{6} \end{bmatrix} \quad .$$

The optimum tap weights can be computed from equation (A-8) as

$$\underline{G}(\text{opt}) = \begin{bmatrix} -0.171 \\ 1.055 \\ -0.171 \end{bmatrix} \quad .$$

These values agree well with those obtained by intuitive reasoning.

Appendix B. Derivation of phase ISI statistics

The correlation function of the unequalized phase ISI process is derived first. From equation (14), the i-th phase ISI sample is

$$\phi(i) = \frac{1}{6}[a_i(b_{i-1} + b_{i+1}) - b_i(a_{i-1} + a_{i+1})] \quad . \tag{B-1}$$

The individual symbols (a_i, b_i) are assumed to be independent and equally probable.

Table B-1 lists the coordinates of all the possible symbols. For reasons of symmetry, the mean of $\phi(i)$ must be zero:

$$E\{\phi(i)\} = 0; \qquad \text{for all } i \quad . \tag{B-2}$$

TABLE B-1. LIST OF SYMBOL COORDINATES*

SYMBOL NO.	x-COORDINATE	y-COORDINATE
0	A	B
1	B	A
2	−B	A
3	−A	B
4	−A	−B
5	−B	−A
6	B	−A
7	A	−B

* A = cos (22.5°).
B = sin (22.5°).

The variance is first evaluated conditioned on (a_i, b_i). From equation (B-1)

$$E\{\phi(i)|a_i = A, b_i = B\} = \frac{1}{36} E\{[A^2(b_{i-1} + b_{i+1})^2 + B^2(a_{i-1} + a_{i+1})^2 - 2AB(b_{i-1} + b_{i+1}) \cdot (a_{i-1} + a_{i+1})]\} \quad . \tag{B-3}$$

Based on the independence of the signals (a_{i-1}, b_{i-1}) and (a_{i+1}, b_{i+1}), the above can be reduced to

$$E\{[\phi(i)|a_i = A, b_i = B]\} = \frac{1}{18} E\{A^2(b_{i-1}^2 + B^2 a_{i-1}^2)\} = \frac{1}{36}(A^2 + B^2)^2 = \frac{1}{36}\,\text{rad}^2 \quad . \tag{B-4}$$

The unconditional expectation is equal to the conditional expectation because of the symmetry in the signal space. The same method can be used to compute $E\{\phi(i)\,\phi(i+1)\}$, as

$$E\{\phi(i)\,\phi(i+1)\} = \frac{-1}{72}\,\text{rad}^2 \quad . \tag{B-5}$$

Also,

$$E\{\phi(i)\,\phi(i+k)\} = 0 \text{ for } |k| > 1 \quad . \tag{B-6}$$

In summary, the covariance function of the phase ISI process is

$$E\{\Phi(i)\,\phi(i+k)\} = \begin{cases} \frac{1}{36} & \text{for } k = 0 \\ \frac{-1}{72} & \text{for } k = \pm 1 \\ 0 & \text{otherwise} \end{cases} \quad . \tag{B-7}$$

Appendix C. Linearized synchronizer transfer function

Figure C-1 shows the equivalent block diagram of a first-order loop under the assumption of perfect decision feedback; that is, it is assumed that the output of the 8-phase decision block shown in Figure 6 is perfect. Using the notation of Figure C-1 yields

$$\begin{aligned} y(k+1) &= y(k) + K_v[x(k) - y(k)] \\ &= (1 - K_v)\,y(k) + K_v x(k) \quad . \end{aligned} \tag{C-1}$$

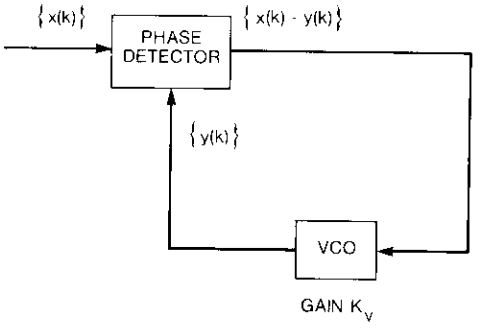

Figure C-1. *Equivalent Synchronizer Block Diagram*

Taking z-transforms on both sides yields

$$\bar{y}(z) = \frac{K_v}{z - (1 - K_v)} \bar{x}(z) \quad . \tag{C-2}$$

The linearized first-order loop transfer function in the Z-domain is therefore

$$H(z) = \frac{K_v}{z - (1 - K_v)} \quad . \tag{C-3}$$

For small values of K_v, the coefficient K_v can be related to the one-sided bandwidth of an equivalent continuous time phase-locked loop by

$$K_v = 4B_L T = 4\frac{B_L}{R_S} \tag{C-4}$$

where R_S is the symbol rate in symbols per second. Therefore,

$$H(z) = \frac{4B_L T}{z - (1 - 4B_L T)} \tag{C-5}$$

Appendix D. Equivalent loop error signal

The channel signal waveform is given by

$$S(t) = Ax(t) \cos(\omega t) + Ay(t) \sin(\omega t) + n(t) \tag{D-1}$$

where $x(t)$ and $y(t)$ are defined in equation (2) and $n(t)$ is the AWGN. The average power of the signal in equation (D-1) is

$$P_s = \frac{3}{8}A^2 \quad , \tag{D-2}$$

and hence the average channel symbol energy is

$$E_s = \frac{3}{8}A^2T \quad . \tag{D-3}$$

Processing the signal, as shown in Figure 1, yields the in-phase and quadrature samples

$$\begin{aligned} X &= (Ax + n_1)\cos\phi - (Ay + n_2)\sin\phi \\ Y &= (Ay + n_2)\cos\phi + (Ax + n_1)\sin\phi \end{aligned} \tag{D-4}$$

where Ax and Ay are the signal samples at the output of the matched filters, and n_1 and n_2 are the corresponding noise samples.

In arriving at equation (D-4), the noise was assumed to be of the form

$$n(t) = n_1(t)\cos\omega t + n_2(t)\sin(\omega t) \quad . \tag{D-5}$$

Note that $n_1(t)$, $n_2(t)$, and $n(t)$ have the same power, P_n, given by

$$P_n = N_o \int_{\infty}^{+\infty} |G(f)|^2 df = N_o \int_{-\infty}^{+\infty} g^2(t)\,dt = N_o \frac{3T}{4} \tag{D-6}$$

where $G(f) = F\{g(t)\}$ and $g(t)$ is the pulse shape defined in equation (3).

The amplitude of the average signal component in the complex sample $X + jY$ (averaging over ISI) is $A \cdot (3T/4)$.

The loop error signal is obtained as in equation (12). Under the assumption of correct feedback decisions, the loop error signal can be shown to be

$$\phi = A\frac{3T}{4}\left[\sin\phi + \frac{n_2\hat{x} - n_1\hat{y}}{3TA/4}\cos\phi + \frac{n_1\hat{x} + n_2\hat{y}}{3TA/4}\sin\phi\right] \tag{D-7}$$

where $\hat{x}$ and $\hat{y}$ are the unit radius feedback decisions. Therefore, the noise entering the equivalent phase-locked loop is

$$n_L = \frac{4}{3AT}\left[(n_2\hat{x} - n_1\hat{y})\cos\phi + (n_1\hat{x} + n_2\hat{y})\sin\phi\right] \quad . \tag{D-8}$$

Using equations (D-3), (D-6), and (D-8), and the fact that $|\hat{x} + j\hat{y}| = 1$, it is easy to show that

$$E\{n_L\} = 0 \qquad E\{n_L^2\} = \frac{P_n}{(3AT/4)^2} = \frac{N_o}{2E_s} \triangleq \sigma^2. \tag{D-9}$$

Successive noise samples n_1 and n_2 taken at the output of the in-phase and quadrature arm filters are correlated because of the pulse overlap. However, the noise samples are independent of the 8-phase PSK data symbols, and the data sequence consists of independent symbols. These facts result in a decorrelation of successive noise samples,

n_L, entering the equivalent phase-locked loop. The correlation function of the sequence of noise samples, n_L, is therefore given by

$$E\{n_L(k) \cdot n_L(k+i)\} = \begin{cases} N_o/(2E_s) & i = 0 \\ 0 & \text{otherwise} \end{cases} \qquad \text{(D-10)}$$

and can be modeled as white noise. The equivalent phase-locked loop is shown in Figure D-1.

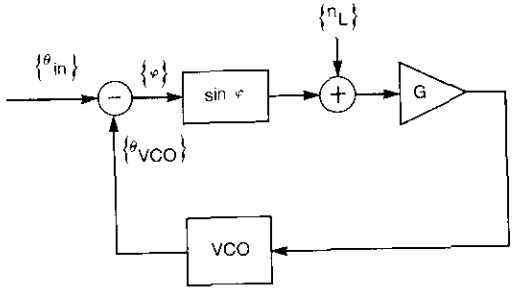

Figure D-1. *Equivalent Phase-Locked Loop Model for Additive White Gaussian Noise Influence*

Walter Hagmann received his Diploma in Electrical Engineering from the Swiss Federal Institute of Technology, Zurich, in 1976, and his Ph.D. from the University of Southern California in 1981. Since joining COMSAT Laboratories in 1981, he has worked on various problems related to satellite communications. His main interests are in the areas of small-user and mobile communications systems.

Index: amplifiers, distortion, transmitters

Wideband klystron high-power amplifiers for FDM/FM/FDMA applications

D. CHAKRABORTY, J. EHRMANN, AND E. W. MCCUNE

(Manuscript received September 14, 1983)

Abstract

The characteristics of a 3-kW, 80-MHz-bandwidth, C-band, klystron high-power amplifier (HPA) were investigated to determine its applicability to FDM/FM/FDMA transmission in the INTELSAT V system. Computations based on experimental data show that the klystron HPA operated at close to 8-dB input backoff meets the 23-dBW/4-kHz out-of-band intermodulation noise emission criteria. Baseband noise resulting from the klystron linear and parabolic delay distortion was insignificant. Crosstalk coupling measurements between two large FDM/FM carriers demonstrated that the klystron HPA could be operated between 5.5- and 8-dB input backoff to meet the 58-dB CCITT specification. At about 8-dB input backoff, 1 kW of output power usable for FDMA operation is more than adequate for two 972-channel FDM/FM carriers accessing an INTELSAT V hemi- or zonal-beam transponder via a Standard A earth station antenna.

Introduction

A 3-kW, 80-MHz-bandwidth, C-band, klystron HPA [1] has been recently developed for 120-Mbit/s QPSK transmission in the INTELSAT V system. Major operational parameters for a 3-kW coupled cavity (CC) TWT-HPA and a 3-kW five-cavity klystron HPA are given in Table 1.

TABLE 1. COMPARISON OF KLYSTRON AND TWT POWER AMPLIFIERS

PARAMETER	3-KW KLYSTRON	3-KW CC-TWTA
AC Consumption (kVA)	12	25
Bandwidth (MHz)	~80	500
Saturation Gain (dB)	30-33	30-36
Floor Space (HPA assembly)	24 x 34 in.	72 x 30 in.
Relative Price (HPA)	1x	4x
Tube Replacement Cost	1y	3y
Tube Life	Similar	Similar

Several operational and economic advantages can be gained by using an 80-MHz bandwidth klystron HPA in conjunction with an INTELSAT V single transponder. Earth stations equipped with high-power multiplexing equipment (80-MHz channelized transmission) [2] can utilize the economic benefits offered by these klystrons.

In the INTELSAT V frequency plan, two large multidestination FDM carriers have been assigned to a common 72-MHz bandwidth transponder for a number of selected earth stations. Examples of this frequency plan are shown in Table 2. In view of this plan, it is logical to explore the feasibility of

TABLE 2. INTELSAT V OPERATIONAL FDM/FM PLAN
(TWO CARRIERS PER TRANSPONDER)

TRANSMITTING COUNTRY	BANDWIDTH SLOT (MHZ)	CAPACITY (CHANNELS)	TRANSPONDER NO.	MAXIMUM e.i.r.p. (dBW)	BEAMS*
		Atlantic Ocean Major Path 2, Mid 1987			
USA	36	792	53	83.8	WZ/EZ
USA	36	792	53	83.8	WZ/EZ
		Indian Ocean Major Path, End 1987			
UK	20	432	21	82.9	WH/EH
UK	36	792	21	83.8	WH/EH
		Pacific Ocean Primary, End 1987			
USA	36	972	11	85.1	EH/WH
USA	36	972	11	85.1	EH/WH
USA	36	972	42	85.1	EZ/WZ
USA	36	972	42	85.1	EZ/WZ

* WZ—west zone
EZ—east zone
WH—west hemi
EH—east hemi

using the newly developed 80-MHz bandwidth, 3-kW klystron HPAs for such applications.

This paper examines, by analysis and experiment, the major transmission impairments encountered when two large FDM carriers are amplified by a klystron HPA. The following tasks will be performed:

a. Match the existing computer program (CIA-4) with measured two-carrier C/I performance [1].

b. Evaluate the intermodulation spectra by computer simulation with modulated carriers using specific frequency plans (Table 2); calculate the out-of-band noise (OBN) per 4 kHz from the modulated intermodulation spectra; and calculate the thermal OBN per 4 kHz from the internally generated tube noise.

c. Compute group delay distortion noise in the baseband of different size carriers from the measured group delay characteristics of the klystron by using the quasistationary approximation.

d. Measure the intelligible crosstalk coupling between two FDM carriers as a function of the input backoff of the klystron HPA; and verify these measurements with computed data by using the AM/PM transfer coefficient and the measured gain slope parameter obtained from a recent experimental program at Andover Earth Station.

e. Discuss the application of klystron HPAs for multicarrier FDM operation in the INTELSAT V system.

Technical Considerations

OBN emission calculations

The INTELSAT specifications state that the (earth station) radiation of intermodulation products resulting from multicarrier FDM/FM operation shall not exceed 23 dBW/4 kHz within the frequency range of 5,925–6,425 MHz in the hemispheric and zonal beam coverage. Furthermore, radiation outside the satellite bandwidth resulting from spurious tones, bands of noise, or other undesirable signals, but excluding the multicarrier intermodulation products, shall not exceed 4 dBW in any 4-kHz band within the 5,925- to 6,425-MHz frequency range.

OBN due to intermodulation

With two equal carriers set at ± 5 MHz from the center of the band, third- and fifth-order C/I ratios were measured as a function of the single-carrier input backoff of the klystron HPA under examination [1]. The measured data

are plotted in Figure 1. Figure 2 shows the klystron power and phase transfer characteristics at the center of the band derived from Reference 1. These

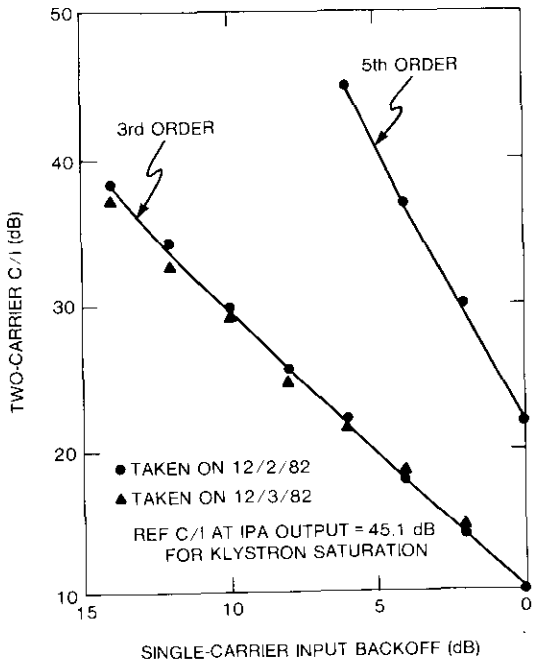

Figure 1. *Two-Carrier C/I Performance*

characteristics have been used to compute two-carrier third- and fifth-order C/I characteristics [3] by using the computer program CIA-4 [4]. In Figure 3, these results are plotted as a function of single-carrier input backoff. The measured two-carrier third- and fifth-order C/I curves derived from Reference 1 are also plotted for comparison.

A significant difference between the computed and measured data at high input backoff, as shown in Figure 3, indicates that the measured transfer curves do not accurately predict the measured C/I without further curve shaping of either power or phase. As the measurement of power is more reliable than that of phase, the computed C/I is matched with the measured values to find the improved value of the phase transfer function.

Figure 4 shows the improved phase transfer function* found by trial and error. The corresponding two-carrier third- and fifth-order C/I results are depicted in Figure 5. The improvement is primarily attributable to lower

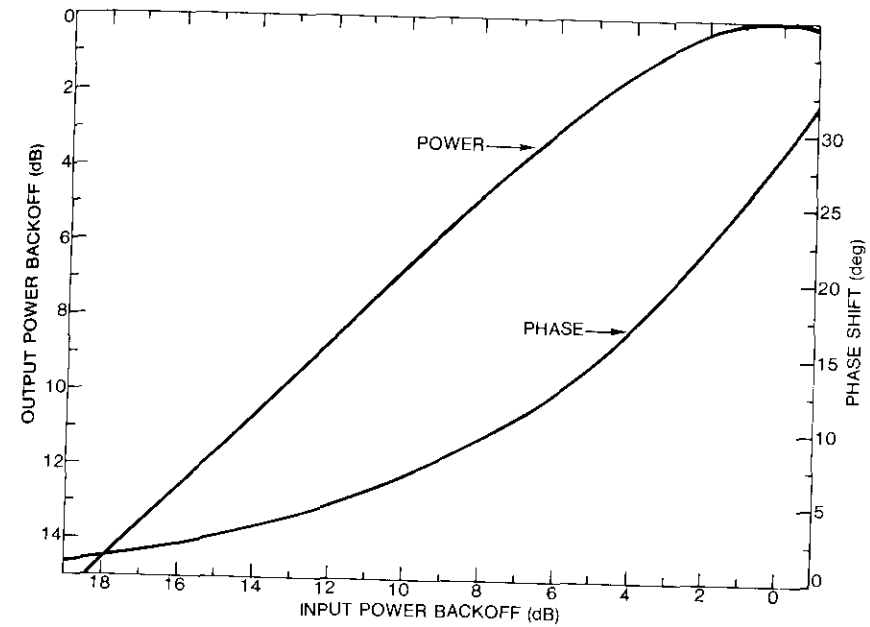

Figure 2. *Klystron Single-Carrier Power and Phase Transfer Characteristics at Band Center*

AM/PM distortion because a smoother phase gradient is used at high input backoff (see the computed curve in Figure 4).

Next, the power and modified phase transfer data are used to compute the intermodulation products of two FDM/FM carriers for three typical cases from Table 2. Table 3 gives the input data for the computation of intermodulation spectra for these cases. The resultant intermodulation spectra for 2- to 14-dB input backoff (single carrier) at 2-dB intervals are shown in Figures 6 through 8. A typical amplifying passband mask of the klystron (1-dB

* The anomalous behavior of the phase transfer curve was further investigated at Varian Associates Laboratories and was attributed to thermal detuning. At about 3-kW output power, the heating effect could change the cavity temperature by 50°C, resulting in a detuning of 2 MHz. This represents a phase shift of about 5°, in addition to the phase change attributable to drive power. Because the measurement was performed by a fast swept technique, the impact of temperature change was eliminated. However, subsequent investigations uncovered a thermal detuning problem caused by the loss elements in cavities 2 and 3. Heating of these elements changed their properties sufficiently to affect cavity tuning. The klystron has since been reworked, and the heat dissipation capability of these loss elements has been greatly increased.

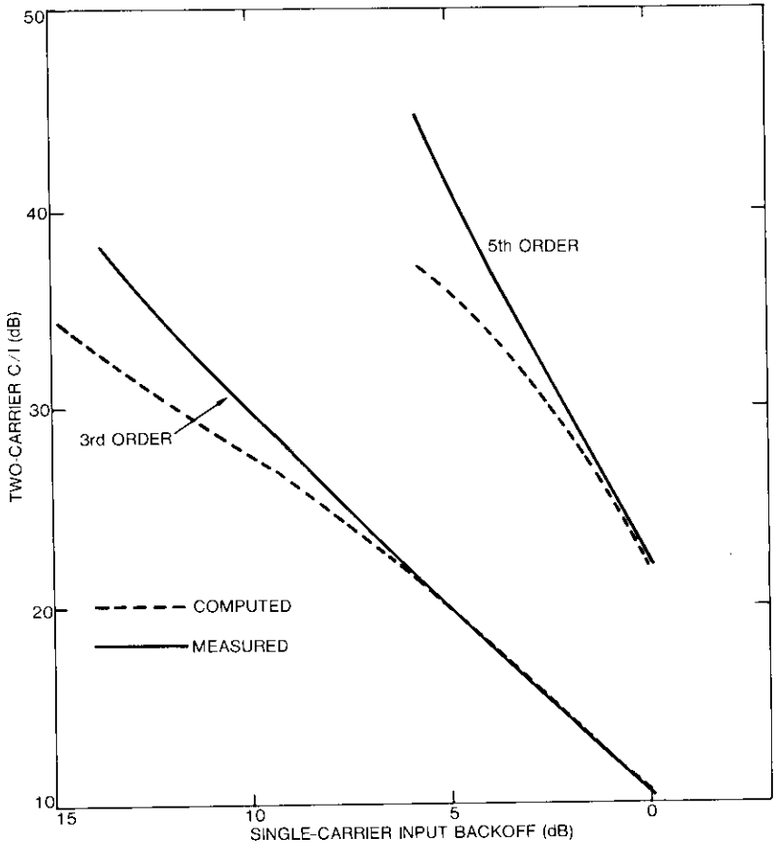

Figure 3. *Two-Carrier C/I Performance (Measured)*

bandwidth ≈ 80 MHz; 3-dB bandwidth ≈ 100 MHz) is superimposed in these figures to identify the position of the out-of-band emission spectra. However, the klystron passband attenuations are not included in the intermodulation spectrum levels. In practice, the intermodulation spectra that fall outside the amplifier passband will be further attenuated by the passband characteristics of the klystron.

In Figures 6 through 8, the intermodulation power is expressed in decibels per megahertz below the single-carrier saturated output power of the klystron HPA, which is 3-kW or 34.8 dBW. By using a net antenna gain of 61 dB at the HPA flange (63-dB gain − 2-dB feeder loss), the e.i.r.p. per 4 kHz

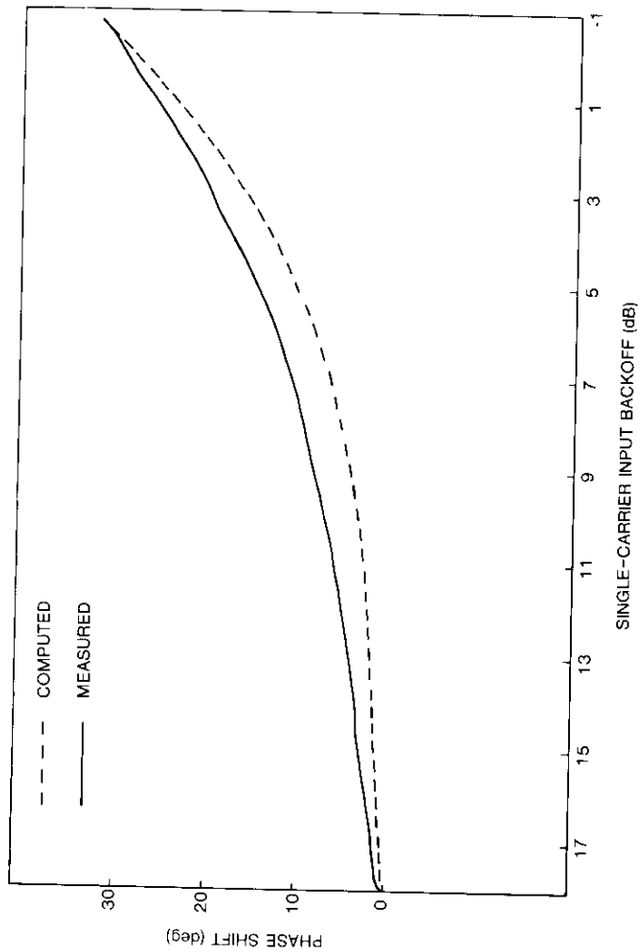

Figure 4. *Phase Transfer Curve Optimization*

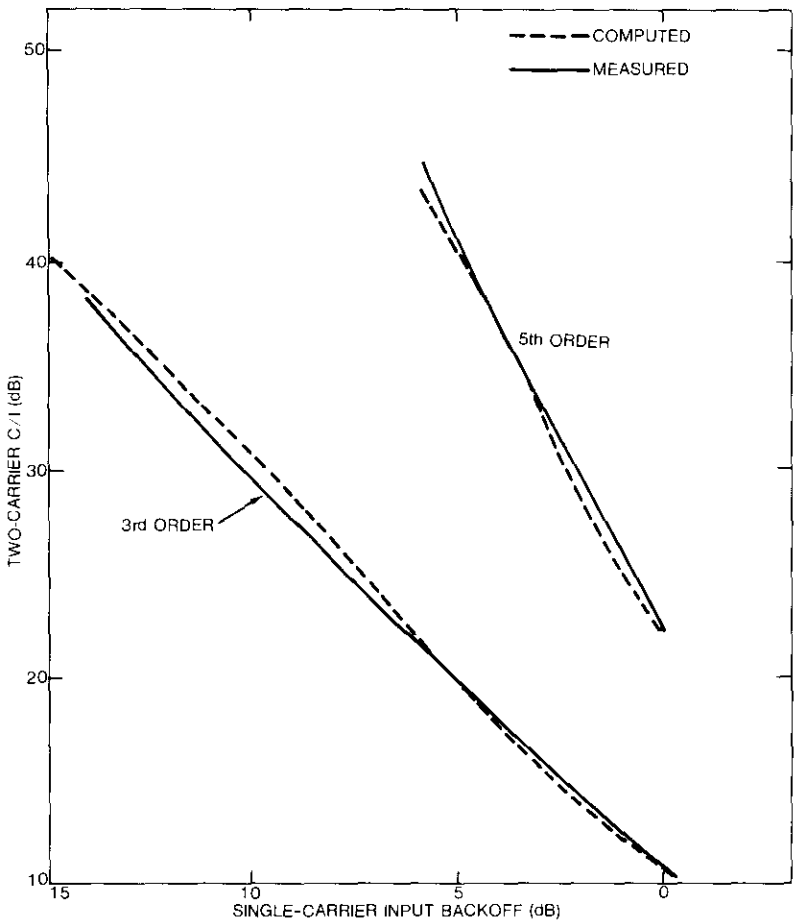

Figure 5. *Two-Carrier C/I Performance (Computed)*

resulting from intermodulation was calculated for different input backoff values of the klystron for the three frequency plans under consideration. Figure 9 shows the calculated e.i.r.p. (OBN)/4 kHz *vs* the HPA input backoff characteristics. It can be seen that, to meet the INTELSAT OBN specification, the klystron should be operated close to 7.5- to 8.5-dB input backoff for FDMA operation. The corresponding maximum output backoff is close to 5 dB (see Figure 2). The resulting available multicarrier output power is approximately 1 kW; that is, the available multicarrier e.i.r.p. is approximately 91 dBW for a typical Standard A earth station.

TABLE 3. INTERMODULATION CALCULATION FDM/FM PLANS

REGION	CARRIER LOCATION FROM BAND CENTER (MHz)	CARRIER SIZE (CHANNELS)	rms DEVIATION (kHz)	MINIMUM BASEBAND (kHz)	MAXIMUM BASEBAND (kHz)	OCCUPANCY PERCENTAGE
Indian Ocean	−28	432	2,276	12	1,796	80
	+18	792	4,085	12	3,284	80
Pacific Ocean	−18	972	4,417	12	4,028	80
	+18	972	4,417	12	4,028	80
Atlantic Ocean	−18	792	4,085	12	3,284	80
	+18	792	4,085	12	3,284	80

Thermal noise emission

In a matched transmission system at room temperature (290 K), the input noise power of the system is

$$N_i = KTB = -125 \text{ dBW over } 80 \text{ MHz} \quad (1)$$

where K = Boltzmann's constant = 1.38×10^{-23} J/K
T = temperature = 290 K
B = amplifier bandwidth = 80 MHz.

In a microwave amplifier, this thermal noise is amplified by the tube, and additional noise is introduced as a result of electron motion in the electron beam. This beam noise is expressed as the tube noise figure in decibels, which adds directly to the thermal noise. Thus, the total output noise power, N_o, of the klystron HPA over the amplifying passband can be defined from the noise figure, F, as follows:

$$F = \frac{(S_i/N_i)}{(S_o/N_o)} = \frac{S_i}{S_o}\frac{N_o}{N_i} \quad (2)$$

$$\therefore N_o = -125 + G_{ss} + F = -54.8 \text{ dBW} \quad (3)$$

where G_{ss} = small signal gain of the klystron = (S_o/S_i)
≃ 35.2 dB at 8-dB input backoff
F = noise figure = 35 dB (typically).

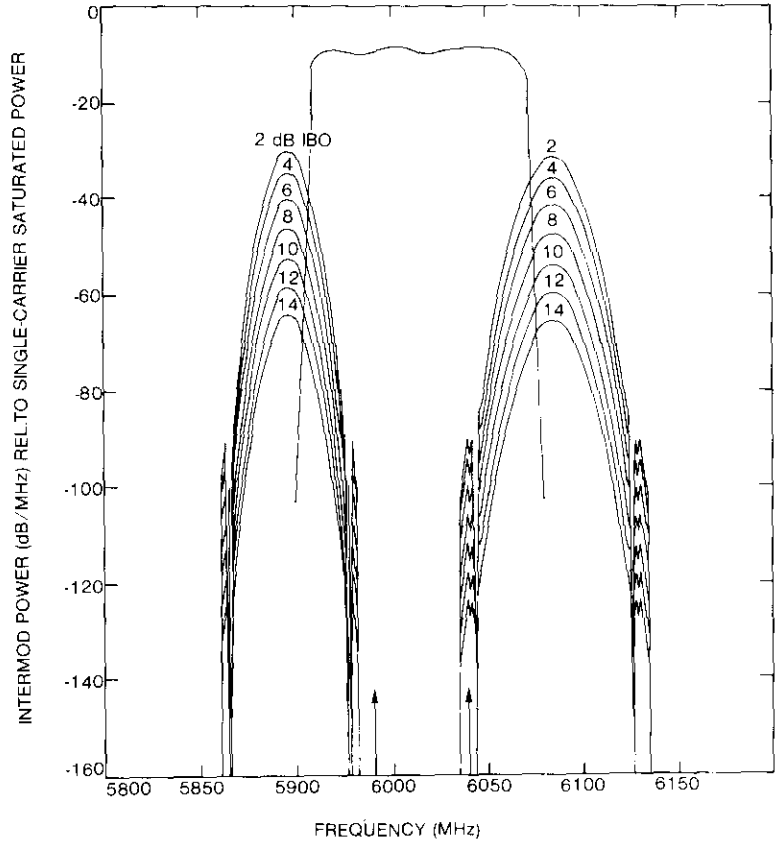

Figure 6. *Indian Ocean Plan Intermodulation Spectra of Two FDM/FM Carriers Amplified by a Common Klystron*

Assuming a flat noise spectrum over the amplification passband of 80 MHz, the OBN emission per 4 kHz becomes

$$-54.8 - 10 \log \frac{80 \times 10^6}{4 \times 10^3} = -97.8 \text{ dBW} \quad .$$

For a net antenna gain of 61 dB referenced at the output flange of the HPA, the e.i.r.p. resulting from thermal noise emission per 4 kHz becomes −36.8 dBW, which is about 41 dB below the specification value (4 dBW per 4 kHz).

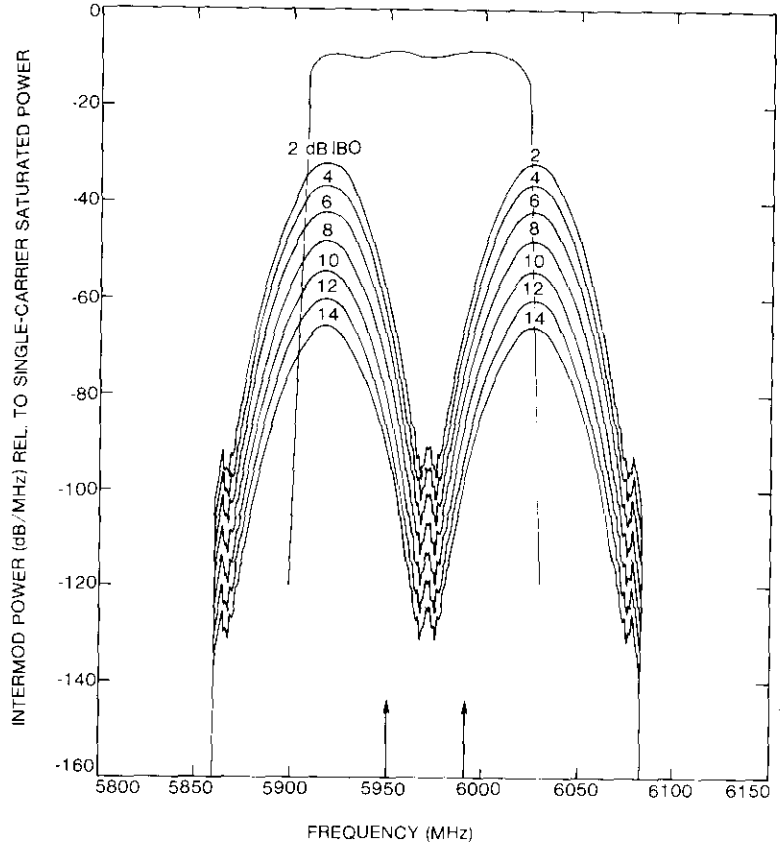

Figure 7. *Pacific Ocean Plan Intermodulation Spectra*

Group delay distortions

The staggered tuning effect of multiple cavities in a klystron introduces a parabolic group delay response. This response introduces differential group velocities to the sidebands of the FM carrier when compared with the phase velocity of the unmodulated carrier. These velocities introduce distortion in the FM carrier baseband which can be calculated by the quasi-stationary approximation, as follows [5], [6]. The output FM signal, $\Delta\omega g_0(t)$, is obtained when the input FM signal, $\Delta\omega g(t)$, is applied to a network whose phase-frequency characteristic is not linear, where

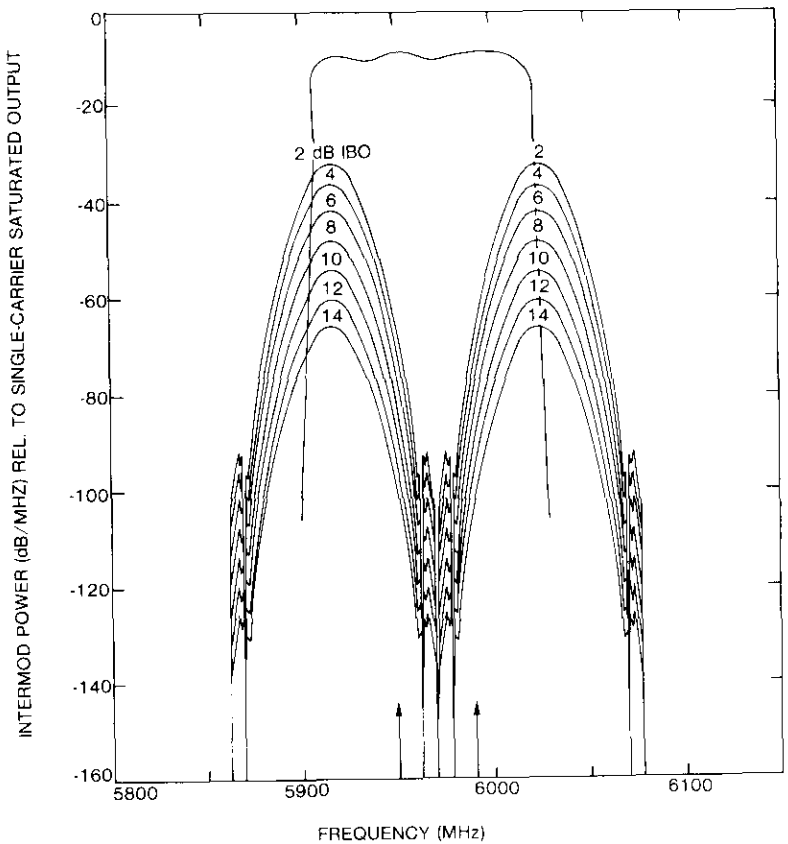

Figure 8. *Atlantic Ocean Plan Intermodulation Spectra*

$$g_0(t) = g(t) + \frac{d}{dt}g(t) \cdot \left[\tau_1 + \tau_2\frac{\Delta\omega g(t)}{B/2} + \tau_3\left(\frac{\Delta\omega g(t)}{B/2}\right)^2 + \ldots\right] \quad ; \qquad (4)$$

τ_1, τ_2, and τ_3 are the group delay coefficients (fixed, linear, parabolic, etc.); and B is the bandwidth (network).

An examination of equation (4) reveals that the output signal contains the input term, plus a number of higher-order terms multiplied by the quadrature (first derivative) component of the input signal (baseband). When the baseband signal is composed of many multiplexed voice frequencies, the additional

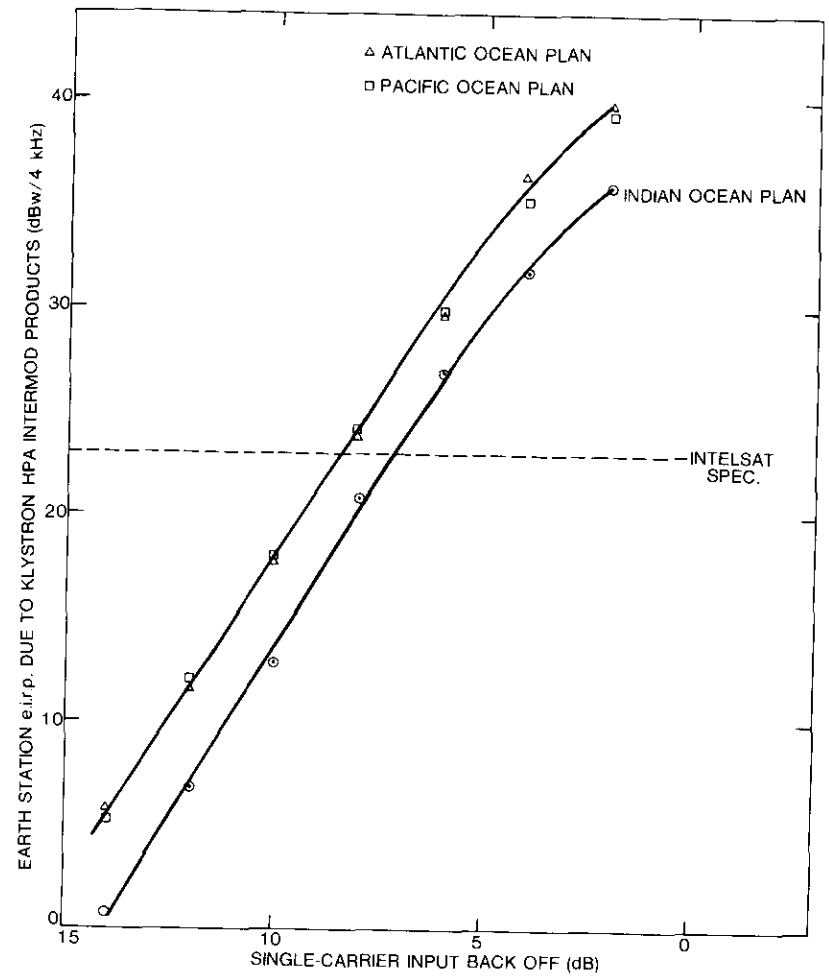

Figure 9. *Out-of-Band Noise Emission Due to Intermodulation*

terms of equation (4) will give rise to an infinitely large number of harmonic terms and baseband intermodulation product terms. These harmonics and the intermodulation product powers extend over a large bandwidth following certain distribution patterns [6], and appear like noise in the baseband.

The top channel noise-power ratio (NPR) caused by group delay distortion can be calculated as follows: for noise resulting from linear group delay distortion

$$\text{NPR} = 20 \log \left[\frac{10^3}{\pi f_m \tau_2 f_{rms}} \right] , \quad (5)$$

and for noise resulting from parabolic group delay distortion

$$\text{NPR} = 20 \log \left[\frac{860}{\pi f_m \tau_3 f_{rms}^2} \right] \quad (6)$$

where f_m = top baseband frequency (MHz)
f_{rms} = multichannel rms deviation (MHz)
τ_2 = linear group delay distortion (ns/MHz)
τ_3 = parabolic group delay distortion (ns/MHz^2).

The relationship between NPR and the weighted signal-to-noise ratio, S/N, is

$$\frac{S}{N} = \text{NPR} + 10 \log \frac{\text{top baseband} - \text{bottom baseband}}{3.1 \text{ (kHz)}} - L + P + W \quad (7)$$

where L = multichannel load factor
$= -15 + 10 \log N$; $N \geq 240$ channels
P = pre-emphasis improvement = 4 dB
W = psophometric weighting = 2.5 dB.

The group delay characteristics of the klystron HPA were measured at three different output powers, as shown in Figure 10. In practice, the group delay characteristics are virtually independent of power output. For multicarrier operation, the characteristic at 1-kW output power is chosen for further analysis. From Figure 10, the extracted linear component over ± 36 MHz (transponder bandwidth) is 1.2 ns/72 MHz, or $\tau_2 \simeq 0.017$ ns/MHz. After extraction of the linear component, the residual component is matched to a parabola by curve fitting over ±36 MHz, as illustrated in Figure 11. The parabolic coefficient is, therefore, 5.8 ns/(36 mHz)^2, or $\tau_3 \simeq 0.004$ ns/(MHz)^2.

The distortion coefficients τ_2 and τ_3 discussed above and equations (5) through (7) with the transmission parameters shown in Table 3 were used to calculate the linear and parabolic delay distortion noise falling on the top channel of the FM carriers under examination. The results are shown in Table 4. The group delay noise is insignificant.

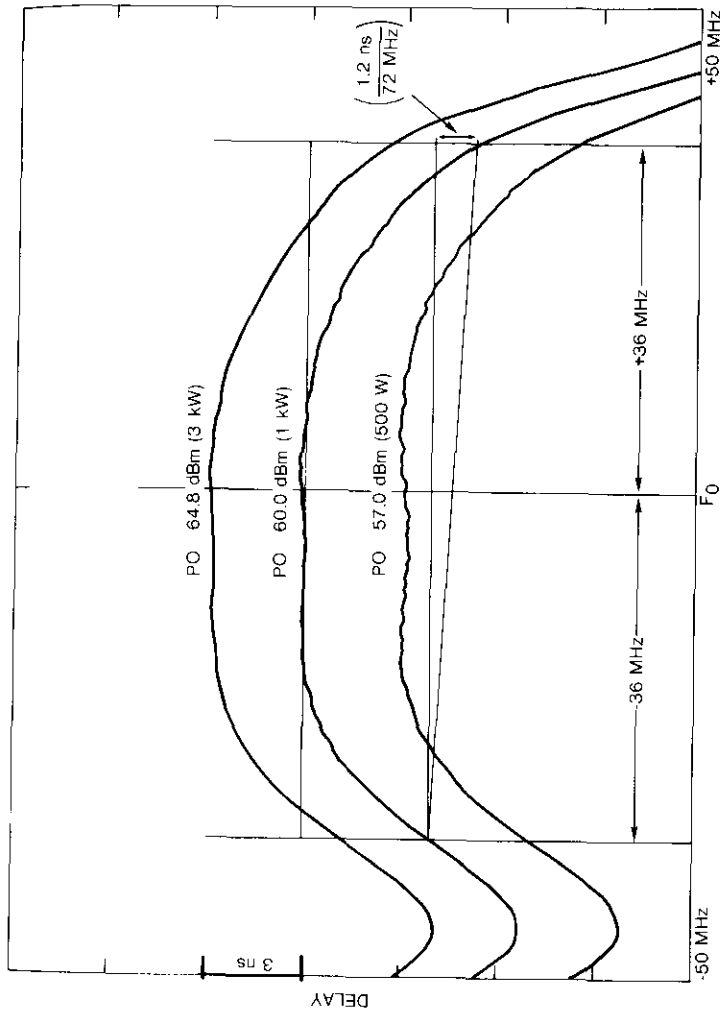

Figure 10. *Klystron Group Delay Characteristics*

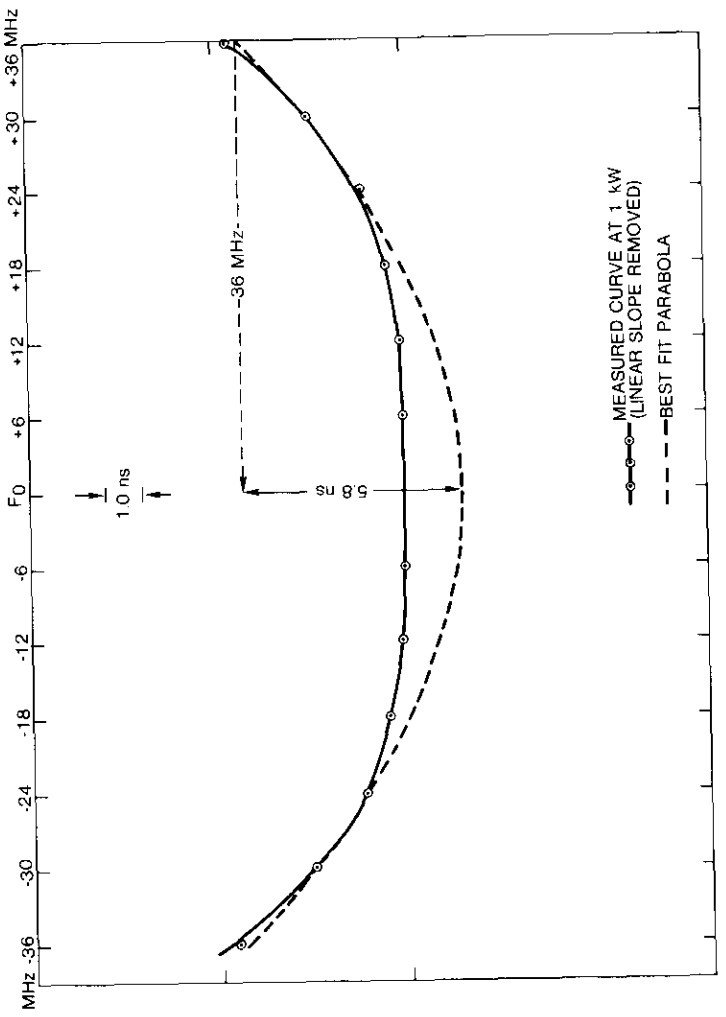

Figure 11. *Group Delay Characteristic After Removal of Linear Component*

TABLE 4. TOP CHANNEL NOISE DUE TO KLYSTRON GROUP DELAY DISTORTION

CARRIER SIZE (CHANNELS)	NOISE IN THE TOP CHANNEL, pWOp		
	LINEAR DELAY DISTORTION	PARABOLIC DELAY DISTORTION	TOTAL
972	5	8	13
792	3	3	6
432	<1	<1	<1

Intelligible crosstalk coupling

When two or more frequency-modulated carriers are amplified through a common nonlinear device with AM/PM characteristics, intelligible crosstalk from one signal to another results. Envelope fluctuations are imposed on FM signals by the gain slopes of transmission networks, such as channel filters, prior to the nonlinearity. These unwanted envelope fluctuations are translated into phase modulation by the AM/PM transfer effect of the nonlinear amplifier, which gives rise to intelligible crosstalk between FM carriers. The crosstalk is intelligible over the entire baseband, and the effect is more prominent on the top channel. Also, crosstalk impairment is most severe in the two-carrier case.

The classic paper on intelligible crosstalk coupling was published by Chapman and Millard [7], who derived an approximate formula for the crosstalk ratio, XTR, as follows:

$$XTR\ (\text{dB}) = 20 \log 2K_1 A_1^2 g\omega \qquad (8)$$

where K_1 = amplifier constant related to phase shift *vs* input power
A_1^2 = power of the crosstalking carrier referenced to single-carrier saturation
g = linear gain slope
ω = baseband angular frequency on which crosstalk occurs.

Crosstalk impairments have been analyzed further in References 8 through 10. Reference 9 gives a general analysis of crosstalk impairment, including the effect of group delay fluctuation. This work has been extended to systems with cascaded nonlinearities [10]. Intelligible crosstalk couplings between large FDM/FM carriers have been measured [11] in a 14-GHz klystron HPA.

In the C-band klystron HPA under examination, intelligible crosstalk couplings between two large FDM/FM carriers were measured by using the frequency plan shown in Table 2. Figure 12 is a block diagram of the intelligible crosstalk measurement setup. The crosstalked carrier is normally unmodulated. However, to establish a reference level, the 0-dBm0 tone on the top bandstop slot is inserted into this carrier, and its level at the demodulator output is measured via the selective level meter (a precision narrowband receiver). The tone is then moved to the crosstalking carrier top slot, which is also white-noise modulated. This tone level is now measured at the output of the selective level meter tuned to the top slot frequency in the crosstalked carrier baseband. The difference between this level and the reference level is the intelligible crosstalk ratio in decibels.

Crosstalk coupling was measured as a function of klystron input backoff for the following six cases:

a. A 972-channel carrier located on the left half of the 72-MHz bandwidth block.

b. The 972-channel carrier shifted to the right.

c. A 792-channel carrier located on the left half of the 72-MHz bandwidth block.

d. The 792-channel carrier shifted to the right.

e. A 792-channel carrier located on the left half of the 72-MHz bandwidth block crosstalking on a 432-channel carrier located on the center of the right half of the bandwidth block.

f. A 792-channel carrier located on the right half of the 72-MHz bandwidth block crosstalking on a 432-channel carrier located on the center of the left half.

The 432-channel carrier in cases (*e*) and (*f*) is located at ±18 MHz from the center of the 72-MHz bandwidth block chosen in the passband of the klystron HPA. This was done to maintain symmetry with cases (*a*) through (*d*). In cases (*e*) and (*f*), crosstalk was measured on the top slot of the 432-channel carrier only because, for two unequal carriers, the impairment is more severe on the weaker carrier. The measured results are shown in Figures 13 through 15.

Discussion on crosstalk measurements

Equation (8) shows that, for given transmission parameters and gain slope in the passband of the crosstalking carrier (prior to the nonlinearity), the crosstalk coupling increases with the power level of the crosstalking carrier. This in turn determines the operating point of the nonlinear device and,

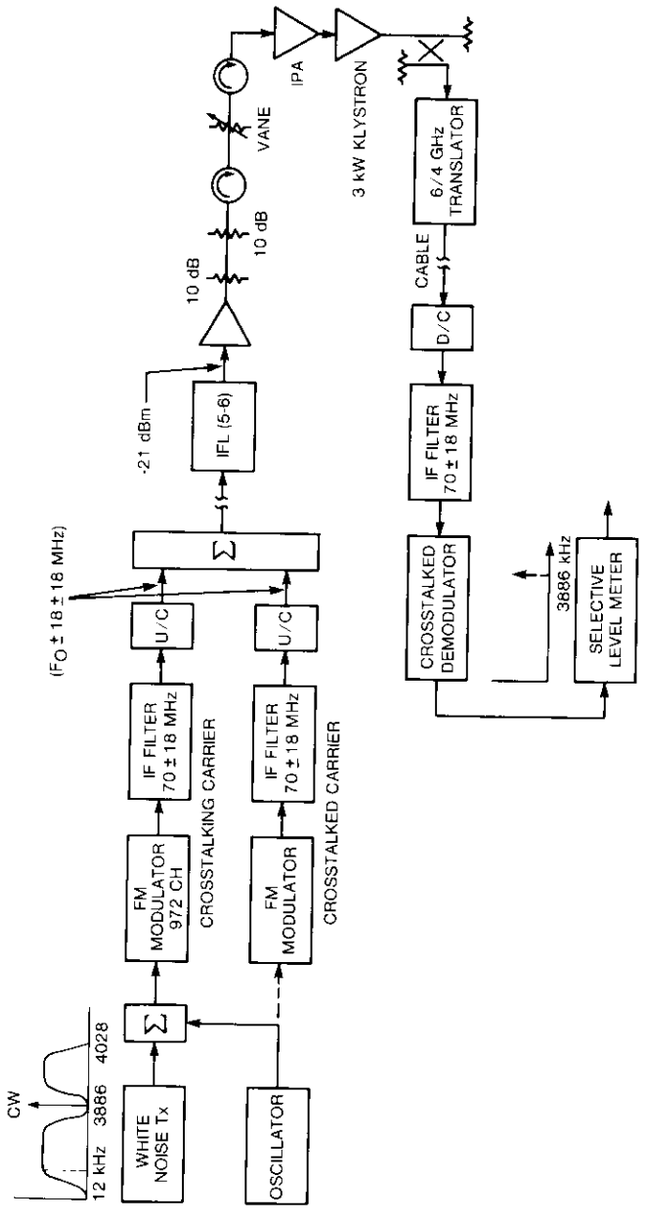

Figure 12. *Block Diagram of Intelligible Crosstalk Measuring Setup*

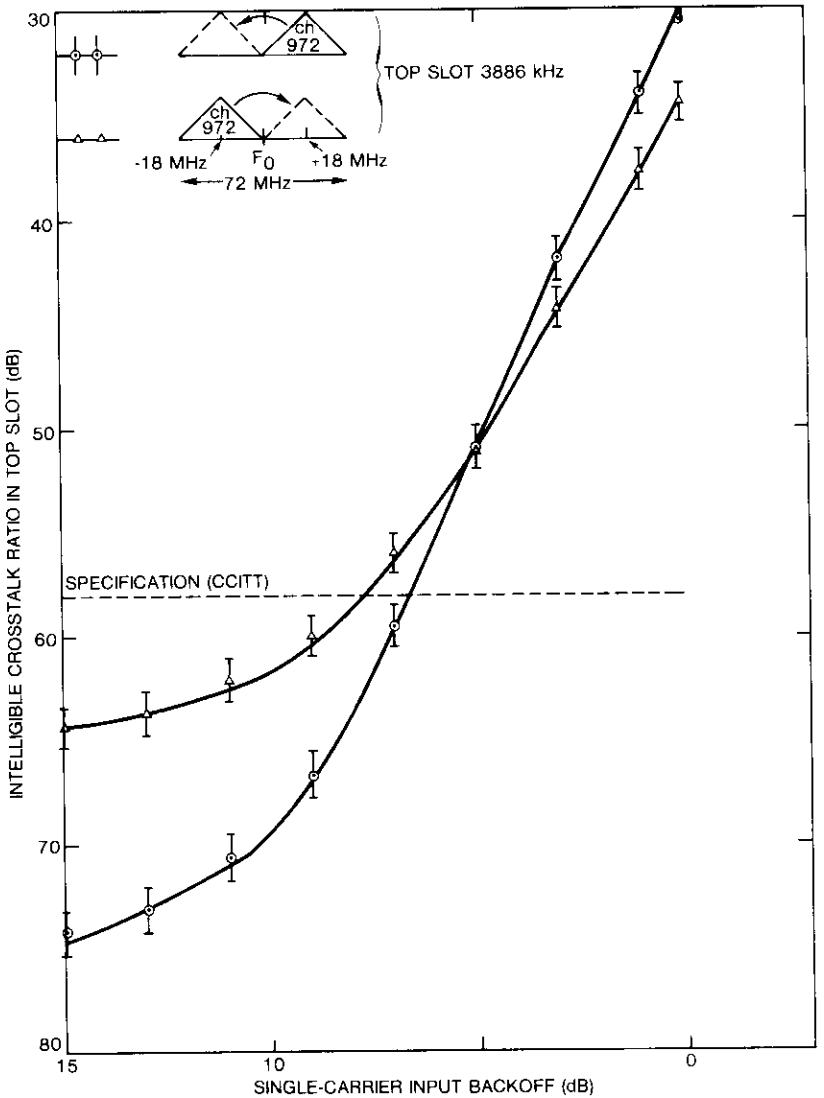

Figure 13. *Intelligible Crosstalk Coupling Between Two 972-Channel FM Carriers via a Common Klystron HPA*

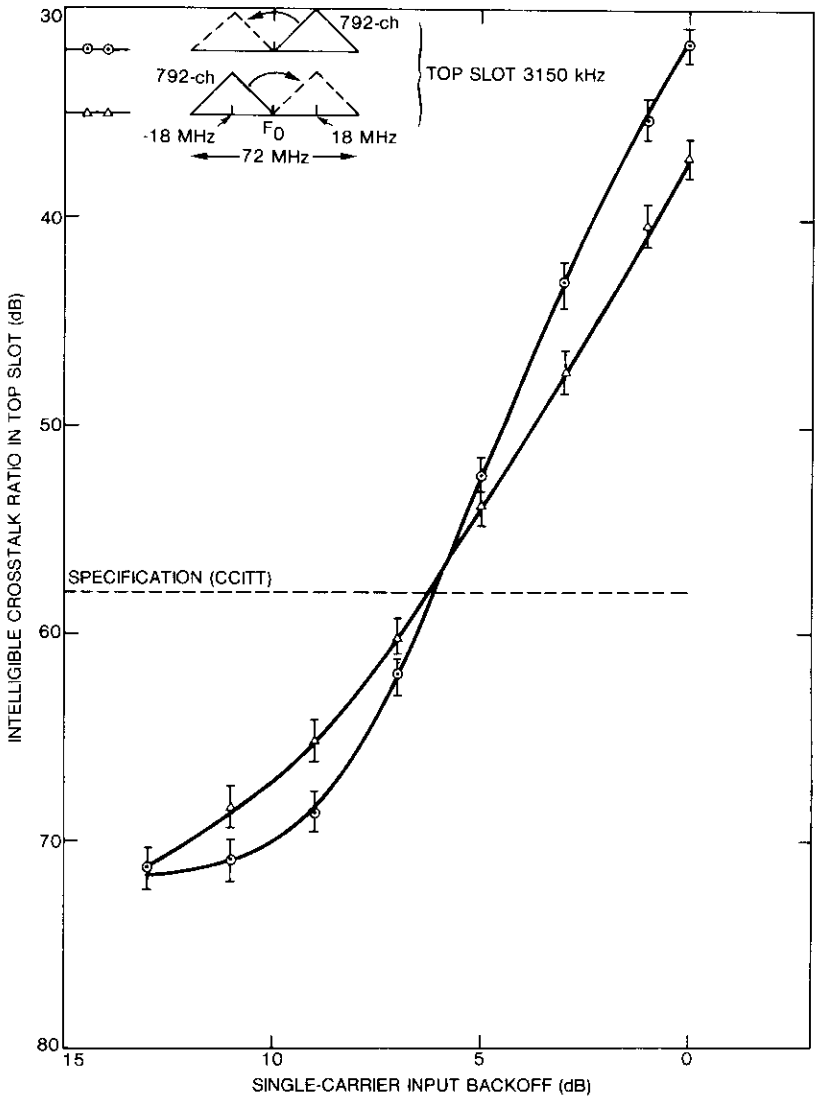

Figure 14. *Intelligible Crosstalk Coupling Between Two 792-Channel FM Carriers via a Common Klystron HPA*

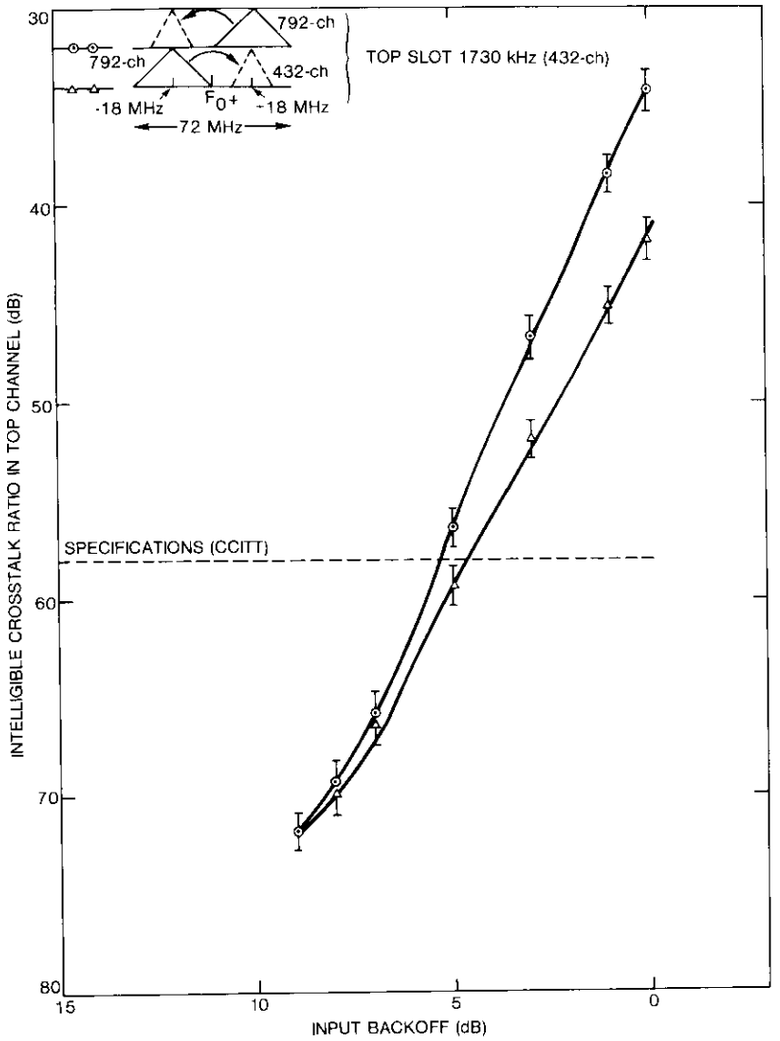

Figure 15. *Intelligible Crosstalk Between 792- and 432-Channel Carriers via a Common Klystron HPA*

hence, the AM/PM transfer effect. In Reference 10, the effect of group delay variation preceding the nonlinearity is also considered. Cases (*a*) and (*b*) are chosen for further study.

Figures 16 and 17 illustrate the measured amplitude and group delay responses over 36-MHz bandwidth FM carrier slots. The AM/PM transfer coefficient of the klystron HPA derived from Figure 4 is shown in Figure 18. The amplitude slope of the FM carrier passband located at F_0 − 18 MHz (see Figure 16) is worse than the amplitude slope of the FM carrier passband located at F_0 + 18 MHz (see Figure 17). Therefore, from equation (8), it is logical to expect that the 972-channel FM carrier at F_0 − 18 MHz will produce a poorer crosstalk ratio when crosstalking on the 972-channel FM carrier at F_0 + 18 MHz [refer to case (*a*)]. On the other hand, the crosstalk ratio should improve when the 972-channel FM carrier at F_0 + 18 MHz is crosstalking on the 972-channel FM carrier at F_0 − 18 MHz [refer to case (*b*)].

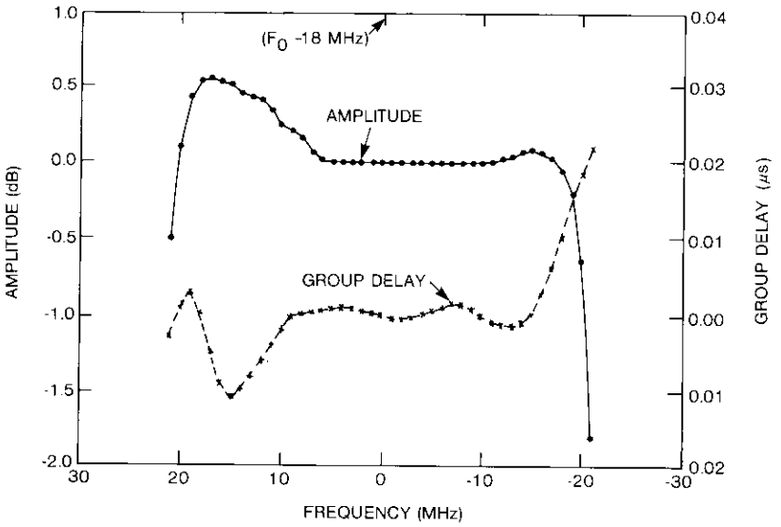

Figure 16. *Channel Input Data: F_0 − 18 MHz*

Figure 13 shows that the argument discussed above holds within the range of 5- to 15-dB input backoff. However, the two curves cross over at 5-dB input backoff and maintain their steep gradients up to 0-dB input backoff. Similar trends are observed in cases (*c*) and (*d*), as illustrated in Figure 14, where the crossover of the two curves at about 6-dB input backoff. In cases (*e*) and (*f*), the crossover occurs at 9-dB input backoff, as shown in Figure 15. Below 9-dB backoff, the system is beyond the acceptable range. This

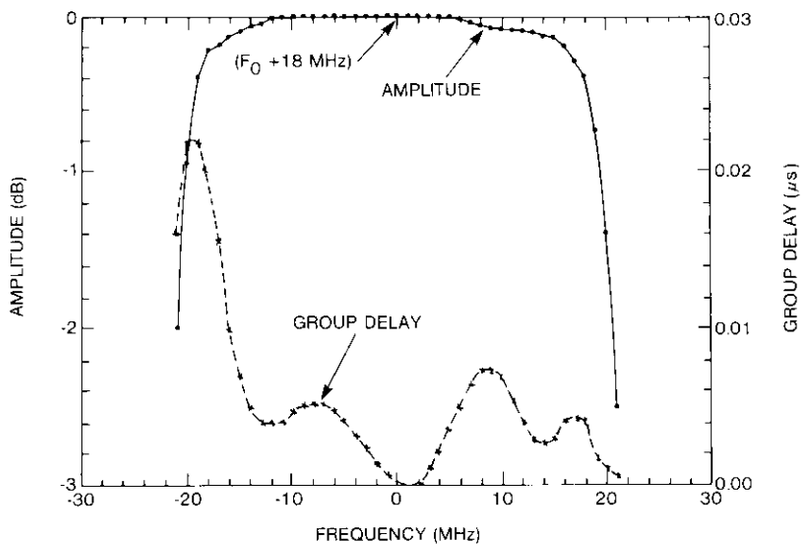

Figure 17. *Channel Input Data: F_0 + 18 MHz*

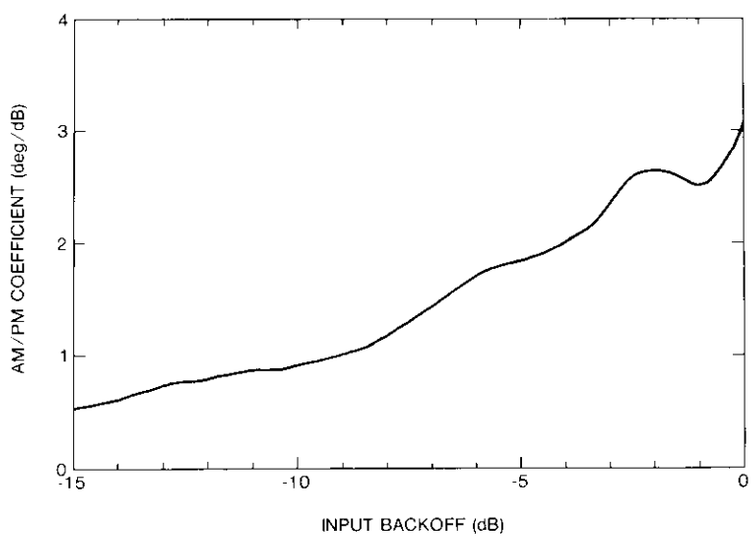

Figure 18. *HPA (Klystron) AM/PM Coefficient for Two Equal-Amplitude Carriers*

crossover phenomenon, and the steep rise of the crosstalk curves in the 6- to 0-dB input backoff range, are not amenable to the theoretical discussion presented above. Similar crosstalk slopes have been observed by Cotner and Barnes [11]. It was therefore considered prudent to verify a set of measurements by computer simulation [9], [10].

The results computed for cases (*a* and (*b*) are shown in Figures 19 and 20, respectively. In Figure 19, an excellent match was achieved between the measured and computed curves within the range of 15- to 6-dB input backoff; while in Figure 20, a reasonable match was achieved within the same range.

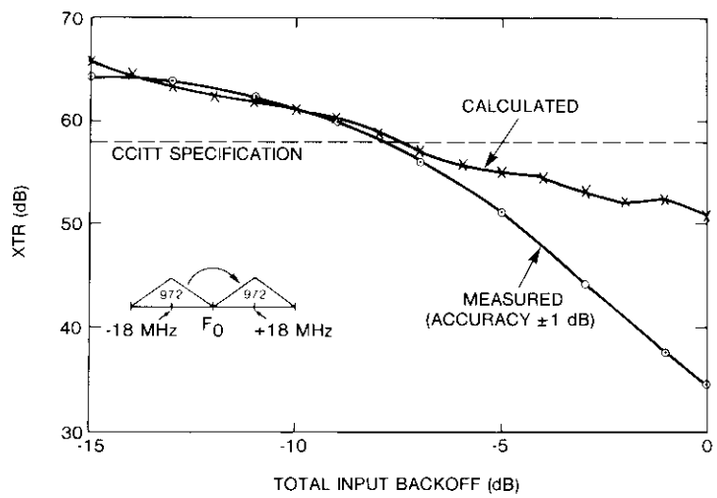

Figure 19. *Intelligible Crosstalk Ratio in a Common HPA: Case a*

A significant divergence exists between the measured and computed results in the 0- to 6-dB input backoff range in both cases. Since crosstalk impairment depends on the gain slope, the klystron intrinsic gain-frequency response was measured at different input backoff points, as shown in Figure 21. From 0- to 6-dB input backoff, the gain slope is significantly large, particularly on the channel centered at + 18 MHz from the band center. Below 6-dB input backoff, klystron intrinsic gain slope is small. The klystron gain slopes were not accounted for in computer simulation, which could explain the divergence observed.

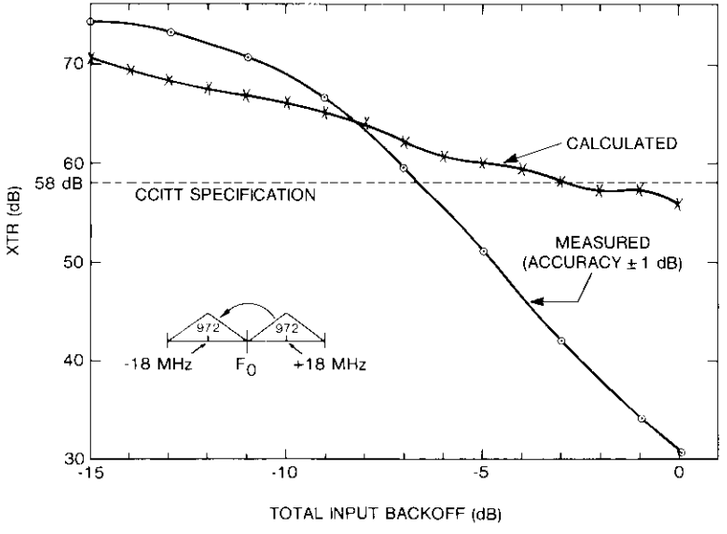

Figure 20. *Intelligible Crosstalk Ratio in a Common HPA: Case b*

System application considerations

In view of the intermodulation product e.i.r.p. (OBN/4 kHz), the klystron HPA can be operated within the 7.5- to 8.5-dB input backoff range (see Figure 9), which corresponds to about 1-kW or 91 dBW of multicarrier e.i.r.p. from a Standard A earth station. Similarly, in terms of the crosstalk coupling, the klystron HPA can be operated within the range of 5.5- to 8-dB input backoff (see Figures 13 through 15) to meet the 58-dB CCITT specification. Therefore, based on combined OBN and crosstalk, the maximum output of the klystron HPA is about 1 kW for multicarrier operation. The e.i.r.p. requirement for three ocean region frequency plans and the margin available from the klystron HPA are shown in Table 5. The thermal noise

TABLE 5. e.i.r.p. MARGIN

REGION	CARRIER SIZE (CHANNELS)	e.i.r.p. REQUIRED (dBW)	e.i.r.p. AVAILABLE (dBW)	MARGIN (dB)
Atlantic Ocean	2 x 792	86.8	91	4.2
Indian Ocean	432, 792	86.3	91	4.7
Pacific Ocean	2 x 972	88.1	91	2.9

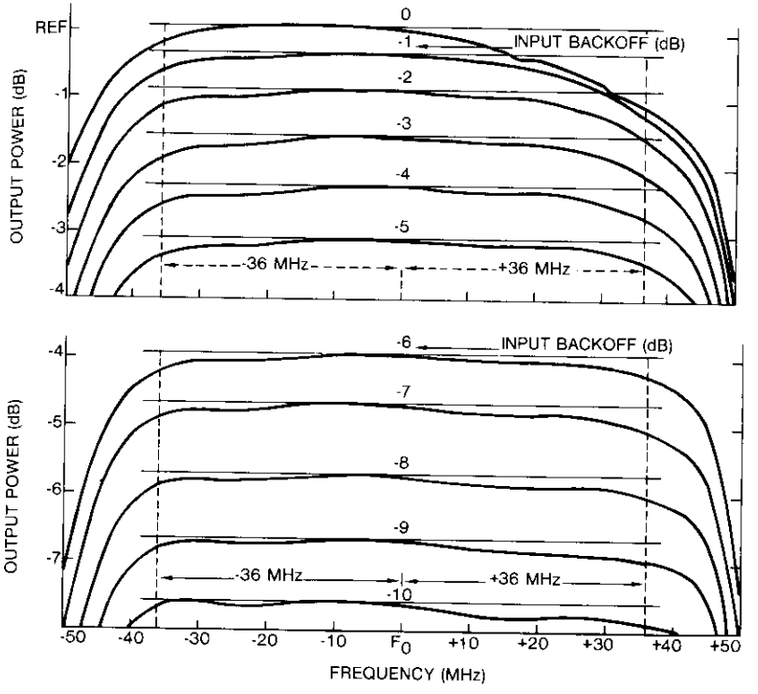

Figure 21. *Gain-Frequency Response of a Klystron HPA*

emission/4 kHz and the group delay distortion noise in the baseband are insignificantly small.

Summary and Conclusion

The technical features of a newly developed 3-kW, 80-MHz-bandwidth, C-band klystron HPA were evaluated to assess its potential for FDM/FM/FDMA operation in the INTELSAT environment. Experimental evidence and computer simulation demonstrated that the klystron HPA can meet the 23-dBW/4-kHz intermodulation product e.i.r.p. limit (OBN/4 kHz INTELSAT specification) when operated close to 8-dB input backoff. Also, the CCITT crosstalk specification of 58 dB can be met when the klystron is operated between 5.5- and 8-dB input backoff, depending on the carrier assignment. Under these conditions, the klystron can deliver about 1 kW of output power for multicarrier operation, which corresponds to an e.i.r.p. of 91 dBW from a

typical Standard A earth station. The e.i.r.p. margin is in the 2.9- to 4.2-dB range, depending on the INTELSAT V frequency plan under consideration. It was also demonstrated that thermal noise/4 kHz and group delay distortion noise in the baseband are insignificant. Thus, it can be concluded that there is no technical barrier to use of the newly developed 3-kW, 80-MHz-bandwidth klystron for FDM/FM/FDMA operation in the INTELSAT environment.

Acknowledgments

This experimental program was carried out for the Project Management Office of COMSAT's World System Division. Thanks are owed to F. Giorgio and W. Bogaert for their interest in this program. The Microwave Component and Subsystem Division of Varian Associates supplied the HPA; and the klystron tube was developed by the Varian Microwave Tube Division. The assistance of the Andover Earth Station staff is gratefully acknowledged. Finally, sincere thanks are given to O. Shimbo, L. N. Nguyen, and C. D. Hsu for many helpful suggestions and computer simulations.

References

[1] D. Chakraborty and E. W. McCune, "A Wideband Klystron HPA Development for 120-Mbit/s QPSK Signaling," Sixth International Conference on Digital Satellite Communications, Phoenix, Arizona, September 19–23, 1983, pp. 1-B-20–1-B-27.

[2] R. W. Gruner and A. E. Williams, "A Low-Loss Multiplexer for Satellite Earth Terminals," *COMSAT Technical Review*, Spring 1975, Vol. 5, No. 1, pp. 157–178.

[3] C. D. Hsu, "Klystron Multi-Carrier Analysis—Computer Simulation," Private Communication.

[4] J. C. Fuenzalida, O. Shimbo, and W. L. Cook, "Time-Domain Analysis of Intermodulation Effects Caused by Nonlinear Amplifiers," *COMSAT Technical Review*, Vol. 3, No. 1, Spring 1973, pp. 89–143.

[5] J. Fagot and P. Magne, *Frequency Modulation Theory*, Elmsford, New York: Pergamon Press, 1961.

[6] S. Fedida and D. S. Palmer, "Some Design Considerations for Links Carrying Multi-Channel Telephony," *Marconi Review*, 4th Quarter, Vol. 18, No. 119, 1955; 1st Quarter, Vol. 19, No. 120, 1956.

[7] R. C. Chapman, Jr., and J. B. Millard, "Intelligible Crosstalk Between FM Carriers Through AM-PM Conversion," *IEEE Transactions on Communications Systems*, CS-12, June 1964, pp. 160–166.

[8] A. L. Berman, C. Mahle, and M. R. Wachs, "Transmission Modeling," *COMSAT Technical Review*, Vol. 2, No. 2, Fall 1972, pp. 489–572.

[9] O. Shimbo and B. A. Pontano, "A General Theory for Intelligible Crosstalk Between Frequency-Division Multiplexed Angle-Modulated Carriers," *IEEE Transactions on Communications*, COM-24, September 1976, pp. 999–1008.

[10] O. Shimbo and L. N. Nguyen, "Intelligible Crosstalk Between Two FDM/FM Carriers Accessing Double Cascaded Nonlinear Amplifiers," *IEEE Transactions on Communications*, COM-30, August 1982, pp. 1993–2000.

[11] C. B. Cotner and A. J. Barnes, "Intelligible Crosstalk Between Large FDM-FM Carriers Amplified by Klystrons," *COMSAT Technical Review*, Vol. 9, No. 2B, Fall 1979, pp. 705–716.

Dayamoy Chakraborty received a Ph.D. in microwave physics from the University of Surrey, England, in 1967. He has been employed by COMSAT since 1968. From 1968 to 1971, he was involved with the satellite system optimization study and the analysis of transmission deviations. In 1971 Dr. Chakraborty transferred to COMSAT Laboratories and has been involved in developing high-speed digital satellite communications systems. Currently, as a Senior Staff Scientist in the Communications Technology Division, he directs research in nonlinear satellite channel design, maximum likelihood sequence estimation, and digital link technology. Prior to joining COMSAT, he was employed by the British Post Office Research Department at Dollis Hill, London. Dr. Chakraborty is the author of numerous publications on microwave techniques and communications technology, and is a Senior Member of IEEE and a corporate Member of IEE.

John W. Ehrmann received a B.S.E.T. from the Capitol Institute of Technology, Washington, D.C., in 1969 and a B.S.E.E. from the George Washington University in 1976. Since joining COMSAT in 1969, he has worked in the Systems Simulator Laboratory, the Earth Station Engineering Division, and the Monitor and Control Engineering Division. He is currently a Staff Engineer at COMSAT World Systems Division's Maintenance and Supply Center, where he is responsible for coordinating various TDMA tasks.

Earl W. McCune is a Senior Scientist with Varian Associates, Inc. He received a B.S.E.E. from the University of California, Berkeley, and an M.S.E.E. from Stanford University. Since joining the Varian Palo Alto Microwave Tube Division in 1956 as a Klystron Engineer, he has been engaged in the design and development of many Varian amplifiers, including the VA-949, a 250-kW CW 8-GHz klystron; the VA-858, a 100-kW CW 2-GHz klystron; and the VA-884D, a 10-kW CW C-band klystron. He has also been extensively involved in the development of depressed collectors for klystrons, broadband tuned klystrons, low-noise klystrons, and high-mu gridded electron guns. Mr. McCune has authored a number of papers and holds several microwave tube patents. He is a member of Eta Kappa Nu and Sigma Xi, and is a Senior Member of IEEE.

Index: antennas, frequency reuse, INTELSAT, polarization, propagation

Cross-polarization measurements at 4 and 6 GHz in the INTELSAT V system*

S. J. STRUHARIK

(Manuscript received November 22, 1983)

Abstract

In satellite systems employing frequency reuse by dual orthogonal polarizations, the depolarizing effects of antennas and the propagation medium are important factors in determining carrier-to-interference ratios. This paper presents the results of cross-polarization measurements conducted at 4 and 6 GHz in the dual-polarized INTELSAT V system on frequency-division-multiplexed/frequency-modulated/frequency-division multiple-access (FDM/FM/FDMA) communications carriers transmitted from seven earth stations in the Atlantic Ocean region (AOR). The stations represent a variety of rain climates, elevation angles, and antenna feed types. Their carriers were continuously monitored at the Mill Village Earth Station in Nova Scotia, Canada, by a specially designed receiver that measured both the cross-polarization discrimination (XPD) in each station's up-link to the satellite and the XPD of each carrier on the down-link to Mill Village.

The measured data provide examples of the effects of depolarization in the actual operating environment of the INTELSAT V system. XPD statistics for each station are presented, as well as examples of recorded data illustrating some of the effects observed. Up-link XPD levels that are not exceeded 0.01 percent of the time range from 8.2 to 25.6 dB for the various stations. Significant XPD degradations resulted

* This paper is based in part on work performed under the sponsorship of the International Telecommunications Satellite Organization (INTELSAT). Views expressed are not necessarily those of INTELSAT.

from both antenna and propagation effects, the latter being more common. Under normal circumstances, antenna tracking methods used in the INTELSAT V system maintained satisfactory XPD levels under clear-sky conditions.

The measurements also confirm, within the INTELSAT V operating environment, expected basic trends in the XPD statistics regarding differences in climate, elevation angle, and frequency scaling of XPD statistics.

Introduction

Frequency reuse by dual orthogonal polarizations began in the INTELSAT system at 4 and 6 GHz with the introduction of the INTELSAT V spacecraft. Dual-polarized operation began in the AOR in mid-1981, in the Indian Ocean region in 1982, and is scheduled to begin in the Pacific Ocean region in 1985. Extensive research and development and a system-wide equipment modification program were conducted in preparation for dual-polarized operation. These efforts focused on the development of hardware and on assessments of the new system's interference environment. One interference aspect unique to satellite systems employing frequency reuse by dual orthogonal polarizations is the degradation of the carrier-to-interference ratio (C/I) that results from depolarization effects in satellite and earth station antennas, and in the propagation medium. Quantifying these effects has been the subject of several studies, experiments, and measurement programs [1]–[10].

This paper presents the results of a cross-polarization measurement program that assessed depolarization effects in the operational frequency-reuse environment of the INTELSAT V system. Measurements were taken at the Teleglobe Canada earth station located in Mill Village, Nova Scotia over a 12-month period beginning in August 1981, just as dual-polarized operation was being initiated.

Long-term data were collected on the XPD maintained in the 6-GHz up-links of seven earth stations in the AOR. In addition to up-link data, 4-GHz down-link XPD was also measured at Mill Village. The earth stations selected represent a variety of rain climates, elevation angles, and antenna feed types. Also, two different INTELSAT V spacecraft were used during the experiment. Measurements were taken over the AOR primary path, using a computer-controlled receiver that continuously monitored communications carriers transmitted by each of the participating earth stations.

The measured data reflect the first year's operation of the dual-polarized INTELSAT V system with respect to depolarization effects and corresponding interference considerations. The data indicate how factors affecting XPD, such as earth station and satellite antenna characteristics, propagation phenomena, and system operating discipline, interact in the operational INTELSAT V frequency-reuse environment to establish the net XPD maintained on a given carrier.

The following sections describe the technique used to perform the measurements, present examples of observed depolarization phenomena (along with statistical results and comparisons to propagation models), and discuss implications of the results for the system.

Measurement configuration

Overview

A block diagram of the measurement configuration is shown in Figure 1. The seven earth stations participating in the experiment transmitted traffic-bearing FDM/FM/FDMA carriers that were monitored by the special-purpose receiver located at Mill Village. The use of operational carriers had the benefit of including all effects present in the operational environment, effects that might not be evident in a strictly controlled experimental environment. Also, since these were commercial carriers normally transmitted by the earth stations, no special prior arrangements were required. Since Mill Village was also one of the transmit earth stations, its carrier was monitored in loopback fashion.

The earth stations were located in the overlapping coverage area of the west zone and west hemispheric (west hemi) beams of the AOR primary path satellite. In this coverage area, the satellite receives and transmits in both right-hand and left-hand circular polarizations (RHCP and LHCP). Each carrier monitored in the experiment was transmitted RHCP. Its copolarized (co-pol) RHCP component was received by the satellite in the west zone beam, translated to the down-link frequency by the west zone receiver, retransmitted RHCP in the west hemi beam, and received RHCP by the Mill Village-2 antenna.

On the up-link, the depolarizing effects of the earth station transmit antenna, the propagation medium, and the satellite receive antenna resulted in a cross-polarized (cross-pol) LHCP component of the transmitted carrier. This component was received by the satellite in the west hemi beam, translated in frequency by the west hemi receiver, retransmitted LHCP in the west zone beam, and received LHCP by the Mill Village-2 antenna.

The up-link cross-polarized component was retransmitted at a slightly different down-link frequency than that of the copolarized signal because the two signals were converted to their down-link frequencies by different receivers, each having a separate translation oscillator. The nominal translation oscillator frequency is 2,225 MHz, which varies by a few kHz among the spacecraft receivers. The variations do not affect the communications function

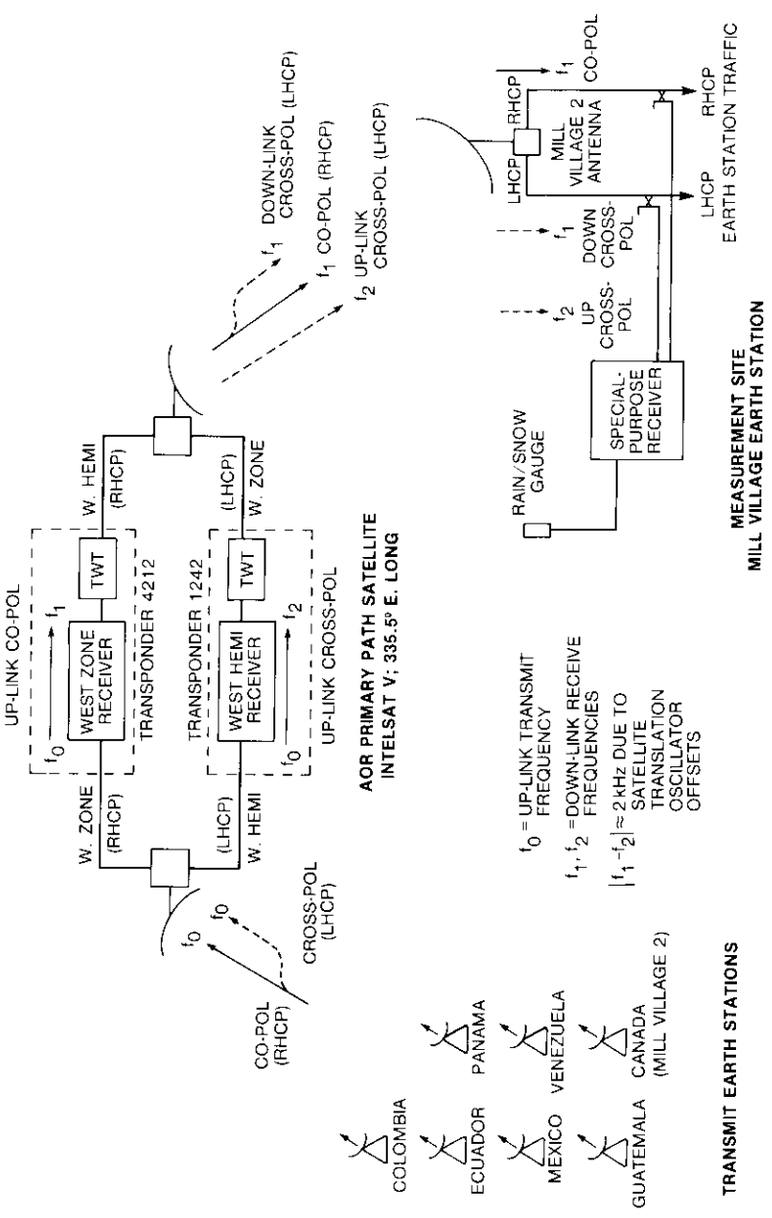

Figure 1. *Overall Measurement Configuration*

of the satellite, but the resulting frequency offset in the down-link between the copolarized signal and the retransmitted up-link cross-polarized signal is used in the detection process of the receiver to separate the up- and down-link cross-polarization signals.

On the down-link, depolarizing effects of the satellite transmit antenna, the propagation medium, and the Mill Village-2 receive antenna resulted in a second cross-polarized signal at the LHCP output of the Mill Village-2 antenna. Because this second signal was generated from the copolarized signal after it had passed through the satellite, the frequency of the second signal was identical to that of the copolarized signal.

Thus, each measured carrier produced three signals at the output of the Mill Village-2 antenna: in the RHCP port, the copolarized signal; and in the LHCP port, two cross-polarization signals (one arising from down-link depolarization effects at the same frequency as the copolarized signal, the other arising from up-link depolarization effects at a slightly offset frequency). The receiver processed the three signals to determine the up-link XPD for each carrier, as would be measured at the output of the satellite receive antenna, and the down-link XPD, as would be measured at the output of the Mill Village-2 antenna. The resulting XPD data reflect the net depolarization brought about by the composite effect of all depolarizing factors in the operational environment. The loopback carrier also allowed 4- and 6-GHz XPD to be monitored simultaneously along the same path.

Site descriptions

Locations of the earth stations that participated in the experiment are shown in Figure 2, which is a map of the AOR as seen from the satellite. Table 1 gives specifics of the location, antenna pointing, and rain climate for each earth station [11]–[13]. The identification numbers assigned were used in the control software of the receiver; they indicate the sequence in which the carriers were measured.

The earth stations were selected to provide information on several factors affecting XPD. The various antennas included in the measurements furnished information on antenna tracking contributions to XPD and on the axial ratio performance of antenna feeds of different manufacturers. Also, to assess the effects of location and climate on XPD, some stations were selected that operate in potentially severe XPD environments (indicated by a low elevation angle) and/or under severe rainfall conditions (indicated by high values of M and β).

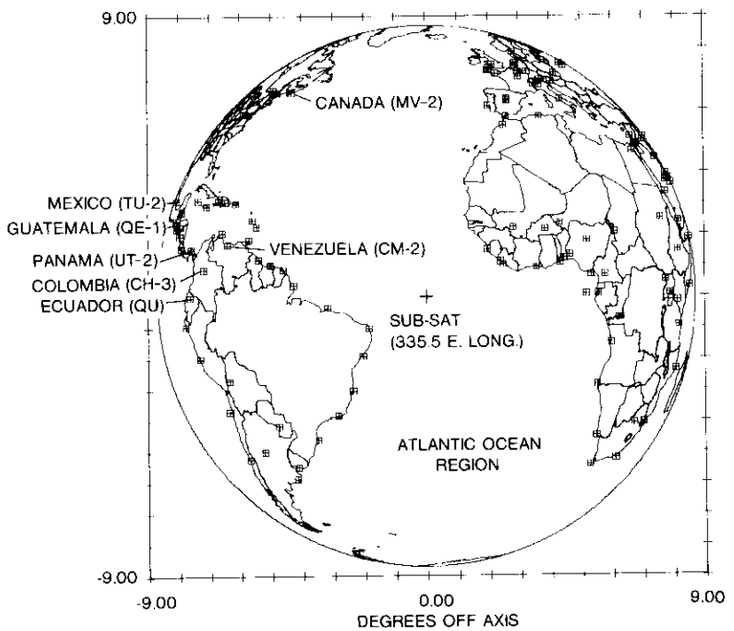

Figure 2. *Atlantic Ocean Region and Earth Station Locations as Seen from the Satellite*

Space segment

The space segment of the experiment was provided by the INTELSAT AOR primary path satellite. During the measurement period, two different spacecraft served this path: INTELSAT V (F-1), or spacecraft 501, and INTELSAT V (F-3), or spacecraft 503. Each was located at 335.5°E longitude during its period of service.

Measurements began on August 31, 1981, using spacecraft 501. On November 1, the spacecraft configuration was altered slightly by substituting hemi receivers in the cross-polarized path through the satellite. This was done to improve the frequency separation between the up-link and down-link cross-polarized components. The receiver at Mill Village could distinguish between up-link and down-link cross-polarized components with frequency separations as small as 90 Hz. When the measurements began, the frequency separation was about 150 Hz; later it gradually narrowed so that the receiver could no longer distinguish between the two cross-polarized components.

TABLE 1. EARTH STATION LOCATIONS AND RAIN CLIMATES

LOCATION (CARRIER IDENTIFICATION NO.)	EARTH STATION	LATITUDE/ LONGITUDE	ELEVATION ANGLE[a] (deg)	M[b] (mm)	β[c]	ANTENNA TYPE[d]	ANTENNA FEED MANUFACTURER
Colombia (1)	Choconta-3 (CH-3)	5.16°N 286.33°E	33.37	870	0.70	New	Thomson CSF
Canada (2)	Mill Village-2 (MV-2)	44.19°N 295.33°E	25.37	1270 (1438)[e]	0.10 (0.05)[e]	Retrofit	Spar Canadian Iron
Ecuador (3)	Quito (QU)	0.27°S 281.53°E	28.38	1235	0.08	Retrofit	Mitsubishi
Mexico (4)	Tulancingo-2 (TU-2)	20.07°N 261.57°E	6.42	550	0.25	New	Rantec E-Systems
Guatemala (5)	Quetzel-1 (QE-1)	14.56°N 269.56°E	14.83	1195	0.75	New	Harris
Panama (6)	Utibe-2 (UT-2)	9.15°N 280.68°E	26.92	1770	0.70	New	GTE
Venezuela (7)	Camatagua-2 (CM-2)	9.81°N 293.12°E	40.06	835	0.70	New	NEC

[a] Elevation angles shown are for the AOR primary path satellite at 335.5°E longitude.
[b] Average annual rainfall accumulation.
[c] Average thunderstorm ratio, *i.e.*, the fraction of total rain accumulation arising from convective storms [14]; $0.00 \leq \beta \leq 1.00$.
[d] All antennas used step tracking; "retrofit" describes an existing antenna that has been modified for dual-polarized operation.
[e] Values measured at Mill Village during the experiment.

The change in spacecraft receivers restored the frequency separation to a value of about 1,200 Hz.

On March 1, 1982, spacecraft 503 replaced spacecraft 501 as the AOR primary path satellite. The configurations of the copolarized and cross-polarized paths in the new spacecraft were the same as those in the old one. The frequency separation between the up-link and down-link cross-polarized components was about 1,800 Hz. Spacecraft 503 was used for the remainder of the measurements, which ended August 31, 1982.

Parameters of the carriers monitored in the experiment are shown in Table 2.

TABLE 2. SUMMARY OF CARRIER PARAMETERS

LOCATION (CARRIER IDENTIFICATION NUMBER)	FREQUENCY UP/DOWN (MHz)	BANDWIDTH (MHz)	CHANNELS
Colombia (1)	6042.5/3817.5	2.5	48
Canada (2)	6037.5/3812.5	5.0	96
Ecuador (3)	6067.5/3842.5	5.0	72
Mexico (4)	6083.5/3858.5	5.0	96
Guatemala (5)	6050.0/3825.0	10.0	252
Panama (6)	6060.0/3835.0	10.0	252
Venezuela (7)	6075.0/3850.0	10.0	252

Figure 3 shows the locations of the carriers in the satellite transponder frequency plan. In the copolarized transponder, the lowest frequency carrier,

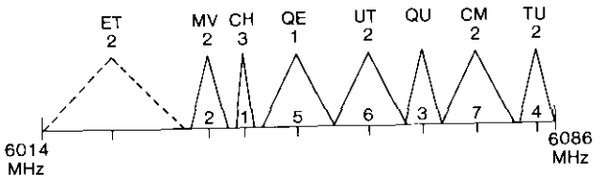

(a) CO-POL TRANSPONDER: 4212, W. ZONE TO W. HEMI. CHANNEL 3-4

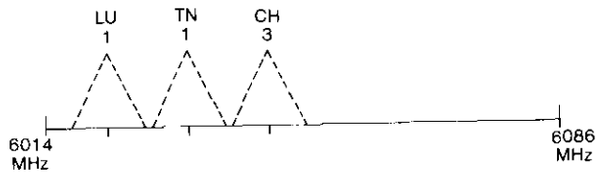

(b) CROSS-POL TRANSPONDER: 1242, W. HEMI TO W. ZONE, CHANNEL 3-4

Figure 3. *Satellite Transponder Frequency Plan*

transmitted by the Etam-2 (USA) earth station, was not monitored in the experiment. Three carriers were present in the cross-polarized transponder. These were transmitted by the Lurin-1 (Peru), Tangua-1 (Brazil), and Choconta-3 (Colombia) earth stations. The cross-polarized components of carriers 1, 2, and 5 were within the allocated bandwidths of the Tangua or Choconta carriers. The cross-polarized components of the other carriers in the experiment were in unoccupied portions of the cross-polarized transponder.

Table 3 summarizes the polarization isolations of the spacecraft and earth station antennas [12], [13]. For the spacecraft antennas, each value of isolation given is for the location in the spacecraft antenna pattern of the earth station. The polarization isolations of both spacecraft are quite similar. For the earth station antennas, the values of isolation given are the maximum and minimum values within $\pm 0.02°$ of beam center for each antenna. Values in parentheses are the weighted average value of isolation within these bounds. In some cases, the earth station antenna isolation can be quite close to that of one or both spacecraft, resulting in a very high net isolation in individual up-links or down-links if the spacecraft and earth station antenna isolations cancel each other out.

Ground equipment

The special-purpose computer-controlled receiver measured the copolarized signal level, up-link XPD, and down-link XPD of each of the seven carriers as well as the clock time and rain/snow gauge activity at Mill Village; it then recorded the data on flexible disks. This measurement cycle was repeated every 70 s. Receiver operation was unattended except for weekly changing of the flexible disks and periodic visual checks of receiver operation by earth station operators. The flexible disks were regularly sent back to COMSAT Laboratories, where the recorded data were processed and analyzed. The receiver used correlation techniques to measure the weak, wideband cross-polarization components in the presence of noise and strong carriers. Its design and operation are described in a companion paper to be published in a future issue of the *COMSAT Technical Review*.

Data processing and analysis

Cumulative distributions of up- and down-link XPD were generated for each carrier between November 5, 1981, and August 28, 1982 (296 days). During the first two months of the experiment (from September to October 1981), minor hardware difficulties in the receiver and changes in the satellite system resulted in calibration uncertainties and some downtime. Data from this time frame exhibit the same relative XPD trends as the rest of the data,

but for the reasons cited are not included in the final statistics. Since the purpose of the experiment was to observe the day-to-day XPD environment in the satellite system, the cumulative distributions generated utilized all of the recorded data. Only invalid data were excluded, such as those recorded when a carrier was off the air or temporarily outside the receiver's dynamic range.

Depolarization phenomena observed in the data reflect the combined action of all the depolarizing factors in the satellite system: satellite and earth station antenna effects, which include polarization isolations as well as earth station antenna pointing and diurnal satellite orbital variations, and propagation medium effects. In this experiment, XPD was derived only from measured amplitudes. In such cases, antenna effects cannot be easily separated from propagation effects [10]; only the net XPD is available. The relative contribution of propagation effects to observed XPD can be estimated, however, using the family of curves shown in Figure 4. This figure depicts the range of XPDs

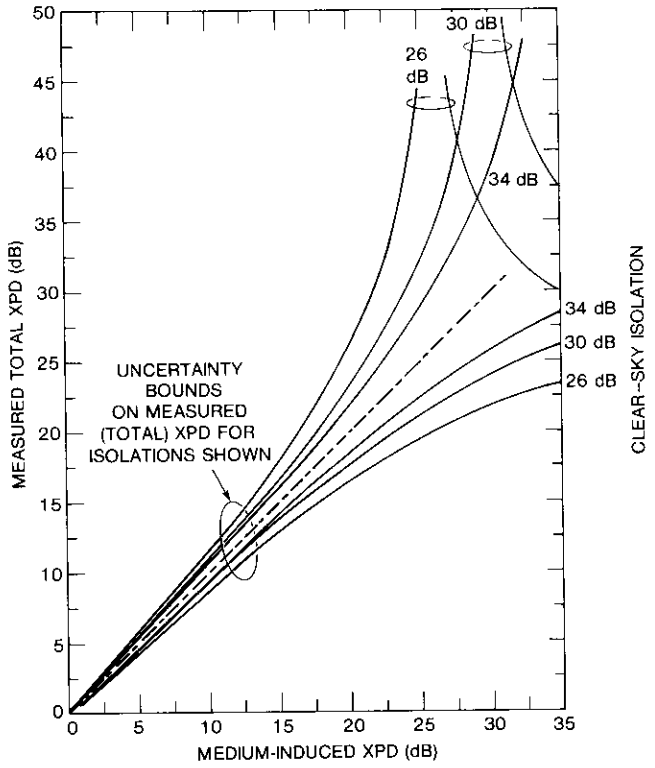

Figure 4. *Measured* vs *Propagation Medium-Induced XPD for Clear-Sky Isolations of 26, 30, and 34 dB*

that could be observed for a given value of propagation medium-induced XPD in a system with a given net value of polarization isolation under clear-sky conditions. The curves were generated by calculating the best and worst case addition of the clear-sky isolation to a range of assumed medium-induced XPDs [10], [15]. At high values of medium-induced XPD, measured XPD approaches the value of the clear-sky isolation in the system. As the medium-induced XPD approaches the value of the clear-sky isolation, a wide range of XPDs could be observed (because the two could add constructively or cancel each other out completely). As the medium-induced XPD becomes severe, however, it becomes the dominant factor, and the XPD observed approaches that of the medium.

It should also be noted that the value of clear-sky isolation in the system is not static. Its value depends on the combination of satellite and earth station polarization isolations. Both of these can change with frequency within a transponder, and their combination can change with time as the spacecraft moves about its ephemeris and as the earth station antenna moves in tracking the satellite.

Results

Selected examples of recorded data

This subsection presents examples of depolarization phenomena observed in the recorded data. Detailed information on earth station operation and weather data beyond the long-term average values of M and β for the sites were available only for Mill Village. In the data analysis, phenomena were identified as propagation-related or antenna-related, using the following guidelines.

With all stations using step tracking, antenna tracking effects tend to appear as abrupt changes in the data. For all stations except Mill village, a change in the copolarized signal level, usually with a simultaneous change in up-link XPD (UXPD), was observed during a tracking update. The down-link XPD (DXPD) data pertain only to the path between the satellite and Mill Village and are not affected by movement of the up-link antenna. For the Mill Village carrier, copolarized signal level, UXPD, and DXPD all change because this carrier is a loopback. In normal operation, the copolarized level improves during a tracking update, which is performed to maintain the copolarized signal level. XPD may improve or degrade in the process because of variability in polarization isolation over the earth station antenna's tracking beamwidth, and because of the vectorial way in which isolations of the earth station and satellite antennas combine. Also, before the tracking update, the copolarized level will have slowly degraded, and XPD will have slowly changed as the satellite drifts to the edge of the tracking beamwidth. The

overall appearance is that of a sawtooth waveform in the copolarized and XPD traces. Antenna tracking effects would not normally be visible with monopulse tracking or with step-tracking antennas whose tracking beamwidth is small and whose polarization isolation is fairly uniform across the tracking beamwidth.

Propagation events appear as fairly smooth degradations in XPD from clear-sky values to the lower ranges, which then return to clear-sky values after the event passes. Frequently, copolar attenuation is also visible during the event as a dip in the copolarized level. If the source of the event is ice crystal depolarization, however, the copolarized level shows little attenuation.

In the figures that follow, the uppermost trace is the copolarized signal level; of the two lower traces, the up-link XPD trace is labeled "U," and the down-link XPD trace is labeled "D." The abscissa is time (GMT); the numbers on the ordinate are XPD (given in dB referred to the reference channel; note that XPD is designated as "crosspol" in these figures) or the relative copolarized signal level, also in decibels. The lowermost scale, when shown, indicates the rain rate at Mill Village in millimeters per hour, averaged over one measurement cycle. Values of peak rain rate quoted below were computed directly from the recorded times of individual rain gauge tips.

It should be noted that the time between samples for one carrier (70 s) is too long to define the structure of short-term XPD fluctuations. It is, however, sufficient to define long-term XPD behavior and allow comparisons of the average values of slowly changing portions of events.

PROPAGATION PHENOMENA

Figures 5 through 9 are examples of some of the propagation events observed. Figure 5 shows the simultaneous up-link and down-link XPD degradations on loopback carrier 2 during a severe depolarization event at Mill Village. The peak rain rate exceeded 150 mm/hr at 0730 GMT; other rain rate peaks are as marked.

The tendency for the down-link of carrier 2 to be degraded more than the up-link is unusual. Down-links of the other carriers all showed less degradation during this event than did the up-link of carrier 2, which is the more expected behavior. These phenomena will be discussed below.

Little copolar attenuation is visible, despite the high point rain rates and the attenuation of the loopback carrier at both 4 and 6 GHz. This, along with the time of year, the northerly location, and the maritime climate of Mill Village, indicates that ice crystal depolarization may have played a major role in this event [15].

Figures 6 and 7 show strong events occurring in Mexico, both with and without significant attenuation (the latter implying ice crystal depolarization).

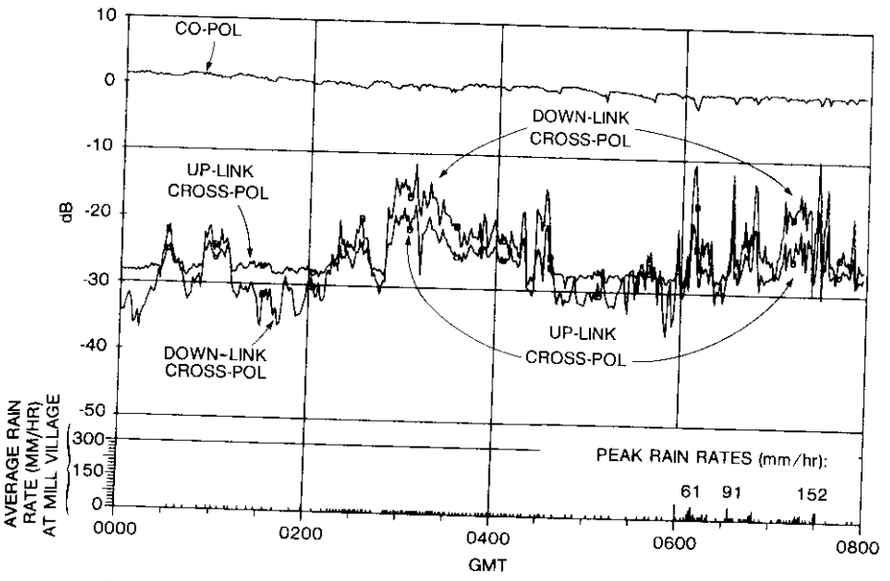

Figure 5. *Propagation Event at Mill Village, Canada, November 21, 1981, as Seen on the Loopback Carrier*

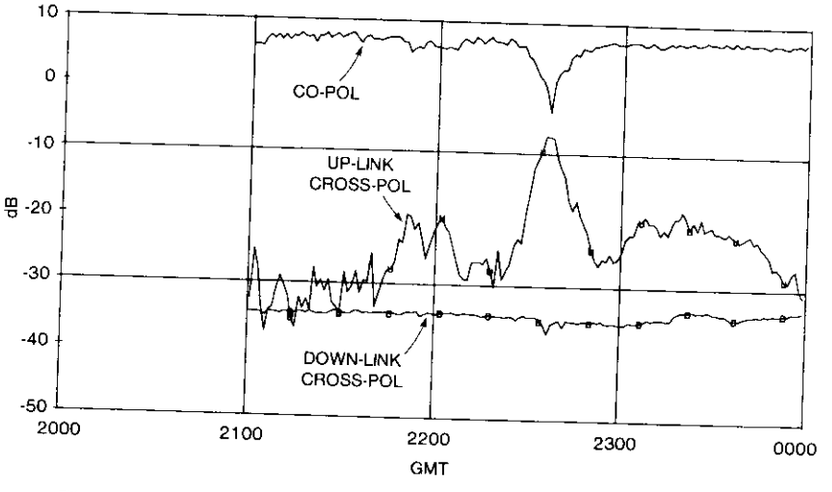

Figure 6. *Propagation Event at Tulancingo, Mexico, May 9, 1982*

These two events also illustrate that even though Tulancingo, Mexico, has low values of M and β, these are long-term averages that do not preclude

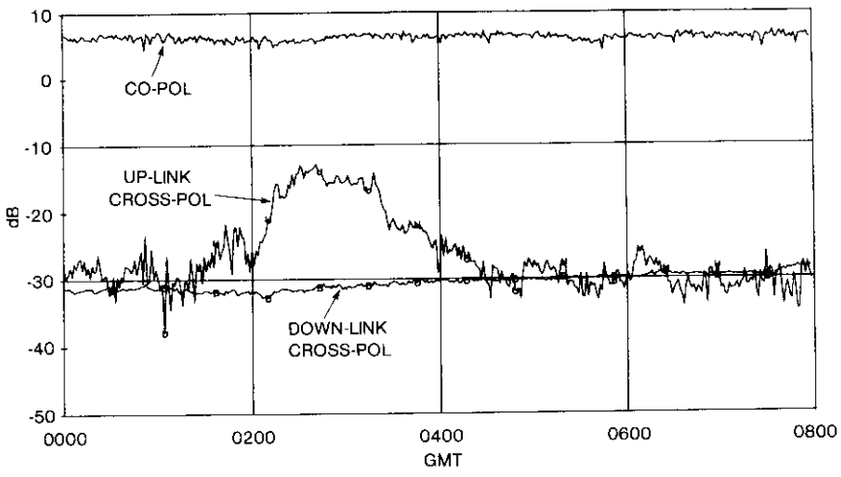

Figure 7. *Propagation Event at Tulancingo, Mexico, March 23, 1982*

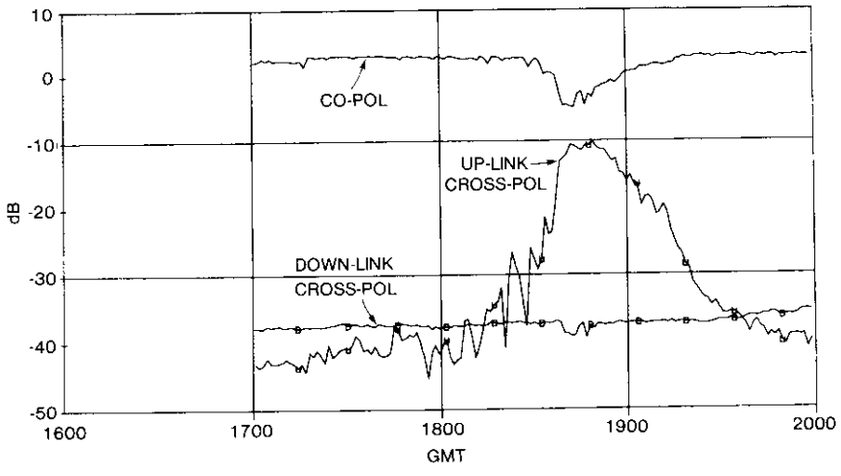

Figure 8. *Propagation Event at Utibe, Panama, May 11, 1982*

the possibility of individual severe weather events. Fluctuations in the copolarized and up-link XPD traces are characteristic of the data and may reflect multipath effects (discussed below) and variability in polarization isolation across the tracking beamwidth (26.2–41.0 dB in Table 3).

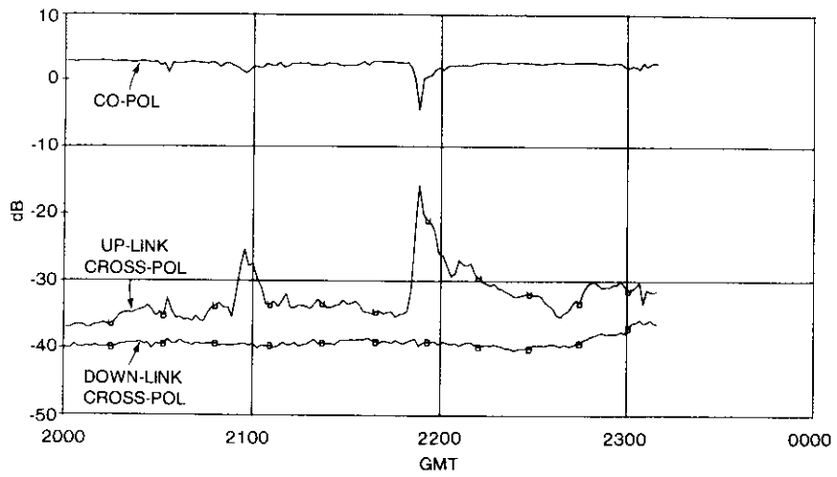

Figure 9. *Propagation Event at Camatagua, Venezuela, May 29, 1982*

Figure 8 shows a severe event occurring in Panama. The XPD fluctuations visible at the onset of the event are characteristic of the cancellations and enhancements that can occur at high XPD levels when transmission medium effects are large enough to affect but too small to dominate the net observed XPD. The presence of these fluctuations at the beginning, but not the end, of the event implies a rapidly changing depolarization component in the propagation medium early in the event. This is probably a signature of the ice crystal depolarization frequently observed at the onset of convective storms.

Approximate rise times in the more sudden events (*e.g.*, Figure 9 for Venezuela) are on the order of 3 to 5 minutes (to degrade from the 30-dB XPD level to values in the mid-teens). After its abrupt onset, there is a smooth decay of the event. Depending on local weather patterns, such phenomena can occur when a storm approaches from the rear of the antenna or from the cross-path rather than from the down-path direction.

ANTENNA TRACKING

Figure 10 is a typical example of antenna tracking observed under clear-sky conditions. The copolarized and up-link XPD traces show the characteristic sawtooth pattern discussed above. In this example, XPD improves as the satellite drifts to the edge of the tracking beamwidth (canceling at one point) and is degraded slightly by the tracking updates.

During a period of abnormal antenna tracking, the measurements showed

TABLE 3. CROSS-POLARIZATION ISOLATIONS OF SATELLITE AND EARTH STATION ANTENNAS

LOCATION (EARTH STATION)	CROSS-POLARIZATION ISOLATION (dB)*					
	SPACECRAFT 501		SPACECRAFT 503		EARTH STATION	
	UP-LINK	DOWN-LINK	UP-LINK	DOWN-LINK	UP-LINK	DOWN-LINK
Colombia (CH-3)	32.6	—	36.2	—	31.9–41.0 (32.7)	—
Canada (MV-2)	33.0	34.0	34.8	33.9	30.3–34.2 (31.7)	33.0–35.0 (34.0)
Ecuador (QU)	35.3	—	31.4	—	32.0–36.0 (32.6)	—
Mexico (TU-2)	31.4	—	31.9	—	26.2–41.0 (32.6)	—
Guatemala (QE-1)	29.8	—	29.2	—	25.0–37.0 (29.0)	—
Panama (UT-2)	30.4	—	32.5	—	29.9–31.8 (30.5)	—
Venezuela (CM-2)	34.6	—	35.3	—	34.1–35.8 (34.6)	—

* Spacecraft isolations are for channel (3-4) midband—up-link: 6,050 MHz; down-link: 3,825 MHz. Earth station isolations are for 6,070 MHz (up-link) or 3,845 MHz (down-link).

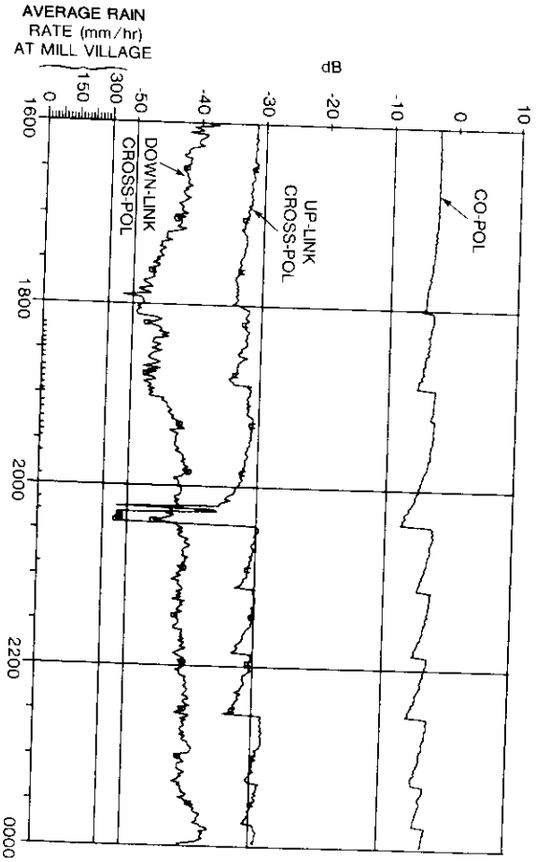

Figure 10. *Example of Antenna Tracking (Quito, Ecuador, March 2, 1982)*

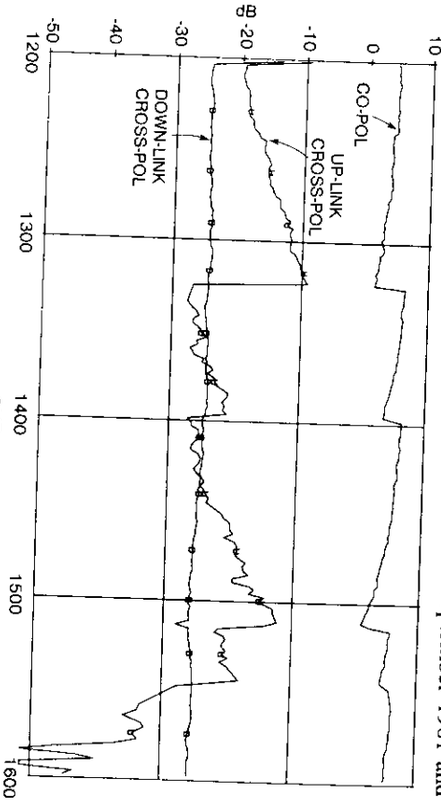

Figure 11. *Abnormal Antenna Tracking at Tulancingo, Mexico, November 12, 1981*

that periodic swings in XPD ranging from the teens to around 30 dB were common. An extreme example of this wide variation is shown in Figure 11. This phenomenon occurred at the station between late September 1981 and

March 1, 1982, when the transition from spacecraft 501 to 503 took place. This suggests that the station may have had trouble with antenna tracking equipment during that time, but made a change at the time of the transition that solved the problem.

Statistical results

RAIN RATE STATISTICS

Annual accumulations of point rainfall and snowfall (liquid equivalent) measured at Mill Village during the experiment were 1,438 and 101 mm, respectively [16]. Figure 12 compares the cumulative distribution of measured rain rate to a distribution calculated from the Rice-Holmberg model [14].

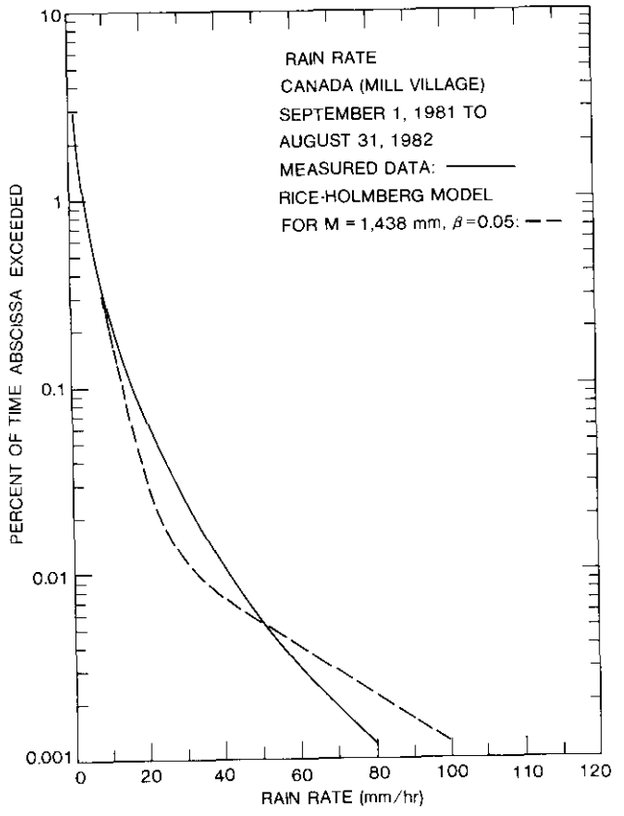

Figure 12. *Cumulative Distribution of Rain Rate at Mill Village*

For M = 1,438 mm, the model appears to give reasonable agreement with the measured data at β = 0.05. The long-term average values for Mill Village are M = 1,270 mm and β = 0.1, which indicate that during the experiment, rain accumulation at Mill Village was slightly greater than average, but the proportion of rain occurring at high rates was less than usual. For the other sites, only the long-term average values of M and β were available, as listed in Table 1.

XPD STATISTICS

Figure 13 presents the measured cumulative up-link XPD (UXPD) statistics for all carriers, from data collected between November 5, 1981, and August 28, 1982. These data were gathered using both spacecraft 501 and 503; they include the effects of all sources of depolarization on the respective up-links. The nominal clear-sky values of UXPD for the carriers are shown in Table 4.

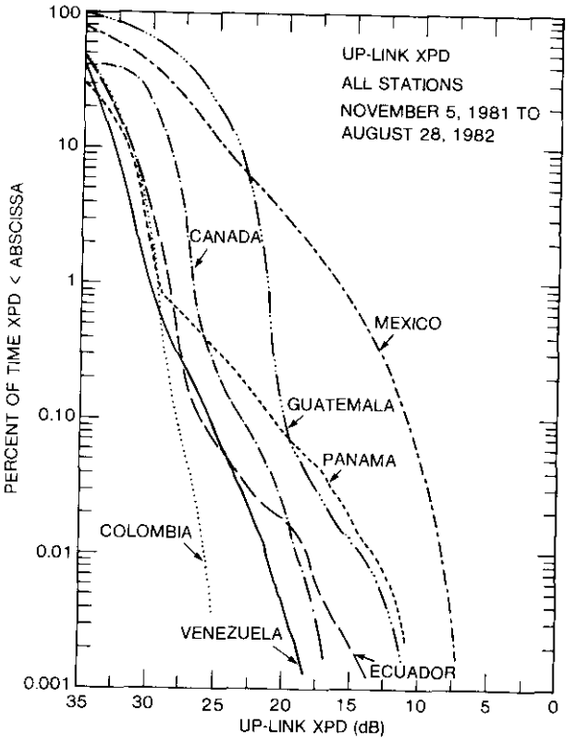

Figure 13. *Up-Link XPD Statistics, All Stations*

TABLE 4. CLEAR-SKY VALUES OF UP-LINK XPD

LOCATION	VALUES (dB) BY STATION AND TIME FRAME		
	SPACECRAFT 501 (11/5/81–3/1/82)	SPACECRAFT 503 (3/2/82–8/28/82)	OVERALL (11/5/81–8/28/82)
Colombia	32	44	42.6
Canada	30	38	37.6
Ecuador	34	33	35.0
Mexico	27	33	31.2
Guatemala	24	29	28.3
Panama	32	44	38.4
Venezuela	35	35	35.3

For data pertaining to a particular satellite, clear-sky values are considered the most commonly occurring (*i.e.*, most probable) values of UXPD observed. For the overall data base, a composite of data from both spacecraft, this definition of clear-sky can be misleading because of double peaks in the resulting probability density functions. In such cases, the values of UXPD shown are those not exceeded 50 percent of the time.

The positions and shapes of the curves in Figure 13, together with the examples of recorded data, allow some qualitative observations on the relative importance of various depolarization mechanisms at the stations. The curves exhibit bimodal structures, and some have very distinct break points. Upper portions of the curves are influenced mainly by antenna effects, while the shapes of the lower portions reflect the relative severity of propagation effects. Compare, for example, the curves for Colombia, Panama, and Mexico.

Data for Colombia were well-behaved. Other than normal step tracking at clear-sky levels, no significant depolarization events or antenna-pointing phenomena were observed. The curve for Colombia is correspondingly steep and in the high XPD range.

Data for Panama indicated no severe antenna-pointing phenomena, but when propagation events did occur, they frequently resulted in severe XPD degradations from the consistently high clear-sky values down to XPD values in the teens. Correspondingly, the curve for Panama is steep in the clear-sky range, but it has a breakpoint midway down that is the beginning of a wide flare to severe XPD levels. Such a curve shape indicates a station with good clear-sky XPD, but which at low time percentages is subjected to severe depolarizing weather events.

Data from Mexico appear to have been influenced considerably by both antenna and propagation effects. Periodic cycling of XPD ranging from values in the teens to around 30 dB was common in portions of the recorded data, suggesting the effects of step tracking. When propagation events occurred,

they tended to be severe. Peak-to-peak XPD fluctuations of 3 to 5 dB centered about the average value of the XPD trace were also common. All of these phenomena are thought to be strongly related to the low elevation angle (6.4°) for this path. This fact plus the station's mountainous locale increase the likelihood of XPD degradations caused by multipath effects. Also, despite the locale's fairly mild climate, the low elevation angle results in a long path through the troposphere, which in turn magnifies the effects of weather-induced propagation events.

The above examples represent mild, intermediate, and severe XPD operating environments; XPD statistics for the remaining stations fall in the intermediate range. The curve for Guatemala has a flare at the low end similar to that of Panama. This is consistent with the station's fairly low elevation angle (14.8°) and the severity of propagation events observed in the data. Also, the upper part of the curve falls in a lower XPD range than most of the other stations because the polarization isolations of the satellite and earth antennas combined to give Guatemala the lowest clear-sky XPD of all the stations.

Table 5 lists the seven earth stations by relative severity of their measured up-link XPD statistics, based on the 0.01 percent XPD levels shown. Similar trends are exhibited by 0.1 percent XPD levels. Also shown are the 0.01 percent XPD levels predicted by a COMSAT propagation model [17].

The results indicate the expected trends of XPD degradations (tending to be more severe at lower elevation angles and/or in climates having higher average values of M and β, with various combinations of these three factors yielding intermediate results).

The relative severity of the the measured XPDs is somewhat different than that predicted by the model, in part because the long-term average values of M and β, used as inputs to the model, are not necessarily those which existed at the sites during the experimental period. Also, as shown in Figure 4, at less severe values of observed XPD, antenna effects introduce increasing uncertainty in comparisons of measured XPD to propagation-induced depolarization predicted by the model. Nevertheless, the three stations measured as having the most severe XPD environments, Guatemala, Panama, and Mexico, were also the three predicted by the model to have the most severe XPD statistics.

The COMSAT model appeared to give reasonable agreement with data for Panama, as shown in Figure 14. This example also illustrates the bimodal structure of the distributions discussed above.

COMPARISON OF 4- AND 6-GHZ XPD

Figure 15 shows the cumulative down-link XPD (DXPD) statistics measured between November 5, 1981, and August 28, 1982, using both spacecraft. The data reflect the effects of all sources of depolarization on the down-link

TABLE 5. COMPARISON OF UP-LINK XPD STATISTICS

LOCATION	M (mm)	β	ELEVATION ANGLE (deg)	FEED Mfgr.[a]	MEASURED DATA 0.1% XPD (dB)	MEASURED DATA 0.01% XPD (dB)	COMSAT MODEL 0.01% XPD (dB)[b]
Colombia	870	0.70	33.4	Thomson-CSF	27.9	25.6	17.9
Venezuela	835	0.70	40.1	NEC	25.5	21.2	20.4
Canada	1270	0.10	25.4	SPAR	23.0	18.8	23.1 (27.5)[c]
Ecuador	1235	0.08	28.4	Mitsubishi	25.7	18.0	26.1
Guatemala	1195	0.75	14.8	Harris	19.9	14.1	9.6
Panama	1770	0.70	26.9	GTE	20.9	13.4	13.4
Mexico	550	0.25	6.4	Rantec	10.9	8.2	14.2

[a] All antennas used step tracking.
[b] Predicted by propagation model based on average M and β.
[c] Based on measured M and β at Mill Village.

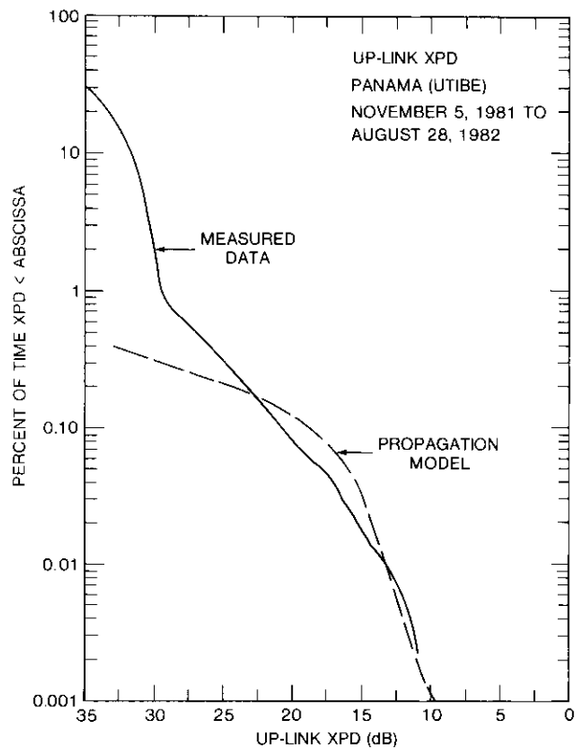

Figure 14. *Comparison of Propagation Model to Up-Link XPD Statistics for Utibe, Panama*

between the satellite and Mill Village. The clear-sky values of DXPD are shown in Table 6. As before, values shown for a particular satellite are the most commonly occurring values of DXPD observed. Values shown for the overall data base are those not exceeded 50 percent of the time.

The curves represent multiple measurements of DXPD along the satellite to Mill Village path. Carriers were measured sequentially, 10 s apart, with carrier frequency the only significant difference among them. The spread in the curves, especially at high XPDs, is caused by variation with frequency of the polarization isolations of the satellite and earth station antennas, and by the manner in which they combine to produce net clear-sky isolations. During

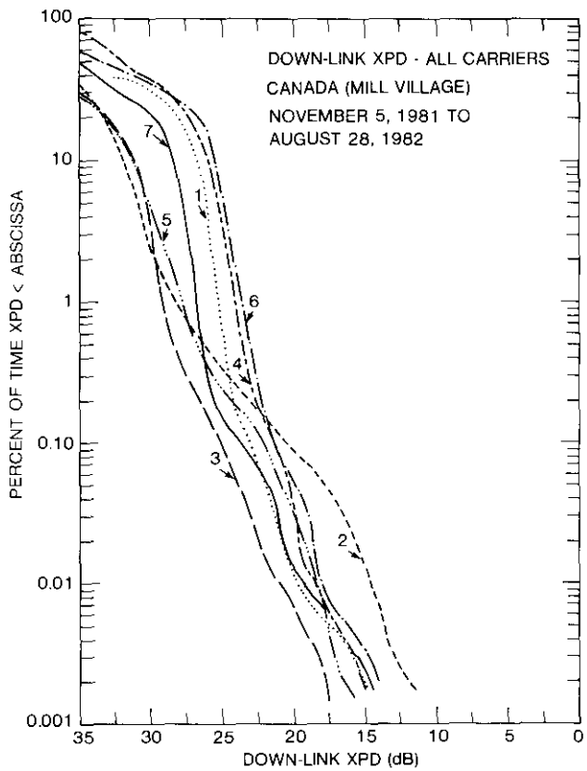

Figure 15. *Down-Link XPD Statistics for Mill Village, All Carriers*

TABLE 6. CLEAR-SKY VALUES OF DOWN-LINK XPD AT MILL VILLAGE

	VALUES (dB) BY CARRIER AND TIME FRAME		
CARRIER	SPACECRAFT 501 (11/5/81–3/1/82)	SPACECRAFT 503 (3/2/82–8/28/82)	OVERALL (11/5/81–8/28/82)
1	27	40	36.6
2	33	38	37.3
3	31	39	37.9
4	28	34	32.3
5	32	39	37.4
6	26	38	33.8
7	29	39	35.2

propagation events, as the transmission medium's contribution to XPD grows, it begins to dominate the observed XPD, and the uncertainty bounds on measured *vs* medium-induced XPD draw closer together, as shown in Figure 4. This effect shows itself in the way the curves begin to bunch together at lower XPDs (Figure 15). To some extent, this bunching is inhibited at low time percentages by the stability of the statistics (with the 0.01-percent level representing 35 samples), but the effect is still visible. The curve for carrier 2 is an exception. The tendency for this carrier's DXPD to show significantly more degradation than that of other carriers during down-link events is present in most of the data base (see, for example, Figure 5). The reason for this increased degradation is unknown, but it is believed to be an anomaly that may be related to the loopback nature of the carrier or to some interference phenomenon. In the discussion that follows, these data will be ignored. Grouping of the remaining curves is consistent with the uncertainty bounds of Figure 4 for clear-sky isolations observed on the respective satellites.

Figure 16 compares the up- and down-link XPD statistics for Mill Village. For clarity, only carrier 7 and carrier 3 DXPD statistics are plotted. The carrier 7 curve is roughly the mean value of the down-link statistics for all carriers. Note the similarity in the shapes of all three curves, which indicates the similarity to be expected in the behavior of up- and down-link XPD along the same path.

For circular polarization, XPD can be scaled between two frequencies in the 4- to 30-GHz range as follows [18]:

$$XPD_2 = XPD_1 - 20 \log (f_2/f_1)$$

where XPD_1 and XPD_2 are the XPD values not exceeded for the same percentage of time at frequencies f_1 and f_2, and all other path parameters are identical. This relationship applies only to XPD effects arising from rain or ice crystal depolarization [19]. For the frequencies involved in this experiment, the equation above indicates that the up-link XPD statistics should be about 3.5 to 4.0 dB more severe than the down-link XPD statistics along the same path for propagation medium effects. Given measurement uncertainties and antenna effects, the results in Figure 16 are consistent with this equation.

For these data, then, the up- and down-link XPD statistics along the same path behave similarly with respect to propagation impairments; differences in their behavior are consistent with current methods used in the frequency scaling of XPD. These results are not surprising, but they do confirm, for the INTELSAT V operating environment, expected basic trends in the frequency scaling of XPD statistics.

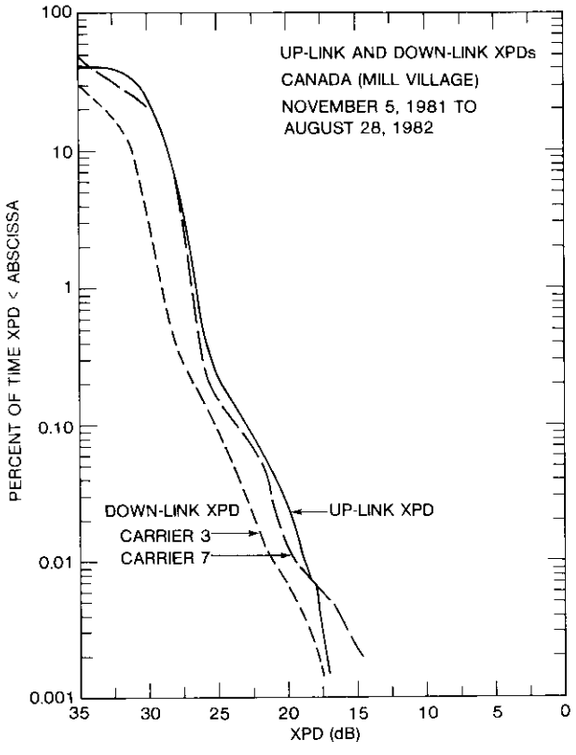

Figure 16. *Comparison of Up-Link and Down-Link XPD Statistics for Mill Village*

Summary and Conclusions

This study has presented the results of a cross-polarization measurement program conducted in the operational INTELSAT V frequency-reuse environment with traffic-bearing FDM/FM/FDMA carriers from seven earth stations in the AOR: Choconta-3 (Colombia), Mill Village-2 (Canada), Quito (Ecuador), Tulancingo-2 (Mexico), Quetzel-1 (Guatemala), Utibe-2 (Panama), and Camatagua-2 (Venezuela). A specially designed receiver located at the Mill Village earth station measured the XPD maintained in each station's up-link to the satellite and the XPD of each carrier on the down-link to Mill Village.

XPD statistics were presented for each station, along with selected examples of recorded data illustrating some of the observed depolarization phenomena.

The experiment produced several significant results: up-link XPD levels not exceeded for 0.01 percent of the time for the various stations ranged from 8.2 to 25.6 dB (measured over a 10-month period); 0.1-percent levels ranged from 10.9 to 27.9 dB over the same period. Also, significant XPD degradations resulted from both antenna effects and propagation effects. The relative importance of the two for a given station could be seen in the shape of the cumulative distribution of XPD. For most stations, propagation effects were more important. Some propagation events were observed in which XPD levels degraded from 30 dB to the mid-teens in about 3 to 5 minutes.

XPD statistics tended to be more severe at lower elevation angles and/or in climates with higher values of M and β. Combinations of these factors yielded intermediate results. Up- and down-link XPD statistics along the same path behaved similarly with respect to propagation impairments. Differences in their behavior are consistent with current methods used in the frequency scaling of XPD. These results confirm expected basic trends within the INTELSAT V operating environment.

Comparison of measured XPD statistics with those predicted by a propagation model yielded only fair agreement in the absence of precise weather information. Also, the model did not account for antenna effects. The model did, however, correctly identify the earth stations that were likely to be subjected to the most severe XPD environments.

Under normal circumstances, antenna tracking methods used in the INTELSAT V system maintained satisfactory XPD levels under clear-sky conditions. The effects of abnormal antenna tracking are more serious in the INTELSAT V frequency-reuse environment than in previous systems because to minimize co-channel interference, acceptable XPD levels must be maintained along with satisfactory copolarized signal levels. Accordingly, tracking malfunctions can become as important as severe depolarization events in the propagation medium, as was seen in one station's data.

No conclusions can be drawn from the results regarding antenna feeds of different manufacturers, although variability in polarization isolation across tracking beamwidths was more visible for some stations than for others.

Acknowledgments

The author thanks the many people who contributed to the success of this experiment: A. Atia, C. Mahle, V. Riginos, and A. Berman, whose collective work brought about the design of the receiver, and all of whom provided helpful technical support and advice; W. Kinsella and D. Lee, for the construction and testing of the equipment; and D. Williams, who provided

valuable hardware and software support throughout the program. Thanks are also due S. Tambe and J. Phiel of INTELSAT and H. Winiarski of Teleglobe Canada, for technical and administrative support; M. Skroch, D. Gesswein, and L. Ortega for the special-purpose software used in the data processing; and P. Fritz, T. Sullivan, and O. Piontek for processing the data.

The author also thanks G. Hyde, D. Weinreich, R. Gruner, J. Effland, D. DiFonzo, and D. Rogers for many beneficial technical discussions; and D. Fang, for his advice and support throughout the measurement program.

An experiment is only as good as the operators at the site. The superb efforts of the Mill Village Earth Station staff, especially C. Gaetan, R. Crouse, and W. Brown, are acknowledged with special thanks.

References

[1] R. R. Taur, "Rain Depolarization: Theory and Experiment," *COMSAT Technical Review*, Vol. 4, No. 1, Spring 1974, pp. 187–190.

[2] R. R. Taur, "Rain Depolarization Measurements on a Satellite-Earth Propagation Path at 4 GHz," *IEEE Transactions on Antennas and Propagation*, Vol. AP-23, 1975, pp. 854–858.

[3] D. J. Fang and J. Jih, "A Model for Microwave Propagation Along an Earth-Satellite Path," *COMSAT Technical Review*, Vol. 6, No. 2, Fall 1976, pp. 379–411.

[4] R. R. Taur and J. Mass, Private Communication.

[5] D. J. Kennedy, "Rain Depolarization Measurements at 4 GHz," *COMSAT Technical Review*, Vol. 9, No. 2B, Fall 1979, pp. 629–668.

[6] D. J. Fang and C. H. Chen, "Propagation of Centimeter/Millimeter Waves Along a Slant Path Through Precipitation," *Radio Science*, Vol. 17, No. 5, 1982, pp. 989–1005.

[7] R. W. Kreutel, "The Orthogonalization of Polarized Fields in Dual-Polarized Radio Transmission Systems," *COMSAT Technical Review*, Vol. 3, No. 2, Fall 1973, pp. 375–386.

[8] D. DiFonzo, W. Trachtman, and A. Williams, "Adaptive Polarization Control for Satellite Frequency Reuse Systems," *COMSAT Technical Review*, Vol. 6, No. 2, Fall 1976, pp. 253–283.

[9] A. E. Williams, "A Dual-Polarized 4/6-GHz Adaptive Polarization Control Network," *COMSAT Technical Review*, Vol. 7, No. 1, Spring 1977, pp. 247–262.

[10] D. F. DiFonzo and W. S. Trachtman, "Antenna Depolarization Measurements Using Satellite Signals," *COMSAT Technical Review*, Vol. 8, No. 1, Spring 1978, pp. 155–185.

[11] P. Kumar, "Propagation Data Base Update," Final Report, INTELSAT Contract INTEL-222, Item 18 (CE), December 1982.

[12] J. F. Phiel, Private Communication.

[13] S. Tambe, Private Communication.

[14] P. L. Rice and N. R. Holmberg, "Cumulative Time Statistics of Surface-Point Rainfall Rates," *IEEE Transactions on Communications*, COM-21, No. 10, October 1973, pp. 1131–1136.

[15] S. J. Struharik, "Rain and Ice Depolarization Measurements at 4 GHz in Sitka, Alaska," *COMSAT Technical Review*, Vol. 13, No. 2, Fall 1983, pp. 403–435.

[16] C. Gaetan, Private Communication.

[17] D. V. Rogers, Private Communication.

[18] CCIR Report 564-1 (MOD F), "Propagation Data Required for Space Telecommunication Systems," *CCIR XVth Plenary Assembly*, Vol. V, International Telecommunication Union, Geneva, Switzerland, 1982.

[19] CCIR Report 722 (MOD F), "Cross-Polarization due to the Atmosphere," *CCIR XVth Plenary Assembly*, Vol. V, International Telecommunication Union, Geneva, Switzerland, 1982.

Steven J. Struharik received B.E.E. and M.S. degrees in electrical engineering from the Ohio State University in 1971 and 1972, respectively. He joined COMSAT Laboratories in 1977, and for 6 years was a Member of the Technical Staff of the Propagation Studies Department, where his principal activities involved the design and implementation of propagation experiments. He is currently a Member of the Technical Staff of the Systems Simulation Department. Mr. Struharik is a member of Tau Beta Pi, Sigma Xi, and Eta Kappa Nu. He is also a member of the IEEE.

Index: Frequency reuse, interference, propagation

Drop-size distribution: cross-polarization discrimination and attenuation for propagation through rain*

J. A. BENNETT

(Manuscript received January 14, 1983)

Abstract

The formula for cross-polarization discrimination (XPD) for propagation through uniform media, though simple, does not provide adequate insight for interpretation of experimental results. This paper presents a theoretical study that helps overcome this problem for the 8- to 33-GHz frequency range. The study is carried out for both Laws-Parsons drop-size distributions (negative exponentials in drop diameter) and a recently proposed, peaked, log-normal distribution of rain from convective systems. A new expression is offered for polarizations that are neither circular nor 45° linear. An interesting by-product of the investigation indicates that for a given drop-size distribution, the curves of XPD *vs* attenuation, A, for the two orthogonal, linear polarizations cross over at A near 8.6 dB.

Introduction

In designing dual-polarization, frequency-reuse, microwave communications systems, it is necessary to know the statistics on depolarization caused by rain. If depolarization is related to attenuation, the required statistics can be deduced from attenuation statistics. Also, if the relationship between

* This paper is based on work performed at COMSAT Laboratories under the sponsorship of the International Telecommunications Satellite Organization (INTELSAT). Views expressed are not necessarily those of INTELSAT.

attenuation and depolarization as a function of elevation angle, polarization, and frequency is known, the time and effort involved in gathering statistics can be greatly reduced.

This paper does not directly examine measured statistics; rather, it calculates attenuation and depolarization in a well-defined, idealized situation. To appreciate the practicality of the calculated results, a comparison was made with the results of one particularly detailed experiment, and good agreement between measured and predicted XPD *vs* attenuation statistics was obtained.

The effect of the distribution of raindrop diameters on the relationship between attenuation and depolarization is of particular interest here. Calculations were performed for the well-known Laws-Parsons distribution [1] as well as for log-normal distributions recently proposed for convective rain (*i.e.*, heavy showers and thunderstorms) [2], [3]. Comparison with experimental results tends to support the validity of the log-normal rather than the Laws-Parsons distribution for rain that is responsible for significant depolarization. Propagation constants used in this study are described in References 2 through 4, all assuming a Pruppacher-Pitter type of raindrop [5] at 10°C.

A formula relating attenuation and cross-polarization discrimination

For propagation through a uniform medium, cross-polarization discrimination, that is, the ratio (in decibels) of the wanted signal of the transmitted polarization to the unwanted signal of the orthogonal polarization, can be related to copolarization attenuation, A (dB), using empirically derived formulae.

Equation (1) below was built up one step at a time [4] by considering circularly polarized waves and horizontal paths with uniformly aligned, vertically falling drops for which the first two terms only of equation (1) are nonzero. Other polarizations were then introduced for horizontal paths and so on, as follows

$$\begin{aligned} \text{XPD} = {} & X_0 - 20\log_{10} A \\ & - 20\log_{10}|\sin 2\gamma| + (-a\cos 2\gamma + b|\cos 2\gamma| \\ & + c\cos^2 2\gamma)(A - A_x) \\ & - 20\log_{10}(\cos^2\theta) + 20\log_{10}(1 + d\sin^2\theta) \\ & - 20\log_{10}\left(\frac{3p-1}{2}\right) \end{aligned} \tag{1}$$

where

$$a = \frac{a_0\cos^2\theta}{1 + e\sin^2\theta}\left(\frac{3p-1}{2}\right)$$

$$b = b_0\cos^4\theta\left(\frac{3p-1}{2}\right)^2$$

$$c = c_0\cos^4\theta\left(\frac{3p-1}{2}\right)^2$$

and p is the degree of randomness in the drop orientations. The angle θ is the complement of the angle between the drop axis of symmetry and the direction of propagation. For vertically falling drops, it is the elevation angle. The polarization is characterized by γ, one of the Poincaré variables, given by

$$\cos 2\gamma = \cos 2\alpha\cos 2\beta \tag{2}$$

where

$$\alpha = \arctan(AR)$$
$$\beta = \beta' - \psi$$

where AR is the axial ratio, β' the tilt angle of the polarization, and ψ the canting angle of the drops. The approach used consisted of modeling an appropriate algebraic structure and then establishing the coefficients by a least-squares regression. The representation was found to be highly adequate. Only in extreme cases, errors of a few tenths of a decibel may occur. For drops with random orientations, the degree of randomness is measured by p ($1 \leq p \leq 1/3$), and both θ and ψ refer to the mean axis of the distribution. Since the intent is a parametric analysis, any change in attenuation is assumed to arise from a change in path length, while all other variables, including rainfall rate, remain constant.

The coefficients X_0, a_0, b_0, c_0, and e all depend on drop-size distribution (DSD), rainfall rate, and frequency. The variable A_x is always around 8.68; it approaches $20\log_{10}\epsilon$ as the differential attenuation and phase approach zero. For practical purposes, the coefficients may be taken as independent of the angle γ, θ, and p. The only significant exception is that in some cases, d shows significant residual dependence on θ. These comments will become clearer as the result expressed in equation (1) is established.

A note on the path length effect is necessary here. On a real path through the atmosphere, the copolarization attenuation, A, may vary either because of a variation in rainfall rate, R, along a path of fixed length or because of a change in path length while the rainfall rate remains constant. The associated change in XPD in each case is not the same. For circular polarization in the case of fixed R, XPD and A vary to a high degree of approximation, as

$$(\text{XPD})_{CP} = X_0 - 20 \log_{10} A \quad . \tag{3}$$

The XPD is not as closely linear in $\log_{10} A$ if L is held constant. Moreover, the slope of the linear approximation depends on frequency and DSD. Because a universal representation is desired, R will always be held fixed, and A will be allowed to vary as a result of changes in L.

Simplified formulation for terrestrial propagation

For a range of 8 to 14 GHz, the approximation given in equation (3) is useful to about 10 dB of attenuation; for 19 to 33 GHz, to about 30 dB. Values of X_0 for the three DSDs considered are plotted in Figures 1 through 3. From about 6 to 11 GHz, X_0 has a 40-dB/decade slope, and from 11 to at least 33 GHz, a 20-dB/decade slope. The DSD gives very little spread in X_0 with rainfall rate R at 11 GHz. Also, there is very little change from one distribution to another. However, at higher frequencies, the Laws-Parsons distribution gives a much larger spread in X_0 for different rain rates than do the other distributions. The results apply equally to circular and linear polarization, with $\beta = 45°$ or $135°$, all along a horizontal path.

For linear polarizations, equation (3) is no longer adequate. The issue in this case is the dependence of XPD on 2γ. For approximately the same attenuation ranges discussed in equation (3), a simple relationship between XPD and A is still possible if a new parameter X is introduced such that

$$X = \text{XPD} + 20 \log_{10} A \tag{4a}$$

where X is related to X_0 by

$$X = X_0 - 20 \log_{10} |\sin 2\gamma| + (-a \cos 2\gamma + b |\cos 2\gamma| + c \cos^2 2\gamma)(A - A_X) \quad . \tag{4b}$$

Equation (4b) leads to a pair of lines for orthogonal polarizations represented by angles 2γ and $2\gamma + \pi$. These lines intersect at a value of attenuation $A = A_X$, where A_X was always near 8.6 dB. Illustrative examples of these lines are shown in Figures 4 through 6. Segments of the lines that apply at each rainfall rate are shown; notice the greater spread that results for the Laws-Parsons distributions.

Two parts of the approximation are expressed by equation (4b). The first, $X = X_0$, refers to the approximately straight lines of a unity slope. Actual

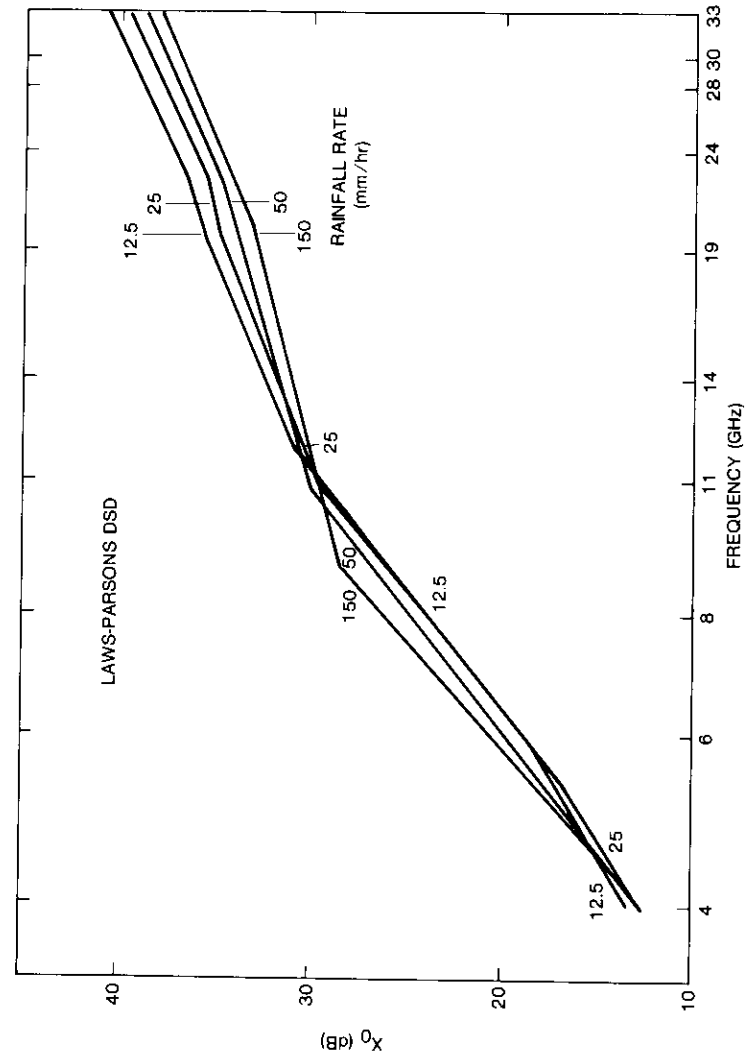

Figure 1. *Parameter X_0 in the XPD Formula for Various Rainfall Rates, Laws-Parsons DSD*

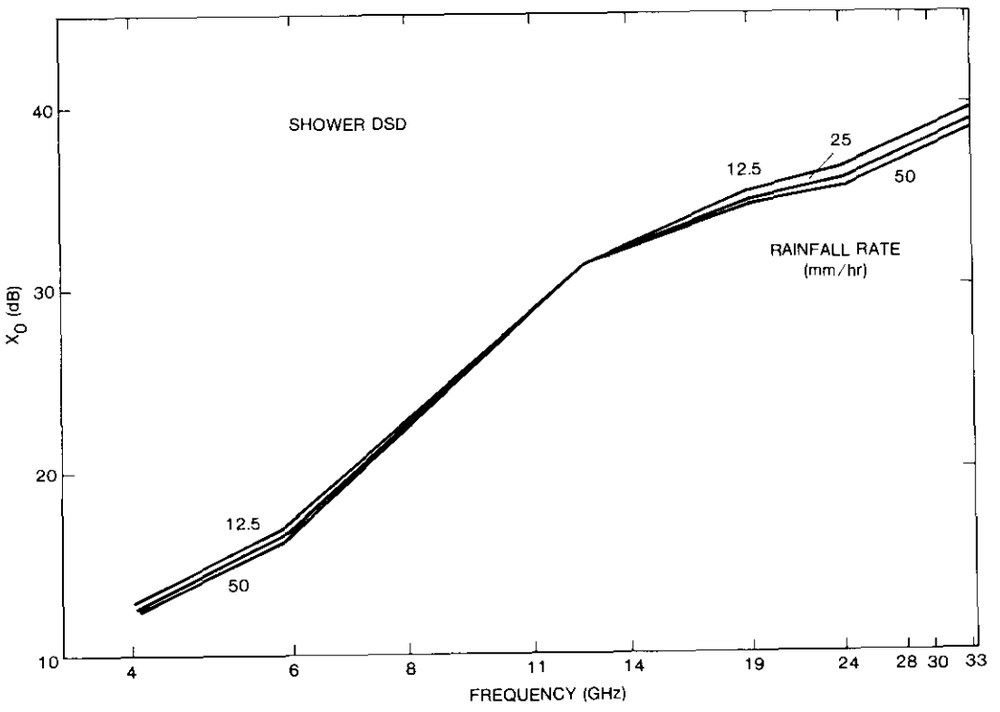

Figure 2. *Parameter X_0 in the XPD Formula for Various Rainfall Rates, Shower DSD*

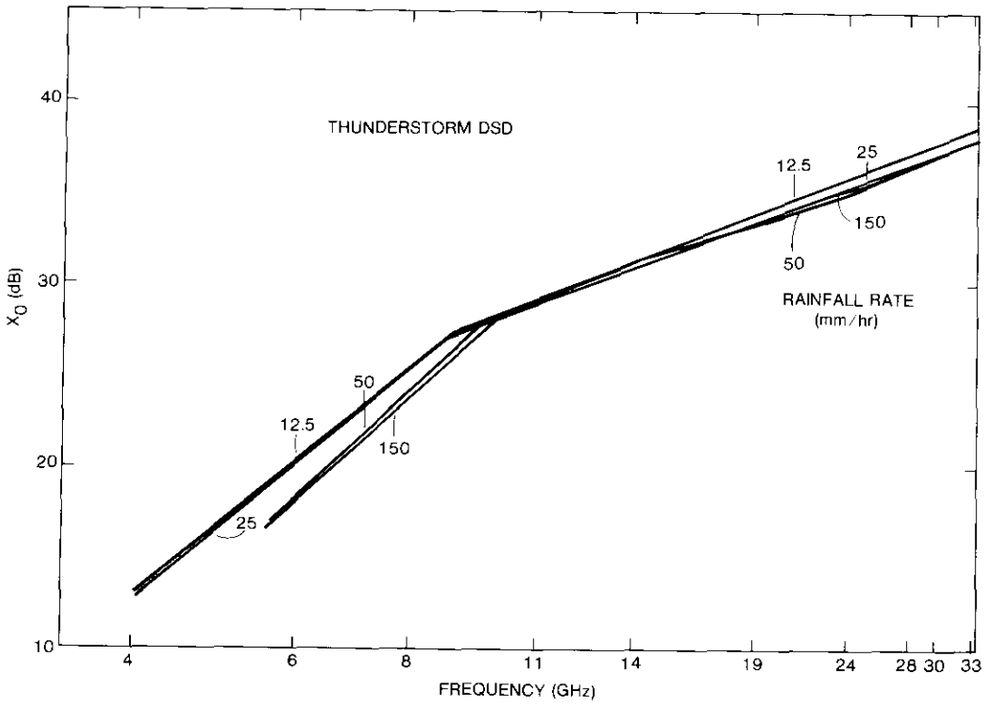

Figure 3. *Parameter X_0 in the XPD Formula for Various Rainfall Rates, Thunderstorm DSD*

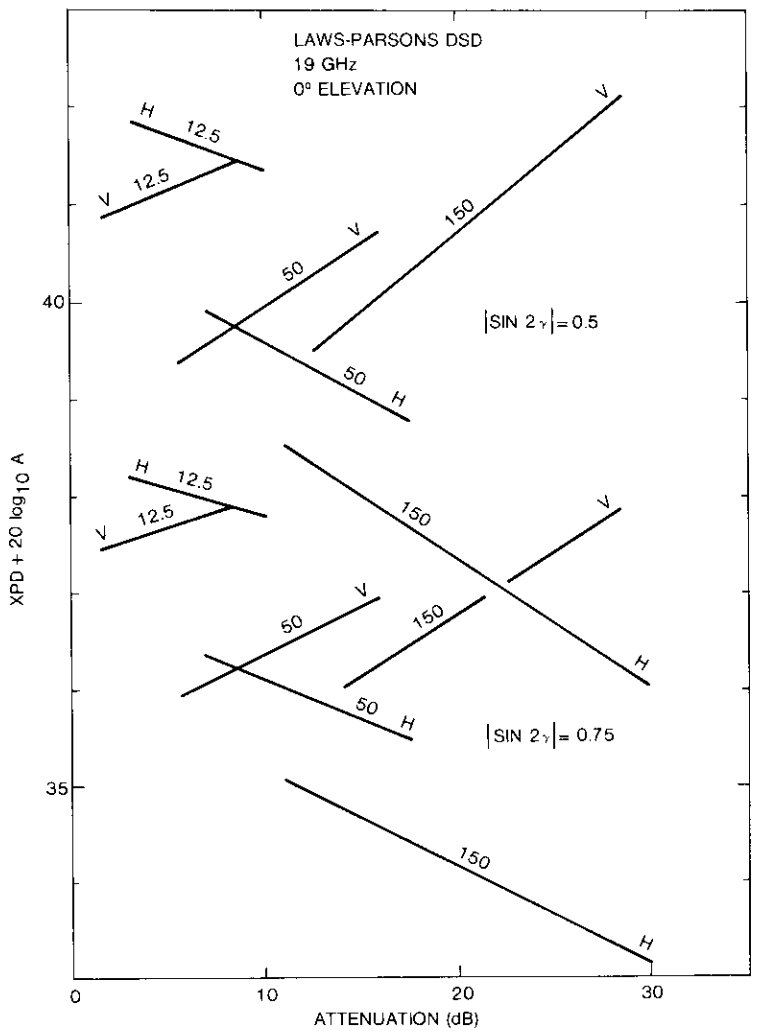

Figure 4. *Plot of XPD + 20 $\log_{10}$ A vs Attenuation A for Linear Polarizations, Laws-Parsons DSD*

data suggest that the departure from unity was at most 6.4×10^{-2} at 8 GHz. At 33 GHz, the largest departure was 1.2×10^{-4}. The second part of the approximation involves two terms describing either the slope or the displacement of the lines. Residual systematic variations in a, b, and c, as determined from data at different angles, indicate that the two terms are

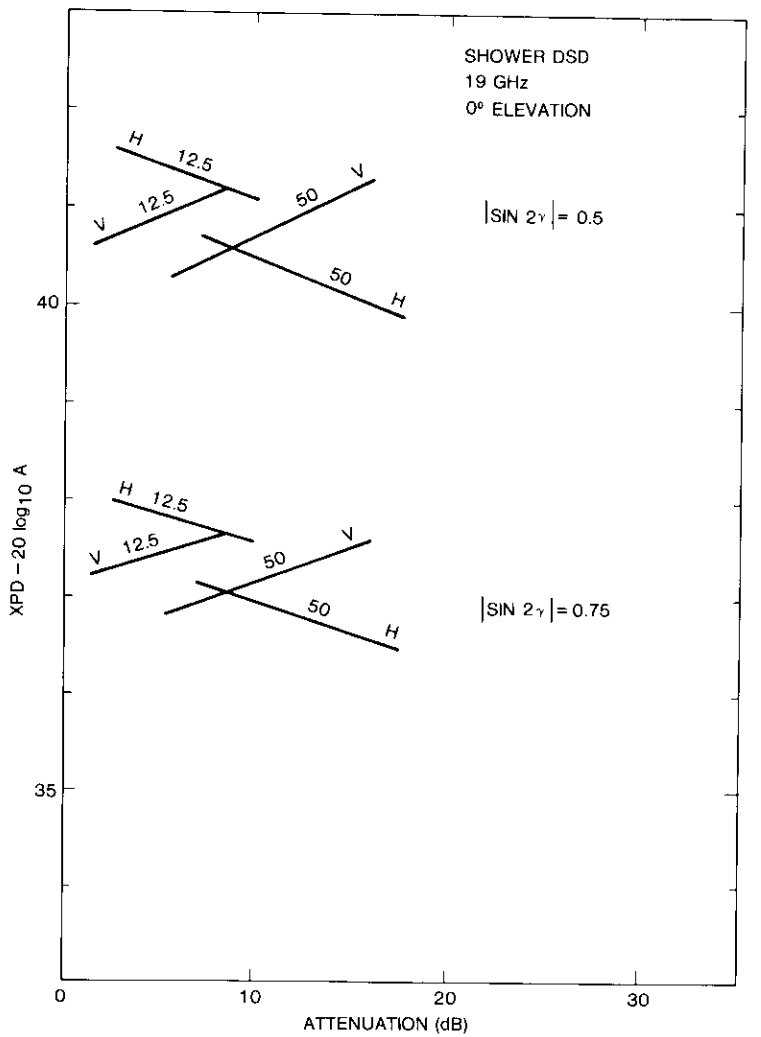

Figure 5. *Plot of XPD + 20 $\log_{10}$ A* vs *Attenuation A for Linear Polarizations, Shower DSD*

highly accurate. In most cases, errors in XPD of only about 0.02 dB would result.

Figures 7 through 9 show values of b and c for the three DSDs considered. These values were determined from $\sin 2\gamma = 0.75$ and $\sin 2\gamma = 0.5$, but can be taken to apply at all values of $\sin 2\gamma$. Note that at low frequencies,

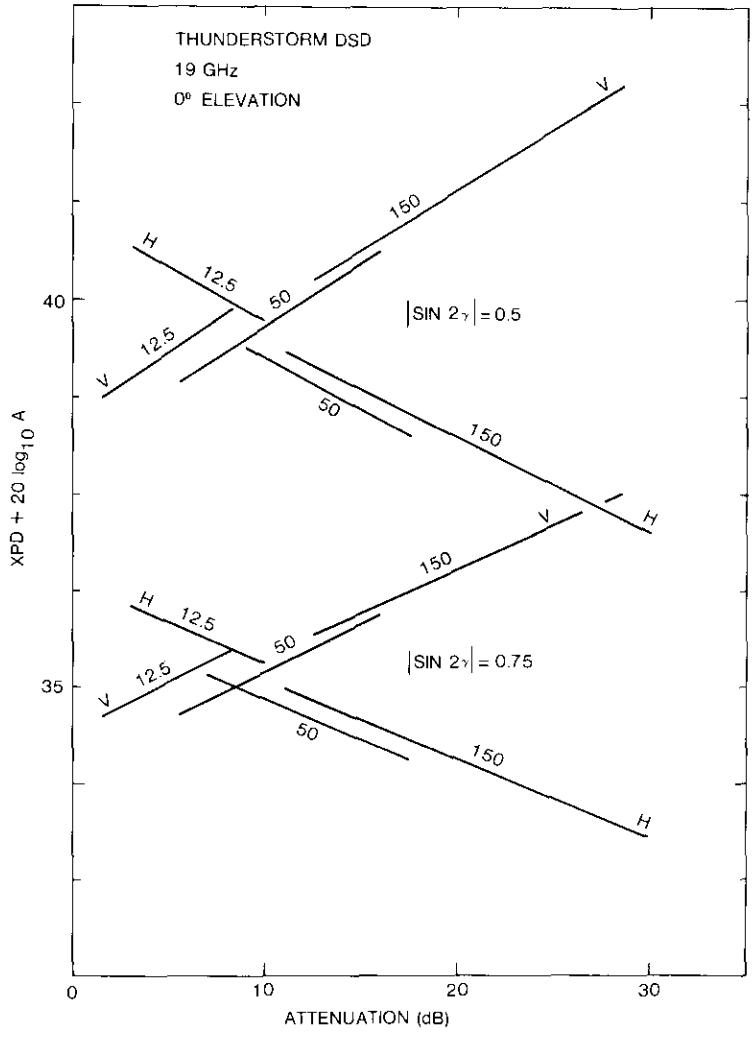

Figure 6. *Plot of XPD + 20 $\log_{10} A$ vs Attenuation A for Linear Polarizations, Thunderstorm DSD*

$b >> |c|$, so that the $|\cos 2\gamma|$ dependence dominates. As the frequency increases, b and c become oscillatory functions of the logarithm of frequency.

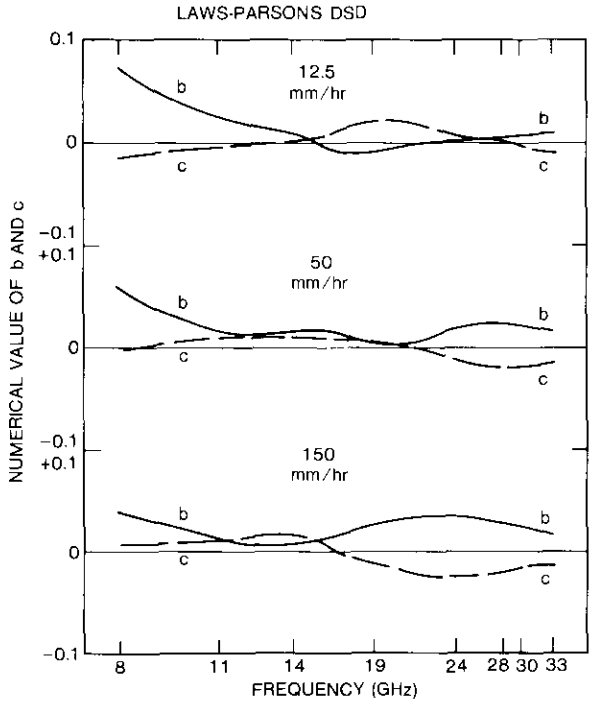

Figure 7. *Plots of Coefficients b and c, Laws-Parsons DSD*

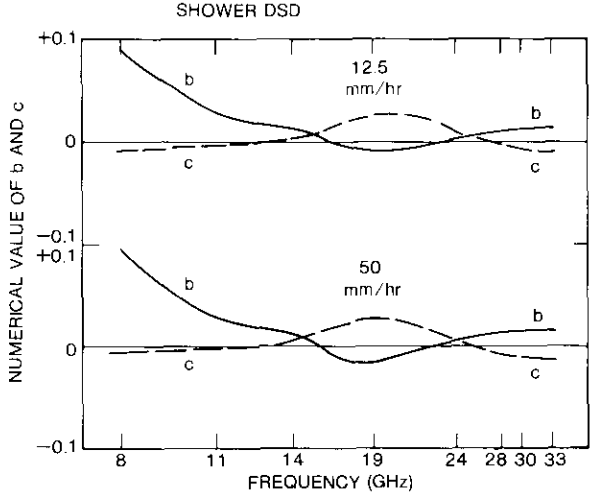

Figure 8. *Plots of Coefficients b and c, Shower DSD*

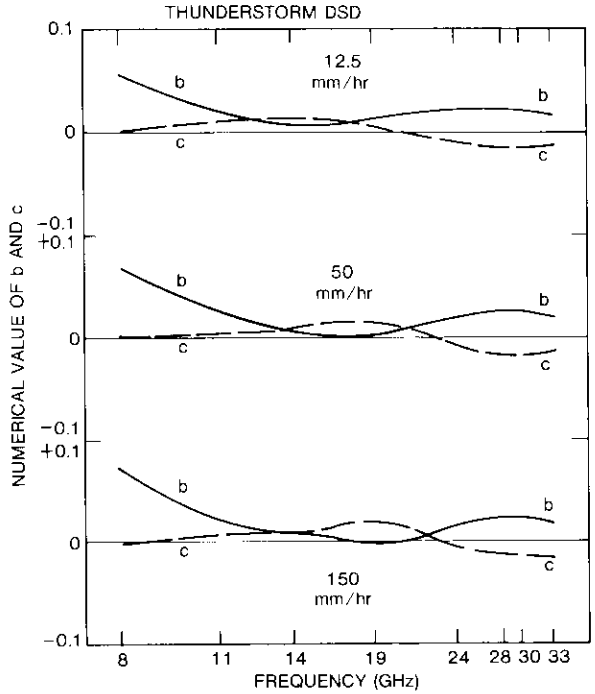

Figure 9. *Plots of Coefficients b and c, Thunderstorm DSD*

Propagation along a slant path

For a path elevated at an angle θ (assuming that the drops are electric and magnetic dipole scatterers [6]), the results for a horizontal path may be extended to slant paths. In the case of circular polarization, it can be shown that the relationship between XPD and attenuation A is approximately as

$$X_{CP} = X_0 - 20 \log_{10} \cos^2 \theta + 20 \log_{10} (1 + d \sin^2 \theta) \qquad (5)$$

where X_0 refers to the case in which $\theta = 0$. Clearly, the term involving the coefficient d arises from the variation of the average attenuation.

For other polarizations, equations (4a) and (4b) are extended by letting

$$a = \frac{a_0 \cos^2 \theta}{1 + e \sin^2 \theta} \qquad (6)$$

where a_0 is the value applying when $\theta = 0$. The correction represented by e is relatively unimportant. Also, b and c are modified by letting

$$b = b_0 \cos^4 \theta \qquad (7)$$

$$c = c_0 \cos^4 \theta \qquad (8)$$

where, again, b_0 and c_0 are the values at $\theta = 0$, already provided.

The numerical values for e at $\theta = 45°$ and for d at either $\theta = 45°$ or 30° are shown in Figures 10 through 12. This variation in d probably arises in part from small departures of about 2 percent, a result of the dipole law exhibited by propagation constants calculated for Pruppacher-Pitter drops. The relative importance of the correction can be judged from the fact that

$$20 \log_{10} (1 + d \sin^2 \theta) \simeq 8.686\ d \sin^2 \theta \qquad (9)$$

which is $2.17d$ when $\theta = 30°$, and $4.34d$ when $\theta = 45°$.

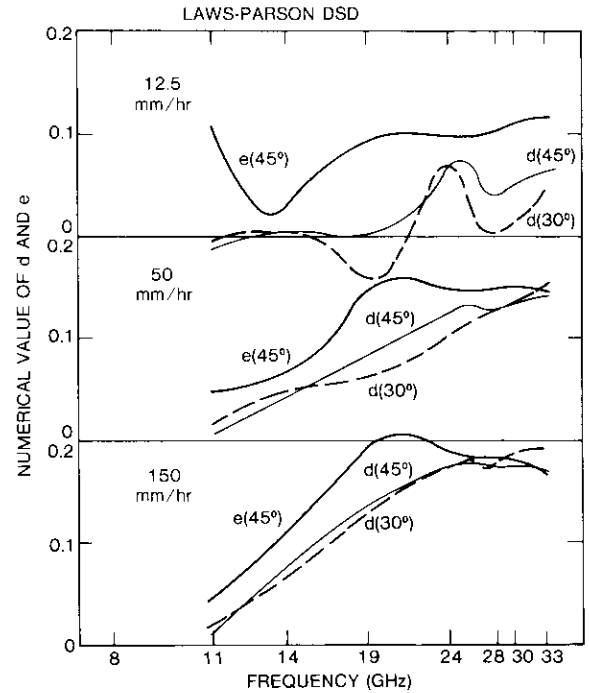

Figure 10. *Plots of Coefficient d (θ = 30°, 45°) and Coefficient e (θ = 45°), Laws-Parsons DSD*

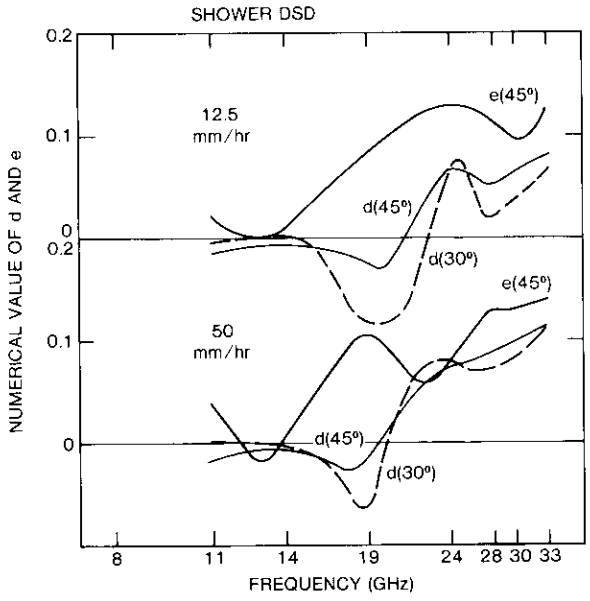

Figure 11. *Plots of Coefficient d (θ = 30°, 45°) and Coefficient e (θ = 45°), Shower DSD*

Distributed drop orientations

The propagation of microwaves through randomly oriented drops has been examined theoretically a number of times. (For a review, see Reference 7). The formulation in terms of electric and magnetic dipole scatterers [6] is convenient because it makes possible the prediction of XPD behavior without extensive numerical calculation.

For axisymmetric distributions of drop orientations, the circular polarization equation can be revised to

$$X_{CP} = X_0 - 20\log_{10}\cos^2\theta - 20\log_{10}\left(\frac{3p-1}{2}\right) + 20\log_{10}(1 + d\sin^2\theta) \quad . \tag{10}$$

And for other values of γ

$$X = X_{CP} + (-a\cos^2\gamma + b|\cos^2\gamma| + \cos^2 2\gamma)(A - A_X) \tag{11}$$

where a, b, and c assume the form shown in equation (1).

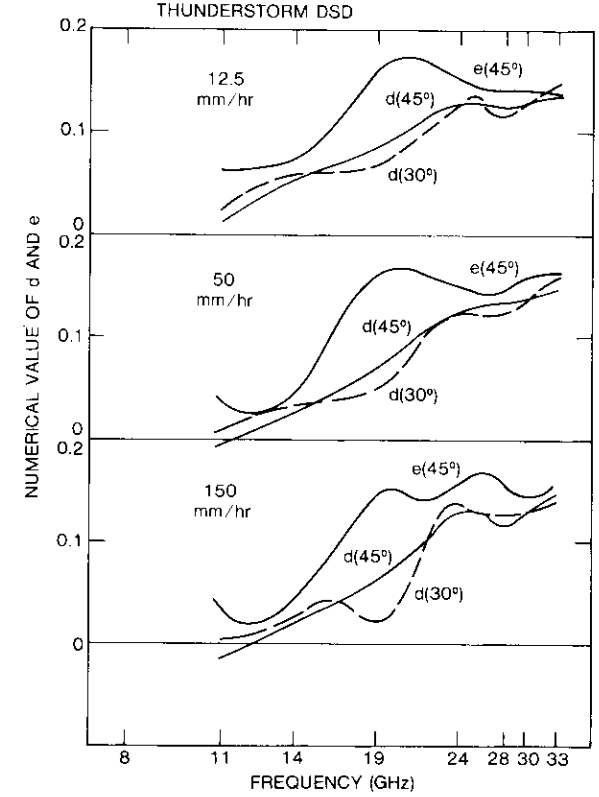

Figure 12. *Plots of Coefficient d (θ = 30°, 45°) and Coefficient e (θ = 45°), Thunderstorm DSD*

Nonvertical drops

Drop orientations of this kind require selection of an appropriate transformation of coordinates. Suppose the axis alignment of the drops' cylindrical symmetry is defined by a zenith angle, η, and an azimuth angle, ζ. For stochastically aligned drops, η and ζ refer to the axis of the distribution.

If θ_{el} is the elevation angle of the propagation path, it can be shown that

$$\sin\theta = \sin\theta_{el} + \cos\theta_{el}\sin\eta\cos\zeta \tag{12}$$

Notice that $\theta = \theta_{el}$ if $\eta = 0$ (vertical drops) or $\zeta = 90°$ (drops tilted in the plane at right angles to the direction of propagation).

Along the direction of propagation, the drops appear to be rotated at an angle ψ, where

$$\cos^2 \psi = \frac{\cos \theta_{el} - \sin \theta_{el} \sin \eta \cos \zeta}{(\cos \theta_{el} - \sin \theta_{el} \sin \eta \cos \zeta)^2 - \sin^2 \eta \sin^2 \zeta} \quad . \tag{13}$$

The angle ψ is the canting angle. Notice that $\psi = 0$ if $\eta = 0$ (vertical drops) or $\zeta = 0$ (drops tilted in the vertical plane containing the direction of propagation). Also, for fixed η and ζ, the angle ζ will usually be a function of the elevation angle θ_{el}.

All previous results apply in the present case if θ given by equation (12) is used along with

$$\beta = \beta' - \psi \tag{14}$$

with ψ given by equation (13).

The International Radio Consultative Committee formula

Equation (1) may be compared with models provided by the International Radio Consultative Committee (CCIR) [7]–[9], and others [10]–[12], although these refer to a slightly different situation.

CCIR documents [8], [9] propose an approximate relationship between XPD and A, as follows:

$$\begin{aligned} \text{XPD} = {} & 0.0053\,\sigma^2 + 30 \log_{10} f - 20 \log_{10} A \\ & - 40 \log_{10} (\cos \theta_{el}) - 20 \log_{10} (\sin 2|\psi - \tau|) \end{aligned} \tag{15}$$

where σ = the standard deviation of the canting angle distribution,
θ_{el} = the elevation angle,
ψ = the mean canting angle, and
τ = the polarization tilt angle.

For circular polarization, $|\psi - \tau| = 0$. Each of the terms in equation (15) will be considered briefly.

Obviously, the term $-20 \log_{10} |(3p - 1)/2|$ in equation (1) corresponds to the $0.0053\,\sigma^2$ term in equation (15). For a narrow distribution of drop orientations,

$$-20 \log_{10} \frac{3p - 1}{2} \simeq 0.0040\,\sigma_\theta^2 \tag{16}$$

where σ (in degrees) is the standard deviation of the conical distribution of drop axes. Thus, the terms are very similar.

Equations (1) and (15) contain the term $-20 \log_{10} A$. It is necessary to consider both X_0 and $20 \log_{10} A$ together for a detailed comparison. Olsen and Nowland [12] proposed a revision as

$$-V \log_{10} A \tag{17}$$

where
$$V = 20, \quad 8 \le f \le 15 \text{ GHz} \tag{18a}$$
$$V = 23, \quad 15 < f \le 35 \text{ GHz} \quad . \tag{18b}$$

Because X_0 depends on rainfall rate, equation (1) will lead to a term similiar to equation (17) for the regression line of XPD *vs* attenuation A. Furthermore, for the Laws-Parsons distribution, V is approximately

$$V = 20, \quad 10 \le f < 14 \tag{19a}$$
$$V = 23, \quad 14 \le f \le 33 \tag{19b}$$

which agrees well with equation (17). On the other hand, for the thunderstorm and shower distributions, V is approximately

$$V = 20, \quad 10 \le f < 19 \text{ GHz} \tag{20a}$$
$$V = 21, \quad 19 \le f \le 33 \text{ GHz} \quad . \tag{20b}$$

The different V values make it possible to distinguish experimentally between the DSDs.

The terms $-40 \log_{10} (\cos \theta_{el})$ in equation (15) and $-20 \log_{10} (\cos^2 \theta)$ in equation (1) are identical if the difference between θ and θ_{el} can be overlooked, since this difference is unlikely to be greater than 1°–3°.

For linear and circular polarizations, the terms $-20 \log_{10} \sin 2|\psi - \tau|$ in equation (15) and $-20 \log_{10} |\sin 2\gamma|$ in equation (1) are identical. However, equation (1) also applies to general elliptical polarizations.

The remaining terms in equation (1) have no corresponding terms in the CCIR formula shown in equation (15), although the effect is shown clearly in results for individual events published by Dilworth [13]. After correlating the term in equation (1) with the $(A - A_X)$ factor, Chu [14] proposed the term

$$\pm\, 0.15\, A \cos^2 \theta_{el} \cos 2\tau \quad .$$

This term overlooks the significance of A_X, taking a fixed value of a_0 $(3p - 1)/2$ and neglecting the small correction represented by the coefficient e. The terms for coefficients b and c have not previously been recognized. Finally, the term for d represents a correction of the XPD elevation dependence.

Equation (15) overestimates XPD for $\psi - \tau$ close to 0° or to 90°; equation (1) neglects effects that in this case are important on real paths.

Comparison with experimental results

The experiment carried out by Bell Laboratories at Crawford Hill with COMSTAR transmissions [15] is particularly useful for comparison because of its measurements of switched, linearly orthogonal polarizations at 19 GHz at an elevation angle of 38.6°. The apparent canting angle of the drops was measured. The tilt angle of the arriving linear polarization was well away from local vertical, so equations (1) and (15) would be expected to apply. Measurements were also made of a continuous, linearly polarized wave at 28 GHz.

Figures 13 and 14 show the relationship between XPD and attenuation A

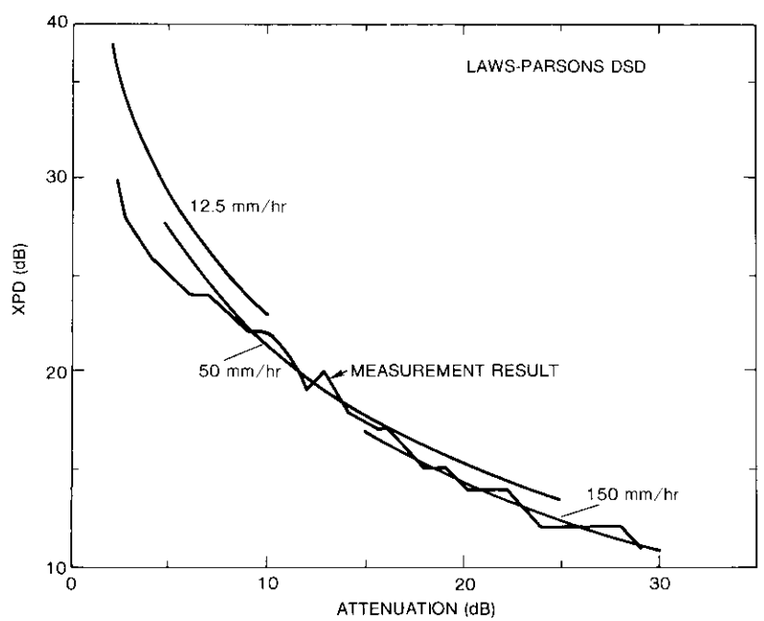

Figure 13. *Comparison Between Experimental and Calculated XPD and Attenuation at 19-GHz, Linear Polarization, Laws-Parsons DSD*

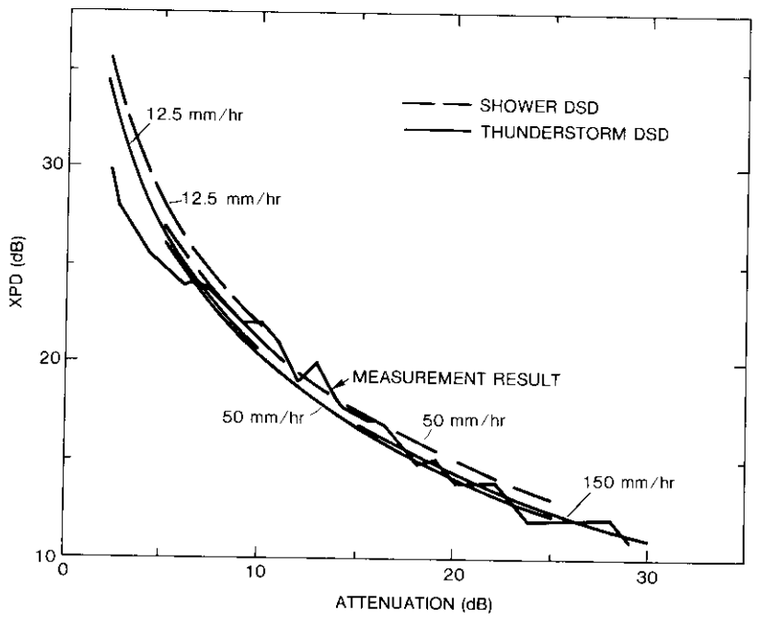

Figure 14. *Comparison Between Experimental and Calculated XPD* vs *Attenuation at 19 GHz, Linear Polarization, Shower and Thunderstorm DSD*

measured in this experiment for linear polarization at 19 GHz [15], [16]. Also shown are segments calculated by using the equation proposed in this paper that covers the approximate range of attenuations expected at that rainfall rate. For the Laws-Parsons distribution, reasonable agreement at high attenuation is obtained by choosing $p = 0.8$. For the thunderstorm DSD, $p = 0.85$ gives reasonable agreement at high attenuations. Both of these values are reasonable. However, the Laws-Parsons distribution gives poorer agreement at low rainfall rates. If p is increased to 0.9 to give agreement at 12.5 mm/hr, agreement is lost at high rates. This disagreement occurs because, for the Laws-Parsons distribution, X_0 is strongly rainfall rate dependent, while for the shower and thunderstorm distributions, this is not so.

Based on Figures 13 and 14, it can be concluded that for linear polarization, a regression line with a term of $-21 \log_{10} A$ gives reasonable agreement from 10 to 30 dB of attenuation.

Figures 15 and 16 show measured XPD related to attenuation A for a pair

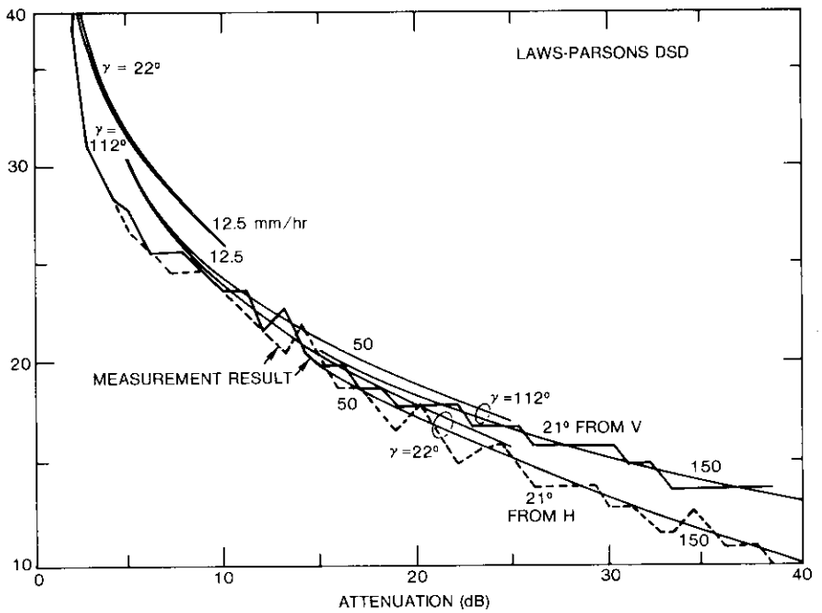

Figure 15. *Comparison Between Experimental and Calculated XPD and Attenuation at 19 GHz, Linear Polarization, Laws-Parsons DSD*

of orthogonal linear polarizations [16], [17]. When allowing for the measured mean canting angle of $-1°$, shower and thunderstorm distributions give good agreement; however, the agreement is not as good for the Laws-Parsons distribution. The experimental results do not exhibit the crossover below 8.6 dB, as predicted by equation (1). Failure of the curves to intersect may be due to a number of causes, one of which may be the effect of ice on the statistics in this range.

Finally, Figures 17 and 18 show measured XPD at 28 GHz related to attenuation A for one of the linear polarizations [15], [16] with an angle of 21° to vertical. Again, the shower and thunderstorm distributions appear to give better agreement.

Conclusions

It has been suggested here that shower and thunderstorm DSDs are more appropriate than the Laws-Parsons distribution for calculating XPD at higher attenuations. In this study, new features of the relationship between XPD and attenuation have been revealed, features that suggest new ways of presenting

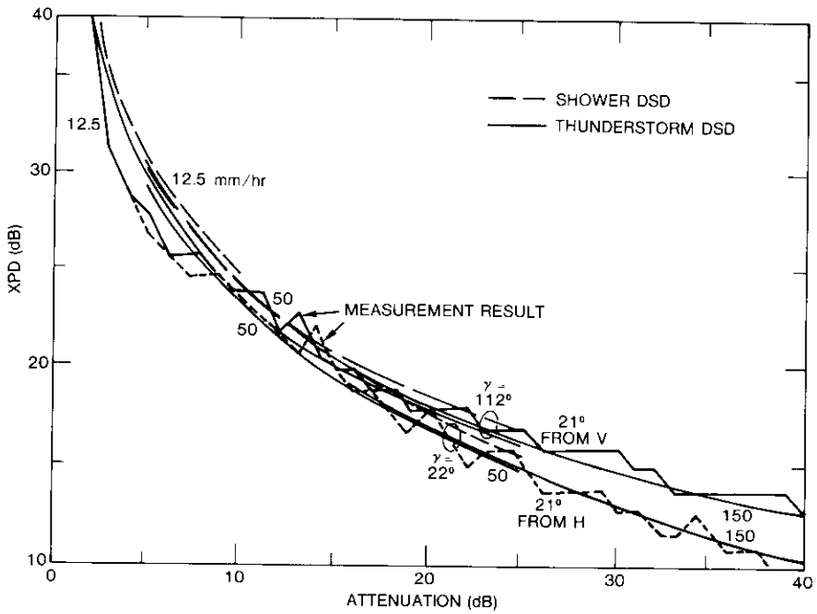

Figure 16. *Comparison Between Experimental and Calculated XPD and Attenuation at 19 GHz, Linear Polarization, Shower and Thunderstorm DSD*

and analyzing experimental results. The range of scatter in these experimental results is greater than can be accounted for merely by using mean DSDs; this scatter may be caused by the departure of instantaneous DSDs from long-term average distributions.

References

[1] J. D. Laws and D. A. Parsons, "The Relationship of Raindrop-Size to Intensity," *Transactions of the American Geophysical Union*, Vol. 24, 1943, pp. 452–460.

[2] J. A. Bennett, P. A. Barclay, and R. C. Boston, "Calculations of the Influence of Drop Size Distributions on the Propagation of Microwave Signals Through Rain," International U.R.S.I. Symposium 1980 on Electromagnetic Waves, Munich, Federal Republic of Germany, August 1980, *Proc.*, pp. 123C/1–123C/4.

[3] D. J. Fang and H. C. Chen, "Propagation of Centimeter/Millimeter Waves Along a Slant Path Through Precipitation," *Radio Science*, Vol. 17, 1982, pp. 989–1005.

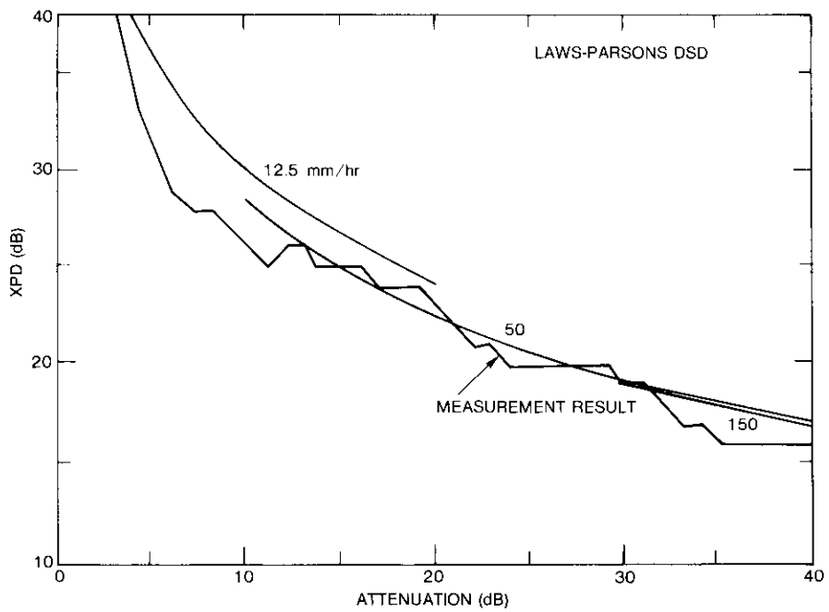

Figure 17. *Comparison Between Experimental and Calculated XPD and Attenuation at 28.6 GHz, Linear Polarization, Laws-Parsons DSD*

[4] J. A. Bennett, "The Relation Between XPD and Attenuation, and Its Dependence Upon Drop Size Distribution," COMSAT Technical Memorandum, CL-61-82, 1982.

[5] H. R. Pruppacher and R. L. Pitter, "A Semi-Empirical Determination of the Shape of Cloud and Raindrops," *Journal of Atmospheric Science,* Vol. 28, No. 1, 1971, pp. 86–94.

[6] J. A. Bennett, "Propagation Through an Assembly of Anisotropic Electric and Magnetic Dipole Scatterers," Submitted for publication in *Radio Science.*

[7] R. L. Olsen, "Cross Polarization During Precipitation on Terrestrial Links: A Review," *Radio Science,* Vol. 16, September-October 1981, pp. 761–779.

[8] International Radio Consultative Committee (CCIR), Report 564-1, Vol. V, Sec. 12.4 (1974–1978), International Telecommunications Union, Geneva, Switzerland, 1978.

[9] International Radio Consultative Committee (CCIR), Draft Modifications to Report 722, "Cross Polarization Due to the Atmosphere," Doc. 5/206: Conclusions of the Interim Meeting of Study Group 5, Geneva, Switzerland, August 29, 1980, pp. 179–189.

[10] T. S. Chu, "Microwave Depolarization of an Earth-Space Path," *Bell System Technical Journal,* Vol. 59, July-August 1980, pp. 987–1007.

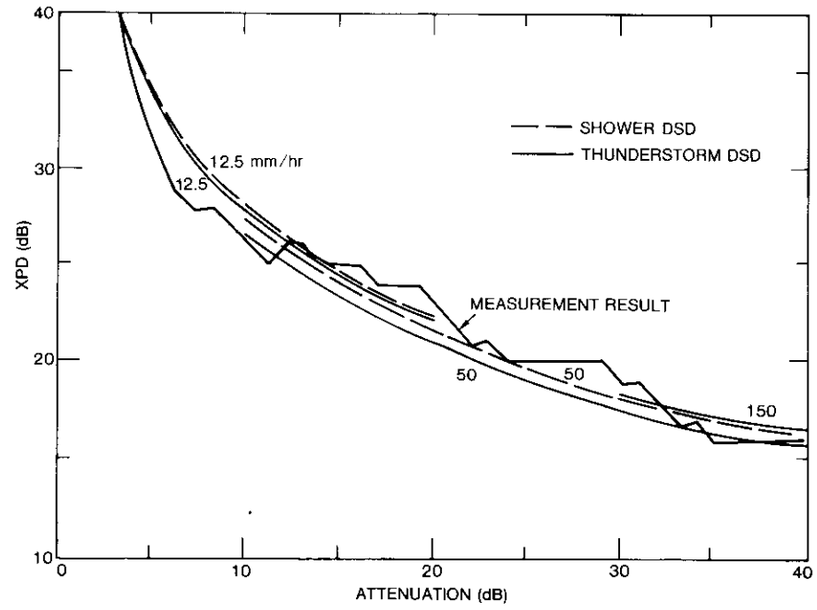

Figure 18. *Comparison Between Experimental and Calculated XPD and Attenuation at 28.6 GHz, Linear Polarization, Shower and Thunderstorm DSD*

[11] T. S. Chu, "Rain-Induced Cross Polarization at Centimeter and Millimeter Wavelengths," *Bell System Technical Journal,* Vol. 58, October 1974, pp. 1557–1578.

[12] R. L. Olsen and W. L. Nowland, "Semi-Empirical Relations for the Prediction of Rain Depolarization Statistics: Their Theoretical and Experimental Basis," International Symposium on Antennas and Propagation, Sendai, Japan, August 1978, *Proc.*, pp. 477–480.

[13] I. A. Dilworth, "Depolarization at 11.6 GHz on a Terrestrial Radio Link," *Annales des Télécommunications,* Vol. 32, 1977, pp. 469–477.

[14] T. S. Chu, "A Semi-Empirical Formula for Microwave Depolarization versus Rain Attenuation on Earth-Space Paths," *IEEE Transactions on Communications,* COM-30, No. 12, December 1982.

[15] D. C. Cox and H. W. Arnold, "Results from the 19- and 28-GHz COMSTAR Satellite Propagation Experiments at Crawford Hill," *Proceedings of the IEEE,* Vol. 70, 1982, pp. 458–488.

[16] H. W. Arnold et al., "Characteristics of Rain and Ice Depolarization for COMSTAR Satellite," *IEEE Transactions on Antennas and Propagation,* AP-28, No. 1, January 1980, pp. 22–28.

[17] D. C. Cox et al., "Properties of Attenuating and Depolarizing Atmospheric Hydrometeors Measured on a 19-GHz Earth-Space Radio Path," *Radio Science*, Vol. 15, No. 4, July-August 1980, pp. 855–865.

John A. Bennett received his B.E., B.Sc., and Ph.D. degrees from the University of Melbourne, Australia, in 1964, 1965, and 1971, respectively. He has carried out research at the University of Alberta, Edmonton, Alberta, Canada; the University of Düsseldorf, West Germany; Cambridge University, England; and Telecom Australia Research Laboratories. He was awarded the Alexander von Humboldt and Australian Radio Research Board Fellowships. As an INTELSAT Assignee, he worked at COMSAT Laboratories from 1982 to 1983. At present, he is a Senior Lecturer at Monash University, Clayton, Victoria, Australia. Dr. Bennett is a Senior Member of the IEEE and a Fellow of the Australian Institute of Physics.

Index: antennas, modeling, propagation, small terminals, communications satellite systems

Land-mobile satellite start-up systems

W. A. SANDRIN

(Manuscript received October 31, 1983)

Abstract

In view of the increasing interest in initiating a Land-Mobile Satellite System (LMSS) to complement cellular terrestrial-mobile communications systems, the relationships between space segment mass, mobile terminal characteristics, and system capacity are presented for a "start-up" (or experimental) contiguous United States (CONUS) coverage LMSS. Multipath fading, mobile terminal antennas, and voice modulation alternatives have been studied. Models for multipath fading *vs* mobile terminal antenna gain, for mobile terminal costs *vs* mobile terminal antenna gain, and for space payload mass are developed for LMSS's operating in the bands near 800 and 1,600 MHz. LMSS configurations are given for three specific examples, which correspond to the payload mass equivalent of an INTELSAT V maritime communications subsystem (MCS) package, an SBS spacecraft, and an INTELSAT V spacecraft. For each of these cases, system alternatives are given that illustrate tradeoffs among mobile terminal cost (and antenna gain), modulation type, and system capacity. One such example is a 10-channel, 800-MHz-band system using adaptive delta modulation and mobile terminals with 5-dBi antenna gains, and requiring a space payload mass of 67 kg.

Introduction

In recent years, NASA, the Canadian Department of Communications, and other organizations, have investigated LMSS's. With the current increased activity in cellular terrestrial-mobile communications, a complementary LMSS for the geographically large areas not serviced by terrestrial systems may

also be commercially attractive. Most studies to date have focused on high-capacity LMSS's using very large spacecraft. While such systems, when mature, may become commercially attractive, it appears advantageous to initiate an LMSS with a relatively small space segment investment.

Hence, it is of interest to investigate a start-up (possibly experimental) LMSS offering only a few channels, which would require only a small dedicated satellite or share a larger spacecraft bus with another system. Tradeoffs can be made among mobile terminal complexity, spacecraft mass, system capacity, and type of modulation and coding. The object of this paper is to quantify such relationships for a CONUS coverage system. The results can be used in conjunction with economic, marketing, and regulatory considerations to help in systems specifications. They can also be used to assess the benefits of new technologies, such as advanced modulation techniques and mobile antenna subsystems. Figure 1 illustrates key features of this study.

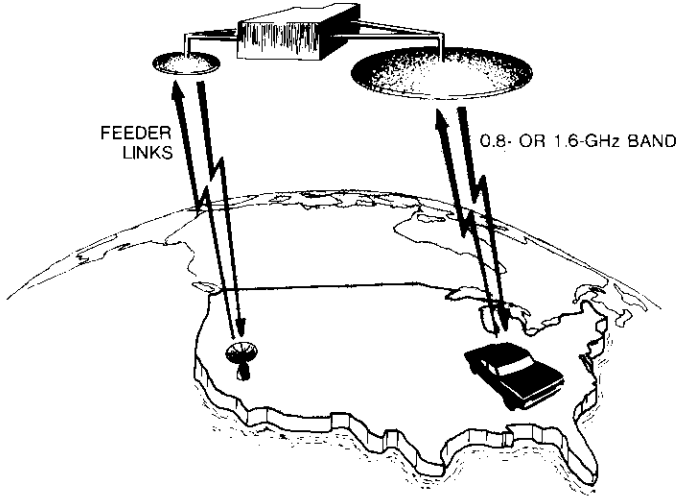

- CONUS COVERAGE
- NUMBER OF BEAMS DEPENDENT ON SYSTEM PARAMETERS
- FREQUENCY DIVISION MULTIPLE ACCESS
- MODEL PERMITS TRADES AMONG SPACECRAFT MASS, MOBILE TERMINAL COMPLEXITY, SYSTEM CAPACITY, AND MODULATION PARAMETERS
- SPACECRAFT PAYLOAD A 'PACKAGE' ON EITHER A LARGER SPACECRAFT OR A SMALL DEDICATED SPACECRAFT.

Figure 1. *Land Mobile Satellite, Start-Up System Model*

After a survey of previous work, attention is focused on factors that strongly influence LMSS performance. These include fading, mobile terminal antennas, and modulation techniques. System tradeoffs are then presented, including models for spacecraft payload mass and mobile terminal costs. Finally, examples of system configurations, obtained from the tradeoff models, are presented.

Although both the 800-MHz band (≈821–831 MHz up-link and ≈866–876 MHz down-link) and the 1.6–GHz band (≈1.645 GHz up-link and ≈1.545 GHz down-link) are treated in this paper for mobile-to-satellite links, the 800-MHz band appears to offer the greatest potential for domestic LMSS's. At the time of this writing, however, specific allocations for LMSS services have not been assigned.

Mobile terminals with circularly polarized antenna designs ranging from very simple and inexpensive single-element configurations to relatively complex and expensive array concepts, with gain ranging from −1 to 12 dBi have been considered.

The number of voice channels supported by the LMSS space segment is used as a measure of system capacity. Computations relating this measure of capacity to distributions of user-mobile terminals are not included in this study. Although only voice transmission has been assumed, the study can be extended to include low-rate-data transmission channels.

Attention is focused on the mobile/satellite up- and down-links. Feeder (*i.e.*, fixed earth terminal-to-satellite) link issues are not addressed, since they will have only a small impact on the LMSS space segment design; however, a provision for feeder link mass and power is included. Only mobile-to-base-station links (and vice versa) are treated; that is mobile-to-mobile links are assumed to be double hop (mobile-to-base-to-mobile).

Space segment comparisons for a CONUS coverage system are made in terms of payload mass requirements, and the results are related to the mass of familiar communications payloads.

Previous LMSS studies

References 1–5 give the background of the LMSS and References 6–9 contain marketing and financial studies.

Jet Propulsion Laboratories (JPL) has studied design concepts for advanced generation LMSS's [10]–[12]. The satellites for these proposed systems have large (55-meter) multibeam (87-beam) UHF antennas and large prime power (10-kW) requirements.

References 13–15 summarize the MSAT program, a joint Canadian-U.S.

LMSS venture. A Swedish company, SRA, has developed the TRUCKSAT program, designed to provide data service to trucks.

The General Electric Company (GE) has conducted LMSS studies and experiments for NASA. In its LMSS studies [16], [17], a relatively large LMSS was proposed with an LMSS satellite having 69 beams and 111 voice channels per beam. Such a satellite would require a 42.4-m antenna with a prime power requirement of 12.5 kW if the system operated in the 800-MHz band, and a 22.9-m antenna with a prime power requirement of 41 kW if the system operated in the 1.6-GHz band. In GE's experiments [18]–[20] the ATS-6 satellite has been used to establish links to trucks and other vehicles.

Ford Aerospace [21] and TRW [22] have also conducted LMSS studies for NASA. Reference 23 summarizes an earlier JPL study, while References 24–26 describe LMSS experiments and studies for ambulance, law enforcement, and other emergency services.

Reference 27 summarizes fading characteristics for LMSS links and examines techniques that can be employed to increase system capacity. At the time of this writing, two firms, Mobile Satellite Corporation and Skylink Corporation, had filed applications with the Federal Communications Commission to operate LMSS's within the U.S. [28].

Fading considerations

Multipath and shadowing fading statistics for the mobile terminal links greatly influence satellite and mobile terminal design as well as system capacity. In two studies of actual satellite-to-land mobile experiments, the results and conclusions are different. Hence, further experiments are desirable. Reference 29 describes current efforts to obtain additional experimental data.

Based on experiments in the 1.6-GHz band, Reference 18 concludes that a 5-dB fading margin is adequate for rural areas and that spatial diversity on a land-mobile terminal is not effective.

References 30 and 31 present different conclusions. This study states that, for both frequency bands, a 10- to 15-dB margin is required in suburban rural locations to ensure service to 90 percent of the locations 90 percent of the time. It also states that about a 4-dB improvement could be obtained in suburban locations by using spatial diversity on a mobile terminal.

A comparison of these studies indicates that differences in experimental transmission paths and in the mobile terminal antennas may have led to the different conclusions. In this paper, the results of References 18, 30, and 31 as well as other references noted in the following section have been used to determine a fading margin model which is a function of the mobile terminal antenna characteristic.

Land-mobile terminal antenna

Theoretical and experimental investigations of candidate mobile terminal antennas for LMSS applications have been reported. Table 1 summarizes the antenna types surveyed. Circular polarization is assumed for the spacecraft antennas to eliminate mechanical alignment of the mobile terminal antennas.

If it is assumed that much of the multipath on an LMSS link is from the horizon or below, the higher gain antennas will provide more discrimination against multipath. It is also assumed that the mobile terminal is operating in an area with generally good satellite visibility (*i.e.*, a rural/suburban location) and that the margins listed are estimates for 90/90 coverage (*i.e.*, 90-percent time coverage for 90 percent of the locations) corresponding to approximately a 20° elevation angle. The 15-dB fading margin in Table 1 for the low-gain antenna is the value given by References 30 and 31 for this condition (supported by References 32 and 33); the remainder of the entries are extrapolations, based on the ability of the higher gain antennas to discriminate against multipath. A minimum fading margin of 5 dB is assumed for the higher gain phased array antennas (to allow for some shadowing).

The values given in Table 1 have been plotted in Figure 2, and piecewise linear models have been fitted to the plotted data. These models are used in this study for system tradeoffs.

The phased array antennas in Table 1 are based on concepts given in

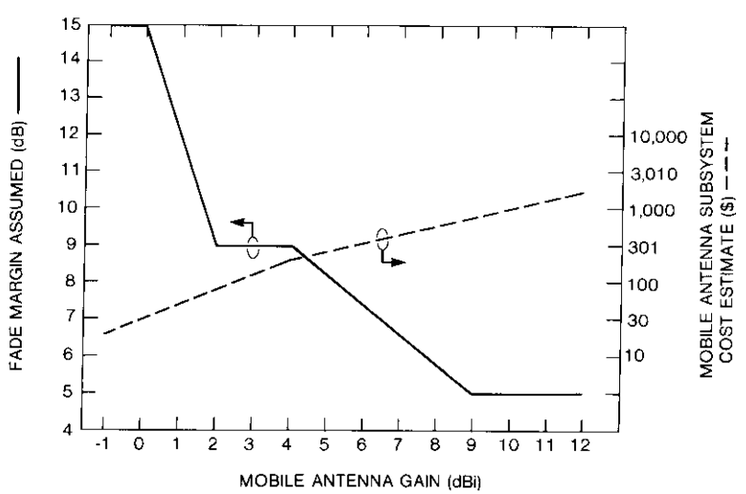

Figure 2. *Cost and Fading Margin Models for Mobile Terminal Antennas*

TABLE 1. SURVEY OF ANTENNA DESIGNS APPLICABLE TO LMSS MOBILE TERMINALS

ANTENNA TYPE	MINIMUM GAIN IN FOV (dBi)	POLARIZATION LOSS (dB)	NET GAIN (dBi)	APPROXIMATE ESTIMATED COST[a] ($)	FADING MARGIN ASSUMED[b] (dB)	REFERENCE
Short monopole ($\lambda/4$)	−2	3	−5	20	15	31
Crossed-drooping dipole	3.5	—	3.5	150	9	34
Quadrifilar helix	5	—	5	200	8	34
Microstrip patch	−1	—	−1	20	15	34
Array of microstrip patches	12	—	12	1,700	5	34
Wheeler array	4.3	3	1.3	200	9	20
Loop above ground plane	1.8	—	1.8	70	9	21
Conical spiral	3	—	3	200	9	22
4-element, linear array, partial mechanical steering	10	—	10	1,200	5	35

[a] Per unit development and manufacturing cost, exclusive of installation, in large quantities.
[b] Rough estimates for 90 percent of time and 90 percent of area in rural/suburban location at approximately 20° elevation angle.

References 34 and 35. Reference 34 illustrates two phased array concepts, each having a minimum gain of 12 dBi within the field of view (FOV). Both consist of low-gain (−1-dBi minimum FOV) microstrip patch elements. One is a 24-element low-profile planar array mounted on a vehicle's roof. (This concept lacks good coverage below about a 20° elevation angle.) The second is an array of 38 elements mounted on a truncated cone, also mounted on a vehicle's roof. Reference 35 describes a linear array consisting of four elements, each having a peak gain of about 6.8 dBi. Such an array can be either vertically or horizontally mounted, and mechanically rotated in azimuth to achieve a minimum FOV gain of 10 dB, including losses.

Modulation

The modulation technique selected for an LMSS has a large impact on capacity and on the development required for successful implementation. Modulation and coding alternatives exist that have varying degrees of power and bandwidth efficiency, and that require different amounts of development.

The approach taken here is to assume a frequency-division multiple-access (FDMA) system and to select candidate modulation schemes that cover a range of required power levels (expressed in terms of C/N_o), as well as a range of required technical innovation. The impact of various modulation schemes on system capacity and on spacecraft mass is assessed in this study by assuming a value of C/N_o for different candidate modulation schemes.

Detailed analysis of modulation, coding, and associated problems such as acquisition, synchronization, Doppler correction, fading performance, and subjective quality have not been included in this study.

After a review of several potential candidates, four specific modulation and coding techniques have been selected to illustrate a range of required C/N_o values. These techniques are identified and summarized in Table 2.

Frequency modulation (FM) with companding represents the most mature technique and requires the highest C/N_o. The use of FM in satellite/mobile applications has been described in References 12, 16, 21, 22, and 36–39; a required C/N_o of 51 dBHz has been selected based on a survey of these references. However, several studies note that intelligible quality can be maintained using FM at C/N_o values several dB lower. For example, Reference 36 assumes that a C/N_o of 46.2 can be used to obtain barely intelligible quality.

Single sideband (SSB) with companding [40] is relatively efficient in terms of required C/N_o and very efficient in terms of bandwidth. As a further advantage, it does not have a pronounced threshold effect. However, issues

TABLE 2. MODULATION AND CODING ASSUMPTIONS

MODULATION TYPE	ASSUMED REQUIRED C/N_o UNDER FADED CONDITIONS (dBHz)	APPROXIMATE REQUIRED BANDWIDTH PER CHANNEL (kHz)	COMMENTS
FM with syllabic companding	51	30	Based on 1-2 dB degraded from "toll" quality; phase locked receiver assumed.
SSB with syllabic companding	46	5	Very bandwidth efficient. Feasibility for mobile satellite application remains to be determined.
12,000-bit/s ADM, PSK rate ½ coding	46	35	Quality assumed to be sufficient for LMSS application. E_b/N_o = 5.2 dB.
2,400-bit/s LPC, PSK rate 1/2 coding	40.5	7	Feasibility for mobile application remains to be determined. E_b/N_o = 6.7 dB.

of frequency stability, interference, and fading performance must be satisfactorily resolved before SSB can be implemented in an LMSS.

The two other modulation and coding techniques shown in Table 2 are digital techniques. The phase shift keying (PSK) adaptive delta modulation (ADM) scheme requires less development than the PSK with linear predictive coding (LPC) scheme, but the savings in C/N_o are greatest with the latter.

A required C/N_o of 46 dBHz for the ADM scheme was selected based on the use of coherent binary PSK (CBPSK); the resultant 5.2-dB E_b/N_o yields a BER between 10^{-4} and 10^{-3}, assuming a 2-dB implementation margin and rate ½ FEC coding. The required C/N_o of 40.5 dBHz for the LPC scheme is also based on the use of CBPSK so that the resultant 6.7-dB E_b/N_o has a BER of about 10^{-6}, assuming a 2-dB implementation margin and rate ½ FEC coding (using a Viterbi decoder). Because a 38-dB C/N_o is about the minimum recommended to maintain carrier synchronization for CBPSK, the two schemes of Table 2 using CBPSK should be feasible from the standpoint of synchronization.

Although FDMA appears to be preferable for a first-generation LMSS, spread spectrum techniques using code-division multiple access (CDMA) should be examined. Spread spectrum techniques have the potential for reducing required fade margins and interference, but mobile terminal complexity, bandwidth requirements, level control, and system capacity must be carefully assessed.

Payload mass, mobile terminal cost, and system capacity tradeoffs

Tradeoffs among factors such as mobile terminal complexity, satellite size, system capacity, and modulation techniques affect the selection of an LMSS. The model developed for these tradeoffs uses the fading, mobile terminal antenna, and modulation parameters described in the previous sections, as well as spacecraft mass, mobile terminal cost, and link analysis relationships. Inputs to this tradeoff model are as follows:

a. range of mobile terminal antenna gains (from −1 to 12 dBi);
b. number of simultaneous channels (*i.e.*, duplex circuits);
c. required C/N_o, which is determined by the modulation assumed; and
d. operating frequency band.

Also included in the model input is an adjustment factor for the impairment caused in the base-station-to-satellite and satellite-to-base-station (*i.e.*, backhaul) links, since it is assumed that the backhaul link and satellite transponder (*i.e.*, intermodulation products) degrade the overall C/N_o by a specified amount. The backhaul degradation value for the tradeoffs in this study is 1.0 dB, based on the assumption that the combined effective C/N_o of the backhaul link and intermodulation noise is about 6 dB greater than the C/N_o of the mobile-to-satellite link when degraded by the assumed fade margin.

Mass model for the spacecraft communications payload

The mass model includes the electronics package (feeds, structure, thermal control, and integration), the antenna reflector and its support structure, the portion of the prime power system required to operate the LMSS payload, and the mass added to the satellite's fixed satellite band transponders for the LMSS backhaul links. It is assumed that either the 800-MHz band or the 1.6-GHz band is used, with a single offset paraboloidal reflector antenna fed to produce a sufficient number of beams for CONUS coverage. One RF high-level amplifier is used per beam, and the spacecraft is assumed to be body-stabilized. Inputs to the model are the total number of channels (assumed to be approximately uniformly distributed over CONUS) and the required beam edge e.i.r.p. per channel.

The principal output of the model is the payload mass. In the computer implementation of the model, two conditions determine the antenna size. First, an antenna diameter that results in minimum spacecraft weight is selected automatically. If the antenna size selected for minimum weight is

not adequate for the required spacecraft G/T, payload mass is computed for a specified antenna diameter. Other outputs of the mass model are the number of beams computed (to provide CONUS coverage), the prime power required by the LMSS package, and the G/T ratio. The appendix gives a detailed description of the payload model and the link analyses that relate the spacecraft mass model to the mobile terminal parameters, and to system capacity.

Mobile terminal cost estimate model

Since it is the sensitivity of terminal costs to satellite performance parameters that is of interest, a relatively crude cost model is used for the LMSS mobile terminal in this study.

Table 3 gives a key to the notation used in the analysis described below. The cost model is composed of three components:

a. the antenna subsystem cost,
b. the power amplifier cost, and
c. the cost of the rest of the terminal.

TABLE 3. MOBILE TERMINAL COST ESTIMATE MODEL NOTATION

ANALYSIS	DEFINITION
G_{MT}	Mobile terminal antenna gain, dBi (minimum field of view gain)
f_B	Frequency band, GHz
P_{MT}	Mobile terminal HPA power output, W
CST	Overall terminal cost estimate, dollars
CST_D	Satellite-sensitive cost estimate, dollars
C_{ANT}	Antenna subsystem costs, dollars
C_{CNT}	Cost of mobile terminal, excluding the antenna subsystem and power amplifier, dollars
C_{HPA}	Power amplifier costs, dollars
C_{FIX}	Cost of terminal excluding antenna and power amplifier, dollars

The piecewise linear model for the mobile terminal antenna, as shown in Figure 2, is

$$\begin{aligned} C_{ANT} &= 20 && \text{dollars}, && G_{MT} \leq -1 \\ C_{ANT} &= 10^{(0.2G_{MT} + 1.5)} && \text{dollars}, && -1 < G_{MT} \leq 4 \\ C_{ANT} &= 10^{(0.118G_{MT} + 1.82)} && \text{dollars}, && 4 < G_{MT} \leq 13 \end{aligned} \qquad (1)$$

From References 21 and 22, and informal cost estimates, the model assumed for the power amplifier is

$$C_{HPA} = 6.0\, P_{MT} \left(\frac{f_B}{0.85}\right)^{0.65}, \quad \text{dollars} \qquad 0.8 < f_B < 1.7\ \text{GHz} \quad . \qquad (2)$$

This model is based on the assumption that 10- and 50-W amplifiers would cost approximately \$60 and \$300, respectively, at 850 MHz, and 1.5 times as much at 1.6 GHz.

An estimate of C_{CNT} = \$1,300 is used for the cost of the mobile terminal, excluding the antenna subsystem and the power amplifier. This estimate can be broken down as follows:

RF, IF, and oscillator (synthesizer)	\$ 655
Logic	75
Baseband electronics and hardware	150
Labor	420
	\$1,300

The satellite-sensitive cost estimate is obtained from

$$CST_D = C_{ANT} + C_{HPA} \qquad (3)$$

and the overall terminal cost estimate from

$$CST = C_{ANT} + C_{HPA} + C_{CNT} \quad . \qquad (4)$$

Tradeoff results

Spacecraft payload mass

As described previously, the payload mass model includes the communications payload (with antenna and antenna support structure) and the prime power subsystem mass. Figure 3 is a sample plot obtained using the space segment mass model. This figure shows that, for a fixed per-channel beam edge e.i.r.p. and a fixed number of channels, there is an optimum antenna size. Below the optimum size, spacecraft mass rises rapidly because of the added prime power and amplifier mass required to maintain a fixed e.i.r.p.; above the optimum size, the mass increases (less rapidly) because of the

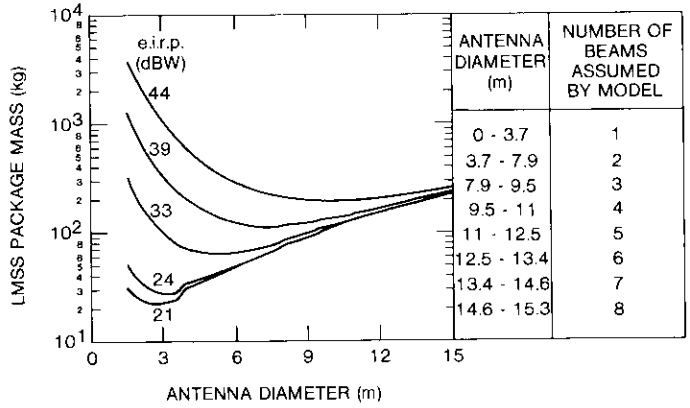

Figure 3. *Example of LMSS Payload Mass* vs *Antenna Diameter, 10-Channel System, 0.8-GHz Band*

increased antenna and antenna support structure mass. The optimum antenna size increases as the total e.i.r.p. requirement increases (*i.e.*, as e.i.r.p.$_C$ $\times$ N_C increases). The discontinuities in Figure 3 can be explained as follows. As the antenna diameter increases, the number of beams increases in integer increments, thus changing the number of feeds and amplifiers, the number of channels per beam, and the output backoff per amplifier. The model mass tradeoffs also show that a lighter space segment (for a fixed e.i.r.p.) results for L-band than for UHF. In the system tradeoffs that follow, the optimum spacecraft antenna diameter is used.

Mobile terminal cost estimate model results

Figure 4 illustrates the UHF mobile terminal cost model based on equation (4). Mobile terminal costs range from about $1,400 to about $3,500 depending primarily on antenna gain, and to a lesser extent, output power and frequency band. It is stressed that the cost data modeled here represent coarse preliminary estimates.

Payload mass/terminal cost/system capacity tradeoff results

System tradeoffs using the models described here have been made for a number of possible system configurations. These include payload mass *vs* mobile terminal antenna gain, and payload mass *vs* mobile terminal costs. Figures 5 and 6 are examples of these tradeoffs.

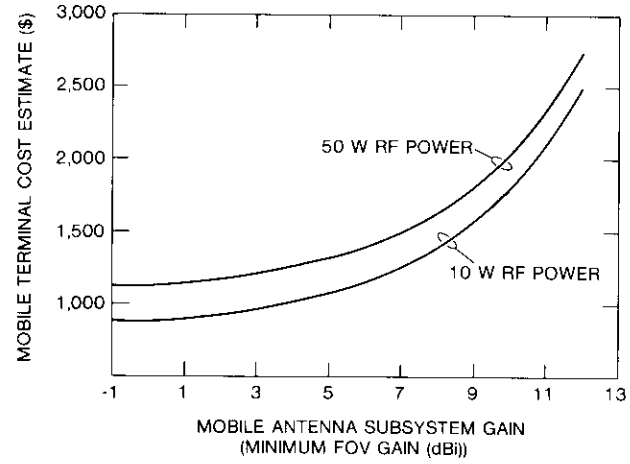

Figure 4. *LMSS Terminal Cost Model* vs *Gain, 0.8-GHz Band*

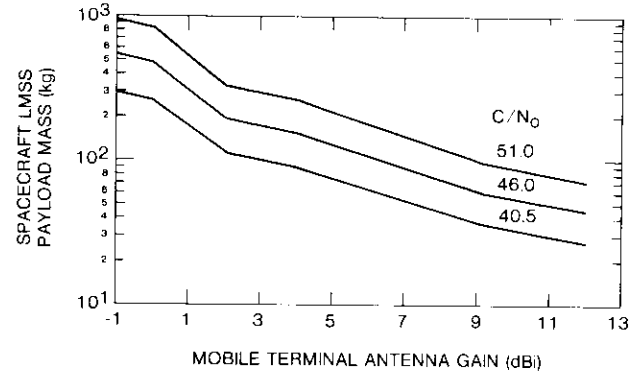

Figure 5. *LMSS Spacecraft Payload Mass* vs *Mobile Antenna Gain for a 50-Channel System, 0.8-GHz Band*

The tradeoff results indicate that the assumed fading model (shown in Figure 2) has a very large impact, especially for mobile terminal antennas having gains below 2 dBi. This effect, when combined with the low cost assumed for low-gain antennas, results in a fairly dramatic "knee" in the mobile terminal cost *vs* space segment weight relationship. That is, if the mobile antenna terminal can provide enough gain for multipath rejection at and below horizon levels, then system performance is greatly enhanced, either by permitting a smaller space segment, or by allowing a higher system capacity.

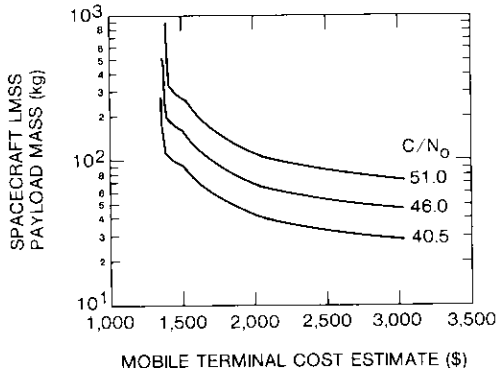

Figure 6. *LMSS Spacecraft Payload Mass* vs *Mobile Terminal Cost for a 50-Channel System, 0.8-GHz Band*

The tradeoff results also show the effect of the different voice modulations assumed, as illustrated in Figures 5 and 6. In Figure 5, where mobile terminal antenna gain is the abscissa, the three curves are generally approximately parallel, except for minor irregularities, due to the fading model discontinuities and to the coarseness in the power/space antenna size optimization. However, in Figure 6, where cost is the abscissa, modulations requiring lower C/N_o values yield little cost advantage for mobile antennas with low gain values. That is, for mobile terminals with antennas having very low gains (<2 dBi), more benefit is realized by a slight increase in antenna gain than by an improved modulation.

Tables 4 through 6 show the results of LMSS tradeoffs. These tables illustrate alternative system configurations that are possible with spacecraft payloads of three different sizes:

a. an LMSS package with about the same mass as the INTELSAT V MCS (maritime communications subsystem) package, *i.e.*, about 70 kg;
b. an LMSS spacecraft (or package) with about the same payload mass as the SBS spacecraft, *i.e.*, about 228 kg; and
c. an LMSS spacecraft (or package) with about the same payload mass as the INTELSAT V spacecraft, *i.e.*, about 439 kg.

The mass values compared in these tables as well as the mass values given above for the MCS, SBS, and INTELSAT V space segments are for the communications payload (including antennas and antenna support structures) and the prime power subsystem required by the LMSS communications payload.

TABLE 4. SUMMARY OF LMSS PAYLOAD MASS/MOBILE TERMINAL COST/SYSTEM CAPACITY TRADEOFF RESULTS (CASE 1: MCS SIZE PACKAGE, 58-73 kg)

				Mobile Terminal Parameters				Payload Parameters			
				Antenna							
Number of Channels	Frequency Band (GHz)	E_b/N_o (dBHz)	Cost Estimate ($)	Gain (Min FOV) (dBi)	Minimum RF Power (W)	Mass* (kg)	Antenna Diameter (m)	Prime Power (W)	e.i.r.p./ Channel (beam-edge) (dBW)	Number of Beams
10	0.8	51	1,900	8	2.8	65.0	4.9	180	32.1	2
10	0.8	46	1,575	5	2.7	67.3	5.2	175	32.5	2
10	0.8	40.5	1,400	2	3.7	58.6	3.7	234	30.8	1
50	0.8	40.5	1,650	6	0.5	71.4	5.2	196	25.2	2
100	0.8	40.5	1,875	8	0.2	73.2	5.5	182	21.6	2
200	0.8	40.5	3,025	12	0.1	70.5	5.2	179	16.8	2
10	1.6	51	1,925	8	4.4	68.6	4.0	269	37.6	2
10	1.6	46	1,600	5	4.8	72.7	4.0	294	38.0	2
10	1.6	40.5	1,400	2	3.3	58.2	4.0	201	36.3	2
50	1.6	46	2,075	9	0.6	71.8	4.9	212	30.8	3
50	1.6	40.5	1,643	6	0.6	71.4	4.9	208	30.8	3
100	1.6	40.5	1,875	8	0.3	72.3	4.9	210	27.1	3
200	1.6	40.5	3,025	12	0.1	67.3	4.9	173	22.3	3

* Communications payload (including antenna and antenna support structure) plus prime power weight.

TABLE 5. SUMMARY OF LMSS PAYLOAD MASS/MOBILE TERMINAL COST/SYSTEM CAPACITY TRADEOFF RESULTS (CASE 2: SBS COMMUNICATIONS PAYLOAD SIZE, 192-268 kg)

			Mobile Terminal Parameters				Payload Parameters			
Number of Channels	Frequency Band (GHz)	E_b/N_o (dBHz)	Cost Estimate ($)	Antenna Gain (Min FOV) (dBi)	Minimum RF Power (W)	Mass* (kg)	Antenna Diameter (m)	Prime Power (W)	e.i.r.p./ Channel (beam-edge) (dBW)	Number of Beams
10	0.8	51	1,450	1.0	15.5	256	9.4	972	45.3	3
10	0.8	46	1,400	0.0	12.3	226	9.4	774	44.3	3
50	0.8	51	1,575	5.0	2.1	240	10.4	713	37.5	4
50	0.8	46	1,400	2.0	1.8	212	9.8	613	36.3	4
50	0.8	40.5	1,350	0.5	2.0	227	10.4	670	36.8	4
100	0.8	51	1,750	7.0	0.9	243	10.4	713	33.9	4
100	0.8	46	1,550	5.0	0.8	210	9.8	586	32.5	4
100	0.8	40.5	1,350	1.0	1.0	266	11.3	711	34.8	5
200	0.8	51.0	2,302	10.0	0.3	226	10.1	627	29.3	4
200	0.8	46	1,750	7.0	0.3	217	9.8	609	28.9	4
200	0.8	40.5	1,450	3.0	0.4	238	10.4	662	29.8	4
10	1.6	51	1,500	1.0	17.2	238	9.1	794	50.8	10
50	1.6	51	1,650	6.0	2.3	211	8.2	726	41.2	8
50	1.6	46	1,400	2.0	2.7	227	8.2	828	41.8	8
50	1.6	40.5	1,375	1.0	2.2	192	7.6	686	40.3	7
100	1.6	51	1,750	7.0	1.3	245	9.1	791	39.4	10
100	1.6	46	1,575	5.0	1.0	211	8.8	629	38.0	9
100	1.6	40.5	1,350	1.0	1.4	268	9.8	847	40.3	11
200	1.6	51	2,075	9.0	0.5	245	9.8	688	35.8	11
200	1.6	46	1,750	7.0	0.4	213	8.8	627	34.4	9
200	1.6	40.5	1,425	3.0	0.5	234	9.1	705	35.3	10

* Communications payload (including antenna and antenna support structure) plus prime power weight.

TABLE 6. SUMMARY OF LMSS PAYLOAD MASS/MOBILE TERMINAL COST/SYSTEM CAPACITY TRADEOFF RESULTS (CASE 3: INTELSAT V COMMUNICATIONS PAYLOAD SIZE, 388-585 kg)

			Mobile Terminal Parameters				Payload Parameters			
Number of Channels	Frequency Band (GHz)	E_b/N_o (dBHz)	Cost Estimate ($)	Antenna Gain (Min FOV) (dBi)	Minimum RF Power (W)	Mass* (kg)	Antenna Diameter (m)	Prime Power (W)	e.i.r.p./ Channel (beam-edge) (dBW)	Number of Beams
50	0.8	51	1,400	1.0	6.4	562	14.6	2,029	45.3	7
50	0.8	46	1,375	0.0	6.1	506	13.4	1,916	44.3	6
100	0.8	51	1,450	3.0	2.0	466	14.9	1,311	40.3	8
100	0.8	46	1,350	1.0	2.0	466	14.9	1,311	40.3	8
100	0.8	40.5	1,325	−1.0	1.9	216	14.3	1,298	39.8	7
200	0.8	51	1,650	6.0	0.8	426	14.0	1,215	35.7	7
200	0.8	46	1,375	2.0	0.9	454	14.3	1,334	36.3	7
200	0.8	40.5	1,350	0.0	1.1	585	16.5	1,702	38.8	9
10	1.6	51	1,625	−1.0	3.4	419	11.6	1,551	55.8	16
50	1.6	51	1,425	2.0	4.5	399	11.3	1,401	46.8	15
50	1.6	46	1,400	0.0	6.1	560	13.7	1,897	49.8	22
100	1.6	51	1,525	4.0	2.4	445	12.2	1,516	44.8	17
100	1.6	46	1,375	1.0	2.8	500	12.8	1,729	45.8	19
100	1.6	40.5	1,350	−1.0	2.6	472	12.5	1,618	45.3	18
200	1.6	51.0	1,650	6.0	1.0	425	12.5	1,313	41.2	18
200	1.6	46.0	1,400	2.0	1.1	453	12.8	1,421	41.8	19
200	1.6	40.5	1,350	1.0	0.9	388	12.2	1,138	40.3	17

* Communications payload (including antenna and antenna support structure) plus prime power weight.

The mobile terminal RF power shown in these tables is the value required to meet the stated E_b/N_o on the mobile-to-base link. As can be seen, in many cases this power is very low since the space-to-mobile down-link determines the optimum LMSS space segment configuration. Thus, in an actual system design, it would perhaps be preferable to use larger mobile terminal RF amplifiers than those indicated in the tables to achieve a better margin in the mobile-to-base-station direction. (This extra margin may be desirable because talkers in mobile terminals are likely to be in environments with high noise backgrounds.)

Conclusions

The purpose of this study has been to obtain parametric relationships between spacecraft payload mass, mobile terminal characteristics, and system capacity for a CONUS coverage LMSS, with emphasis on start-up systems. To accomplish this objective, relevant aspects of LMSS systems, fading, mobile terminal antennas, and modulation were surveyed, and the appropriate system models developed.

The major results of this study have been presented in Tables 4–6, where each row describes a separate sample system. These results describe a large number of different start-up LMSS options, and illustrate tradeoffs among the key system parameters.

Table 7 condenses the relationships obtained in this study by showing a few sample LMSS configurations. The examples selected for this table demonstrate quantitatively various combinations of spacecraft payload mass, system capacity, mobile terminal antenna complexity, and modulation type. As shown, the number of channels that a payload of a particular mass can provide increases dramatically as the C/N_o required by the modulation technique is reduced, and as the gain of the mobile terminal antenna increases.

To summarize the principal conclusions of this study, the development of voice modulation and coding techniques, such as SSB, ADM, or LPC, that require small C/N_o values will have a large impact on LMSS design. Also, the development of mobile terminal antennas having both a relatively high gain and an ability to reject multipath interference will affect both the capacity of an LMSS and the quality of service. Finally, the results of this study are highly sensitive to the assumptions made regarding fading, especially for mobile terminals having antennas with relatively low gains.

Acknowledgment

The assistance of Mingo Lin in developing the computer programs for the tradeoff models described in this report is very much appreciated.

TABLE 7. SAMPLE LMSS CONFIGURATIONS FOR START-UP TYPE UHF SYSTEM

Spacecraft Payload	Number of Channels	Modulation (C/N_o) (dBHz)	Estimated Mobile Terminal Cost ($)	Mobile Terminal Antenna Gain (Min FOV) (dBi)	Comments
Equivalent to Mass of INTELSAT V MCS Package (70 kg)	10	51 (FM)	1,900	8.0	These three cases show impact of improved modulation techniques on mobile terminal antenna requirement.
	10	46 (SSB or ADM)	1,575	5.0	
	10	40.5 (LPC)	1,400	2.0	
	200	40.5 (LPC)	3,025	12.0	Higher system capacity achieved with both advanced modulation and antenna designs.
Equivalent to Mass of SBS Comm. Payload (228 kg)	50	51 (FM)	1,575	5.0	Fourfold increase in system capacity results with SSB or ADM and slightly better mobile antenna.
	200	46 (SSB or ADM)	1,750	7.0	
Equivalent to Mass of INTELSAT V. Comm. Payload (439 kg)	100	51 (FM)	1,450	3.0	Mobile terminals with relatively modest requirements.
	200	46 (SSB or ADM)	1,375	2.0	

References

[1] G. H. Knouse, "Terrestrial/Land Mobile Satellite Considerations, NASA Plans, and Critical Issues," *IEEE Transactions on Vehicular Technology*, VT-29, November 1980, pp. 370–374.

[2] G. H. Knouse and P. A. Castruccio, "The Concept of an Integrated Terrestrial/Land Mobile Satellite System," *IEEE Transactions on Vehicular Technology*, VT-30, August 1981, pp. 97–101.

[3] J. Freibaum, "Satellite Aided Land Mobile Communications, A World Need," Communicaciones Expo '82, April 25–28, 1982.

[4] P. A. Castruccio, Z. C. Marantz, and J. Freibaum, "Need for, and Financial Feasibility of Satellite-Aided Land Mobile Communications," IEEE International Conference on Communications, June 1982, *Conference Record*, pp. 7H.1.1–7H1.6.

[5] B. E. LeRoy, "Satellite-Aided Land Mobile Communications System Implementation Considerations," IEEE International Conference on Communications, June 1982, *Conference Record*, pp. 7H.3.1.–7H.3.5.

[6] P. A. Castruccio, "The Technical and Economic Role of Space Technology in Terrestrial Mobile Communications," NTC '79, November 1979.

[7] "Analysis of the Oil and Gas Industry Market for a Land Mobile Communications Satellite Service," Final Report prepared for NASA (Headquarters) by ECO Systems International, January 18, 1982.

[8] "Analysis of the Tracking Industry Market for a Land Mobile Communications Satellite Service," Final Report prepared for NASA (Headquarters) by ECO Systems International, January 11, 1981.

[9] "Financial Study for a Satellite Land Mobile Communications System," Prepared for NASA (JPL) by Corporate Finance Division-Merchant Banking Group, Citibank, N.A., December 16, 1981.

[10] F. Naderi, "An Advanced Generation Land Mobile Satellite System and its Critical Technologies," *NTC '82 Conference Record*, November 1982, pp. B1.1.1–B1.1.8.

[11] F. Naderi, Editor, "Land Mobile Satellite Service (LMSS), Part I: Executive Summary," JPL Report, February 15, 1982.

[12] F. Naderi, Editor, "Land Mobile Satellite Service (LMSS), Part II: Technical Report," JPL Report No. 82-19, February 15, 1982.

[13] P. Boudreau, R. Breithaupt, and J. McNally, "The Canadian Mobile Satellite Program," *NTC '82 Conference Record*, November 1982, pp. B1.2.1–B1.2.5.

[14] "M-Sat Spacecraft Conceptual Design Studies—Executive Summary," SPAR Document DOC-CR-SP-81-047B (Canada), November 1981.

[15] R. Lovell, G. Knouse, and W. Weber, "An Experiment to Enable Commercial Mobile Satellite Service, *NTC '82 Conference Record*, November 1982, pp. B1.3.1–B1.3.5.

[16] R. Anderson and R. Milton, "Satellite-Aided Mobile Radio Concepts Study," Final Report, GE Document 79SDS4240, June 1979.

[17] R. Anderson, R. Milton, and J. Brown, "Communications Satellite Studies Applicable to Mobile Telephone Services," *NTC '79 Conference Record*, November 1979, pp. 30.5.1–30.5.7.

[18] R. Anderson, R. Frey, and J. Lewis, "Satellite Mobile Communications Limited Operational Test in the Trucking Industry," Final Report, N81-20337 (General Electric), July 1980.

[19] R. Anderson, "Signaling Characteristics in Satellite-Aided Land Mobile Communications," *GLOBECOM '82 Conference Record*, November 1982, pp. E5.7.1–E5.7.5.

[20] R. Anderson, et al., "Satellite-Aided Mobile Communications: Experiments, Applications, and Prospects," *IEEE Transactions on Vehicular Technology*, VT-30, May 1981, pp. 54–61.

[21] J. J. Jones et al., "A Study and Experiment Plan for Digital Mobile Communication via Satellite, Final Report," Ford Aerospace, NASA Report CR-152213, November 1978.

[22] TRW, "Mobile multiple Access Study—Final Report," NASA Contract NAS5-23454, August 1977.

[23] N. Reilly and J. Smith, "A National Voice Network With a Satellite and Small Transceivers," 1978 AIAA Conference on Communications Satellites, AIAA Paper 78-626.

[24] C. Drumheller, et al., "Benefits and Cost Effectiveness of Satellite-Aided Communications for Emergency Medical Services, Fighting Forest Fires, and Pick-up and Delivery Trucking Applications," *NTC '79 Conference Record*, November 1979, pp. 30.2.1–30.2.6.

[25] J. Parness, "Satellite Based Law Enforcement Communications," *NTC '79 Conference Record*, November 1979, pp. 30.3.1–30.4.6.

[26] C. Burge and R. Zuschlag, "Initial Results and Assessment of a Communications Experiment Using NASA's ATS-3 for Emergency Medical Services," *NTC '79 Conference Record*, November 1979, pp. 30.6.1–30.6.5.

[27] D. O. Reudink, "Estimates of Path Loss and Radiated Power for UHF Mobile Satellite Systems," *Bell System Technical Journal*, October 1983, pp. 2493–2512.

[28] "NASA Studies Shift in Mobile Satellite Effort," *Aviation Week and Space Technology*, October 10, 1983.

[29] J. S. Butterworth and E. E. Matt, "The Characterization of Propagation Effects for Land Mobile Satellite Service," IEE Conference on Satellite Systems for Mobile Communications and Navigation, June 7–9, 1983.

[30] G. C. Hess, "Land Mobile Satellite Path Loss Measurements," Motorola Inc., September 6, 1978.

[31] G. C. Hess, "Land Mobile Satellite Excess Path Loss Measurements," *IEEE Transactions on Vehicular Technology*, VT-29, May 1980, pp. 290–297.

[32] "Satellite Sound Broadcasting With Portable Receivers and Receivers in Automobiles," *Recommendations and Reports of CCIR 1982 XVth Plenary Assembly*, Geneva, 1982, Vol. X and XI, Part 2, pp. 267–281.

[33] "Factors Affecting the Choice of Antennas for Mobile Stations of the Land Mobile Satellite Service," Draft Report AW/8, CCIR Document 8/338-E, February 10, 1981.

[34] K. Woo, "Low Gain and Steerable Vehicle Antennas for Communications With Land Mobile Satellite," *NTC '82 Conference Record,* November 1982, pp. B1.6.1–B1.6.5.

[35] W. A. Sandrin and E. W. Carpenter, "Antenna Studies for INMARSAT Standard C Terminals," IEE Conference on Satellite Systems for Mobile Communications and Navigation, June 7–9, 1983.

[36] W. D. Hindson et al., "Communications System Concept for the 800 MHz Service on the Demonstration MSAT," Canadian Department of Communications, January 31, 1981.

[37] "Modulation Techniques and Voice Processing for Telephone Circuits in the Marine Mobile Satellite Service," Report 752, *CCIR Recommendations and Reports,* 1978, Vol. VIII, pp. 288–303.

[38] D. W. Lipke et al., "MARISAT—A Maritime Satellite Communications System," *COMSAT Technical Review,* Vol. 7, No. 2, Fall 1977, pp. 351–391.

[39] "Link Power Budgets for a Maritime Mobile Satellite Service," Report 760, *CCIR Recommendations and Reports,* 1978, Vol. VIII, pp. 409–420.

[40] B. Lusignan, "Single Sideband Transmission for Land Mobile Radio," *IEEE Spectrum,* July 1978, pp. 33–37.

Appendix A. LMSS spacecraft payload mass model and link analyses

The text has described basic assumptions made for the payload mass model. Table A-1 is a key to the notation used in the description of the payload model.

TABLE A-1. NOTATION FOR SPACECRAFT PAYLOAD MASS MODEL DESCRIPTION

ANALYSIS NOTATION	DEFINITION
D_{SC}	Spacecraft (S/C) antenna diameter, m
e.i.r.p.$_C$	Beam-edge e.i.r.p. per channel required, dBW
N_C	Total number of satellite channels
W_{SC}	Total LMSS communications payload weight, including prime power system mass, kg
N_B	Total number of beams required for CONUS coverage
P_{SC}	Total spacecraft package prime power, W
f_B	Frequency band, GHz (either 0.85 or 1.6)
G/T_S	Satellite G/T, dBi/K
K_S	Added reflector mass factor for reflector structure
K_R	Mass of reflector per unit area, kg/m^2
W_{REF}	Mass of reflector subsystem including support structure, kg
λ	Wavelength, m
η_A	Spacecraft antenna efficiency factor
G_{SCBE}	Beam edge gain of spacecraft antenna, dBi
$N_{C/B}$	Number of channels per beam
BO_{OUT}	Output backoff per RF amplifier, dB
P_{CdB}	Required RF power per channel, dBW
P_C	Required RF power per channel, W
P_{RFS}	Required saturated RF power per amplifier, W
W_E	Mass of electronics package including feeds, kg
η_P	DC-to-saturated RF power efficiency
W_{PWR}	Mass of prime power subsystem, kg
K_{PP}	Per unit mass of prime power system, kg/W
W_{BS}	Base station link added mass, kg
T_{SS}	Satellite receiver system noise temperature, K
$L_{\ell fd}$	Feed and line RF losses, dB
P_{RE}	Power required by the receiver and electronics per beam, W

Reflector mass

The mass of the reflector and its support structure is modeled as

$$W_{REF} = \frac{(1 + K_s)\, K_R \pi D_{SC}^2}{4} \quad kg \qquad \text{(A-1)}$$

where

$$K_R = 0.979\ kg/m^2$$
$$K_S = 0.3.$$

This relationship is based on the following considerations. The TDRSS 4.9-m unfurlable antenna weighs 22.7 kg, and the ATS-F and ATS-G 9.1-m antennas weigh 81.8 kg. Assuming that reflector mass is proportional to projected area, the mass of both of these antennas is close to 1.22 kg/m^2. In equation (A-1) this factor, K_R, is reduced to 0.979 because less surface tolerance and therefore fewer support ribs are required at UHF and L-band, and because advances in the state of the art since the ATS and TDRSS antennas should result in a slightly lighter design.

An additional 30 percent (K_S = 0.3) has been added to the reflector mass in equation (A-1) for the reflector support structure.

Number of beams

To provide CONUS coverage, the satellite antenna is assumed to produce a number of contiguous equal size beams. Using the approximation that

$$\text{beamwidth} = \frac{70}{D_{SC}/\lambda} \quad \text{degrees} \tag{A-2}$$

and that CONUS is approximately 6.5 ° × 3° from synchronous altitude yields the following relationship for the number of beams to cover CONUS:

$$\begin{aligned} N_B &= \text{largest integer of } \left[\frac{D_{SC}^2}{\lambda^2}\frac{19.5}{70^2}\right] + 1, && \frac{D_{SC}}{\lambda} \geq 22.5 \\ N_B &= 2, && 10.8 < \frac{D_{SC}}{\lambda} < 22.5 \\ N_B &= 1, && 0 < \frac{D_{SC}}{\lambda} \leq 10.8 \quad . \end{aligned} \tag{A-3}$$

This approximation is considered sufficiently accurate for mass modeling and closely matches Figure 4-11 of Reference A-1.

Antenna beam edge gain

The widely used approximation for the gain of a parabolic antenna is used with 3 dB subtracted to obtain beam edge gain:

$$G_{SCBE} = 10 \log_{10}(107.6\eta_A f_B^2 D_{SC}^2) - 3 \text{ dBi} \quad . \tag{A-4}$$

RF Amplifier output backoff

An SCPC FDMA system is assumed with one power amplifier per beam and an approximately uniform channel distribution among all beams. Hence, the number of channels per amplifier is assumed to be

$$N_{C/B} = N_C/N_B \quad . \tag{A-5}$$

To keep intermodulation products at an acceptable level, it is necessary to operate the output amplifiers backed off from saturation. The amount of backoff required depends on both the number of carriers and the carrier frequency plan.

For mass modeling, it is assumed that a total bandwidth of 4 MHz is allocated, and that each channel occupies 30 kHz. If it is assumed that the carrier-to-intermodulation ratio, C/IM, is to be maintained at levels of 19 dB or greater, and that judiciously selected frequency plans are used, than the following relationships are obtained using a bound in Reference A-2 and other frequency planning considerations:

$$\begin{aligned} BO_{OUT} &= 0 \text{ dB}, && N_{C/B} = 1 \\ BO_{OUT} &= 2 \text{ db}, && 2 \leq N_{C/B} \leq 9 \\ BO_{OUT} &= (1.003)^{N_{C/B}}\, \ell n\,(0.75 N_{C/B}), && N_{C/B} \geq 10 \quad . \end{aligned} \tag{A-6}$$

Required saturated RF power per amplifier

From link considerations,

$$P_{C/B} = \text{e.i.r.p.}_C - G_{SCBE} + L\ell_{fd} \quad \text{dBW} \tag{A-7}$$

where $L\ell_{fd}$ is assumed to have a value of 0.8 dB,

$$P_C = 10^{P_{C/B}/10} \quad W \tag{A-8}$$

and

$$P_{RFS} = P_C N_{C/B}\, 10^{BO_{OUT}/10} \quad W \quad . \tag{A-9}$$

Electronics package and feed mass

From data on the INTELSAT MCS package, and from Reference 12, the following expression has been derived to approximate the mass of the LMSS electronics package and feeds:

$$\begin{aligned} W_E = 2.2 N_B[12.3 - 2.67 f_B + 0.4 P_{RFS}] \quad \text{kg}, \\ 0.8 < f_B < 1.7 \text{ GHz} \quad . \end{aligned} \tag{A-10}$$

This expression includes the weights of the radiating feed elements, LNAS, diplexers, power amplifiers, filters and converters, interconnect cabling and electronics, thermal control, and structure and integration structure.

Required prime power and prime power subsystem mass

The DC-to-RF efficiency at saturation assumed for the power amplifiers is

$$\eta_P = 0.3 + 0.1\left[\frac{BO_{OUT}}{4}\right], \quad 0 \leq BO_{OUT} \leq 8 \text{ dB} \quad . \tag{A-11}$$

This models a solid-state amplifier or a multicollector TWT whose equivalent saturation efficiency improves with increasing output backoff.

The total prime power required for the LMSS package is assumed to be

$$P_{SC} = \left(\frac{P_{RFS}}{\eta_P}\right) + P_{RE}N_B \quad W \tag{A-12}$$

where P_{RE} is assumed to be 4 W.

The mass of the portion of the spacecraft prime power subsystem devoted to the LMSS package is

$$W_{PWR} = K_{PP}P_{SC} \quad kg \quad . \tag{A-13}$$

In this analysis, K_{PP} is assumed to be 0.091 kg/W. This assumes a body-stabilized spacecraft with full eclipse power.

Total LMSS package mass

The total LMSS package mass is

$$W_{SC} = W_{REF} + W_E + W_{PWR} + W_{BS} \quad \text{kg} \quad . \tag{A-14}$$

In this analysis, W_{BS} is assumed to be only 4.5 kg, since it is assumed that the spacecraft already has fixed satellite frequency band transponders, and that the LMSS portion of the fixed satellite frequency traffic will be very small.

Satellite G/T

The satellite receiving system noise temperature, based on a survey of the state of the art and forecasts of future performance capability, is assumed to be

$$T_{SS} = 25f_B + 450, \quad \text{Kelvin} \quad . \tag{A-15}$$

The satellite G/T at beam edge is

$$G/T_S = G_{SCBE} - 10\log_{10}(T_{SS}) \quad . \tag{A-16}$$

Down-link analysis

The required per-channel satellite e.i.r.p. for the satellite-to-mobile terminal link is

$$\text{e.i.r.p.}_C = C/N_o + L_{PL} + L_{fade} - G_{MT} + T_{MI} - 228.6\,\text{dBW} \quad . \tag{A-17}$$

The notation for this equation is defined in Table A-2, and

$$L_{PL} = 183.1 + 20\log_{10}\left(\frac{f_B}{0.85}\right) \tag{A-18}$$

which corresponds to free space loss at a 15° elevation angle. The fading loss, L_{fade}, model used is the one given in Figure 2.

TABLE A-2. NOTATION FOR DOWN-LINK ANALYSIS

ANALYSIS NOTATION	DEFINITION
e.i.r.p._C	Required satellite e.i.r.p. per channel, dBW
C/N_o	Required C/N_o, dBHz
L_{PL}	Path loss, dB
L_{fade}	Fading loss, dB
G_{MT}	Mobile terminal antenna gain, dBi
T_{MT}	Mobile terminal system noise temperature, K
f_B	Frequency band, GHz

The mobile terminal system noise temperature used in this study is assumed to be 600 K. This is consistent with that used in other studies, although some studies use a more conservative noise temperature figure (900°) to allow for high background noise levels (from ignition systems and other interference sources).

Up-link analysis

In this study, the required mobile terminal output power is computed as a function of satellite antenna gain. However, if this value exceeds 50 W, the mobile terminal power is fixed at 50 W, and the required satellite antenna diameter is computed. Otherwise, as discussed previously, the antenna gain that minimizes satellite mass is used in the model.

Using the notation defined in Table A-3, the mobile terminal's required output power is computed as

$$P_{MT} = 10^{(P_{MTDB}/10)} \quad \text{W} \tag{A-19}$$

TABLE A-3. NOTATION FOR MOBILE TERMINAL RF POWER COMPUTATION MODEL

ANALYSIS NOTATION	DEFINITION
C/N_o	Required C/N_o, dBHz
G_{MT}	Mobile terminal antenna gain, dBi
f_B	Frequency band, GHz
D_{SC}	Spacecraft antenna diameter, m
P_{MT}	Mobile terminal power amplifier output, W
L_{MT}	Mobile terminal antenna feed loss, dB
P_{MTDB}	P_{MT}, dBW
L_{fade}	Fading loss, dB
G_{SCBE}	Beam edge gain of S/C antenna, dBi
η_A	Spacecraft antenna efficiency factor
L_{PL}	Path loss, dB

where

$$P_{MTDB} = C/N_o + L_{MT} - G_{MT} + L_{\text{fade}} + L_{PL} - G_{SCBE} + 10\log_{10} T_{SS} - 228.6 \quad \text{dBW} \tag{A-20}$$

$$L_{MT} = 0.5\ \text{dB} \tag{A-21}$$

L_{fade} and L_{PL} are defined in the previous section, and

$$T_{SS} = 25 f_B + 450 \quad \text{Kelvin} \tag{A-22}$$

$$G_{SCBE} = 10\log_{10}(107.6\,\eta_A f_B^2 D_{SC}^2) - 3 \quad \text{dBi} \ . \tag{A-23}$$

To compute the required spacecraft antenna diameter when P_{MT} is set at a fixed level (50 W), equations (A-20) and (A-21) are solved for D_{SC}.

References

[A-1] TRW, "Mobile Multiple Access Study—Final Report," NASA Contract NAS5-23454, August 1977.

[A-2] Y. Hirata, "A Bound on the Relationship Between Intermodulation Noise and Carrier Frequency Assignment," *COMSAT Technical Review*, Vol. 8, No. 1, Spring 1978, pp. 141–154.

William A. Sandrin received a B.S.E.E. degree from the University of Vermont in 1963 and an M.E.E. degree from Rensselaer Polytechnic Institute in 1966. From 1966 to 1971, he worked for the Boeing Company, Aerospace Group, where he was involved in space communications system design and in the development of phased array antennas. In 1971 he joined COMSAT Laboratories, where he has been engaged in multibeam antenna studies; transponder linearizer development; transmission impairments analysis; studies of domestic, maritime, and aeronautical satellite systems; a study of adaptive phased array antennas for small-terminal applications; and frequency planning studies. He is presently a Staff Scientist in the Communications Systems Studies Department of the Communications Techniques Division. Mr. Sandrin is a member of IEEE, Tau Beta Pi, and Eta Kappa Nu.

CTR Notes

A derivation of the boundary of the glistening region for rough surface scatter

D. L. BRANDEL AND L. KLEIN

(Manuscript Received November 23, 1983)

The well-known text by Beckmann and Spizzichino [1] provides an expression for the boundary contour of the glistening region that results from reflection from a rough planar surface. This expression, given in equation (53) on page 276 of Reference 1, contains a typographical error. This note is intended to provide a derivation for the correct expression.

The coordinate system for the discussion is shown in Figure 1. The point P is on the planar surface and is defined by the coordinates

$$u = \text{angle}\,(OX, OP)$$
$$v = \text{angle}\,OPR.$$

The equation of the boundary is obtained by using the angle β between the bisector of the angle TPR and the vertical. One terminal, assumed to be the transmitter (T), is at infinity in a direction lying in the xz plane and making an angle γ with the x axis. The origin O is chosen so that the receiver (R) lies on the z axis at height h above the planar surface.

The unit vector in the direction from P to R is given by

$$\bar{a}_{PR} = -\bar{i}\cos v\cos u - \bar{j}\cos v\sin u + \bar{k}\sin v$$

D. L. Brandel was Director of Service Development, Maritime Services, World Systems Division. He is currently Program Manager for the Advanced Communications Technology Satellite Program in NASA's Office of Space Science and Applications.

L. Klein is a Communications Systems Analyst in the Communications Systems Analysts Department, World Systems Division.

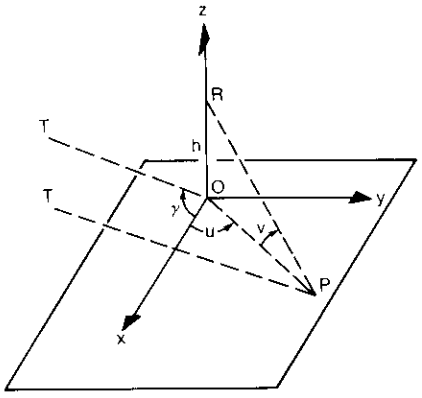

Figure 1. *Reflection Geometry*

where $\bar{i}, \bar{j}, \bar{k}$ are unit vectors in the x, y, z directions, respectively. Similarly, in the direction from P to T, the unit vector is

$$\bar{a}_{PT} = \bar{i}\cos\gamma + \bar{k}\sin\gamma \quad .$$

The bisector of angle TPR is given as

$$\bar{a}_{PB} = \frac{\bar{a}_{PR} + \bar{a}_{PT}}{|\bar{a}_{PR} + \bar{a}_{PT}|}$$

where $\bar{a}_{PR} + \bar{a}_{PT} = \bar{i}(\cos\gamma - \cos v\cos u) - \bar{j}\cos v\sin u + \bar{k}(\sin v + \sin\gamma)$.

Then,

$$\cos\beta = \bar{a}_{PB}\cdot\bar{k} = \frac{\sin v + \sin\gamma}{D^{1/2}}$$

where $D = \cos^2\gamma - 2\cos\gamma\cos v\cos u + \cos^2 v + \sin^2 v + 2\sin v\sin\gamma + \sin^2\gamma$.

Substituting $1 - \sin^2\beta$ for $\cos^2\beta$ yields

$$\cos^2\gamma - 2(1 - \sin^2\beta)\cos\gamma\cos v\cos u + \cos^2 v - \sin^2\beta(\cos^2\gamma + \sin^2\gamma + \cos^2 v + \sin^2 v + 2\sin v\sin\gamma) = 0$$

Solving for u and substituting $\cos^2\beta$ for $1 - \sin^2\beta$,

$$2\cos u = \frac{\cos^2\gamma\cos^2\beta + \cos^2 v\cos^2\beta - \sin^2\beta(\sin^2\gamma + \sin^2 v + 2\sin v\sin\gamma)}{\cos^2\beta\cos\gamma\cos v}$$

Dividing out terms and substituting β_o, which is the value of β on the boundary of the glistening surface, and which is defined in terms of surface roughness parameters [see equation (8) on page 251 of Reference 1], yields the desired result:

$$2\cos u = \frac{\cos v}{\cos\gamma} + \frac{\cos\gamma}{\cos v} - \tan^2\beta_o\frac{(\sin\gamma + \sin v)^2}{\cos\gamma\cos v}$$

This expression differs from that given in Reference 1 in that the numerator of the final term is squared.

Reference

[1] P. Beckmann and A. Spizzichino, *The Scattering of Electromagnetic Waves*, New York: Pergamon Press, 1963.

Geosynchronous Satellite Log

CARL H. SCHMITT

(Manuscript received March 5, 1984)

This note provides lists of current and future geosynchronous satellites for the Fixed Satellite Service (FSS), the Maritime Mobile Satellite Service (MMSS), and the Broadcasting Satellite Service (BSS). Satellites in the Space Research Service (SRS) are listed only when their frequencies overlap those of satellites in the other services. Future satellites are listed when information has been published by the International Frequency Registration Board (IFRB), or when satellite construction has commenced. The lists are ordered along increasing East longitude orbit position and update the previously published material [1] through December 1983.

Table 1 lists the satellites that are operating as of late December 1983, or satellites that may be capable of operating. Satellites being moved to new orbital positions are shown at their planned final positions for 1984, unless another satellite occupies the position. Refer to the remarks column for further information.

Table 2 lists newly proposed and replacement satellites and their currently planned orbital positions. Additional technical characteristics may be found in the IFRB circulars referenced, as published weekly in the circular's special sections [2] or obtained from the country or organization given.

Table 3 is the key to the frequency bands used in Tables 1 and 2. It also shows the service allocations and the applicable ITU region when the band is not allocated worldwide. The author invites inquiries and comments, and would appreciate receiving information on newly planned satellite networks as they become available.

References

[1] C. H. Schmitt, "Geosynchronous Satellite Log," *COMSAT Technical Review*, Vol. 13, No. 1, Spring 1983, pp. 193–204.

[2] *IFRB Circulars*, AR11/A/ or /C/ and SPA/AA/ or AJ/, The International Telecommunications Union IFRB, CH 1211, Geneva 20, Switzerland.

Carl H. Schmitt is an Assistant to the Director for Communications on the Staff of the Division Director, Engineering and System Integration, System Technology Services, COMSAT General Corporation.

TABLE 1. IN-ORBIT GEOSYNCHRONOUS SATELLITES FOR FIXED, BROADCAST, AND MARITIME-MOBILE SERVICES, LATE DECEMBER 1983

Subsatellite Longitude[a]	Launch Date	Satellite Designation	Country or Organization	Function	Up/Down-Link Frequency (GHz)	Remarks
5°E	11 May 1978	OTS 2	ESA	FSS, BSS	14/11	Experimental
12.9°E	16 June 1983	EUTELSAT 1 (F-1)	EUTELSAT	FSS	14/11	Designated ECS 1 before acceptance by EUTELSAT
22.9°E	18 Oct 1983	INTELSAT V (F-7)	INTELSAT	FSS	6,14/4,11	Drifting to 60°E to replace INTELSAT V (F-1), which will be relocated to 57°E
33.9°E	26 Nov 1982	RADUGA 11	USSR	FSS	6/4	
41.6°E	25 Aug 1983	RADUGA 13	USSR	FSS	6/4	
50.8°E	29 Feb 1980	RADUGA 6	USSR	FSS	6/4	
52.5°E	15 March 1982	GORIZONT 5	USSR	FSS	6,8/4,7	
55.6°E	26 June 1981	EKRAN 7	USSR	BSS	6/UHF	
57°E	29 Jan 1976	INTELSAT IV-A (F-2)	INTELSAT	FSS	6/4	Indian Ocean Region--spare; to be retired to 356°E when replaced by INTELSAT V (F-1)
60°E	23 May 1981	INTELSAT V (F-1)	INTELSAT	FSS	6,14/4,11	Indian Ocean Region--primary; INTELSAT V (F-7) to arrive mid-February
62.7°E	18 March 1981	RADUGA 8	USSR	FSS	6/4	
62.9°E	28 Sept 1982	INTELSAT V (F-5)	INTELSAT	FSS MMSS	6,14/4,11 1.6,6/1.5,4	Indian Ocean Region--Major Path 1; contains Maritime Communications System package
65°E	26 Aug 1977	SIRIO 1	Italy	BSS	UHF,17/12b,UHF	Experimental
71.3°E	21 Feb 1979	EKRAN 3	USSR	BSS	6/UHF	
72.5°E	10 June 1976	MARISAT 2	US-COMSAT General	MMSS	1.6,6/1.5,4	INMARSAT Indian Ocean Region--spare; also carries UHF capability
73.4°E	30 Aug 1983	INSAT 1B	India	FSS	6/4	
77°E	13 March 1977	PALAPA A-2	INDONESIA	FSS	6/4	
83.1°E	7 July 1976	PALAPA A-1	INDONESIA	FSS	6/4	
84.4°E	9 Oct 1981	RADUGA 10	USSR	FSS	6/4	
85.3°E	8 April 1983	RADUGA 12	USSR	FSS	6/4	
87.3°E	30 Nov 1983	GORIZONT 8	USSR	FSS	6,8/4,7	
89.1°E	6 July 1979	GORIZONT 2	USSR	FSS	6,8/4,7	
89.5°E	20 Oct 1982	GORIZONT 6	USSR	FSS	6,8/4,7	
90.5°E	26 Dec 1980	EKRAN 6	USSR	BSS	6/UHF	
95.5°E	30 July 1981	RADUGA 9	USSR	FSS	6/4	
96.4°E	16 Sept 1982	EKRAN 9	USSR	BSS	6/UHF	
97.1°E	30 Sept 1983	EKRAN 11	USSR	BSS	6/UHF	
98.5°E	12 March 1983	EKRAN 10	USSR	BSS	6/UHF	
98.7°E	5 Feb 1982	EKRAN 8	USSR	BSS	6/UHF	
110°E	18 July 1978	RADUGA 4	USSR	FSS	6/4	
114.7°E	15 Dec 1977	SAKURA (C.S.)	Japan-NTT and NASDA	FSS	6,30/4,20	Experimental

TABLE 1. IN-ORBIT GEOSYNCHRONOUS SATELLITES FOR FIXED, BROADCAST, AND MARITIME-MOBILE SERVICES, LATE DECEMBER 1983 (CONT'D)

Subsatellite Longitude[a]	Launch Date	Satellite Designation	Country or Organization	Function	Up/Down-Link Frequency (GHz)	Remarks
131.5°E	4 Feb 1983	CS 2A	Japan	FSS	6,30/4,20	
136°E	5 Aug 1983	CS 2B	Japan	FSS	6,30/4,20	
173.9°E	31 March 1978	INTELSAT IV-A (F-6)	INTELSAT	FSS	6/4	Pacific Ocean Region--primary
176.6°E	14 Oct 1976	MARISAT 3 (F-2)	US-COMSAT General	MMSS	1.6,6/1.5,4	Pacific Ocean Maritime satellite; leased to INMARSAT; also carries UHF capability
178.9°E	7 Jan 1978	INTELSAT IV-A (F-3)	INTELSAT	FSS	6/4	Pacific Ocean Region--spare
216.8°E (143.2°W)	26 Oct 1982	SATCOM V (F-5) AURORA	US-Alascom, Inc.	FSS	6/4	
220.8°E (139.2°W)	11 April 1983	SATCOM VI	US-RCA	FSS	6/4	
225.8°E (134.2°W)	28 June 1983	GALAXY 1	US-Hughes	FSS	6/4	
226.5°E (133.5°W)	13 Dec 1975	SATCOM I (F-1)	US-RCA	FSS	6/4	
229°E (131°W)	21 Nov 1981	SATCOM IIIR (F-3R)	US-RCA	FSS	6/4	On 2/25 drifting 3.5°E/day from 128.6°W
230.1°E (129.9°W)	25 Feb 1979	RADUGA 5	USSR	FSS	6/4	
232.9°E (127.1°W)	21 Feb 1981	COMSTAR 4	US-COMSAT General	FSS	6/4	
237°E (123°W)	9 June 1982	WESTAR 5	US-Western Union	FSS	6/4	
240.8°E (119.2°W)	26 March 1976	SATCOM II (F-2)	US-RCA	FSS	6/4	
242.4°E (117.6°W)	12 Nov 1982	ANIK C3 (E)	Canada-TELESAT	FSS	14/12a	
246°E (114°W)	7 May 1975	ANIK 3 (A-3)	Canada-TELESAT	FSS	6/4	
251°E (109°W)	16 Dec 1978	ANIK B1 (4)	Canada-TELESAT	FSS	6,14/4,12a	
253.5°E (106.5°W)	5 Nov 1967	ATS 3	US-NASA	Experimental	UHF,6/UHF,7,4	
255°E (105°W)	18 June 1983	ANIK C2	Canada-TELESAT	FSS	14/12a	
255.4°E (104.6°W)	26 Aug 1982	ANIK D1	Canada-TELESAT	FSS	6/4	
260°E (100°W)	15 Nov 1980	SBS 1	US-Satellite Business Systems	FSS	14/12a	
261°E (99°W)	26 Feb 1982	WESTAR 4	US-Western Union	FSS	6/4	
263°E (97°W)	24 Sept 1981	SBS 2	US-Satellite Business Systems	FSS	14/12a	
263.9°E (96.1°W)	28 July 1983	TELSTAR 3A	US-AT&T	FSS	6/4	At 262.9°E (47.1°W) on 20 Dec 1983

TABLE 1. IN-ORBIT GEOSYNCHRONOUS SATELLITES FOR FIXED, BROADCAST, AND MARITIME-MOBILE SERVICES, LATE DECEMBER 1983 (CONT'D)

Subsatellite Longitude[a]	Launch Date	Satellite Designation	Country or Organization	Function	Up/Down-Link Frequency (GHz)	Remarks
265°E (95°W)	11 Nov 1982	SBS 3	US-Satellite Business Systems	FSS	14/12a	At 263.9°E at end of 1983
269°E (91°W)	10 Aug 1979	WESTAR 3	US-Western Union	FSS	6/4	
273°E (87°W)	29 June 1978	COMSTAR 3	US-COMSAT General	FSS	6/4	
275.9°E (84.1°W)	16 Jan 1982	SATCOM IV	US-RCA	FSS	6/4	
279.8°E (80.2°W)	10 Oct 1974	WESTAR 2	US-Western Union	FSS	6/4	
284°E (76°W)	13 May 1976	COMSTAR 1	US-COMSAT General	FSS	6/4	Colocated for operational reasons
284°E (76°W)	22 July 1976	COMSTAR 2	US-COMSAT General	FSS	6/4	Colocated for operational reasons
284.9°E (75.1°W)	22 Sept 1983	GALAXY 2	US-Hughes	FSS	6/4	
288°E (72°W)	8 Sept 1983	SATCOM IIR (VII)	US-RCA	FSS	6/4	Operational 29 Nov 1983
307°E (53°W)	22 May 1975	INTELSAT IV (F-1)	INTELSAT	FSS	6/4	Atlantic Ocean Region
317°E (43°W)	20 Dec 1971	INTELSAT IV (F-3)	INTELSAT	FSS	6/4	Retired from operational service[b]
319°E (41°W)	5 April 1983	TDRS East	US-NASA US-Systematics	SRS FSS	2,15/2.2,13 6/4	
320.6°E (39.4°W)	23 Aug 1973	INTELSAT IV (F-7)	INTELSAT	FSS	6/4	Retired from operational service[b]
325.5°E (34.5°W)	6 Dec 1980	INTELSAT V (F-2)	INTELSAT	FSS	6,14/4,11	Atlantic Ocean Region--Major Path 1
329°E (31°W)	26 Sept 1975	INTELSAT IV-A (F-1)	INTELSAT	FSS	6/4	Atlantic Ocean Region
332.5°E (27.5°W)	4 March 1982	INTELSAT V (F-4)	INTELSAT	FSS	6,14/4,11	Atlantic Ocean Region--spare
333°E (27°W)	20 Dec 1981	MARECS-A	INMARSAT	MMSS	1.6,6/1.5,4	INMARSAT Atlantic Ocean Region
335.4°E (24.6°W)	15 Dec 1981	INTELSAT V (F-3)	INTELSAT	FSS	6,14/4,11	Atlantic Ocean Region--primary
335.8°E (24.2°W)	5 Oct 1980	RADUGA 7 (STATSIONAIR 8)	USSR	FSS	5,6/3	Operates below INTELSAT V frequencies
338.5°E (21.5°W)	25 May 1977	INTELSAT IV-A (F-4)	INTELSAT	FSS	6/4	Atlantic Ocean Region--spare
341.6°E (18.4°W)	19 May 1983	INTELSAT V (F-6)	INTELSAT	FSS MMSS	6,14/4,11 1.6,6/1.5,4	Atlantic Ocean Region--Major Path 2; contains Maritime Communications System package
344.9°E (15.1°W)	30 June 1983	GORIZONT 7	USSR	FSS	6,8/4,7	
345.4°E (14.6°W)	19 Feb 1976	MARISAT 1	US-COMSAT General	MMSS	UHF 1.6,6/ UHF 1.5,4	
346.2°E (13.8°W)	14 June 1980	GORIZONT 4	USSR	FSS	6,8/4,7	

TABLE 1. IN-ORBIT GEOSYNCHRONOUS SATELLITES FOR FIXED, BROADCAST, AND MARITIME-MOBILE SERVICES, LATE DECEMBER 1983 (CONT'D)

Subsatellite Longitude[a]	Launch Date	Satellite Designation	Country or Organization	Function	Up/Down-Link Frequency (GHz)	Remarks
348.8°E (11.2°W)	27 Aug 1975	SYMPHONIE 2(B)	France/ Germany	SRS	6/4	Experimental; 4.7° inclination
359°E (1°W)	21 Nov 1974	INTELSAT IV (F-8)	INTELSAT	FSS	6/4	Atlantic Ocean Region

[a]The list of satellite longitudes was compiled from the best information available.
[b]Retired INTELSAT satellites are located between 1° and 7°E or 316° and 322°E. Operations are limited to telemetry and command.

TABLE 2. PLANNED GEOSYNCHRONOUS SATELLITES FOR FIXED, BROADCAST, AND MARITIME-MOBILE SERVICES, LATE DECEMBER 1983 (CONT'D)

Subsatellite Longitude	Launch Date	Satellite Designation	Country or Organization	Function	Up/Down-Link Frequency (GHz)	IFRB Circular or Other References
1°E	1985	GDL 5	Luxembourg	FSS/BSS	6.5-7,14/11,12b	AR11/A/93/1594
4°E	1985	TELECOM 1C	France	FSS/BSS[a]	2,6,8,14/2.2,4, 7,12b,12d	AR11/A/29/1339 AR11/C/157/1598, AR11/C/131/1594
5°E	1985-86	TELE-X	Norway, Sweden	FSS/BSS	30,17/2,12b,20	AR11/A/27/1535

7°E	1984	EUTELSAT I-3	France	FSS/BSS	14/11,12b,12d	AR11/A/59/1578
7°E	1987	F-SAT 1	France	FSS	2,14,30/12d,20	AR11/A/79/1587
10°E	1984	EUTELSAT I-2 (Spare)	France	FSS/BSS	14/11,12b,12d	AR11/A/61/1578
10°E	1986	APEX	France	BSS/FSS	30/2,4,20,40,90	AR11/A/62/1578
12°E	Unknown	PROGNOZ 2	USSR	SRS	-/3,4	SPA-AA/317/1471
13°E	1984	EUTELSAT I-2	France	FSS/BSS	14/11,12b,12d	SPA-AJ/328/1492, AR11/A/61/1578&1589&1582
14°E	Unknown	Nigerian National System	Nigeria	FSS	6/4	SPA-AA/209/1346
15°E	1986	AMS 1	Israel	FSS	6,14/4,11	AR11/A/39/1554, AR11/B/30/1593
15°E	1986	AMS 2	Israel	FSS	6,14/4,11	AR11/A/39/1554
16°E	1987	SICRAL 1A	Italy	FSS	8,14a,43/7,12d,20, 43	AR11/A/44/1588
17°E	1984	SABS	Saudi Arabia	BSS	14/11	SPA-AA/235/1387
19°E	1985	GDL 6	Luxembourg	FSS,BSS	6.5-7,14/11,12d	AR11/A/94/1594
19°E	1984-85	ARABSAT I	Arab League	FSS/BSS	6/4,2.5	SPA-AJ/172/1388 RES-33/C/1/1597
20°E	Unknown	Nigerian National System	Nigeria	FSS	6/4	SPA-AA/209/1346
22°E	1987	SICRAL 1B	Italy	MMSS/FSS	UHF,8,14b,43/7, 12d,20	AR11/A/45/1557, AR11/A/45/1588

TABLE 2. PLANNED GEOSYNCHRONOUS SATELLITES FOR FIXED, BROADCAST, AND MARITIME-MOBILE SERVICES, LATE DECEMBER 1983 (CONT'D)

Subsatellite Longitude	Launch Date	Satellite Designation	Country or Organization	Function	Up/Down-Link Frequency (GHz)	IFRB Circular or Other References
23.5°E	1987	DFS 1	Germany	FSS	2,14,30/22,11, 12d,20	AR11/A/40/1556
26°E	1984-85	ARABSAT II	Arab League	FSS/BSS	6/4,2.5	SPA-AJ/173/1388, RES 33/C/2/1597
26°E	Unknown	ZOHREH 2	Iran	FSS	14/11	SPA-AA/164/1278 SPA-AJ/76/1303
28.5°E	1987	DFS 2	Germany	FSS	2,14,30/11,12d,20	AR11/A/41/1556
32°E	1987	VIDEOSAT 1	France	BSS	14/2,12b	AR11/A/80/1588
34°E	Unknown	ZOHREH 1	Iran	FSS	14/11	SPA-AA/163/1278
35°E	Unknown	PROGNOZ 3	USSR	SRS	-/3,4	SPA-AA/318/1471
38°E	1986	PAKSAT 1	Pakistan	FSS	14/11,12d	AR11/A/90/1592
40°E	1983-84	STATSIONAR 12	USSR	FSS	6/3	SPA-AA/271/1425, AJ/304/1469
41°E	Unknown	ZOHREH 4	Iran	FSS	14/11	SPA-AA/203/1330
41°E	1986	PAKSAT 2	Pakistan	FSS	14/12d	AR11/A/91/1592
45°E	Unknown	VOLNA 3	USSR	MMSS	UHF,1.6/1.5,WHF	SPA-AA/274/1425
45°E	Unknown	LOUTCH-P2	USSR	FSS	14/11	SPA-AA/178/1289 SPA-AJ/122/1340
47°E	Unknown	ZOHREH 3	Iran	FSS	14/11	SPA-AA/165/1278
53°E	Unknown	LOUTCH 2	USSR	FSS	14/11	SPA-AJ/85/1318 Leased to Intersputnik
57°E	1987	INTELSAT VI (IND 2)	INTELSAT	FSS	5,6,14/3,4,11	AR11/A/72/1584
57°E	1984	INTELSAT V-A (IND 2)	INTELSAT	FSS	6,14/4,11	AR11/A/68/1580
57°E	1984	INTELSAT V (IND 3)	INTELSAT	FSS	6,14/4,11	SPA-AA/262/1423
		INTELSAT MCS (IND C)	INTELSAT	MMSS	1.6,6/1.5,4	SPA-AA/274/1425
60°E	1984	INTELSAT V-A (IND 1)	INTELSAT	FSS	6,14/4,11	AR11/A/67/1580
60°E	1987	INTELSAT VI (IND 1)	INTELSAT	FSS	5,6,14/3,4,11	AR11/A/71/1584
64.5°E	Unknown	MARECS (IND 1)	INMARSAT (F)	MMSS	1.6,6/1.5,4	SPA-AJ/243/1432
66°E	1984	INTELSAT IV-A (IND 1)	INTELSAT	FSS	6/4	SPA-AA/82/1182/52/1162
66°E	1984	INTELSAT V (IND 4)	INTELSAT	FSS	6,14/4,11	SPA-AA/253/1419
		INTELSAT MCS (IND D)-spare	INTELSAT	MMSS	1.6,6/1.5,11	SPA-AA/275/1425
70°E	1984	STW 2	China, Peoples Republic of	FSS	6/4	SPA-AA/142/1255
73°E	Unknown	MARECS (IND 2)	INMARSAT (F)	MMSS	1.6,6/1.5,4	AR11/D/3/1551
80°E	1984	STATSIONAR 13	USSR	FSS	6/4	SPA-AA/276/1426 SPA-AJ/305/1469

TABLE 2. PLANNED GEOSYNCHRONOUS SATELLITES FOR FIXED, BROADCAST, AND MARITIME-MOBILE SERVICES, LATE DECEMBER 1983 (CONT'D)

Subsatellite Longitude	Launch Date	Satellite Designation	Country or Organization	Function	Up/Down-Link Frequency (GHz)	IFRB Circular or Other References
80°E	Unknown	POTOK 2	USSR	FSS	6/4	SPA-AA/345/1485
85°E	Unknown	LOUTCH P3	USSR	FSS	14/11	SPA-AA/179/1289 SPA-AJ/123/1340
85°E	Unknown	VOLNA 5	USSR	MMSS	UHF,1.6/1.5,UHF	SPA-AA/173/1286; SPA-AJ/100/1329
90°E	Unknown	LOUTCH 3	USSR	FSS	14/11	SPA-AJ/86/1318
90°E	Unknown	VOLNA 8	USSR	MMSS	1.6/1.5	SPA-AA/289/1445 AR11/C/15/1589
95°E	1985	CSDRN	USSR	SRS	15/10,11,13	SPA-AA/342/1484
99°E	Unknown	STATSIONAR-T	USSR	FSS/BSS	6/UHF	RES-SPA2-3-AA2-1153
99°E	Unknown	STATSIONAR-T2	USSR	FSS/BSS	6/UHF	RES-SPA2-3-AA10/1426 SPA-AJ/316/1473
108°E	Unknown	PALAPA-B1	Indonesia	FSS	6/4	SPA-AA/197/1319
110°E	1984	BS 2	Japan TCSJ	BSS	2,14/12b,2	SPA-AA/305/1459 AR11/C/10/1556
110°E	1985	BS 2	Japan	BSS	2,14/12b,2	Spare in Orbit
113°E	1984	PALAPA-B2	Indonesia	FSS	6/4	SPA-AA/198/1319
118°E	1984	PALAPA-B3	Indonesia	FSS	6/4	SPA-AA/196/1319

125°E	1984	STW 1	China, Peoples Republic of	FSS	6/4	SPA-AJ/240/1431
128°E	1984	STATSIONAR 15	USSR	FSS	6/4	SPA-AA/273/1425 SPA-AJ/307/1469
135°E	Unknown	CSE	Japan (KATSURA)	BSS	6,20/2,4,30	SPA-AJ/19/1226
140°E	Unknown	LOUTCH 4	USSR	FSS	14/11	SPA-AJ/87/1318
140°E	Unknown	STATSIONAR 7	USSR	FSS	6/4	SPA-AJ/31/1251
145°E	1987	STATSIONAR 16	USSR	FSS	6/4	AR11/A/76/1593&1586
156°E	1985	AUSSAT 1	Australia (OTC)	FSS/BSS	14/12b	RES SPA2-3/AA/12/1456, 115/1575, SPA-AA/372/1575
160°E	1985	AUSSAT 2	Australia (OTC)	FSS/BSS	14/12b	RES SPA2-3/AA/13/1456, 116/1575, SPA-AA/373/1575, RES33/B/1/1583
165°E	1985	AUSSAT 3	Australia (OTC)	FSS/BSS	14/12b	RES SPA2-3/AA/14/1456, 117/1575, SPA-AA/374/1575
173°E	1984	INTELSAT V (PAC 1)	INTELSAT	FSS	6,14/4.11	AR11/C/170/1600
173°E	1987	INTELSAT V-A (PAC 1)	INTELSAT	FSS	6,14/4,11	AR11/A/65/1580
176°E	1986	INTELSAT V (PAC 2)	INTELSAT	FSS	6,14/4,11	AR11/A/81/1588 SPA-AA/255/1419
176°E	1987	INTELSAT V-A (PAC 2)	INTELSAT	FSS	6,14/4,11	AR11/A/66/1580

TABLE 2. PLANNED GEOSYNCHRONOUS SATELLITES FOR FIXED, BROADCAST, AND MARITIME-MOBILE SERVICES, LATE DECEMBER 1983 (CONT'D)

Subsatellite Longitude	Launch Date	Satellite Designation	Country or Organization	Function	Up/Down-Link Frequency (GHz)	IFRB Circular or Other References
177.5°E	1984	MARECS B (PAC 1)	INMARSAT (F)	MMSS	1.6,6/1.5,4	SPA-AA/220/1353
179°E	1984	INTELSAT V (PAC 3)	INTELSAT	FSS	6,14/4,11	SPA-AJ/377/1511
		INTELSAT MCS (PAC A)	INTELSAT	MMSS	1.6,6/1.5,4	SPA-AA/332/1476 SPA/AJ/477/1517
189°E (171°W)	1984-85	TDRS West	USA-NASA/SPACECOM	SRS	2,15/2.2,13	SPA-AA/232/1381, AR11/C/47/1568
			USA-SYSTEMAT. GEN	FSS	6/4	See FCC Filing
190°E (170°W)	Unknown	LOUTCH-P4	USSR	FSS	14/11	SPA-AA/180/1289 SPA-AJ/124/1340
190°E (170°W)	Unknown	STATSIONAR 10	USSR	FSS	6/4	SPA-AJ/64/1280
190°E (170°W)	Unknown	VOLNA 7	USSR	MMSS	UHF,1.6/1.5,UHF	SPA-AA/175/1286
192°E (168°W)	Unknown	POTOK 3	USSR	FSS	6/4	SPA-AA/346/1485
200°E (160°W)	1985	ESDRN	USSR	SRS	15/10,11,13	SPA-AA/343/1484
214°E (146°W)	1985	AMIGO 2	Mexico	BSS	17/12b	RES 33/A/2/1560
215°E (145°W)	Unknown	ILHUICAHUA 4	Mexico	FSS	6,14/4,12a	AR11/A/25/1533
219°E (141°W)	1986	ILHUICAHUA 3	Mexico	FSS	6,14/4,12a	AR11/A/24,1533
224°E (136°W)	1985	AMIGO 1	Mexico	BSS	17/12b	RES 33/A/1/1560
241°E (119°W)	1984	SPACENET-I	US - GTE	FSS	6,14/4,12a	AR11/A/10/1525&ADD-1/ 1548
243.5°E (116.5°W)	1985	ILHUICAHUA 2 (MORELOS)	Mexico	FSS	6,14/4,12a	AR11/A/30/1540
246°E (114°W)	1984	TELESAT D2 (ANIK)	Canada-TELESAT	FSS	6/4	SPA-AA/358/1500
246.5°E (113.5°W)	1985	ILHUICAHUA 1 (MORELOS)	Mexico	FSS	6,14/4,12a	AR11/A/28/1539
247.5°E (112.5°W)	1984-85	ANIK C1	Canada-TELESAT	FSS	14/12a	TELESAT
253.5°E (106.5°W)	1987	MSAT	Canada	FSS/MMSS	UHF-EHF/UHF-EHF	AR11/A/55/1563
254°E (106°W)	1985	GSTAR-I	US-GTE Satellite	FSS	14/12a	AR11/A/14/1525,& -ADD-1/1548
257°E (103°W)	1986	GSTAR-II	US-GTE Satellite	FSS	14/12a	AR11/A/15/1525,& -ADD-1/1548
259.2°E (100.8°W)	1987	STC-ECSA	US-Satellite Television Corp.	BSS	17/12b	Satellites under construction by RCA
266°E (94°W)	1984	USASAT 6C	US	FSS	14/12a	AR11/A/35/1553
273°E (87°W)	1984	TELSTAR-III B	US-AT&A	FSS	6/4	AR11/A/9/1524
277°E (83°W)	1988	STSC 1	Cuba	FSS	6/4	AR11/A/58/1578

TABLE 2. PLANNED GEOSYNCHRONOUS SATELLITES FOR FIXED, BROADCAST, AND MARITIME-MOBILE SERVICES, LATE DECEMBER 1983 (CONT'D)

Subsatellite Longitude	Launch Date	Satellite Designation	Country or Organization	Function	Up/Down-Link Frequency (GHz)	IFRB Circular or Other References
281°F (79°W)	1984-85	TDRS Central	USA-NASA/SPACECOM USA-SYSTEMAT. GEN	SRS FSS	2,15/2.2,13 6/4	SPA-AA/233/1381 FCC Filing by Systematics Gen
281°E (79°W)	1984	USASAT 7D	USA	FSS	6,14/4,12a	AR11/C/50/1568 AR11/A/12/1525
284.6°E (75.4°W)	1986 1986	SATCOL 1A SATCOL 1B	Colombia Colombia	FSS FSS	6/4 6/4	SPA-AA/322,323/1474 AR11/C/79/1573
284°E (75°W)	1986	SATCOL 2	Colombia	FSS	6/4	SPA-AJ/127,128/1343 AR11/C/80/1587
286°E (74°W)	1985	USASAT 7-A	USA	FSS	6/4	SPA-AA/312/1465
290°E (70°W)	1985	SBTS A-1	Brazil	FSS	6/4	AR11/A/16/1526, AR11/C/94/1576
290°E (70°W)	1985	USASAT 7C	USA	FSS	6/4	AR11/A/11/1525
294°E (66°W)	1985	USASAT 8A	USA	FSS	6/4	AR11/A/36/1553
295°E (65°W)	1985	SBTS A-2	Brazil	FSS	6/4	AR11/A/17/1526
298°E (62°W)	1986	USASAT 8B	USA	FSS	6/4	AR11/A/37/1553, AR11/C/99/1576
302°E (58°W)	1987	USASAT 8C	USA	FSS	6/4	AR11/A/38/1553

307°E (53°W)	1984[c]	INTELSAT IV (ATL 5)	INTELSAT	FSS	6/4	SPA-AA/89/1188 SPA-AJ/351/1500
307°E (53°W)	1984[c]	INTELSAT IV-A (ATL 3)	INTELSAT	FSS	6/4	SPA-AJ/208/1418
307°E (53°W)	1986[c]	INTELSAT V CONTINENTAL 1	INTELSAT	FSS	6,14/4,11	AR11/A/82/1588
307°E (53°W)	1986	INTELSAT V-B	INTELSAT	FSS	6,14,14a/4,11,12a, 12d	Under construction by Ford Aerospace
310°E (50°W)	1984[c]	INTELSAT IV (ATL 1)	INTELSAT	FSS	14,6/4,11	AR11/A/75/1586
310°E (50°W)	1984[c]	INTELSAT IV-A (ATL 2)	INTELSAT	FSS	6/4	AR11/C/140/1596
310°E (50°W)	1985[c]	INTELSAT V CONTINENTAL 2	INTELSAT	FSS	6,14/4,11	AR11/A/75/1586 AR11/C/139/1596
310°E (50°W)	1986	INTELSAT V-A CONTINENTAL 2	INTELSAT	FSS	6,14/4,11	AR11/A/74/1586
319.5°E (40.5°W)	1986	INTELSAT V-B	INTELSAT	FSS	6,14,14a/4,11,12a, 12d	Under construction by Ford Aerospace
322.5°E (37.5°W)	1987	VIDEOSAT-2	France	BSS	14/2,12b	AR11/A/86/1589
325.5E (34.5°W)	1987	INTELSAT V-A (ATL 3)	INTELSAT	FSS	6,14/4,11	AR11/A/63/1580
325.5°E (34.5°W)	Unknown	INTELSAT MCS (ATL E)	INTELSAT	MMSS	1.6,6/1.5,4	SPA-AA/284/1432
329°E (31°W)	1986	UNISAT I	U.K.-BRITISH TELECOM	FSS	14/11,12b,12d	AR11/A/26/1534
332.5°E (27.5°W)	1985	INTELSAT V-A (ATL 2)	INTELSAT	FSS	6,14/4,11	SPA-AA/335/1478 AR11/C/123/1592

TABLE 2. PLANNED GEOSYNCHRONOUS SATELLITES FOR FIXED, BROADCAST, AND MARITIME-MOBILE SERVICES, LATE DECEMBER 1983 (CONT'D)

Subsatellite Longitude	Launch Date	Satellite Designation	Country or Organization	Function	Up/Down-Link Frequency (GHz)	IFRB Circular or Other References
332.5°E (27.5°W)	1987	INTELSAT VI (ATL 2)	INTELSAT	FSS	5,6,14/3,4,11	AR11/A/70/1584
335°E (25°W)	Unknown	LOUTCH-P1	USSR	FSS	14/11	SPA-AA/177/1289
335°E (25°W)	Unknown	STATSIONAR 8	USSR	FSS	6/4	SPA-AJ/62/1280
335°E (25°W)	Unknown	VOLNA 1	USSR	MMSS	UHF,1.6/1.5,UHF	SPA-AA/169/1286
335.5°E (24.5°W)	1984	INTELSAT V-A (ATL 1)	INTELSAT	FSS	5,6,14/3,4,11	SPA-AA/334/1478 AR11/C/122/1592
335.5°E (24.5°W)	1987	INTELSAT VI (ATL 1)	INTELSAT	FSS	6,14/4,11	AR11/A/69/1584
335.5°E (24.5°W)	Unknown	INTELSAT MCS (ATL D)	INTELSAT	MMSS	1.6,6/1.5,4	SPA-AJ/349/1500
336°E (24°W)	Unknown	PROGNOZ 1	USSR	SRS	-/3,4	SPA-AA/316/1471
338.5°E (21.5°W)	1986	INTELSAT V (ATL 5)	INTELSAT	FSS	6,14/4,11	SPA-AA/252/1419
		MCS ATC	INTELSAT	MMSS	1.6,6/1.4,4	SPA-AA/282/1432
340°E (20°W)	1985	GDL 4	Luxembourg	FSS/BSS	6.5-7,14/11,12d	AR11/A/92/1594
341°E (19°W)	1986	LUXSAT	Luxembourg	BSS	17/12b	AR11/A/20/1529
341°E (19°W)	1984-85	TDF 1	France	BSS	17/12b	AR11/A/57/1570 AR11/C/107/1578
341°E (19°W)	1985	L-SAT	ESA (France)	BSS/FSS	13,14a,30/12b,20	SPA-AA/308/1463 AR11/A/33/1544 AR11/A/88/1590 AR11/A/57/1570 AR11/C/124/1592
341°E (19°W)	1986	HELVESAT 1	Switzerland	BSS	17,18/12b,2	SPA-AA/365/1512
341°E (19°W)	1984	TV-SAT	Germany	BSS	17,18/11,12b	SPA-AA/311/1464 SPA-AA/325/1474
341°E (19°W)	1986	SARIT	Italy	BSS	17,18/12b	SPA-AA/360/1505 SPA-AA/371/1547
341.5°E (18.5°W)	1986-87	INTELSAT V-A (ATL 4)	INTELSAT	FSS	6,14/4,11	AR11/A/64/1580
341.5°E (18.5°W)	1986	INTELSAT V-B	INTELSAT	FSS	6,14/4,11,12a,12d	Under construction by Ford Aerospace; replaces INTELSAT V-A, above
344°E (16°W)	1983-84	STATSIONAR 11	USSR	FSS	6/4	SPA-AA/270/1425 SPA-AJ/303/1469
344°E (16°W)	1985	WSDRN	USSR	SRS	15/10,11,13	SPA-AA/341/1484
346°E (14°W)	Unknown	LOUTCH 1	USSR	FSS	14/11	SPA-AA/157/1262 SPA-AJ/84/1318
346.5°E (13.5°W)	Unknown	POTOK 1	USSR	FSS	-/4	SPA-AA/344/1485
347.5°E (12.5°W)	Unknown[b]	MAROTS-B	France	MMSS	1.6,UHF/1.5,UHF	SPA-AA/204/1333

TABLE 2. PLANNED GEOSYNCHRONOUS SATELLITES FOR FIXED, BROADCAST, AND MARITIME-MOBILE SERVICES. LATE DECEMBER 1983 (CONT'D)

Subsatellite Longitude	Launch Date	Satellite Designation	Country or Organization	Function	Up/Down-Link Frequency (GHz)	IFRB Circular or Other References
349°E (11°W)	1986	F-SAT 2	France	FSS	2,14,30/12d,20	AR11/A/73/1586
352°E (8°W)	1984	TELECOM 1-A	France	FSS/BSS[a]	2,6,8,14/2.2,4,7, 12b,12d	SPA-AJ/299/1461 AR11/C/125/1593
355°E (5°W)	1984	TELECOM 1-B	France	FSS/BSS[a]	2,6,8,14/2.2 4,7,12b,12d	SPA-AJ/300/1461 AR11/C/128/1593
356°E (4°W)	Unknown[c]	INTELSAT IV (ATL 1)	INTELSAT	FSS	6/4	AR11/C/139/1596
356°E (4°W)	1985[c]	INTELSAT IV-A (ATL 1)	INTELSAT	FSS	6/4	AR11/C/121/1591
359°E (1°W)	1984[c]	INTELSAT IV-A (ATL 2)	INTELSAT	FSS	6/4	SPA-AJ/371/1509
359°E (1°W)	1986	INTELSAT V CONTINENTAL 4	INTELSAT	FSS	6,14/4,11	AR11/A/83/1588

[a]Community BSS only.
[b]Launch failed; no current plans to replace.
[c]Already launched; moves to new location at date shown.

TABLE 3. FREQUENCY BAND KEY WITH SERVICE ALLOCATIONS*

Frequency Abbreviation	ITU Frequency Band (GHz) and Service	Link Direction
UHF	0.13 to 1.5	Up or Down (see Tables 1 and 2)
1.5	1.530 to 1.535, 1.535 to 1.544, MMSS	Down
1.6	1.6265 to 1.6455, MMSS	Up
2.-	Various 2-GHz frequencies	Up or Down (see Tables 1 and 2)
2.5	2.5 to 2.69 GHz, BSS	Down
3	3.400 to 3.900, FSS	Down
4	3.700 to 4.200, FSS; 4,175–4,200 MMSS feeder	Down
5	5.725 to 5.925, FSS	Up
6	5.925 to 6.425, FSS; 6,404–6,425 MMSS feeder	Up
11	10.700 to 11.700, FSS	Down
12a	11.7 to 12.2, FSS, Region 2	Down
12b	11.7 to 12.5, BSS, Regions 1 and 3	Down
12c	12.2 to 12.7, BSS, Region 2	Down
12d	12.5 to 12.75, FSS, Regions 1 and 3	Down
13	13.0 to 13.25, FSS/SRS, secondary†	Up
13a	13.25 to 14.0, SRS	Up
14	14.0 to 14.5, FSS	Up
14a	14.0 to 14.25, FSS	Up
15	14.5 to 15.35, SRS secondary	Up
17	17.3 to 18.1, FSS, BSS feeder	Up
20	17.7 to 20, FSS, 20.2 to 21.2, FSS	Down
30	29.5 to 30, FSS, 30 to 31, FSS	Up
43.5	43.5 to 47.0, MSS	Not Specified

*If regions (ITU) are not shown, the allocation is worldwide.
†The Link direction for the SRS is Down.

Translations of Abstracts

Expérience internationale de commutation par paquets à grande vitesse

J. S. McCoskey, W. Redman, W. Morgart,
B. Hung et A. Agarwal

Sommaire

Une liaison expérimentale de transmission de données à grande vitesse a été établie entre Clarksburg (Maryland) et Oberpfaffenhofen (République fédérale d'Allemagne), pour permettre d'effectuer les essais pratiques et examiner le fonctionnement d'un processeur de télécommunications utilisé dans des circuits numériques de satellite à vitesse élevée, et démontrer la faisabilité de certains services de télécommunications. A cette fin, on a connecté deux processeurs de télécommunications au moyen de liaisons à 1,544 Mbit/s assurées par des stations terriennes installées sur le toit, et des répéteurs à pinceaux à 14/11 GHz d'un satellite INTELSAT V de la région de l'océan Atlantique.

Les résultats de l'expérience ont révélé que des services intégrés, tels que le service de téléconférence à analyse lente, les transferts de fichiers principaux à grande vitesse, le fac-similé, ainsi que les télécommunications asynchrones à faible vitesse entre terminaux et ordinateurs principaux, peuvent être transmis de cette façon. L'effet des protocoles de transmission de données sur le rendement de débit et sur le fonctionnement global du réseau a été examiné. Un système de multiplexage hybride a été mis en oeuvre, qui a permis d'utiliser une voie commune pour les courants de trafic et le trafic par paquets.

a 800 y 1600 MHz. Se ofrecen configuraciones del LMSS para tres ejemplos específicos, correspondientes a la masa de carga útil equivalente de un subsistema de comunicaciones marítimas de INTELSAT V (MCS), un satélite dotado de equipo para servicios empresariales (SBS) y un satélite INTELSAT V. Se dan alternativas de sistemas para cada uno de estos casos a fin de ilustrar las distintas permutaciones entre el costo de una terminal móvil (y ganancia de antena), tipo de modulación y capacidad del sistema. Uno de dichos ejemplos consiste en un sistema de 800 MHz y 10 canales que utiliza modulación delta adaptable y terminales móviles con ganancias de antena de 5 dBi y sólo requiere una masa de carga útil de 67 kg.

Author Index, CTR 1983

The following index gives the code numbers that are to be used for ordering reprints from Lab Records, COMSAT Laboratories, 22300 Comsat Drive, Clarksburg, Maryland 20871.

† INTELSAT Assignee.

MARTIN, J., Arnstein, D., and Adams, C., "Communications Performance Specifications of the INTELSAT V with Maritime Communications Subsystem," Spring, pp. 173–179 [CTR83/248].

McNALLY, P. J., "Ion Implantation of Boron in GaAs Devices," Fall, pp. 437–450 [CTR83/259].

MEULENBERG, A., JR., and Arndt, R. A., "Limitations on Solar Cell Open-Circuit Voltage and Efficiency," Spring, pp. 57–70 [CTR83/240].

MINER, R., see Chakraborty, D. [CTR83/253].

OLSEN, R. L., see Rogers, D. V. [CTR83/257].

ONUFRY, M., see Gupta, V. [CTR83/247].

PARK, Y. L., see Shimi, T. N. [CTR83/245].

REDMAN, M. D., see Yam, E. S. [CTR83/239].

RHODES, S. A., Fang, R. J., and Chang, P. Y., "Coded Octal Phase Shift Keying in TDMA Satellite Communications," Fall, pp. 221–258 [CTR83/251].

ROGERS, D. V., "Simple Method for Estimating Atmospheric Absorption at 1 to 15 GHz," Spring, pp. 157–163 [CTR83/246].

ROGERS, D. V., and Olsen, R. L.,* "Multiple Scattering in Coherent Radio-Wave Propagation Through Rain," Fall, pp. 385–401 [CTR83/257].

ROSCH, G., see Chakraborty, D. [CTR83/253].

SCHAEFER, D. J., see Hammer, A. [CTR83/243].

SCHMITT, C. H., "Geosynchronous Satellite Log," Spring, pp. 193–204 [CTR83/250].

SHENOY, A., and Johnson, P., "Serial Implementation of Viterbi Decoders," Fall, pp. 315–330 [CTR83/254].

SHIMI, T. N., and Park, Y. L., "Efficient Approaches to Erlang Loss Function Computations," Spring, pp. 143–155 [CTR83/245].

STRUHARIK, S. J., "Rain and Ice Depolarization Measurements at 4 GHz in Sitka, Alaska," Fall, pp. 403–435 [CTR83/258].

SUYDERHOUD, H., see Gupta, V. [CTR83/247].

SZARVAS, G. G., and Campanella, S. J., "Impact of Speech Interpolation and Data on FDM/FM Transmission," Fall, pp. 259–274 [CTR83/252].

VIRUPAKSHA, K., see Gupta, V. [CTR83/247].

YAM, E. S., and Redman, M. D., "Development of a 60-Channel FDM-TDM Transmultiplexer," Spring, pp. 1–56 [CTR83/239].

ZAGHLOUL, A. I., "Matching Networks in Linear Phased Arrays," Spring, pp. 71–86 [CTR83/241].

* Non-COMSAT author.

Index of 1983 Presentations and Publications by COMSAT Authors

The following is a cross-referenced index of publications and presentations by COMSAT authors in 1983, not including papers published in the *COMSAT Technical Review*. The code number at the end of an entry is the reprint number by which copies may be ordered from Lab Records, COMSAT Laboratories, 22300 Comsat Drive, Clarksburg, MD 20871.

ALLNUTT, J. E.,* and Rogers, D. V., "A Site Diversity Model for Satellite Communications Systems," Third Int. Conf. on Antennas and Propagation, Norwich, UK, April 12–15, 1983, *Proc.*, pp. 106–110 [83CLR12].

APPLE, J. H., see Assal, F. T. [83CLR04].

ARNSTEIN, D. S., see Suyderhoud, H. [83CLR26].

ASSAL, F. T., Gupta, R. K., Betaharon, K.*, Zaghloul, A., and Apple, J. H., "A Wideband Satellite Microwave Switch Matrix for SS/TDMA Communications," *IEEE Journal on Selected Areas in Comm.*, Jan. 1983, Vol. SAC-1, No. 1, pp. 223–231 [83CLR04].

ASSAL, F. T., see Cahana, D. [83CLR46]; Gupta, R. [83CLR55]; Mott, R. [83CLR70]; Forcina, G. [83CLR36]; Potukuchi, J. R. [83CLR52], [83CLR56].

ATIA, A. E., see Egri, R. A. [83CLR20]; Zaki, K. A. [83CLR75], [83CLR24].

BAKER, S., see Mattis, W. [83CLR34].

BANGARA, S.,* Betaharon, K.,* Mahle, C., and Riginos, V., "INTELSAT V In-Orbit Test," *Journal of Electrical and Electronics Engineering*, Australia, Vol. 3, No. 3, Sept. 1983, pp. 155–164 [83CLR62].

BANGARA, S.,* Riginos, V., and Fullett K., "Maritime Communication System Package of INTELSAT V," Third Int. Conf. on Sat. Systems for Mobile Comm. and Navigation, London, UK, June 7–9, 1983, *Proc.*, pp. 55–59 [83CLR14].

BARGELLINI, P. L., "Communications Satellites," *McGraw-Hill Encyclopedia of Science and Technology*, 6th ed., McGraw-Hill Book Company, 1983 (in press).

BARGELLINI, P. L., "Satellite and Space Communications," *Reference Data for Radio Engineers*, 7th ed., E. C. Jordan, Editor, Howard W. Sams & Co., Inc. (in press).

* Non-COMSAT author.

BOYER, K. L., "Transform-Based Image Coder," Sixth Int. Conf. on Dig. Sat. Comm., Phoenix, AZ, Sept. 19–23, 1983, *Proc.*, pp. VII-A-31–VII-A-36 [83CLR35].

BRANDEL, D. L., see Kaminsky, Y. [83CLR17].

BRISKMAN, R. D., "Domestic Satellite Services for Rural Areas," IEEE Global Telecomm. Conf., San Diego, CA, Nov. 28–Dec. 1, 1983, *Conf. Rec.*, Vol. 1, pp. 266–269.†

BRISKMAN, R. D., and Savage, M., "Economical Domestic/Regional Satellite Communications Systems for Developing Areas," 23rd International Scientific Space Convention, Rome, Italy, March 24–25, 1983, *Proc.*, pp. 90–98.†

BURNHAM, J.,* and Williams, J. W., "New Techniques for Dealing with Corona in Compact High-Voltage Converters," 10th Int. Solid State Power Electronics Conf., San Diego, CA, March 22–24, 1983, *Proc.*, pp. H1-2-1–H1-2-15 [83CLR64].

CAHANA, D., "A New Transmission Line Approach for Designing Spiral Microstrip Inductors for Microwave Integrated Circuits," IEEE MTT-S Int. Microwave Symp., Boston, MA, May 31–June 3, 1983, *Digest*, pp. 245–247 [83CLR22].

CAHANA, D., and Assal, F., "Power-Efficient Communications Satellite Configuration for Small Mobile Systems," IEEE Global Telecom. Conf., San Diego, CA, Nov. 28–Dec. 1, 1983, *Conf. Rec.*, Vol. 1, pp. 523–529 [83CLR46].

CAMPANELLA, S. J., "Companded Single Sideband (CSSB) AM/FDMA Performance," *Int. Journal of Sat. Comm.*, Vol. 1, No. 1, July–Sept. 1983, pp. 25–29 [83CLR42].

CAMPANELLA, S. J., and Colby, R. J.,* "Network Control for Multibeam TDMA and SS/TDMA," *IEEE Journal on Selected Areas in Comm.*, Jan. 1983, Vol. SAC-1, No. 1, pp. 174–187 [83CLR02].

CAMPANELLA, S. J., and Inukai, T., "Satellite Switch State Time Plan Control," Sixth Int. Conf. on Dig. Sat. Comm., Phoenix, AZ, Sept. 19–23, 1983, *Proc.*, pp. X-16–X-26 [83CLR37].

CAMPANELLA, S. J., see Inukai, T. [83CLR03], [83CLR39].

CARPENTER, E. W., see Sandrin, W. A. [83CLR15].

CHAKRABORTY, D., and Kappes, J. M., "Characterization of 12-kW TWT HPAs for Mixed TDMA/FDMA Operation Using INTELSAT V Frequency Plan," Sixth Int. Conf. on Dig. Sat. Comm., Phoenix, AZ, Sept. 19–23, 1983, *Proc.*, pp. I-B-13–I-B-19 [83CLR27].

* Non-COMSAT author.

† Reprints can be obtained by contacting COMSAT General Corporation.

CHAKRABORTY, D., Kappes, J. M., and Phiel, J.,* "120-Mbit/s QPSK Signal Transmission Tests via INTELSAT V and Andover II Link," Sixth Int. Conf. on Dig. Sat. Comm., Phoenix, AZ, Sept. 19–23, 1983, *Proc.*, pp. II-24–II-33 [83CLR30].

CHAKRABORTY, D., Kato, K.,* and Lei, R.,* "Consideration of 120-Mbit/s Burst-Mode Adaptive Threshold Detection with Estimated Sequence Processor Development," Sixth Int. Conf. on Dig. Sat. Comm., Phoenix, AZ, Sept. 19–23, 1983, *Proc.*, pp. VI-9–VI-15 [83CLR33].

CHAKRABORTY, D., and McCune, E. W.,* "A Wideband Klystron HPA Development for 120-Mbit/s QPSK Signaling," Sixth Int. Conf. on Dig. Sat. Comm., Phoenix, AZ, Sept. 19–23, 1983, *Proc.*, pp. I-B-20–I-B-27 [83CLR28].

CHAKRABORTY, D., and Wolejsza, C. J., "A Survey of Modem Design and Performance in Digital Satellite Communications," *IEEE Journal on Selected Areas in Comm.*, Jan. 1983, Vol. SAC-1, No. 1, pp. 5–20 [83CLR01].

CHANG, P., see Fang, R. [83CLR50].

CHEN, C. H., Zaghloul, A., and Tulintseff, A., "Slot Array Design for K_u-Band Satellite Communications," IEEE Int. Symp. on Antennas and Propagation, Houston, TX, May 23–26, 1983, *Digest*, Vol. 2, pp. 401–404 [83CLR60].

CHITRE, D. M., "Data Broadcast Protocols and Their Throughput Efficiencies," Sixth Int. Conf. on Dig. Sat. Comm., Phoenix, AZ, Sept. 19–23, 1983, pp. XII-1–XII-7 [83CLR40].

CHITRE, D. M., and Garber, S. L., "International Packet Network Service," IEEE COMPCON '83, Fall, Arlington, VA, Sept. 25–29, 1983, pp. 56–65 [83CLR65].

CORCORAN, F. L., see Suyderhoud, H. [83CLR26].

DEVIEUX, C. L., see Klisch, F. M.†

DHADESUGOOR, V. R., "Voice and Data Integration Using Digital Silence Detection for Satellite Applications," IEEE Global Telecomm. Conf., San Diego, CA, Nov. 28–Dec. 1, 1983, *Conf. Rec.*, Vol. 3, pp. 1201–1206 [83CLR51].

DHADESUGOOR, V. R., see Wu, C. T. [83CLR49].

DOBYNS, T., see Inukai, T. [83CLR39].

EAVES, R. E., see Lee, Y. S. [83CLR19].

EGRI, R. G., Williams, A. E., and Atia, A. E.,* "A Contiguous-Band Multiplexer Design," IEEE MTT-S Int. Microwave Symp., Boston, MA, May 31–June 3, 1983, *Digest*, pp. 86–88 [83CLR20].

* Non-COMSAT author.

† Reprints can be obtained by contacting COMSAT General Corporation.

EGRI, R. G., see Williams, A. E. [83CLR23].

ERDLE, F. E., Feigenbaum, I. A., and Talcott, J. W., Jr., "Reliability Programs for Commercial Communications Satellites," *IEEE Trans. on Reliability*, August 1983, Vol. R-32, No. 3, pp. 236–239 [83CLR66].

FANG, D. J., "A Practical Model for Rain Depolarization Evaluation at Centimeter and Millimeter Wavelengths," *Proc.*, 1983 IEEE Military Comm. Conf., IEEE Publication 83CH1909-1, pp. 124–133 [83CLR67].

FANG, D. J., and Liu, C. H., "A Morphological Study of Gigahertz Equatorial Scintillations in the Asian Region," *Radio Science*, March–April 1983, Vol. 18, No. 2, pp. 241–252 [83CLR07].

FANG, D. J., and Ott, R. H., "A Low-Elevation Angle L-Band Maritime Propagation Measurement and Modeling," Third Int. Conf. on Sat. Systems for Mobile Comm. and Navigation, London, UK, June 7–9, 1983, *Proc.*, pp. 45–50 [83CLR13].

FANG, D. J., see Ott, R. H. [83CLR44]; Wang, T. [83CLR57].

FANG, R., Chang, P., and Hemmati, F., "Coded 8-PSK Transmission Over 72-MHz Nonlinear Transponders at 140-Mbit/s Information Rate for Trunking Applications," IEEE Global Telecom. Conf., San Diego, CA, Nov. 28–Dec. 1, 1983, *Conf. Rec.*, Vol. 2, pp. 1013–1020 [83CLR50].

FANG, R., and Mackenthun, K., "A Low-Cost Thin Route Digital Communications System for the Pacific Island Nations," IEEE Global Telecom. Conf., San Diego, CA, Nov. 28–Dec. 1, 1983, *Conf. Rec.*, Vol. 1, pp. 279–286 [83CLR45].

FANG, R., see Hagmann, W. [83CLR53].

FEIGENBAUM, I. A., see Erdle, F. E. [83CLR66].

FORCINA, G.,* Pontano, B.,* Assal, F., and Gupta, R., "Fault Detection/Diagnostics for the INTELSAT VI SS-TDMA Subsystem," Sixth Int. Conf. on Dig. Sat. Comm., Phoenix, AZ, Sept. 19–23, 1983, *Proc.*, pp. X-1–X-8 [83CLR36].

FULLETT, K., and Riginos, V., "Desktop Test Orbiting Communications Satellites," *Microwave Systems News*, Feb. 1983, Vol. 13, No. 2, pp. 77–78 [83CLR05].

FULLETT, K., see Bangara, S. [83CLR14].

GARBER, S. L., see Chitre, D. M. [83CLR65].

GETSINGER, G. W., "Circuit Duals on Planar Transmission Media," IEEE MTT-S Int. Microwave Symp., Boston, MA, May 31–June 3, 1983, *Digest*, pp. 154–156 [83CLR21].

* Non-COMSAT author.

GLASGOW, R. J., "Digital Electronic Message Service: An Overview," IEEE Global Telecom. Conf., San Diego, CA, Nov. 28–Dec. 1, 1983, *Conf. Rec.*, Vol. 2, pp. 814–818 [83CLR48].

GREENE, K. H., see Paul, D. K. [83CLR72].

GUPTA, R., Assal F., and Potukuchi, J., "Ground-Based Techniques for Monitoring Performance of SS-TDMA Communications Satellites," IEEE National Telesystems Conf., San Francisco, CA, Nov. 14–16, 1983, *Proc.*, pp. 336–342 [83CLR55].

GUPTA, R., see Assal, F. T. [83CLR04]; Forcina, G. [83CLR36].

HAGMANN, W., "Influence of Phase Noise and Fading on PSK Synchronization," IEEE Int. Conf. on Comm., Boston, MA, June 19–22, 1983, *Conf. Rec.*, Vol. 1, pp. 504–508 [83CLR18].

HAGMANN, W., Rhodes, S., and Fang, R., "International Business Communications via INTELSAT K-band Transponders," IEEE 1983 Global Telecom. Conf., San Diego, CA, Nov. 28-Dec. 1, 1983, *Conf. Rec.*, Vol. 3, pp. 1351–1357 [83CLR53].

HEMMATI, F., see Fang, R. [83CLR50].

HORNA, O. A., "Cancellation of Acoustic Feedback in Teleconference Rooms," IEEE SOUTHEASTCON '83, Orlando, FL, April 11–14, 1983 *Proc.*, pp. 284–289 [83CLR06].

HORNA, O. A., "Echo Control in Teleconferencing," IEEE Global Telecom. Conf., San Diego, CA, Nov. 28–Dec. 1, 1983, *Conf. Rec.*, Vol. 1, pp. 536–542 [83CLR47].

HYMAN, N. L., "Numerical Method for Spacecraft Radiator Mass Minimization," AIAA 18th Thermophysics Conf., Montreal, Canada, June 1–3, 1983, [83CLR10].

INUKAI, T., and Campanella, S. J., "Optimal On-Board Clock Control," *IEEE Journal on Selected Areas in Comm.*, Jan. 1983, Vol. SAC-1, No. 1, pp. 208–213 [83CLR03].

INUKAI, T., Campanella, S. J., and Dobyns, T., "On-Board Baseband Processing: Rate Conversion," Sixth Int. Conf. on Dig. Sat. Comm., Phoenix, AZ, Sept. 19–23, 1983, *Proc.*, pp. XI-24–XI-31 [83CLR39].

INUKAI, T., see Campanella, S. J. [83CLR37].

JOHNSON, R. R., see Williams, A. E. [83CLR23].

JONES, M. E., "Laboratory Hardware Simulation Measurements of 120-Mbit/s QPSK/TDMA Transmission Performance in the INTELSAT V System," Sixth Int. Conf. on Dig. Sat. Comm., Phoenix, AZ, Sept. 19–23, 1983, *Proc.*, pp. I-A-1–I-A-8 [83CLR25].

KAMINSKY, Y.,* and Brandel, D. L., "U. S. Satellite EPIRB Test

* Non-COMSAT author.

Results," Third Int. Conf. on Sat. Systems for Mobile Comm. and Navigation, London, UK, June 7–9, 1983, *Proc.*, pp. 216–224 [83CLR17].

KAPPES, J. M., see Chakraborty, D. [83CLR27], [83CLR30].

KAUL, A., McCoskey, J., Lang, H.,* and Dodel, H.,* "An Experiment in International High-Speed Packet Switching via Satellite," Sixth Int. Conf. on Dig. Sat. Comm., Phoenix, AZ, Sept. 19–23, 1983, *Proc.*, pp. II-34–II-43 [83CLR31].

KELLY, W. H., and Reisenweber, J. H., "Thermal Modeling and Design Considerations for Large Communications Spacecraft," AIAA 18th Thermophysics Conf., Montreal, Canada, June 1–3, 1983 [83CLR11].

KIRKENDALL, T. D., and Remmel, T. P., "Thermal Wave Imaging of GaAs Material and Devices," *Proc.*, 10th Int. Cong. on X-Ray Optics and Microanalysis, Toulouse, France, Sept. 1983 [83CLR61].

KLISCH, F. M., and Devieux, C. L., "Developments in Broadcast Satellite Systems," Presented at NCY '83 International Telecommunications Forum, Seoul, Korea, Aug. 5, 1983.†

KOEPF, G. A., "Amplification by Simulated Raman Scattering in Low-Loss Optical Fibers," *Electronics and Communications*, 1983, Vol. 37, pp. 145–152 [83CLR68].

KRICHEVSKY, V., "The Optimum Beam Scanning in the Offset Single and Dual Reflector Antennas," IEEE Int. Symp. on Antennas and Propagation, Houston, TX, May 23–26, 1983, *Digest*, Vol. 1, pp. 72–75 [83CLR58].

KROLL, R., see Mott, R. [83CLR70].

KUMAR, P. N., see Wang, T. [83CLR57].

LEE, Y. S., and Eaves, R. E., "Implementation Issues of Intersatellite Links for Future INTELSAT Requirements," IEEE Int. Conf. on Comm., Boston, MA, June 19–22, 1983, *Conf. Rec.*, Vol. 3, pp. 1189–1195 [83CLR19].

LEWIS, H., see Suyderhoud, H. [83CLR26].

LIN, H. C., see Shenai, K. [83CLR75].

LINDSTROM, R., see Ridings, R. [83CLR29].

LIPKE, D. W., "INMARSAT Second Generation Space Segment," IEEE Nat. Telesystems Conf., San Francisco, CA, Nov. 14–16, 1983, *Proc.*, pp. 321–324 [83CLR54].

LIPKE, D. W., "Use of INMARSAT Facilities for Aeronautical Satellite Communications," Third Int. Conf. on Sat. Systems for Mobile Comm. and Navigation, London, UK, June 7–9, 1983, *Proc.*, pp. 212–215 [83CLR16].

* Non-COMSAT author.

† Reprints can be obtained by contacting COMSAT General Corporation.

LIU, C. H., see Fang, D. J. [83CLR07].

LUNSFORD, J., see Ridings, R. [83CLR29].

MACKENTHUN, K., see Fang, R. [83CLR45].

MAHLE, C., see Bangara, S. [83CLR62].

MARSHALEK, R. G., and Davidson, F. M.,* Photoresponse Characteristics of Thin-Film Nickel-Nickel Oxide-Nickel Tunneling Junctions," *IEEE Journal of Quantum Electronics*, April 1983, Vol. QE-19, No. 4, pp. 743–754 [83CLR69].

MATTIS, W., Wolejsza, C., and Baker, S., "Digitally Controlled Transversal Equalizer," Sixth Int. Conf. on Dig. Sat. Comm., Phoenix, AZ, Sept. 19–23, 1983, *Proc.*, pp. VI-23–VI-29 [83CLR34].

McCOSKEY, J., see Kaul, A. [83CLR31].

MOTT, R., Assal, F., and Kroll, R., "Guard Space and Burst Duration Monitor for TDMA," International Satellite Communications Conference, Ottawa, Canada, June 14–17, 1983, *Proc.*, pp. 8.5.1–8.5.5 [83CLR70].

MOTT, R., see Potukuchi, J. [83CLR52].

OSLUND, R. J., "Hurricane Iwa: Hawaii's Unwelcome Guest," *Telephony*, Vol. 205, Sept. 26, 1983, pp. 60–66 [83CLR77].

OSLUND, R. J., Pacific Facilities Planning Process: An Appropriate Mechanism," Pacific Telecom. Conf., Honolulu, HI, Jan. 16–19, 1983, *PTC '83 Directions*, pp. 41–53 [83CLR76].

OTT, R. H., "Computational Problems with the EBC Method Applied to Scattering by Lossy Periodic Surfaces," IEEE Int. Symp. on Antennas and Propagation," Houston, TX, May 23–26, 1983, *Digest*, Vol. 1, pp. 240–243 [83CLR59].

OTT, R. H., and Fang, D. J., "Comparison of the Extended Boundary Condition Method and Perturbation Method for Scattering from a Sinusoidal Sea Surface," *Journal of Mathematical Physics*, Vol. 24, No. 8, 1983, pp. 2240–2249 [83CLR44].

OTT, R. H., see Fang, D. J. [83CLR13].

PAUL, D. K., and Greene, K. H., "Digital Optical Repeater for Submerged Communications Systems," Los Alamos Conf. on Optics, Albuquerque, NM, *Proc.*, SPIE, Vol. 380, pp. 376–388 [83CLR72].

PHIEL, J. F.,* and Thorne, C. R., "INTELSAT TDMA System Monitor," Sixth Int. Conf. on Dig. Sat. Comm., Phoenix, AZ, Sept. 19–23, 1983, *Proc.*, pp. IV-14–IV-21 [83CLR32].

PONTANO, B. A.,* and Szarvas, G. G., "Introduction of Companded FDM/FM Operation into the INTELSAT System," Int. Journal of Sat. Comm., Vol. 1, No. 1, July–Sept. 1983, pp. 31–38 [83CLR43].

* Non-COMSAT author.

POTTS, J. B., "ISDN," *Satellite Communications*, Dec. 1983, Vol. 7, No. 13, pp. 45–47 [83CLR71].

POTUKUCHI, J., and Assal, F., "TDMA Performance Monitoring of Communications Satellite Transmitters," IEEE Nat. Telesystems Conf., San Francisco, CA, Nov. 14–16, 1983, *Proc.*, pp. 410–414 [83CLR56].

POTUKUCHI, J., see Gupta, R. [83CLR55].

POTUKUCHI, J., Assal, F., and Mott, R., "Communications Satellite System Monitoring for Time-Division Multiple Access," IEEE Global Telecom. Conf., San Diego, CA, Nov. 28–Dec. 1, 1983, *Conf. Rec.*, Vol. 3, pp. 1338–1346 [83CLR52].

REINHART, E. E., "Development of Direct Broadcasting Satellite Systems in the USA," Presented at Symposium Satelliten für Rundfunk und Fernsehen (Symposium on TV Broadcasting Satellites), the Hermann-Oberth-Gesellschaft, Berlin, West Germany, Sept. 2–3, 1983.‡

REINHART, E. E., "Direct Broadcasting of Television by Satellite," Presented at IEEE Southcon Conference, Jan. 1983, Atlanta, Georgia.‡

REINHART, E. E., "Orbit-Spectrum Efficiency of the 12-GHz Broadcasting Satellite Plans," IEEE Global Telecommunications Conference (Globecom-83), Nov. 28–Dec. 1, 1983, San Diego, CA.‡

REISENWEBER, J. H., see Kelly, W. H. [83CLR11].

REMMEL, T. P., see Kirkendall, T. D. [83CLR61].

REVESZ, A. G., and Walrafen, G. E.,* "Structural Interpretations for Some Raman Lines from Vitreous Silica," *Journal of Non-Crystalline Solids*, March 1983, Vol. 54, No. 3, pp. 323–333 [83CLR08].

RHODES, S., see Hagmann, W. [83CLR53].

RIDINGS, R., Lunsford, J., Lindstrom, R., and Rieser, J., "Verification Tests of a Prototype INTELSAT TDMA/DSI Terminal," Sixth Int. Conf., on Dig. Sat. Comm., Phoenix, AZ, Sept. 19–23, 1983, *Proc.*, pp. II-14–II-23 [83CLR29].

RIESER, J., see Ridings, R. [83CLR29].

RIGINOS, V., see Bangara, S. [83CLR14], [83CLR62]; Fullett, K. [83CLR05].

ROGERS, D. V., see Allnutt, J. E. [83CLR12].

SANDRIN, W. A., "Program for Three-Dimensional Polar Plots," *IEEE Trans. on Antennas and Propagation*, Vol. AP-31, No. 3, May 1983, pp. 542–544 [83CLR09].

* Non-COMSAT author.

‡ Reprints can be obtained by contacting Satellite Television Corporation.

SANDRIN, W. A., and Carpenter, E. W., "Antenna Studies for INMARSAT Standard C Terminals," Third Int. Conf. on Sat. Systems for Mobile Comm. and Navigation, London, UK, June 7–9, 1983, *Proc.*, pp. 212–215 [83CLR15].

SAVAGE, M., see Briskman, R. D.†

SHENAI, K., and Lin, H. C., "Analytical Solutions for Avalanche-Breakdown Voltages of Single-Diffused Gaussian Junctions," *Solid-State Electronics*, Vol. 26, No. 3, pp. 211–216 [83CLR75].

SNYDER, J. S., "High-Speed Viterbi Decoding of High-Rate Codes," Sixth Int. Conf. on Dig. Sat. Comm., Phoenix, AZ, Sept. 19–23, 1983, *Proc.*, pp. XII-16–XII-23 [83CLR41].

SUYDERHOUD, H., Corcoran, F. L., Arnstein, D. S., and Lewis, H., "Investigation of 9.6-kbit/s Data Transmission via a PCM Link at 64-kbit/s With and Without Link Errors," Sixth Int. Conf. on Dig. Sat. Comm., Phoenix, AZ, Sept. 19–23, 1983, *Proc.*, pp. I-A-26–I-A-33 [83CLR26].

SZARVAS, G. G., see Pontano, B. A. [83CLR43].

TALCOTT, J. W., Jr., see Erdle, F. E. [83CLR66].

THORNE, C. R., see Phiel, J. F. [83CLR32].

TULINTSEFF, A.,* see Chen, C. H. [83CLR60].

WANG, T., Kumar, P. N., and Fang, D. J., "Laser Rain Gauge: Near-Field Effect," *Applied Optics*, Dec. 15, 1983, Vol. 22, No. 24, pp. 4008–4012 [83CLR57].

WELTI, G. R., "Some Design Concepts for INTELSAT VII," Sixth Int. Conf. on Dig. Sat. Comm., Phoenix, AZ, Sept. 19–23, 1983, *Proc.*, pp. XI-1–XI-8 [83CLR38].

WILLIAMS, A. E., Egri, R. G., and Johnson, R. R., "Automatic Measurement of Filter Coupling Parameters," IEEE MTT-S Int. Microwave Symp., Boston, MA, May 31, 1983, *Digest*, pp. 418–420 [83CLR23].

WILLIAMS, A. E., see Egri, R. G. [83CLR20].

WILLIAMS, J. W., see Burnham, J. [83CLR64].

WOLEJSZA, C. J., see Chakraborty, D. [83CLR01]; Mattis, W. [83CLR34].

WU, C. T., and Dhadesugoor, V. R., "An Adaptive Multiple Access Protocol for Integrated Voice/Data Local Area Networks," IEEE Global Telecom. Conf., San Diego, CA, Nov. 28–Dec. 1, 1983, *Conf. Rec.*, Vol. 2, pp. 959–963 [83CLR49].

ZAGHLOUL, A., see Assal, F. T. [83CLR04]; Chen, C. H. [83CLR60].

* Non-COMSAT author.

† Reprints can be obtained by contacting COMSAT General Corporation.

ZAKI, K. A.,* and Atia, A. E., "Modes in Dielectric Loaded Wa
and Resonators," *IEEE Trans. on Microwave Theory and Tec*
Vol. MTT-31, No. 12, pp. 1039–1045 [83CLR75].
ZAKI, K. A.,* and Atia, A. E., "Resonant Frequencies of Dielectri
Waveguide Cavities," IEEE MTT-S Int. Microwave Symp., Bost
May 31–June 3, 1983, *Digest,* pp. 421–423 [83CLR24].

* Non-COMSAT author.